The Role of AP2σ Variants in Calcitropic and Non-Calcitropic Disorders

A DPhil Thesis in Biomedical and Clinical Sciences submitted to the University of Oxford



by

Victoria J Stokes

Academic Endocrine Unit
Radcliffe Department of Medicine
University of Oxford

Oriel College,
University of Oxford

Hilary Term 2022

Contents

ACKNOWLEDGEMENTS 5
1 ABSTRACT 6
2 ABBREVIATIONS 7
3 INTRODUCTION 9
3.1 The Adaptor Proteins 9
3.2 The role of the Adaptor Protein 2 complex in clathrin mediated endocytosis 13
3.3 G-protein coupled receptors (GPCRs) are transmembrane receptors internalised by CME 17
3.4 The calcium-sensing receptor 18
3.4.1 The calcium-sensing receptor in calcium homeostasis 19
3.4.2 The CaSR in non-calcitropic physiology 25
3.5 Signalling via the CaSR 29
3.6 Disorders of calcium signalling 43
3.6.1 Amino acid structure and size 43
3.6.2 Familial Hypocalciuric Hypercalcaemia (FHH) 45
3.6.3 Autosomal Dominant Hypocalcaemia 49
3.6.4 Role of drug treatments in calcitropic and non-calcitropic disorders 52
3.7 The role of Ap2σ mutations in FHH3 57
3.7.1 Bone and non-calcitropic effects of AP2σ mutations 60
3.8 *In vivo* models of disorders of calcium homeostasis 63
4 AIMS 67
5 METHODS 69
5.1 Patients 69
5.1.1 Informed consent 69
5.2 Generation of plasmid expression constructs 69
5.3 Cells 71
5.3.1 Transient transfection of cells 72

5.3.2 Western blotting 72
5.3.3 CASR signalling response assays 74
5.3.4 Drug compound studies 74
5.3.5 Co-immunoprecipitation of FLAC2 cells 75
5.4 Mouse studies 75
5.4.1 Ethical approval 75
5.4.2 Maintenance of mouse colonies 75
5.4.3 CRISPR-Cas induced mutations in mice 75
5.4.4 Methods of genotyping mice 79
5.4.5 Characterisation of Arg15Leu, Arg15Cys and Met117Ile mice 79
5.4.6 Administration of cinacalcet to Arg15Leu mice 80
5.4.7 Three-dimensional micro-computerised tomography (micro-CT) imaging of *Ap2s1-Arg15Leu* mouse embryos 81
5.5 Bioinformatic analysis 81
5.6 Crystal structure modelling of variants and mutations 82
5.7 Statistical analysis 82
6 RESULTS - INVESTIGATION OF AP2σ VARIANTS IN LARGE POPULATION DATASETS 84
6.1 Identification of AP2σ variants in the Regeneron DiscovEHR, ExAC and dbSNP Datasets 84
6.2 Bioinformatic and experimental assessment of AP2σ variants identified in the DiscovEHR, ExAC and dbSNP datasets 87
6.2.1 Examination of residue conservation and secondary structure of AP2σ variants 87
6.2.2 PyMOL analysis of AP2σ variants 88
6.2.3 SIFT and PolyPhen-2 analysis of AP2σ variants 95
6.2.4 Assessment of the effect of the AP2σ variants on CaSR-mediated Ca^{2+}_i signalling 97
7 RESULTS – ESTABLISHING MOUSE MODELS OF FHH3 104

7.1 CRISPR-Cas-induced *Ap2s1* mutant Arg15Leu mice 107
7.1.1 Generation of *Ap2s1-Arg15Leu* mice 107
7.1.2 *Ap2s1-Arg15Leu* mouse biochemical phenotyping 109
7.1.3 *Ap2s1-Arg15Leu* mouse bone phenotyping 114
7.1.4 Analysis of the 2 surviving $Ap2s1^{L15/L15}$ mice 115
7.1.5 Analysis of the effect of cinacalcet on serum calcium and PTH in the *Ap2s1-Arg15Leu* mouse 118
7.1.6 Assessment of serum PTH concentrations with increasing mouse age in the *Ap2s1-Arg15Leu* mouse 120
7.1.7 Structural analysis of *Ap2s1-Arg15Leu* mouse embryos using micro-CT 122
7.2 CRISPR-Cas-induced *Ap2s1* mutant Arg15Cys mice 127
7.2.1 Generation of Arg15Cys mice 127
7.2.2 Arg15Cys mouse biochemical phenotype 128
7.2.3 Arg15Cys mouse bone phenotyping 132
7.2.4 Assessment of serum PTH concentrations with increasing mouse age 133
7.3 CRISPR-Cas-induced *Ap2s1* mutant Met117Ile mice 133
7.3.1 Generation of Met117Ile mice 133
7.3.2 Met117Ile mouse biochemical phenotype 134
7.4 Evaluation of the Arg15Leu, Arg15Cys and Met117Ile mice as *in vivo* models of FHH3 136
8 RESULTS - INVESTIGATION OF *AP2S1* VARIANTS IN PATIENTS WITH NEUROCOGNITIVE DISORDERS 144
8.1 Neurocognitive disorders in patients with FHH3 144
8.2 Identification of AP2σ-Arg10 variants associated with impaired neurocognition .146
8.2.1 Genotypic and phenotypic characteristics of the *AP2S1* Arg10 variant cohort 146
8.2.2 *In silico* assessment of the AP2σ-Arg10 variants 147
8.2.3 *In vitro* assessment of AP2σ–Arg15Leu and the AP2σ-Arg10 variants 154

9 DISCUSSION 164
9.1 Investigation of AP2σ variants in large population datasets 164
9.2 Establishing mouse models of FHH3 169
9.2.1 The Ap2s1-Arg15Leu and Ap2s1-Arg15Cys mouse models 170
9.2.2 The Ap2s1-Met117Ile mouse 180
9.3 Investigation of *AP2S1* variants in patients with neurocognitive disorders 181
10 FUTURE STUDIES 184
11 APPENDIX 191
12 REFERENCES 193

THE ROLE OF AP2σ VARIANTS IN CALCITROPIC AND NON-CALCITROPIC DISORDERS

ACKNOWLEDGEMENTS

First and foremost, I would like to thank Professor Raj Thakker. I first met Raj as an enthusiastic Registrar, having decided fairly late on in my training that I would like to complement my clinical skills with research. Raj was incredibly supportive of this move, and helped me get experience and preliminary data which led to me being awarded a Wellcome Trust Clinical Fellowship. This support has continued throughout my DPhil, extended by 2 periods of maternity leave, and finally into a post as an Endocrine Consultant at Addenbrooke's hospital, Cambridge, where I am lucky enough to have the opportunity to combine research and clinical practice in my career.

I am very grateful for the support I have received from my other supervisors: Prof Roger Cox and Prof Patrik Rorsman, and also from Dr Fadil Hannan, who have all provided invaluable advice on different aspects of my thesis. Additionally, undertaking these studies would not have been possible without the day to day guidance and patience of my post-doctoral supervisors, Dr Caroline Gorvin, Dr Asha Bayliss and Dr Mark Stevenson.

I have been incredibly lucky to have the wider support of the Thakker lab and OCDEM staff, for which I am very grateful. I feel very privileged to have undertaken my DPhil studies at Oriel college, Oxford University and would like to thank the founders of the University and the college support staff for this inspiring academic environment. Throughout my DPhil I have been generously funded by the Wellcome Trust and I would like to thank the Trust for this financial support.

I would like to thank my collaborators who have made this work possible. I would like to thank the team at MRC-Harwell, in particular Michelle Stewart and Dr Lydia Teboul, for their help with my mouse studies. I am grateful to my collaborators at Regeneron for allowing me to use their excellent DiscovEHR dataset. I would also like to thank my collaborators in the USA for providing data on the nine patients with *AP2S1* variants and neurodevelopmental disorders.

Getting through my DPhil has required more than academic support and I could not have done it without my friends and family. My Mum, who has provided constant and consistent emotional support, as well as enduring long stories about experiments gone wrong. My beautiful children, born during these studies, for giving me perspective, cuddles, and the desire to make them proud. And my wonderful husband Andrew, who's done his fair share of boring stories, perspective-giving and cuddles, but has also supported me in following my chosen career path and all of the day-to-day allowances that entails! Finally, this DPhil thesis is dedicated to my Dad, Alan, who managed the difficult task of imparting wisdom with a cutting sense of humour, and of being simultaneously fatherly and a best friend from an early age. I could not have done this without him.

1 ABSTRACT

The Adaptor Protein 2 (AP2) is a heterotetrameric complex comprising of α, β, μ and σ-subunits, and it has an integral role in clathrin-mediated endocytosis (CME). CME is the process by which plasma membrane constituents are internalised, and this is the major endocytic pathway in mammalian cells. Missense mutations of AP2σ (Arg15Cys, Arg15His and Arg15Leu) cause impaired internalisation of the calcium-sensing receptor (CaSR), a G-protein coupled receptor (GPCR), and lead to Familial Hypocalciuric Hypercalcaemia type 3 (FHH3), a condition associated with moderate to severe hypercalcaemia, which may be symptomatic and associated with low bone mineral density and pancreatitis. Patients with FHH3-associated mutations may also have non-calcitropic disorders, including neurodevelopmental disorders.

This thesis aims to further explore the role of AP2σ variants in calcitropic and non-calcitropic disorders by studying large population datasets to search for novel *AP2S1* variants; generating mutant mouse models of FHH3; and investigating the role of AP2σ mutations in neurodevelopmental disorders.

My studies have identified 3 additional *AP2S1* variants in humans, Thr112Met, Met117Ile and Glu142Lys, that affect intracellular calcium (Ca^{2+}_i) signalling *in vitro*. Clinical data was available for the Met117Ile only, and the patient had mild hypercalcaemia. The identification of these novel variants potentially increases the spectrum of known mutations in *AP2S1*, suggesting a change in practice to include exon 5 in addition to exon 2 when screening the gene in FHH patients, and demonstrates the utility of large-scale sequencing databases in identifying genetic variants.

The heterozygote *Ap2s1*$^{+/L15}$, *Ap2s1*$^{+/C15}$ and *Ap2s1*$^{+/I117}$ mice were viable and reached adulthood. However, the homozygote *Ap2s1*$^{L15/L15}$ died in the early neonatal period, whilst the *Ap2s1*$^{C15/C15}$ mice were subviable with significantly fewer mice surviving weaning and by adulthood, whereas the *Ap2s1*$^{I117/I117}$ mice were viable and reached adulthood. The *Ap2s1*$^{+/L15}$ and *Ap2s1*$^{+/C15}$ mice had hypercalcaemia, with the hypercalcaemia being significantly greater in the *Ap2s1*$^{+/L15}$ than the *Ap2s1*$^{+/C15}$ mice. The homozygote *Ap2s1*$^{L15/L15}$ and *Ap2s1*$^{C15/C15}$ mice had significantly greater elevations in plasma calcium than their heterozygote counterparts. The *Ap2s1*$^{+/I117}$ and *Ap2s1*$^{I117/I117}$ mice did not have hypercalcaemia. In conclusion, my studies have expanded the phenotypic spectrum associated with *AP2S1* mutations, and have also established *Ap2s1* mouse models that will enable the evaluation of the roles of AP2σ in calcium homeostasis and endosomal trafficking of the CaSR through pathophysiological studies that are difficult to undertake in patients. The *Ap2s1*$^{+/L15}$ and the *Ap2s1*$^{+/C15}$ mutant mice represent models for human FHH3.

Finally, I describe nine children with heterozygous variants of *AP2S1* Arg10 in association with neurodevelopmental delay, thereby suggesting a wider role in non-calcitropic phenotype of *AP2S1* mutations.

2 ABBREVIATIONS

$1,25(OH)_2D_3$	1,25-hydroxyvitamin D_3
24h uCa	24 hour urinary calcium
$25(OH)D_3$	25-hydroxyvitamin D_3
ADH	autosomal dominant hypocalcaemia
ADHD	attention deficit hyperactivity disorder
ADIS	agonist-driven insertional signalling
ALP	alkaline phosphatase
ANOVA	analysis of variance
AP2	adaptor protein 2
AP2S1	adaptor-related protein complex 2, sigma 1 subunit gene
AP2σ	AP2 sigma-subunit
ARMS-PCR	amplification refractory mutation system-PCR
BMC	bone mineral content
BMD	bone mineral density
$[Ca^{2+}]_e$	extracellular calcium concentration
$[Ca^{2+}]_i$	intracellular calcium concentration
CaSR	calcium-sensing receptor
CASR	calcium-sensing receptor gene
CCCR	calcium-creatinine clearance ratio
CCV	clathrin coated vesicle
CME	clathrin-mediated endocytosis
CR domain	cysteine rich domain
CRISPR	class 2 clustered regularly interspaced short palindromic repeat
CTX-1	C-terminal cross-linking telopeptide of type 1 collagen
DAG	diacylglycerol
DMSO	dimethyl sulfoxide
DNA	deoxyribonucleic acid
DXA	dual-energy X-ray absorptiometry
ECD	extracellular domain
ECL	extracellular loop
EDTA	ethylenediaminetetraacetic acid
ELISA	enzyme-linked immunoassay
ENU	N-ethyl-N-nitrosourea
ERK1/2	extracellular signal-regulated kinase 1/2
ExAC	exome aggregation consortium
FACS	fluorescence-activated cell sorting
FGF-23	Fibroblast Growth Factor-23
FHH	Familial Hypocalciuric Hypercalcaemia
GABABR	γ-amino isobutyric acid B receptor
GDP	guanine diphosphate
GTP	guanine triphosphate
GNA11	G-protein subunit alpha 11 gene

gnomAD	genome aggregation database
GPCR	G-protein coupled receptor
$G\alpha_{11}$	Guanine nucleotide-binding protein subunit alpha-11
gRNA	guide RNA
mRNA	messenger RNA
HA	haemagglutinin
HEK293 cells	human embryonic kidney 293 cells
HDR	homology directed repair
ICL	intracellular loop
IP_3	inositol triphosphate
LB	lysogeny broth
MAF	minor allele frequency
MAPK	mitogen-activated protein kinase
mGluR	metabotropic glutamate receptor
NHEJ	non-homologous end joining
NR	normal range
NSHPT	neonatal severe primary hyperparathyroidism
$25(OH)D_3$	25-hydroxyvitamin D_3
$1,25(OH)_2D_3$	1,25-hydroxyvitamin D_3
PAM	protospacer adjacent motif
PBS	phosphate buffered saline
PCR	polymerase chain reaction
PKC	protein kinase C
PLC	phospholipase C
pLOF	predicted loss-of-function
P1NP	procollagen type 1 N-terminal propeptide
PTH	parathyroid hormone
PTH	parathyroid hormone gene
RNA	ribonucleic acid
RFP	red-fluorescent protein
sCa	serum calcium
sCr	serum creatinine
SEM	standard error of the mean
SNP	single nucleotide polymorphism
SNV	single nucleotide variant
spCas	*s. pyogenes* Cas9
sPO_4	serum phosphate
sPTH	serum PTH
TMD	transmembrane domain
TPM	transcripts per million
UCCR	urinary calcium to creatinine clearance ratio
UTR	untranslated region
VFTD	venus flytrap domain
WES	whole-exome sequencing
WT	wild-type

3 INTRODUCTION

3.1 The Adaptor Proteins

Adaptor protein (AP) complexes are each comprised of 4 subunits, including two large subunits (one γ, α, δ, ε, or ζ-subunit and one β1, β2, β 3, β4 or β5-subunit), one medium subunit (μ1, μ2 , μ3, μ4 or μ5), and one small subunit (σ1, σ2, σ3, σ4, or σ5). There are 5 different AP complexes that have been identified to date: AP1, AP2, AP3, AP4, and AP5, each made up of different combinations of these subunits. AP1, AP2 and AP3 have multiple subunit isoforms which are encoded by different genes. AP1 has two large γ-subunit isoforms (γ1 and γ2), two medium μ-subunit isoforms (μ1A and μ1B) and three small σ-subunit isoforms (σ1A, σ1B and σ1C); AP2 has two large α-subunit isoforms (αA and αC); and AP3 has two large β-subunit isoforms (β3A and β3B), two medium μ-subunit isoforms (μ3A and μ3B) and two small σ-subunit isoforms (σ3A and σ3B). AP4 and AP5 have only one isoform (Table 1). Disorders of APs are associated with disease, and different combinations of the subunit isoforms within each AP complex produces different tissue-specific expression and function (1). For example, mutations of the σ2-subunit of AP2 results in Familial Hypocalciuric Hypercalcaemia type 3 (FHH3), a disorder of calcium homeostasis. The AP3β3A subunit isoform is ubiquitously expressed, whereas the -β3B isoform is only expressed in neurons. Mutations of *AP3B1*, which encodes AP3β3A, are associated with Hermansky-Pudlak syndrome 2 (HPS2) a multi-system disorder characterized by oculocutaneous albinism, bleeding diathesis, neutropenia and in some, pulmonary fibrosis (2). In contrast, mutations of *AP3B2*, which encodes AP3β3B, give rise to Early Infantile Epileptic Encephalopathy 48 (EIEE48), a severe condition affecting the neurological system in isolation, characterised by global developmental delay with absent

speech, poor / absent motor development and onset of seizures typically in the first year of life (3) (Table 1) (4).

The action of APs is to form short-lived complexes with other proteins and transduce membrane activation signals to the major cytoplasmic signalling pathways. The five AP complexes localize to different intracellular compartments and mediate membrane trafficking in distinct pathways (Figure 1). AP1 complexes have been extensively studied and it has become convention that AP1 complexes containing μ1A or μ1B are referred to as AP1A or AP1B, regardless of differences in the other subunits (4). AP1A is ubiquitously expressed, whereas AP1B is epithelial-specific. Both isomers of AP1 are found in the trans-Golgi network (TGN) and endosomes and mediate bidirectional transport between them (5, 6). They appear to act to mediate polarized sorting in biosynthetic and endocytic pathways (4, 7-9). AP2 localises to the plasma membrane and facilitates the CME of a wide range of proteins. It is discussed in more detail below. AP3 occurs in tubular endosomal compartments, mediates cargo transport to late endosomes and has a role in lysosome-related organelle (LRO) biogenesis (4); and AP4 localises to the TGN and is involved in unidirectional transport from the TGN to endosomes, or to the basolateral plasma membrane in a clathrin-dependent manner in both neurons and epithelial cells (10-12). AP5 is the least studied of the APs. It interacts with SPG11 (spastic paraplegia type 11) and SPG15 (spastic paraplegia type 15) proteins, and it has been hypothesised that they form a complex, with AP5 facilitating protein sorting, SPG15 involved in membrane docking by interacting with PI3P (phosphatidylinositol 3-phosphate), and SPG11 (possibly together with SPG15) forming a scaffold (13).

Table 1. Details of the 5 Adaptor Protein complexes (AP1-5), their comprising subunits and subunit isomers. Adapted and updated from Park et al (2014)(4) and Dell'Angelica et al (2019) (14). *AP1 has either γ1 or γ2 subunit. TGN=trans-Golgi network; OMIM=Online Mendelian Inheritance in Man reference number; CME=Clathrin-mediated endocytosis; LRO=lysosome-related organelle.

Adaptor	Subunit	Isomer	Gene	Expression	Localisation	Sorting signal	Function	Associated disease (OMIM and ref)
AP1	γ1 / γ2*	-	*AP1G1 / AP1G2*		TGN and	YXXØ	Bidirectional transport	
	β1	-	*AP1B1*		endosomes	[DE]XXXL[LI]	between TGN and	
	μ1	μ1A	*AP1M1*	Ubiquitous			endosomes; basolateral	
		μ1B	*AP1M2*	Epithelium			sorting in epithelial cells	
	σ1	σ1A	*AP1S1*	May function in neurons and skin				MEDNIK syndrome (Erythrokeratodermia variabilis 3, EKV3) OMIM 609313 Montpetit et al., 2008 (15)
		σ1B	*AP1S2*	Neurons				Fried syndrome, Pettigrew syndrome (PGS), or X-linked syndromic mental retardation 5 (MRXS5) OMIM 304340 Tarpey et al., 2006 (16), Saillour et al., 2007 (17)
		σ1C	*AP1S3*	Skin				Susceptibility to pustular psoriasis 15 (PSOR15) OMIM 616106 Setta-Kaffetzi et al., 2014 (18)
AP2	α	αA	*AP2A1*	Ubiquitous	Plasma	YXXØ	CME	
		αC	*AP2A3*		membrane	YXXØ		
	β2	-	*AP2B1*			[DE]XXXL[LI]		
	μ2	-	*AP2M1*					Developmental and epileptic encephalopathy Helbig et al. 2019 (19)
	σ2	-	*AP2S1*					Familial hypocalciuric hypercalcemia 3 (FHH3) OMIM 600740 Nesbit et al., 2013(20)
AP3	δ	-	*AP3D1*		Endosomes	YXXØ	LRO biogenesis	Hermansky-Pudlak syndrome 10 (HPS10) OMIM 617050 Ammann et al., 2016 (21)
	β3	β3A	*AP3B1*	Ubiquitous		[DE]XXXL[LI]		Hermansky-Pudlak syndrome 2 (HPS2) OMIM 608233 Dell'Angelica et al., 1999 (2)

		β3B	*AP3B2*	Neurons		[DE]XXXL[LI]		Early infantile epileptic encephalopathy 48 (EIEE48) OMIM 617276 Assoum et al., 2016 (3)
	μ3	μ3A	*AP3M1*	Ubiquitous				
		μ3B	*AP3M2*	Neurons				
	σ3	σ3A	*AP3S1*	Ubiquitous				
		σ3B	*AP3S2*	Neurons				
AP4	ε	-	*AP4E1*		TGN	YX[FYL][FL]E	Transport from TGN to endosomes or basolateral plasma membrane; polarised sorting	Hereditary spastic paraplegia 51 (SPG51) OMIM 613744 Moreno-De-Luca et al., 2011 (22), Abou Jamra et al., 2011 (23)
								Familial persistent stuttering 1 (STUT1) OMIM 184450 Raza et al., 2015 (24)
	β4	-	*AP4B1*					Hereditary spastic paraplegia 47 (SPG47) OMIM 614066 Abou Jamra et al., 2011 (23), Bauer et al., 2012 (25)
	μ4	-	*AP4M1*					Hereditary spastic paraplegia 50 (SPG50) OMIM 612936 Verkerk et al., 2009 (26)
	σ4	-	*AP4S1*					Hereditary spastic paraplegia 52 (SPG52) OMIM 614067 Abou Jamra et al., 2011 (23)
AP5	ζ	-	*AP5Z1*		Late endosomes	Unknown	Unknown	Hereditary spastic paraplegia 48 (SPG48) OMIM 613647 Slabicki et al., 2010 (27)
	β5	-	*AP5B1*					
	μ5	-	*AP5M1*					
	σ5	-	*AP5S1*					

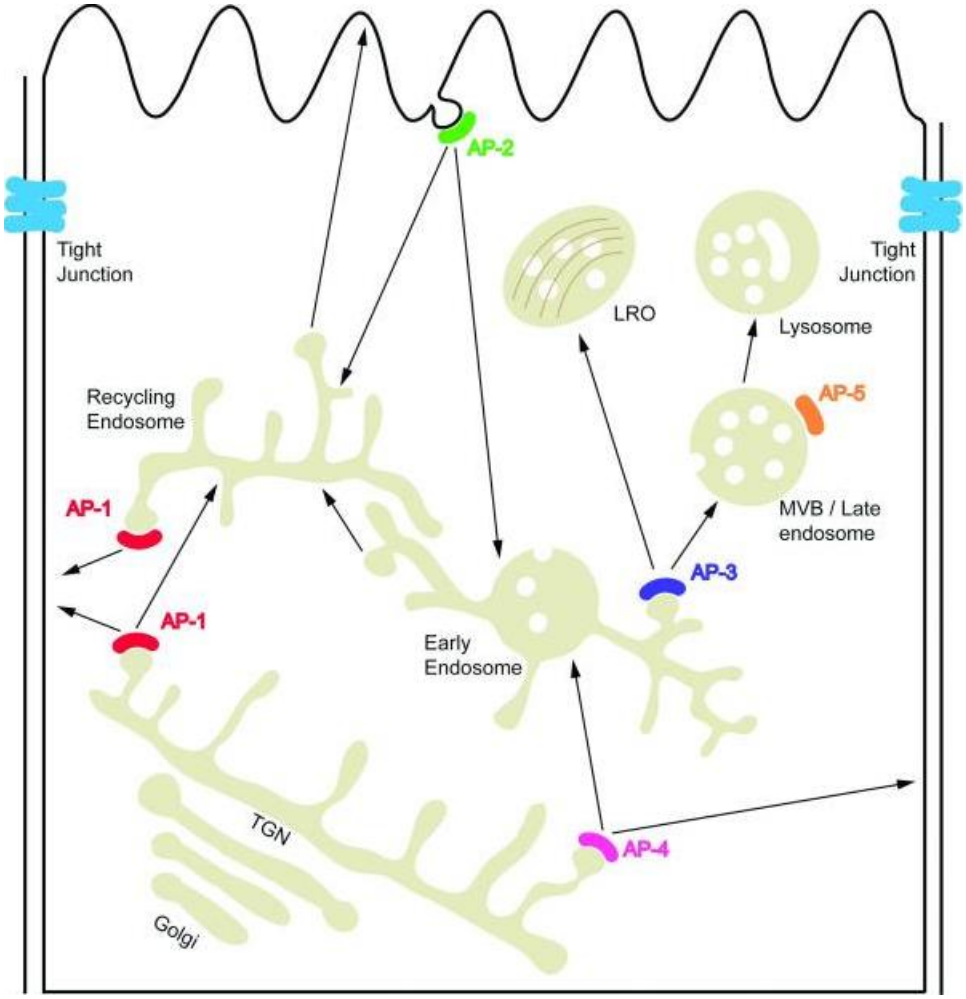


Figure 1. Localisation and trafficking of AP complexes, Reproduced from Park et al (2014) (4). "AP1 is localised to TGN and REs, and mediates bidirectional transport between them. AP1 also mediates basolateral sorting in epithelial cells. AP2 plays a role in clathrin-dependent endocytosis from the plasma membrane. AP3 is localised to endosomes, and responsible for the LRO biogenesis. AP4 is localised to TGN, and mediates vesicle trafficking from TGN to endosomes or basolateral plasma membrane. AP5 is localised to the late endosomes, and its function is largely unknown." TGN=trans-Golgi network; LRO= lysosome-related organelle; MVB= multivesicular body.

3.2 The role of the Adaptor Protein 2 complex in clathrin mediated endocytosis

The Adaptor Protein 2 (AP2) complex is a ubiquitously expressed, heterotetrameric protein. It is the major contributor to clathrin-mediated endocytosis (CME), the process by which plasma membrane constituents, including receptors, adhesion molecules and viral proteins,

are internalised and the major endocytic pathway in mammalian cells. It is responsible for regulating cell surface signalling, remodelling plasma membrane composition in response to environmental changes, and for the uptake of transmembrane receptors (28).

The AP2 complex is comprised of α-, ß2-, μ2- and σ2-subunits, which for ease of reference will be referred to as α-, ß-, μ- and σ-subunits in this thesis. The complex is formed through the assembly of an AP2α-AP2σ heterodimer with an AP2ß-AP2μ heterodimer into a tetrameric complex (Figure 2) (29-31). The α- and ß2-subunits (AP2α and AP2ß) are the largest subunits, at 955 and 933 amino acids respectively. The μ-subunit (AP2μ2) is 433 amino acids long and the σ-subunit (AP2σ) is the smallest AP2 subunit at 142 amino acids long.

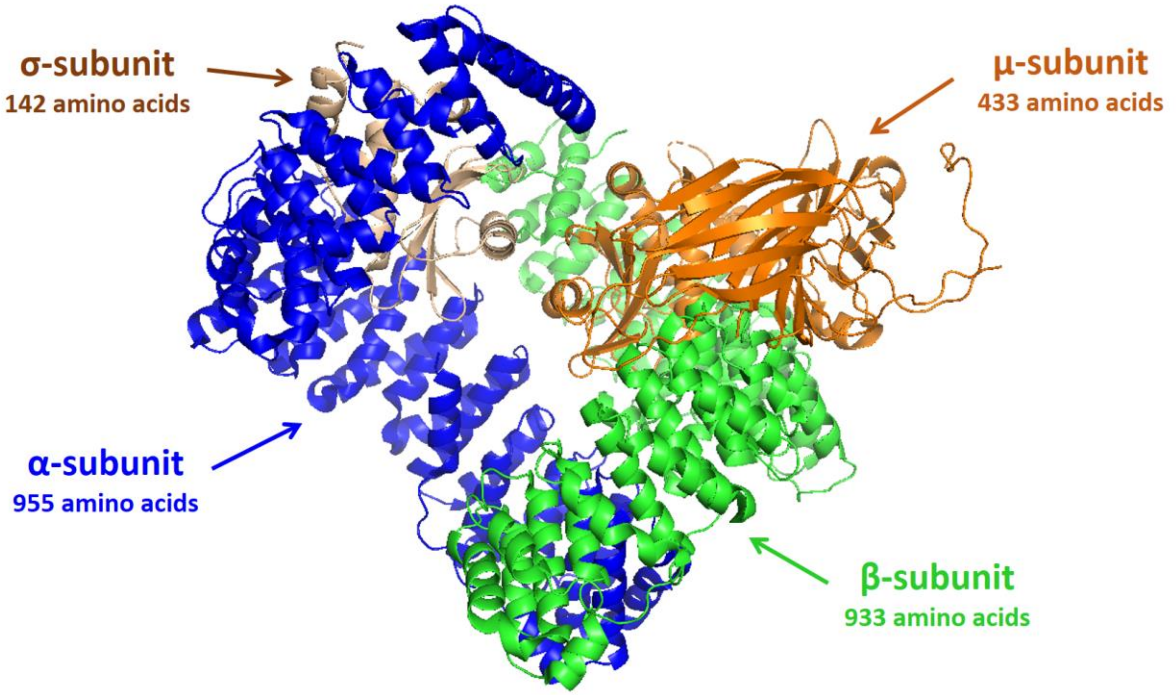


Figure 2. Crystal structure of the heterotetrameric protein AP2 in its open, active state. The α-, ß-, σ- and μ-subunits are shown in blue, green, brown and orange, respectively. The AP2 complex exists as 2 heterodimers, one comprised of AP2α and AP2σ, and the other comprised of AP2β and AP2μ. Adapted from *Kelly et al* (2008) (32).

The role of AP2σ variants in calcitropic and non-calcitropic disorders

The AP2 complex is comprised of a large globular core structure with two appendage domains connected via long flexible linkers. The N-termini of AP2α and AP2β, together with AP2μ and AP2σ form the core structure. The two appendage domains are formed by the C-termini of AP2α and AP2β (29-31) (Figure 3). The complex exists in 2 states: an open, active state where it is able to facilitate CME, and a closed, inactive state. In the closed state, AP2α and AP2β form an outer complex, and AP2μ, AP2σ and the AP2β appendage domain are buried within the AP2 core (29-35). The complex undergoes a large conformational change when it switches to an open state, which exposes the binding sites of AP2μ, AP2σ and the AP2β appendage domain which allows binding of internalisation motifs on transmembrane cargo proteins (30) and clathrin (35) (Figure 2). AP2μ and AP2σ subunits bind to tyrosine-based and dileucine-based endocytic motifs on transmembrane cargo, respectively (32). The AP2α appendage domain binds to and recruits accessory proteins necessary for maturation of the budding clathrin-coated vesicle (CCV) during CME (36), and the AP2β appendage domain and linker are necessary for clathrin binding (35).

The dileucine motif on transmembrane cargo is recognised by the σ-subunit of AP2 and CME then occurs in 4 steps (20, 28, 37) (Figure 4):

1) Initiation where the AP2β appendage domain nucleates assembly of clathrin triskelia on cargo proteins (35);

2) Cargo recruitment and stabilisation of the growing CCV where adaptins continue to polymerise clathrin, and the CCVs recruit cargo, grow and gain curvature (31);

3) Membrane bending and maturation of the CCV, which requires multiple accessory proteins recruited by the AP2α appendage domain (36);

4) Membrane scission where the CCV finally pinches off from the plasma membrane, catalysed by scission proteins including dynamin, and the cargo is fully internalised into the cell.

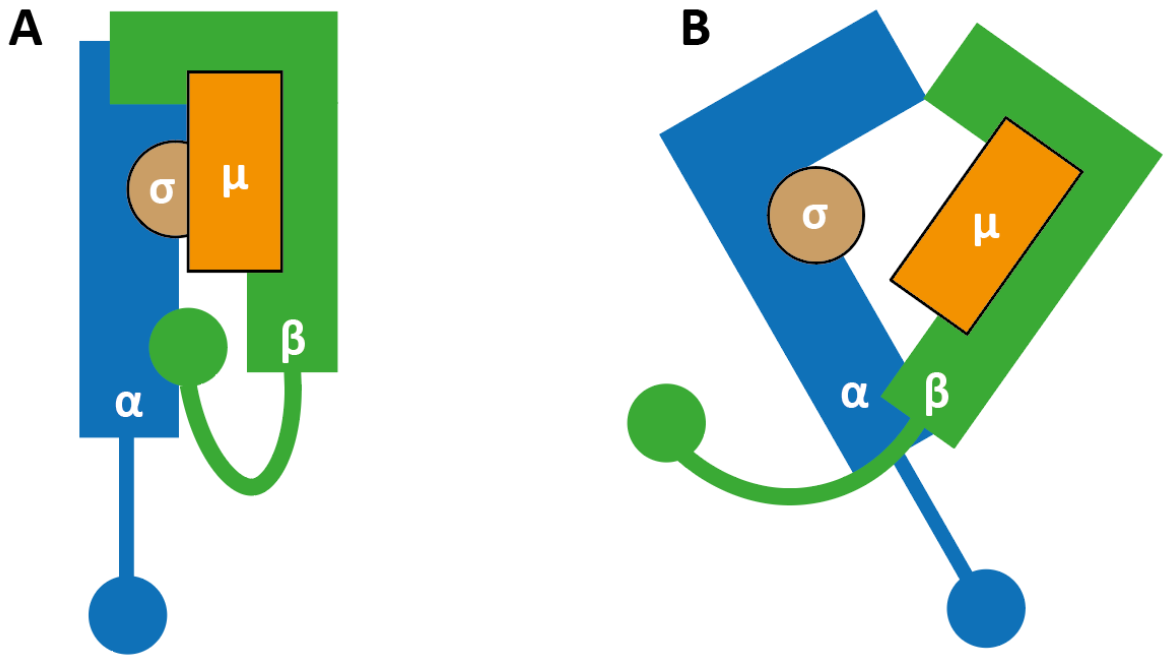


Figure 3. Schematic representation of the AP2 heterotetramer in the (A) closed, inactive; and (B) open, active state. The α-, ß-, σ- and μ-subunits are shown in blue, green, brown and orange, respectively. AP2 is comprised of 2 heterodimers, one formed by AP2α and AP2σ, and the other formed from AP2ß and AP2μ. (A) In the closed state, AP2α and AP2β form an outer complex, and AP2μ, AP2σ, and the appendage domain of AP2β are buried within the AP2 core. (B) In the open state the binding sites of AP2μ and AP2σ, and the AP2β appendage domain and linker are exposed. Figure adapted from *Kadlecova et al* (2017) (31).

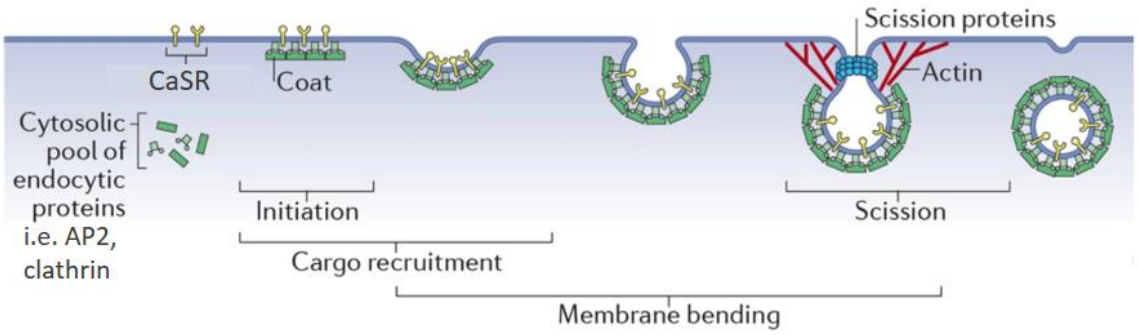


Figure 4. Stages of clathrin-mediated endocytosis. Figure reproduced and modified from *Kaksonen et al* (2018) (37). CME is initiated by the sequential assembly of endocytic proteins from the cytosolic pool, e.g. the intracellular domain of the calcium sensing receptor (CaSR) is recognised and bound to by AP2σ. Cargo recruitment then occurs, the plasma membrane bends and invaginates, and CME is initiated. Scission proteins, including dynamin, facilitate scission of the vesicle from the plasma membrane. The result of CME is an intracellular CCV, with an outer layer comprised of clathrin, and an inner layer containing the cargo proteins.

3.3 G-protein coupled receptors (GPCRs) are transmembrane receptors internalised by CME

G-protein coupled receptors (GPCRs) are a large family of heptahelical or 7-transmembrane signalling receptors comprising around 900 members in 6 classes (A, B, C, D, E and F) (38). Their chief function is to effect intracellular responses to extracellular stimuli, including ions, metabolites and hormones. Mutations in GPCRs result in a variety of diseases from tumour development to endocrine dysregulation, and they are an important drug target due to their involvement in the signalling pathways related to many diseases, including metabolic, endocrine and cancer. The CME process forms an important part of the regulation of GPCRs. Traditionally, CME was considered a mechanism by which the activated receptor was desensitised through removing it from the cell surface. However, several GPCRs have been shown to signal after CME, with postendocytic organisation providing another mechanism to augment complex signalling responses and spatial control of GPCR signalling is an emerging

concept (39). Additionally, GPCRs have been demonstrated to regulate their own endocytic rate in a ligand and receptor-dependent manner with consequences for intracellular signalling (40), which adds further nuance to the traditional picture. Any disruption to CME might therefore be expected to disrupt signalling from GPCRs and, with the potential to result in disease pathogenesis.

3.4 The calcium-sensing receptor

The calcium-sensing receptor (CaSR) is a class C GPCR that is internalised and regulated through CME where AP2 plays an integral role (20) (Figure 4). The taxonomic distribution of CaSRs is restricted to vertebrates, with CaSR-like receptors only present in non-vertebrate chordates, suggesting that it arose during vertebrate evolution, and has been shown to be functionally active in vertebrates ranging from cartilaginous fishes to terrestrial tetrapods (41).

The CaSR senses small fluctuation in extracellular calcium concentrations ($[Ca^{2+}]_e$) and modulates PTH secretion from parathyroid cells and the resorption of calcium ions (Ca^{2+}) from the kidney to maintain homeostasis (42-44). The CaSR is widely expressed in tissues including the parathyroids, kidney, bone, colon, heart, liver, lung, pancreas, and central nervous system, but expression is highest in the parathyroids and kidneys where its role in calcium homeostasis is best understood (45, 46). Additionally it has recently been reported that the CaSR can also sense moderate changes in extracellular phosphate concentration and act as a phosphate sensor (47-49).

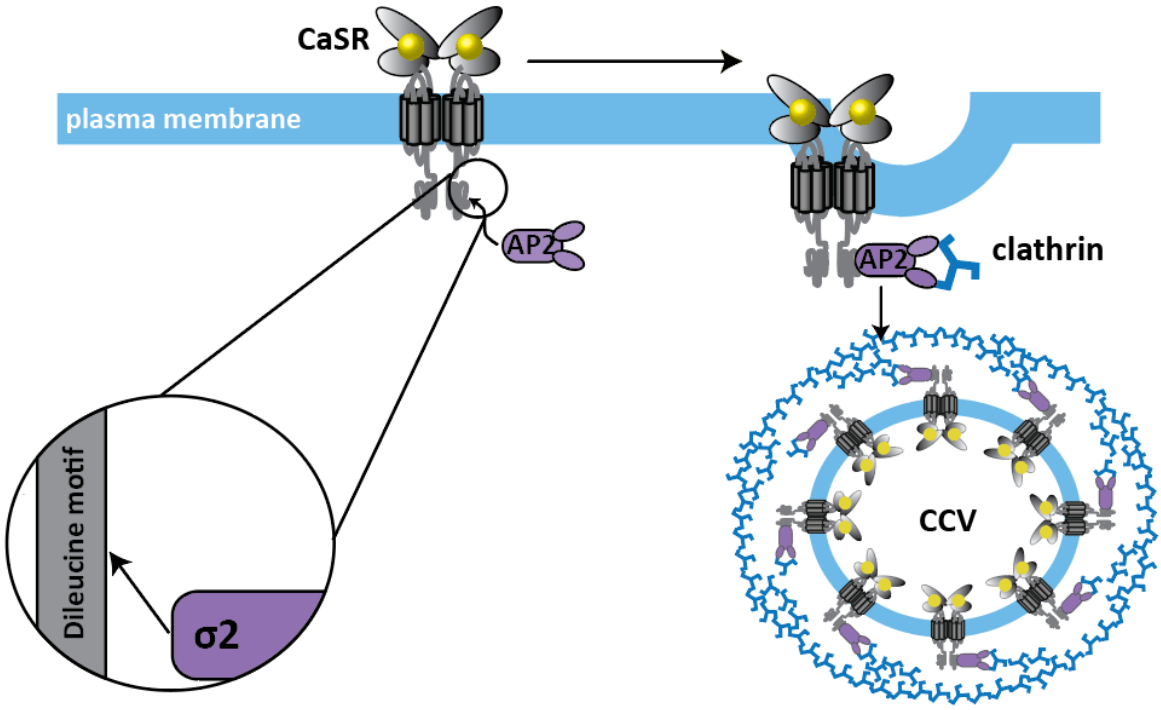


Figure 5. Proposed schematic model of clathrin mediated endocytosis (CME) of the calcium-sensing receptor (CaSR). AP2σ (in purple) recognises and binds to the dileucine motif on the intracellular domain of the CaSR. AP2 then recruits clathrin triskelia (darker blue), the plasma membrane invaginates, and CME is initiated. The result of CME is an intracellular CCV, with an outer layer comprised of clathrin, and an inner layer containing the CaSR. Figure adapted from *Nesbit et al* (2013) (20).

3.4.1 The calcium-sensing receptor in calcium homeostasis

The regulation of extracellular calcium concentration ($[Ca^{2+}]_e$) is vital to a number of physiological activities including muscle contraction, neurotransmission, coagulation and intracellular processes that range from signal transduction to exocrine secretory function (50, 51) and is therefore maintained within narrow parameters. Normal ranges of $[Ca^{2+}]_e$ in adults are usually an ionised calcium (Ca^{2+}) of 1.16-1.32 mmol/l, and a total serum calcium, which comprises 55%-60% Ca^{2+} plus 40%-45% protein bound (mainly to albumin) calcium, of 2.20-2.60 mmol/l (8.5-10.5 mg/dl) (52). The implication of hypercalcemia outside of these normal ranges may vary from an incidental asymptomatic biochemical finding to bone pains, abdominal pain, pancreatitis, kidney stones, renal failure, psychiatric symptoms and reduced

consciousness (53-55). Similarly, hypocalcaemia may be asymptomatic, or present acutely with seizures, paraesthesia, tetany, prolonged QT interval, laryngospasm and bronchospasm, or chronically with chronic joint deformity, and short stature.

Calcium homeostasis is maintained by the action of calcitropic hormones, a general term for any hormone which plays a major role in calcium homeostasis, principally parathyroid hormone (PTH) produced by the parathyroid glands, and 1,25-hydroxyvitamin D_3 ($1,25(OH)_2D_3$). These hormones act on target calcitropic organs which include the kidneys and small intestine, which shift Ca^{2+} between the extracellular fluid and external environment, and the skeleton which is the main Ca^{2+} reservoir and buffers acute fluxes in $[Ca^{2+}]_e$ concentrations (52, 56). Increasing $[Ca^{2+}]_e$ and $1,25(OH)_2D_3$, concentrations induce feedback inhibition of PTH secretion from the parathyroid glands (Figure 6) (52, 57). The CaSR is expressed in the parathyroid glands, kidneys and bone and mediates this calcitropic response (58). The CaSR is also expressed in the mammary glands which become calcitropic endocrine organs during lactation, secreting PTH-related peptide (PTHrP) which acts on bone in a similar way to PTH (59, 60) (Table 2, Figure 6).

3.4.1.1 The parathyroid gland

The CaSR is most highly expressed in the parathyroid glands (58) where it has been shown to interact with Klotho, a transmembrane protein, to regulate PTH secretion in response to $[Ca^{2+}]_e$ (61). Thus, low $[Ca^{2+}]_e$ detected by CaSR expressed on the chief cells of the parathyroid glands leads to an increase in PTH secretion and high $[Ca^{2+}]_e$ results in suppression of PTH release (62). Expression of the parathyroid CaSR is also upregulated through the action of $1,25(OH)_2D_3$ on vitamin D response elements (VDREs) within the CASR gene promoter (63).

PTH acts on the PTH1 receptor (PTH1R) in bone and the kidneys to increase $[Ca^{2+}]_e$ (Table 2, Figure 6).

3.4.1.2 The kidney

The CaSR has discrete calcitropic effects in the renal proximal convoluted tubule (PCT), the thick ascending limb (TAL) of the loop of Henle, the distal convoluted tubule (DCT), and the collecting ducts (CDs) (64). It has also been reported to be expressed in the juxtaglomerular apparatus, where it inhibits renin secretion independent of PTH (65), although the physiological consequence of this finding remain unclear.

The CaSR is highly expressed in the basolateral membrane of the TAL where it regulates Ca^{2+} reabsorption independently of PTH (66, 67). The CaSR is expressed at a lower level in the renal tubules (64); in the PCT it mediates renal 1 α-hydroxylase activity to produce $1,25(OH)_2D_3$ (67), and has been shown to inhibit PTH-mediated phosphate excretion (68); and in the DCT, it is thought to increase Ca^{2+} reabsorption via the transient receptor potential vanilloid member 5 (TRPV5) channels (69). CaSR expression in the CDs enhances urinary acidification and polyuria to facilitate the excretion of large amounts of soluble calcium, necessary to prevent nephrocalcinosis (70) (Table 2, Figure 6). CaSR expression in the kidney is therefore considered to play a key role in the defence against hypercalcaemia in 3 main ways: 1. Promoting renal Ca^{2+} excretion independently of the actions of PTH (66),(70); 2. Acting to prevent the formation of nephrocalcinosis (70); and 3. Potentially inhibiting $1,25(OH)_2D_3$ synthesis (67, 71).

3.4.1.3 The skeleton

The CaSR is expressed within both the bone and the growth plate, and acts to promote osteoclast-mediated bone resorption with a net calcium releasing effect by counteracting

PTH-related protein (PTHrP)/PTH1R signalling (72) (Table 2, Figure 6). Further insights into the role of the CaSR in bone homeostasis have been gained through mouse studies where the CaSR has been implicated in bone mineralisation, long bone growth and propensity to fracture (72-74).

3.4.1.4 The intestines

Intestinal Ca^{2+} absorption is regulated by $1,25(OH)_2D$ and can occur by both paracellular and transcellular routes (75). CaSR transcripts have been identified in whole and mucosal samples of rat duodenum, jejunum, ileum, cecum, and colon (76, 77). Recent studies have demonstrated that activation of the apical intestinal CaSR reduces Ca^{2+} absorption although, the specific mechanisms of how CaSR activation affects the $1,25(OH)_2D$-dependent intestinal Ca^{2+} absorption are largely unknown (78) (Table 2, Figure 6). Activation of intestinal CaSR has also been shown to affect transcellular transport of Ca^{2+} through decreased apical TRPV6-mediated intestinal Ca^{2+} absorption through the PLC pathway (79).

3.4.1.5 The lactating mammary gland

The CaSR is expressed in human and mouse breast epithelial cells, and its expression increases during lactation (59, 80). During lactation the mammary glands act as a calcitropic endocrine organs and signalling through the CaSR ensures a steady supply of Ca^{2+} for milk production, and also protects against maternal hypocalcaemia during lactation (60).

The CaSR maintains the supply of Ca^{2+} for milk production by stimulating plasma membrane Ca^{2+}-ATPase 2 (PMCA2), which transports Ca^{2+} from the mammary cell into milk (81). In lactating mice, mammary CaSR maintains $[Ca^{2+}]_e$ by mediating osteoclastic resorption of skeletal Ca^{2+} by augmenting PTHrP production (59, 60). Therefore, when $[Ca^{2+}]_e$ is low, activation of the breast CaSR is reduced and PTHrP production from breast epithelial cells is

increased, which in turn stimulates of Ca^{2+} from bone and increases $[Ca^{2+}]_e$ (Table 2, Figure 6) (60).

Table 2. The major calcitropic cellular roles of the CaSR. Adapted and updated (06.02.22) from Hannan et al (2018) (56). Stimulatory action of the CaSR is shown in blue type; Inhibitory action of the CaSR is shown in red type. GNRH=Gonadotrophin-releasing hormone; PTH=parathyroid hormone; H^+=hydrogen ion; PTHrP=parathyroid-related protein; TAL=thick ascending limb of the Loop of Henle.*increasing extracellular phosphate concentrations have been shown to inhibit the CaSR and thus stimulate PTH secretion. **Heteromer formation between CaSR and γ-amino-butyric acid-B1 receptor (GABAB1R) has been shown to regulate tonic PTH secretion.

Reference	Cell type	Role
Parathyroid:		
Brown EM, et al (2001)(82) Fan Y et al (2018) (61)		PTH secretion
Centeno PP et al (2019) (47)		PTH secretion*
Brown EM, et al (82) Mizobuchi M et al (2004) (83)		Proliferation
Chang Wen al (2020) (49)		PTH secretion**
Kidney:		
Ba J et al (2003) (68)	Proximal tubule	Phosphate excretion
Toka HR et al (2014) (84)		$1,25(OH)_2D$ synthesis
Loupy A et al (2012) (66) Riccardi D et al (2016) (85)	TAL	Ca^{2+} reabsorption
Topala CN et al (2009) (69)	Distal convoluted tubule	Ca^{2+} reabsorption
Renkema KY et al (2009)(70)	Collecting duct	H^+ excretion
Renkema KY et al (2009)(70)		Water excretion
Atchison DK et al (2010) (65)	Juxtaglomerular apparatus	Renin secretion
Bone:		
Chang W et al (2008)(74) Dvorak-Ewell MM et al (2011) (73)	Osteoblast	Differentiation and mineralization
Chang W et al (2008) (74)	Growth plate chondrocyte	Differentiation
Intestine:		
Wongdee K et al (2018) (78)	Epithelium	Paracellular Ca^{2+} absorption
Lee JJ et al (2019) (86)		Transcellular Ca^{2+} absorption
Breast epithelium:		
Kim W, et al (2016)(60)		Ca^{2+} transport into milk

VanHouten JN et al (2007) (81)	
Kim W, et al (2016)(60) VanHouten JN et al (2007) (81)	PTHrP production

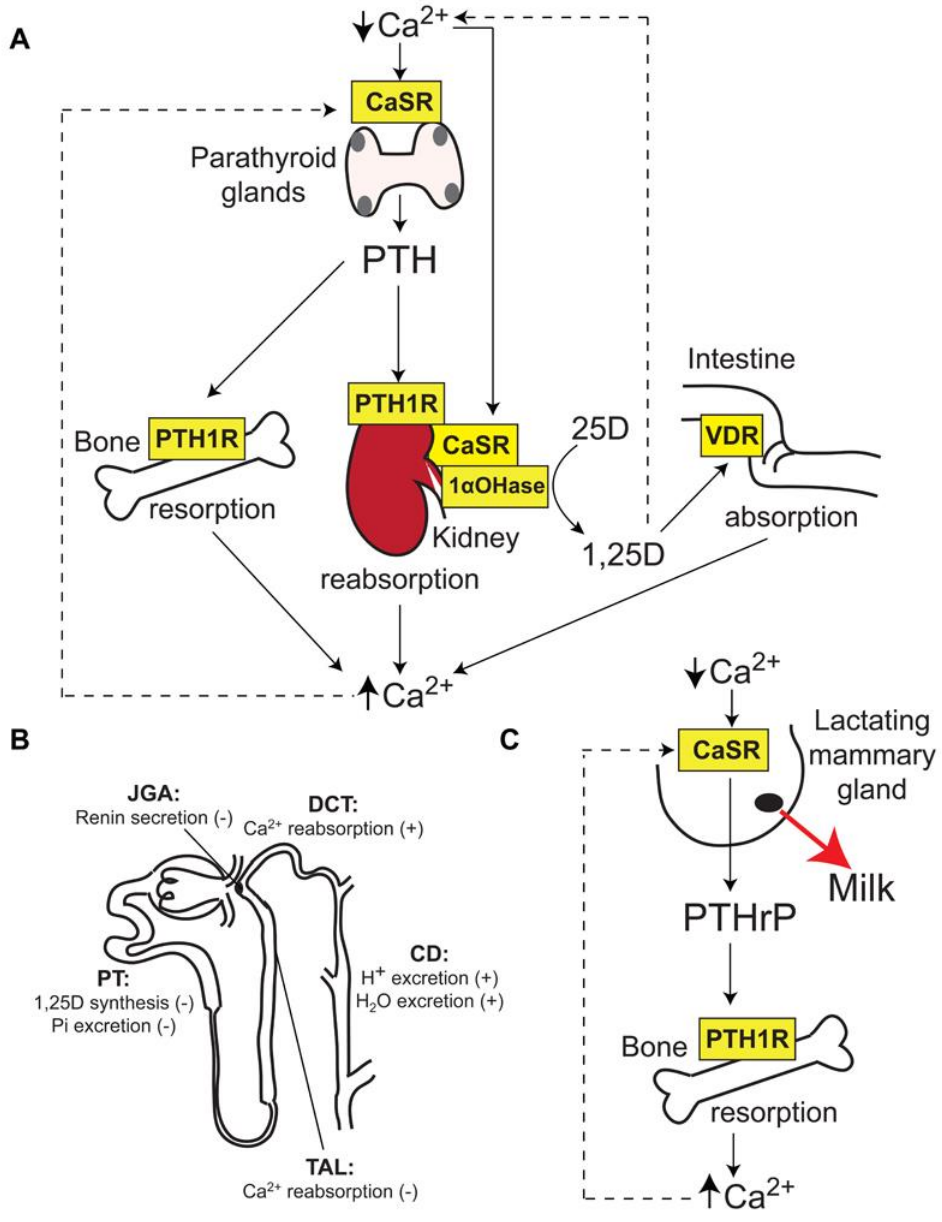


Figure 6. "The role of the CaSR in Ca^{2+}_e homeostasis". Reproduced from Hannan et al, (2018) (56). "(A) The CaSR is highly expressed in the parathyroid glands (grey), which are located adjacent and posterior to the thyroid gland (pink). The parathyroid CaSR detects reductions in Ca^{2+}_e, which leads to the release of PTH. PTH acts on the PTH1 receptor (PTH1R) to increase resorption of Ca^{2+}_e from bone, promote urinary Ca^{2+} reabsorption, and enhance expression of the renal 1-α-hydroxylase (1αOHase) enzyme,

which converts the 25-hydroxyvitamin D (25D) precursor metabolite to biologically active 1,25-dihydroxyvitamin D (1,25D). The elevated 1,25D increases absorption of dietary calcium by acting on the intestinal vitamin D receptor (VDR)3. The kidney CaSR acts independently of PTH to regulate urinary Ca^{2+} reabsorption. Increases in Ca^{2+}_e and 1,25D concentrations lead to negative feedback on the parathyroid glands, thereby inhibiting further PTH release. (B) Nephron segment-specific roles of the CaSR. The CaSR is expressed in the: apical membrane of the proximal tubule (PT), where it regulates 1,25D synthesis and phosphate (Pi) excretion; basolateral membrane of the cortical thick ascending limb (TAL) of the Loop of Henle, and apical and basolateral membranes of the distal convoluted tubule (DCT), where it regulates Ca^{2+} reabsorption; apical and basolateral membranes of the collecting duct (CD), where it regulates H^+ and water excretion; and juxtaglomerular apparatus (JGA), where it regulates renin secretion. (+), stimulatory action of CaSR; (-), inhibitory action of CaSR. (C) During lactation, the mammary gland CaSR detects reductions in Ca^{2+}_e, which leads to increased PTHrP secretion from mammary epithelial cells into the circulation. PTHrP acts on the PTH1R to increase bone resorption, which in turn releases Ca^{2+}_e for milk production. Stimulatory and inhibitory actions are indicated by solid lines and dashed lines, respectively."

3.4.2 The CaSR in non-calcitropic physiology

The expression of the CaSR in a wide variety of tissues unrelated to extracellular calcium homeostasis suggests that it may have a role in a diverse range of cellular functions outside of calcium homeostasis (87). Research has uncovered increasing examples of the non-calcitropic effects of CaSR signalling, ranging from stimulation of arterial contractility (88), fluid secretion in the lung (89) and cholecystokinin secretion (90), to inhibition of ghrelin secretion (91), neuronal chemotaxis (45) and myelinogenesis (92) (Table 3). I have briefly summarised some of the reported roles of the CaSR in the major organ systems below:

3.4.2.1 Cardiovascular system

The CaSR has been implicated in the development and progression of various cardiovascular diseases, including myocardial ischaemia, vascular calcification, hypertension, atherosclerosis and obesity induced cardiovascular disease (93). It has been shown to be expressed in human vascular smooth muscle cells (VSMCs) and endothelial cells (94) and a variety of studies have

been performed to investigate its effect on cardiovascular biology. Ablation of the VSMC CaSR in mice has been shown to cause endothelium-independent decreases in the contractility of the aorta and mesenteric arteries, and also to decreases in diastolic and mean arterial blood pressures suggesting a role in the regulation of blood pressure and blood vessel tone (88). Conversely, stimulating the CaSR induced endothelium-dependent vasorelaxation in rabbit mesenteric arteries (95). Additionally, the CaSR is thought to play a role in VSMC proliferation (96) and experiments on rodent ventricular cardiomyocytes have demonstrated that the CaSR is functionally active in these cells and promotes apoptosis (97). Not surprisingly, the CaSR has been targeted as a potential therapeutic target in patients with vascular calcification. Cinacalcet, a positive allosteric modulator of the CaSR, was shown to have beneficial effects on arterial calcification in a randomised controlled trial involving CKD patients on haemodialysis (98) (Table 3).

3.4.2.2 Respiratory system

The CaSR is expressed in foetal lungs and has been reported to have a role in mediating lung growth and development and in lung branching morphogenesis (89, 99). The expression of CaSR has been demonstrated to be increased in asthmatic adult airway smooth muscle and bronchial epithelium, compared to their non-asthmatic counterparts, and inhaled calcilytics are being investigated as a potential treatment for asthma (100). Patients with idiopathic pulmonary artery hypertension have also been shown to have pathological upregulation of CaSR expression and calcilytic treatment has been demonstrated to prevent the development of this disorder and ameliorate the secondary occurrence of right ventricular hypertrophy in rodent models of the disorder (101) (Table 3).

3.4.2.3 Gastro-intestinal system

The CaSR is expressed along the entire GI tract, from the parietal cells of the stomach (102), to the epithelial and entero-endocrine cells of the small and large intestine (103), and neurons of the submucosal and myenteric plexuses (104, 105). It has been reported to function as a nutrient sensor and demonstrated to bind L-amino acids, and di- and polypeptides such as poly-L-lysine in addition to Ca^{2+} and other cations. The CaSR has been shown to regulate gastric acid and hormone secretion, and demonstrated to have a role in nutrient absorption, intestinal fluid homeostasis, energy metabolism, cellular differentiation and proliferation, motility and enteric nerve activity, maintenance of gut microbiota, immune homeostasis, and intestinal inflammation (105, 106). Additionally, the CaSR has been shown to have a role in the regulation of pancreatic islet mass, and in α- and β-cell function. Finally, the CaSR in the GI tract has become a drug target, and a calcimimetic suggested as a novel therapy for secretory diarrhoea, by targeting the CaSR and reducing cholera-toxin induced fluid secretion (105) (Table 3).

3.4.2.1 Nervous system

The CaSR is widely expressed in the central and peripheral nervous system and is considered to play a role in the development of the hippocampus, granule cell layer of the cerebellum, sympathetic nervous system, and also in GnRH neuronal migration (45, 92, 107). Abnormal CaSR function has been implicated in central nervous system disorders such as Alzheimer's disease (AD), ischaemic brain injury and epilepsy, and CaSR mutations have been reported in patients with epilepsy (45). The CaSR has been suggested as a novel target for ischaemic neuroprotection and calcilytic treatment in mice with brain injury has also been shown to be neuroprotective and result in improved learning and memory retention (108) (Table 3).

Table 3. The major non-calcitropic cellular roles of the CaSR. Adapted and updated (06.02.22) from Hannan et al (2018) (56). Stimulatory action of the CaSR is shown in blue type; Inhibitory action of the CaSR is shown in redtype. GNRH=Gonadotrophin-releasing hormone; PTH=parathyroid hormone; PTHrP=parathyroid-related protein; TAL=thick ascending limb of the Loop of Henle.

Reference	Cell type	Role
Cardiovascular		
Molostov G et al (2008) (96)	Vascular smooth muscle cell	Proliferation
Schepelmann M, et al. (2016) (88)		Arterial contractility
Greenberg HZE et al (2016) (95)	Endothelial cell	Nitric oxide production
Sun Y-H et al (2006) (97)	Ventricular cardiomyocyte	Apoptosis
Respiratory		
Brennan SC et al (2016) (89) Finney BA et al (2008) (99)	Foetal lung epithelium	Fluid secretion
Finney BA et al (2008) (99)		Proliferation and lung branching morphogenesis
Xu J et al (2021) (101)	Pulmonary arterial smooth muscle cell	Hypoxia-induced pulmonary arterial smooth muscle cell proliferation
Gastrointestinal		
Ceglia L et al (2008) (109) Dufner MM et al (2005) (110)	Gastric parietal cell	H^+ excretion
Alamshah A et al (2017) (91) Engelstoft MS et al (2013) (111)	Gastric mucosal cell	Ghrelin secretion
Feng J et al (2010) (112)	Gastric G cell	Gastrin secretion
Liou AP et al (2011) (90)	Duodenal I cell	Cholecystokinin secretion
Alamshah A et al (2017) (91)	Intestinal L cell	Glucagon-like peptide-1
Alamshah A et al (2017) (91) Wu W et al (2017) (113) Igarashi A et al (2021) (114)		Peptide YY
Guo Y et al (2021) (115)	Jejenum and ileum	Intestinal motility
Cheng SX et al (2014) (103)	Colon	Barrier function
Cheng SX et al (2012) (116)		Enteric nervous system
Geibel J et al (2006) (104) Cheng SX et al (2012) (116)		Fluid secretion
Macleod RJ et al (2013) (117)		Proliferation
Pancreatic islet		
Babinsky VN et al (2017) (118) Grey E et al (2006) (119)	α-cell	Glucagon secretion
Grey E et al (2006) (119)	β-cell	Insulin secretion
Adipocyte		
Bravo-Sagua R et al (2016) (120)		Proliferation
Bravo-Sagua R et al (2016) (120)		Differentiation

Bravo-Sagua R et al (2016) (120)		Inflammatory cytokine expression
Skin keratinocyte		
Tu CL et al (2013) (121)		Proliferation
Tu CL et al (2013) (121)		Differentiation
Tu CL et al (2013) (121)		Apoptosis
Central nervous system		
Tharmalingham S et al (2016) (107)	Cerebellar granule cell	Differentiation and migration
Chattopadhayay et al (2008) (92)	Oligodendrocyte	Differentiation and myelinogenesis
Ruat M et al (2013) (45)	GNRH neuron	Chemotaxis
Ruat M et al (2013) (45)	Sub-fornical organ	Neuronal excitability and blood pressure regulation
Reproduction		
Boisen IM et al (2020) (122)	Spermatazoa	Acrosome reaction, sperm activating signals

3.5 Signalling via the CaSR

3.5.1.1 CaSR structure and activation

The crystal structures of the resting and active conformations of the CaSR ECD were solved by Geng et al (48) and Zhang et al in 2016 (123). This work was built on through groundbreaking cryo-EM studies of several full-length class C receptors, including mGluR5 (124) and $GABA_B$ receptors (125-129). Following on from this, Ling et al (2021) (130) solved the cryo-EM structures of full-length CaSR in active and inactive states, however, they were unable to conclusively demonstrate the fully inactive state (130). Further work using cryo-EM by Chen et al (2021) (131) was finally able to demonstrate the structures of full-length CaSR in inactive and agonist and positive allosteric modulator (PAM) bound conformations. Additionally, studies of >400 germline CaSR mutations resulting in disorders of calcium homeostasis have demonstrated that they tend to cluster in discrete regions of the CaSR and have given insight into the functional significance of these areas (132, 133). These mutations may be CaSR-inactivating which act to reduce the sensitivity of the CaSR to $[Ca^{2+}]_e$ and result in Familial Hypocalciuric Hypercalcaemia type 1 (FHH1) when heterozygous and Neonatal Severe Hyperparathyroidism (NSHPT) when homozygous or compound heterozygous. CaSR

mutations may also result in increased receptor activation, thereby increasing the sensitivity of the CaSR to $[Ca^{2+}]_e$ and resulting in Autosomal Dominant Hypocalcaemia type 1 (ADH1) or Bartter syndrome type V (Figure 7). The CaSR classically functions as a disulphide-linked homodimer, but has also been shown to form functionally active heterodimers (134-136). Each monomer comprises a large extracellular domain (ECD), seven transmembrane domains (TMDs), and an intracellular domain (ICD). The ECD of each consists of a bilobed extracellular venus flytrap domain (VFTD), homologous to bacterial periplasmic proteins involved in scavenging or sensing nutrients (137), and a cysteine rich domain (CRD) (Figure 8). Covalent and non-covalent interactions that involve the N-terminal VFTD of each monomer maintain the CaSR as a dimer and these interactions go through conformational changes on ligand binding (Figure 8). The TMD includes seven hydrophobic helical domains linked by 3 extracellular loops (ECLs) and 3 intracellular loops (ICLs) and anchors the CaSR in the plasma membrane. On ligand binding, the TMD undergoes conformational changes that allow signal transduction from the bound VFTD and CRD to the ICD. As the name GPCR suggests, the ICD of the CaSR interacts with intracellular guanine-nucleotide binding proteins (G-proteins), however it has also been proposed that the CaSR may mediate some of its effects in a G-protein independent manner (138). It has been proposed that G-protein binding is facilitated by the CaSR homodimer adopting an asymmetric TMD conformation that primes one protomer over the other for G-protein coupling (139). The ICD ultimately functions to mediate downstream signalling events as a result of CaSR activation (140) and can also undergo phosphorylation and ubiquitination to facilitate desensitisation and degradation or recycling of the CaSR (141, 142).

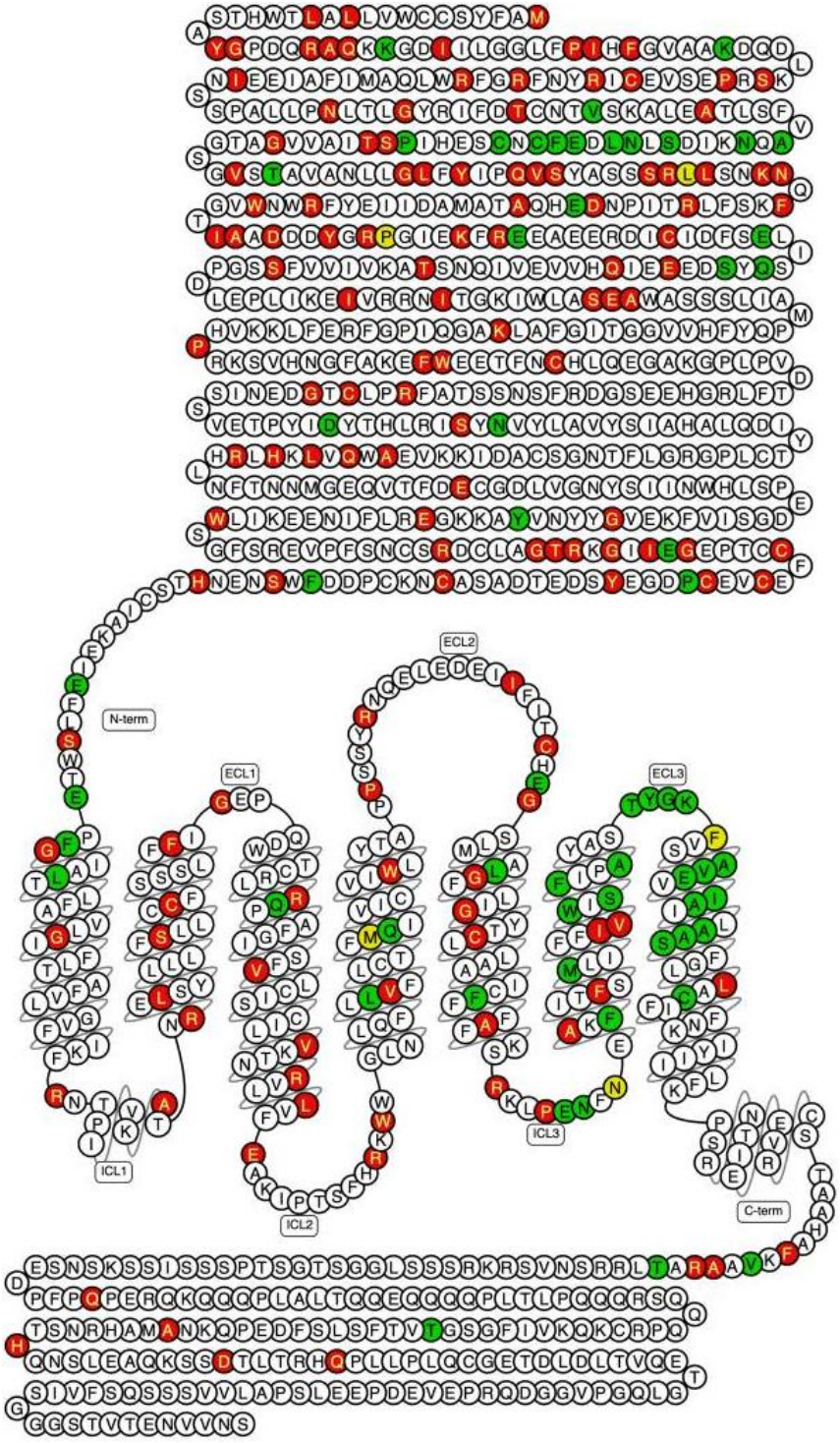


Figure 7. "CaSR snakeplot with residues linked to loss- and gain-of-function germline mutations." Reproduced from Leach et al 2020 (143). Snake-plot of the CaSR showing the location of the ECD, 7TM, ICLs, ECLs and ICD. Sites of loss-of-function germline mutations causing FHH1/NSHPT are shown in red Sites of gain-of-function causing ADH1 or Bartter syndrome type V are shown in green. Sites where mutations may result in either FHH1/NSHPT or ADH1/Bartter syndrome type V termed "switch

residues" are shown in yellow. Snake-plot generated by GPCRdb (144) with data from the Human Gene Mutation Database (145).

The VFTD is made up of 2 lobes, lobe 1 closest to the C-terminus, and lobe 2. In the inactive, unbound state, the dimerization interface largely comprises the two lobe 1 domains which form a predominately hydrophobic core made up of residues on the two central helices of each protomer (130) (Figure 8A). The CaSR VFTD is predicted to contain binding sites for anions such as phosphate and sulphate, which are thought to stabilise the CaSR in this inactive conformation (48). Clusters of mutations that result in disorders of calcium homeostasis have been found in the ECD homodimer interface, demonstrating the functional importance of this region (48, 123, 146). Activation of the CaSR occurs on ligand binding. Ca^{2+} binding takes place at four distinct sites, three are located within the VFTD, and the fourth is located between the VFT and CRD (48). This ligand-binding induces conformational changes that result in lobe 2 rotating in relation to lobe 1, resulting in a new dimerization interface comprising lobe 2-lobe 2 and the two CR domains in the bound, active state (48, 123, 130, 131). In addition to Ca^{2+}, the function of the CaSR may be activated or modulated by other ions, for example Mg^{2+} ions function as activators, whereas SO_4^{2-} and PO_4^{3-} act as negative allosteric modulators (NAMs) (47, 48). Amino acids, polyamines like spermine and L-1,2,3,4-tetrahydronorharman-3-carboxylic acid (TNCA), a tryptophan derivative ligand, have also been shown to modulate CaSR function (48, 147, 148). It has been suggested that amino acid binding may also be required to fully activate the CaSR (48) and there are amino acid binding sites within the cleft of the VFT (48, 123). However, more recent work has proposed that Ca^{2+} ions alone are sufficient to fully stabilise the active conformation (147).

Following CaSR activation, large-scale transitions of the TMDs, and inter- and intrasubunit conformational changes of the TMDs occur and facilitate intracellular signal transduction (131) (Figure 8B). Again, these findings are supported by the results of mutational analysis of patients with disorders of calcium homeostasis which have been found throughout the TMD (132, 149) (Figure 7). It has been shown that upward movement of LB2 on ligand binding translates into a rearrangement of the 7 TMDs through ECL2 (130). Studies show that loss-of-function GPCR mutations concentrate in the TM1 –TM2–TM7 interface, and consistent with this, FHH1 mutations have also been shown to cluster here in the CaSR (132, 149) (Figure 7). The configuration of the 7 TMDs of the CaSR in the active state have yet to be determined, but TM6–TM6 contact is considered to be a hallmark of class C GPCR activation (130). Interestingly, TM6 has recently been shown to move in a different direction upon activation in the CaSR compared to many family A GPCRs (139). Activating-CaSR mutations cluster at the extracellular side of TM6–ECL3–TM7 interface suggesting that they favour receptor activation (48, 123, 132) (Figure 7). Clusters of inactivating-CaSR mutations have also been found at TM5 (Figure 7). TM5 has been shown to be important in class C GPCR dimerization in the inactive state and to evolve into a TM6–TM6 interface on receptor activation (130, 150, 151). It may be that these inactivating mutations therefore prevent TMD transitions that are important for receptor activation (132).

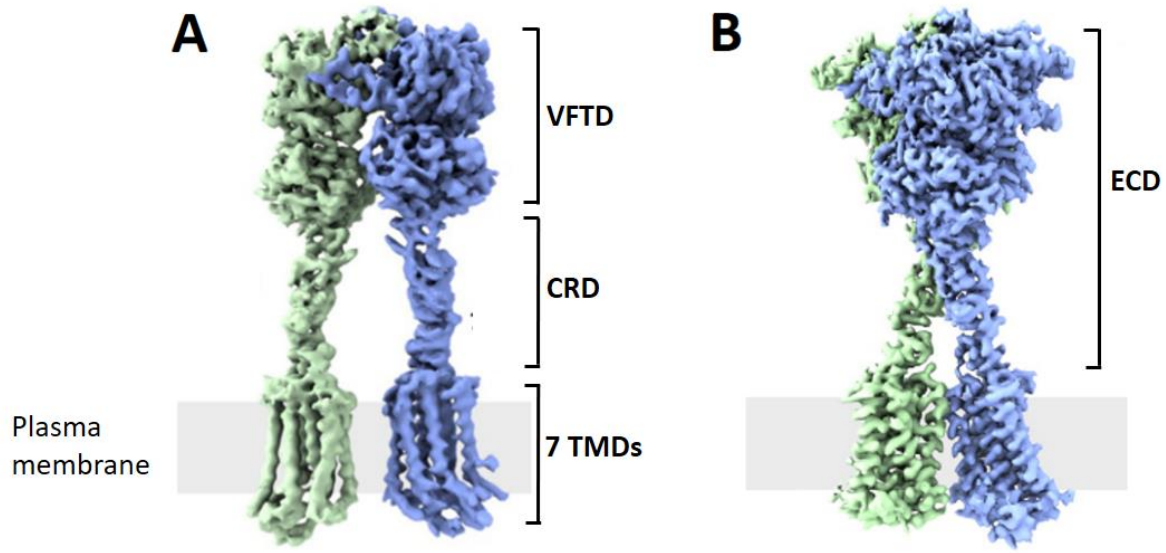


Figure 8. Adapted from Gao et al (2021) (139). (A) Inactive and (B) active confirmations of the CaSR. One homodimer is shown in green and one homodimer is shown in blue. (A) In the inactive state the CaSR homodimer adopts an extended parallel conformation with an interface between the top lobe of the VFTs. The 7 TMDs are separated. (B) In the active state the CaSR ECD (comprising the VFTD and CRD) adopts a symmetrical closed-closed conformation. The 7 TMDs adopt marked asymmetrical conformations. (139). VFTD=venus flytrap domain; CRD=cysteine-rich domain; TMDs=transmembrane domains; ECD=extracellular domain.

3.5.1.2 Agonist driven insertional signalling (ADIS)

The CaSR is an unusual GPCR in that it is chronically exposed to its ligand at baseline concentrations and undergoes very little functional desensitization (152). It is also able to continue to signal for as long as it is exposed to elevated $[Ca^{2+}]_e$ (153). Studies of CaSR signalling and trafficking suggest that the receptor is expressed at the plasma membrane at low levels when $[Ca^{2+}]_e$ are at baseline. However, elevation of $[Ca^{2+}]_e$ leads to a rapid increase of CaSR expression at the plasma membrane in a process called agonist-driven insertional signalling (ADIS), allowing a rapid increase in the maximum signalling response (153). Prolonged signalling is maintained by a large intracellular reserve of CaSR that relocates to the plasma membrane as part of ADIS. This pool of CaSRs is constantly expanded by signalling-mediated increases in biosynthesis (154) (Figure 9, Figure 10).

3.5.1.3 G protein signalling

As described, the CaSR activates downstream signalling cascades by coupling to G-proteins (155, 156). G-proteins are intracellular receptors that span the 7 TMDs of GPCRs and ultimately convey messages from specific extracellular stimuli to intracellular signalling. G-proteins are heterotrimeric, comprised of α-, β- and γ-subunits, termed Gα, Gβ, and Gγ subunits. The β- and γ-subunits are able to form a stable dimeric complex referred to as the βγ-complex (Gβγ).

Classical activation of G proteins occurs through conformational changes in the GPCR that allow it to function as a guanine nucleotide exchange factor (GEF) that exchanges GDP, bound to the Gα subunit, for GTP. This allows dissociation of the Gα subunit from the Gβγ subunits, and from the GPCR, which is free to activate another G-protein. Both the Gα subunit and the Gβγ subunit are able to independently activate various intracellular signalling pathways, however, much of the signalling specificity lies with the Gα subunit. The Gα subunit has inherent enzymatic activity that ultimately allows it to hydrolyse the attached GTP back to GDP so that it may reassociate with the Gβγ subunit and the GPCR signalling process can start again.

G-proteins are classified into 4 families according to their α-subunit: $G\alpha_q$, $G\alpha_i$, $G\alpha_s$ and $G\alpha_{12/13}$ families. The G_q family consists of four members: G_q, G_{11}, G_{14}, and $G_{15/16}$ and their respective α subunits are therefore termed $G\alpha_q$, $G\alpha_{11}$, $G\alpha_{14}$, and $G\alpha_{15/16}$ (157). Members of the $G\alpha_q$ family have the highest amino acid sequence homology in humans of all G protein families identified, with $G\alpha_{11}$, $G\alpha_{14}$, and $G\alpha_{16}$ sharing 90, 80, and 57% sequence similarities, respectively (158). The $G\alpha_q$ and $G\alpha_{11}$ proteins, termed $G\alpha_{q/11}$ proteins, are thought to be most critical for CaSR signal transduction. $G\alpha_q$ and $G\alpha_{11}$ are two isoforms that arise from the same

chromosome, have an identical number of amino acids and are functionally almost identical (159). However, they are distinct gene products with distinct distributions within tissues (159). Inactivating mutations of G-protein subunit α_{11} ($G\alpha_{11}$) have been shown to cause FHH type 2 (FHH2) and activating mutations have been shown to cause ADH type 2 (ADH2) (155) (Figure 9).

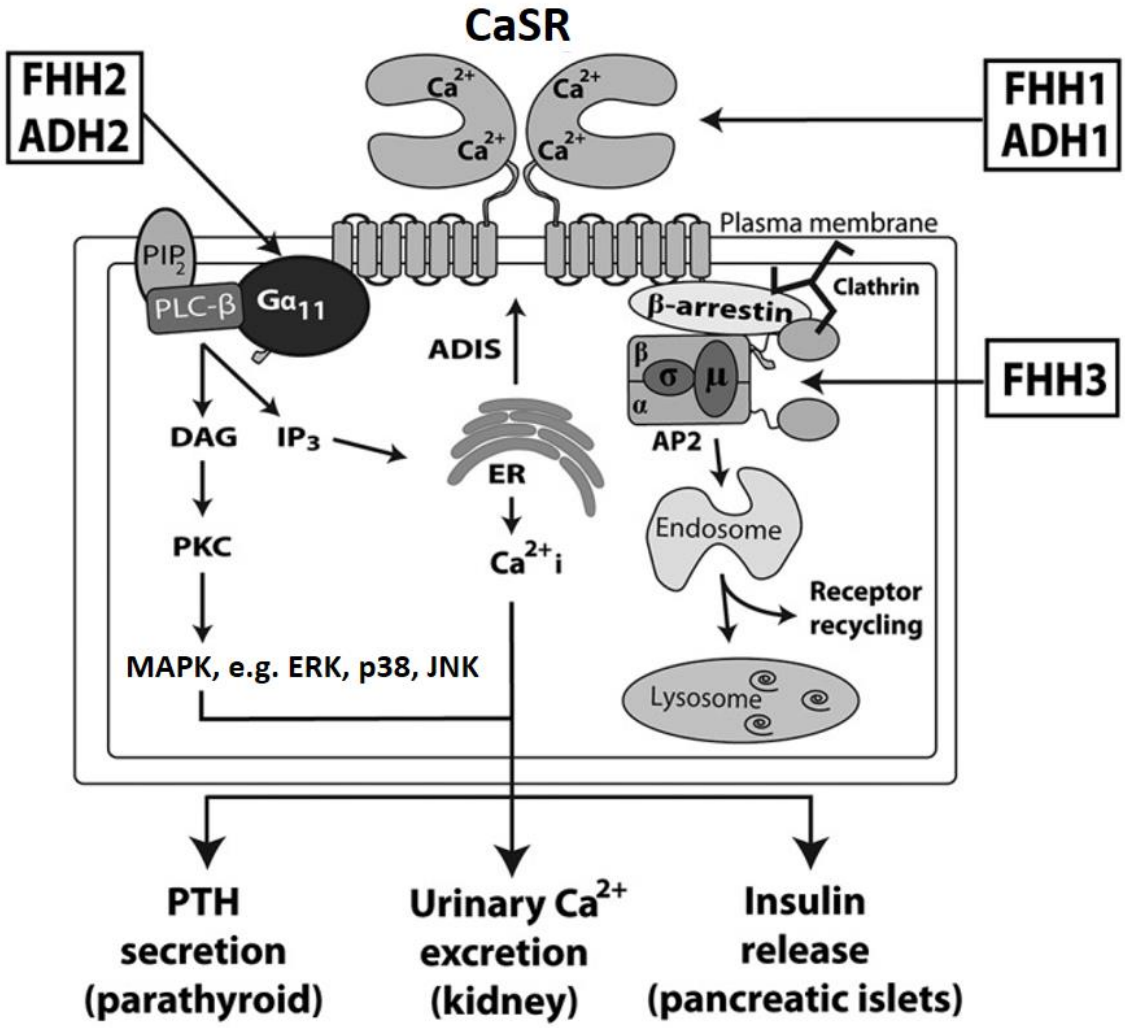


Figure 9. "Overview of calcium-sensing receptor signalling and trafficking". Reproduced from Hannan et al (2018)(160). The binding of calcium (Ca^{2+}) to the CaSR ECD leads to $G\alpha_{11}$-dependent activation of PLC-β and the production of DAG and inositol 1,4,5-trisphosphate (IP_3) from membrane-bound phosphatidylinositol 4,5-bisphosphate (PIP_2). The increase in intracellular IP_3 levels facilitates the release of Ca^{2+} from intracellular stores such as the ER. DAG activates PKC and MAPK pathways, e.g. ERK, p38 and JNK. These signalling events lead to a decrease in PTH secretion and reduction in renal

tubular calcium reabsorption and also enhance insulin release from pancreatic islets. ADIS acts to increase CaSR cell-surface expression in response to increasing $[Ca^{2+}]_e$. An endocytic complex comprising clathrin, β-arrestin and the AP2 complex also facilitates trafficking to the endosomal–lysosomal degradation pathway or recycling of the CaSR back to the cell surface. Loss- and gain-of function mutations of the CaSR lead to FHH1 and ADH1 respectively, loss- and gain-of function mutations of $G\alpha_{11}$ cause FHH2 and ADH2 respectively, and loss-of-function mutations of AP2 results in FHH3.

Signalling via the G-protein-$\alpha_{q/11}$ ($G\alpha_{q/11}$) pathway results in activation of phospholipase C (PLC), which in turn, converts phosphatidylinositol 4,5-bisphosphate (PIP2) into the secondary messenger molecules inositol triphosphate (IP_3) and diacylglycerol (DAG). IP_3 activates $Ca^{2+}{}_i$ release from the endoplasmic reticulum via store-operated channels located in the plasma membrane by binding to IP_3 receptors on endoplasmic reticulum (155). DAG activates protein kinase C (PKC) which regulates protein phosphorylation cascades involved in cell survival, differentiation and proliferation such as the mitogen-activated protein kinases (MAPKs) (155, 161). Key components of this cascade include the extracellular-signal regulated kinases 1/2 (ERK1/2), p38 kinase (p38K) and c-Jun N-terminal kinase (JNK) (162). Ultimately, activation of the protein phosphorylation cascade results in diverse changes in gene transcription to exert the effect of the CaSR signalling (163) (Figure 9,Figure 10).

CaSR signalling via the pertussis toxin-sensitive $G_{i/o}$ proteins inhibits adenylyl cyclase (AC) activation and causes a decrease in cyclic AMP (cAMP) production (164), and also stimulates MAPKs such as ERK1/2 through epidermal growth factor receptor (EGFR) transactivation (155, 161) (Figure 10). Studies of CaSR signalling via $G\alpha_{12/13}$ are complicated by a lack of inhibitors and suitable functional readouts (106). However, CaSR coupling to the $G_{12/13}$ proteins has been linked to RhoA, a small GTPase protein in the Wnt3a-beta-catenin signalling cascade via phospholipase D (PLD) (165). It has been suggested $G\alpha_{12/13}$ activate Rho by activation of a Rho

GEF that allows it to interact with downstream effectors such as Rho kinase. Activation of Rho-kinase has been linked to regulation of contraction of actomysin and the formation cadherin-mediated intercellular adhesion in epithelial cells (157, 166) (Figure 10). The CaSR has also been shown to signal through G_s in both immortalized and malignant breast cells and the AtT-20 pituitary-derived cell line, which results in increasing intracellular cAMP levels which activate PKA and stimulates PTH related protein (PTHrP) release (167, 168). This effect is not observed in HEK293 cells expressing the CaSR (138) and the mechanism by which it occurs in breast cancer and AkT-20 cells is unknown (106).

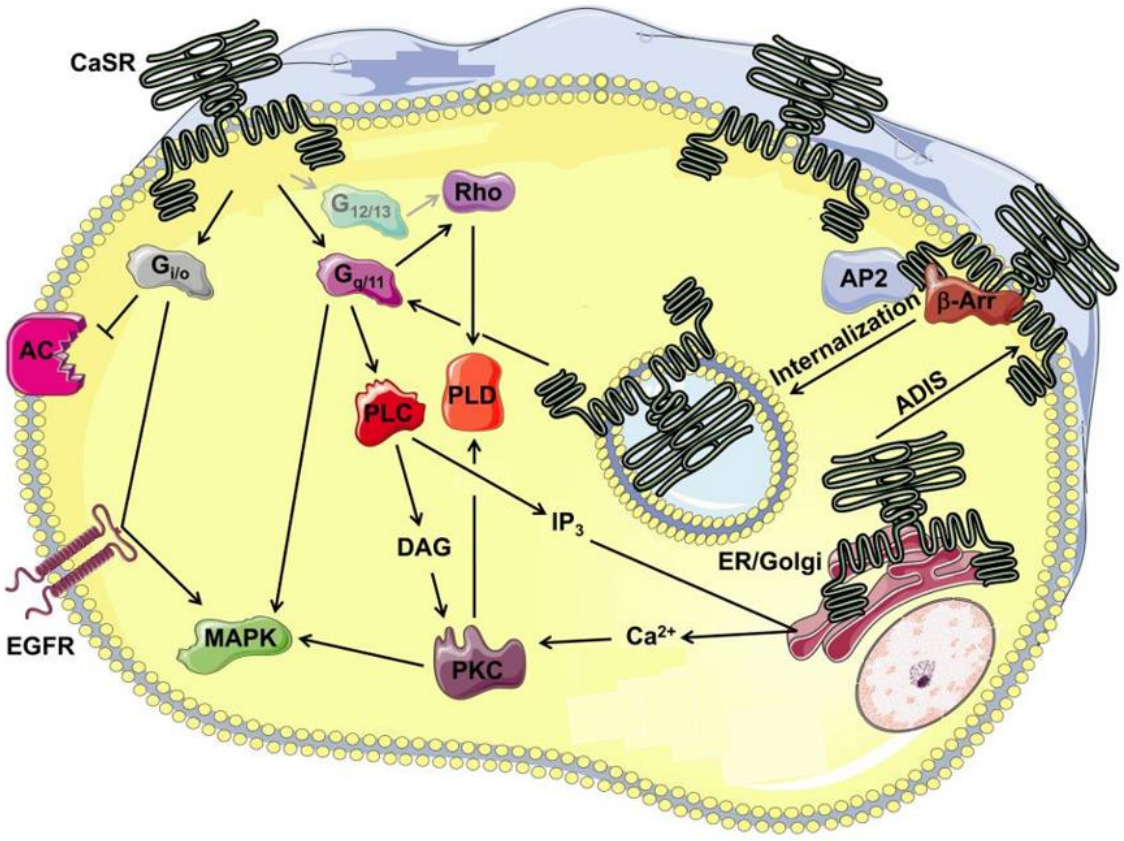


Figure 10. Figure adapted from Leach et al (2020) (106). CaSR signalling and trafficking. The CaSR primarily couples to $G_{q/11}$ and $G_{i/o}$ proteins and may also couple to $G_{12/13}$ but the physiological relevance of this is unknown, therefore $G_{12/13}$ is semi-transparent in the figure. CaSR coupling to $G_{i/o}$ proteins inhibits adenylyl cyclase (AC) activation and MAPK through epidermal growth factor receptor (EGFR) transactivation. CaSR coupling to $G_{q/11}$ proteins results in activation of phospholipase

C (PLC), which in turn, activates the secondary messenger molecules inositol triphosphate (IP_3) and diacylglycerol (DAG). IP_3 activates intracellular calcium (Ca^{2+}) release from the endoplasmic reticulum (ER). DAG activates protein kinase C (PKC) which regulates protein phosphorylation cascades such as the mitogen-activated protein kinases (MAPKs). CaSR coupling to $G_{12/13}$ is linked to Rho and phospholipase D (PLD) activation. CaSR internalisation is facilitated through interaction with AP2 and β-arrestin (β-Arr) and CaSR is able to continue signalling via the endosome and $G_{q/11}$ after internalisation. The CaSR is replenished at the cell surface through ADIS.

3.5.1.4 Biased signalling

Signalling through the CaSR has been demonstrated to effect a wide variety of physiological functions in different cell types (Table 2, Table 3). Additionally, the CaSR has been demonstrated to exhibit differing responsiveness to extracellular Ca^{2+} in different cell systems. For example, the calcimimetic compound R-568, which acts as an agonist to the CaSR, is 40 times more potent at suppressing PTH secretion in parathyroid cells than it is in stimulating calcitonin secretion from thyroid C-cells in *in vivo* studies (169). This diversity of signalling may be explained by the flexibility of its signalling cascade to modulation, or the phenomenon of "biased signalling". Biased signalling is defined as the selective activation of one of the signalling pathways of a GPCR over the others and may be induced "by biased ligands, biased receptors or system bias, any of which can result in preferential signalling through G proteins or β-arrestins" (170).

Ligands that have been confirmed to induce biased signalling in the CaSR include L-amino acids, polyamines, Mg^{2+}, strontium, calcimimetics, and calcilytics (138, 171, 172). It is thought that these different ligands may stabilise the CaSR in different active conformations, which each promote intracellular signalling through different pathways (138). Studies of an autoantibody to the CaSR, which causes acquired hypocalciuric hypercalcemia (AHH), has

similar findings. The autoantibody targets the VFTD near its Ca^{2+} binding site and acts as an allosteric modulator that promotes activation of Ca^{2+}_i and impairs pERK signalling (173).

Studies into FHH1 and ADH1-causing CaSR mutations have also provided important insights into "biased receptors" (174). Five residues, Gln27, Asn178, Ser657, Ser820 and Thr828, affected by FHH and ADH mutations have been identified (174). These residues, termed "switch residues" have been demonstrated to induce signalling bias (Figure 7). For example, the FHH-associated mutations p.Asn178Asp has been shown to impair Ca^{2+}_i signalling without altering ERK phosphorylation, whereas, the ADH-associated p.Ser657Cys mutation increased Ca^{2+}_i mobilization while decreasing ERK phosphorylation (174). Additional insights have been gained through the recent characterization of a novel gain-of-function ADH-causing mutation, Arg680Gly. Gorvin et al (2018) demonstrated that Arg680Gly elicits biased signalling towards enhanced MAPK pathways via a G-protein–independent β-arrestin–mediated pathway (175). Modelling studies suggested that the mutation disrupts a salt bridge formed between Arg^{680} and Glu^{767}, which is located between the CaSR TMD3 and ECL2 (175). The disruption of this salt-bridge is predicted to result in displacement of TM3 away from TM4 and TM5 which may facilitate β-arrestin binding, resulting in biased signalling (175). This study has also demonstrated the ability of the CaSR to signal in a G-protein independent manner (175).

The CaSR also appears to be subject to tissue-specific biased signalling. For example, in osteoblasts the CaSR activates Akt pathways that promote expression of genes involved in differentiation and growth (176). Studies using human osteoblasts have shown that Ca^{2+}-induced phosphorylation of Akt is dependent on the presence of the scaffold protein Homer1 and that silencing either the CaSR, or Homer1 reduced Akt signaling (177). HEK-293 cells that express the CaSR do not express Homer1, and in these cells Ca^{2+}_e did not phosphorylate Akt.

However, transfection of Homer1 restored Akt signaling, suggesting that the expression of Homer1 in some tissues allows tissue-specific biased signalling (177).

3.5.1.5 CaSR desensitization, internalization and sustained signalling

The CaSR is subject to two types of internalisation: a constitutive pathway (153), and an agonist-driven pathway (178), both of which utilise AP2 complex-mediated CME (Figure 5, Figure 10). Two recent studies have investigated CaSR internalization in detail. Gorvin et al (2018) utilised total internal reflection fluorescence microscopy (TIRFm) to measure ADIS and CaSR internalization simultaneously and demonstrated that the CaSR was endocytosed by constitutive and agonist-driven mechanisms simultaneously, and that $G\alpha_{q/11}$ is required for internalization (179). Mos et al (2019) used diffusion-enhanced resonance energy transfer (DERET) assays to investigate CaSR internalisation and confirmed that the CaSR was endocytosed by constitutive and agonist-driven mechanisms simultaneously (180) and their studies also showed that constitutive internalization and agonist-driven internalization required β-arrestin1/2. However, in contrast to Gorvin et al (2018) they were able to demonstrate that this internalisation was largely G protein–independent (180) and more studies are required to investigate this discrepancy.

Gorvin et al (2018) also investigated the effect of the inactivating FHH3-causing AP2σ mutations on CaSR internalisation, as AP2 is known to be an integral component of the CME machinery (Figure 11). The effect of introducing these AP2σ mutations was to both reduce ADIS and prolong CaSR residency time in clathrin structures which resulting in impaired CaSR internalization. Overall there was a net increase in CaSR surface expression (179). One hypothesis for the increased presence of CaSR on the cell surface, but overall reduction in CaSR signalling, was that in usual circumstances the CaSR may continue to signal after

endocytosis, like some other GPCRs such as the vasopressin type 2 receptor (181), PTH receptor (182) and the thyroid stimulating hormone (TSH) receptor (183). CaSR signalling in response to a bound ligand typically occurs rapidly, within 2-5 minutes, at the cell surface. However, the TIRFm experimental studies using toxins that inhibit different stages of CME, have demonstrated that there is also a sustained signal, typically more than 30 minutes later, from the CaSR originating from endosomal compartments suggesting that this may well be the case, and FHH3-associated AP2σ mutations abolish, or markedly reduce, signalling via this pathway (178) (Figure 11).

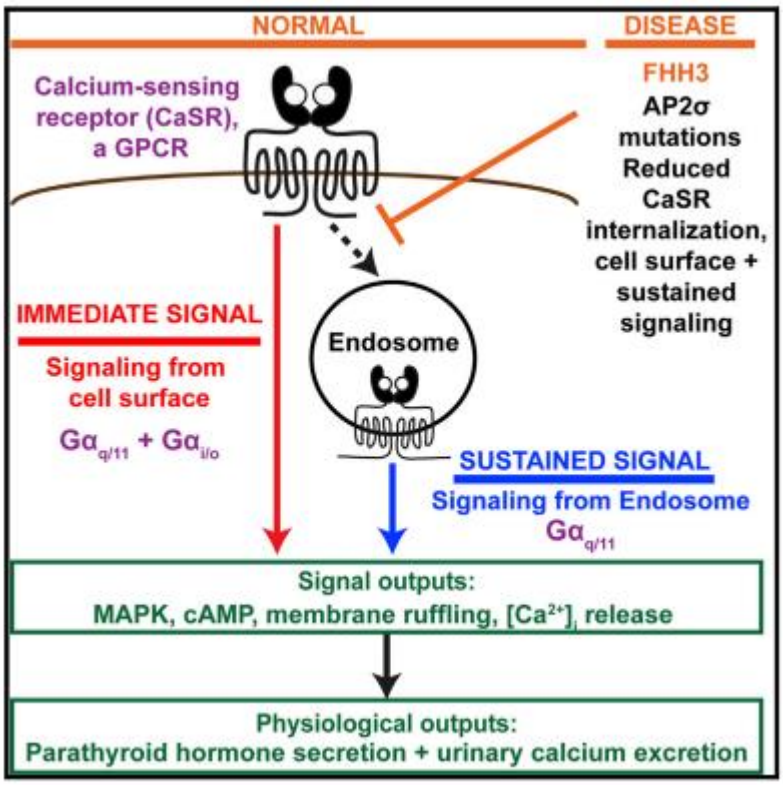


Figure 11. Reproduced from Gorvin et al (2018) (179). Immediate and sustained signalling from the CaSR. The CaSR mediates immediate signalling from plasma membranes using $G\alpha_{q/11}$ and $G\alpha_{i/o}$. This results in the signal outputs MAPK, cAMP, membrane ruffling and $[Ca^{2+}]_i$ release, and physiological outputs of PTH secretion and urinary calcium excretion. The CaSR is also able to continue signalling from the endosome after CME. This sustained signal acts via $G\alpha_{q/11}$ only and results in the same signal outputs and physiological outputs as immediate signalling. AP2σ mutations, as seen in FHH3, reduce

CaSR internalisation and reduce both cell surface signalling and sustained signalling from the endosome.

3.6 Disorders of calcium signalling

The critical role of the CaSR in extracellular calcium homeostasis is supported by its involvement in the aetiology of hypercalcaemic and hypocalcaemic disorders. Thus, loss-of-function CaSR mutations cause FHH1, whilst gain-of-function CaSR mutations cause ADH1. Moreover, mutations of CaSR signalling pathway components also cause human disorders; thus loss- and gain-of-function $G\alpha_{q/11}$ cause FHH2 and ADH2 respectively, and loss-of-function AP2σ mutations cause FHH3 (Figure 9).

3.6.1 Amino acid structure and size

Proteins are comprised of chains of amino acids, molecules that have a carboxylic acid group and an amine group each attached to a carbon atom. There are 20 amino acids each defined by a specific side chain, known as an R group, that is also attached to this carbon atom. The side chains may be polar, hydrophobic, basic or acidic, and vary in molecular weight (typically measured in Daltons (Da)). The average molecular weight of an amino acid is 110Da, and the structure of the amino acids affects how bulky they are. The differing properties of the amino acid side chains allow each protein to fold into a particular 3-dimensional shape and interact with other molecules in specific ways. Substituting one amino acid for another may affect the protein structure and/or function, particularly if the WT amino acid and variant amino acid have differing characteristics.

Table 4. Amino acid abbreviations and molecular weights. Da=Daltons. There are 20 amino acids and each can be referred to by either their full name, a 3-letter abbreviation or one-letter symbol. Each

amino acid has a different molecular weight, with the average molecular weight being 110Da. Adapted from promega.co.uk/resources (184)

Amino Acid	Three-Letter Abbreviation	One-Letter Symbol	Molecular Weight (Da)
Alanine	Ala	A	89
Arginine	Arg	R	174
Asparagine	Asn	N	132
Aspartic acid	Asp	D	133
Asparagine or aspartic acid	Asx	B	133
Cysteine	Cys	C	121
Glutamine	Gln	Q	146
Glutamic acid	Glu	E	147
Glutamine or glutamic acid	Glx	Z	147
Glycine	Gly	G	75
Histidine	His	H	155
Isoleucine	Ile	I	131
Leucine	Leu	L	131
Lysine	Lys	K	146
Methionine	Met	M	149
Phenylalanine	Phe	F	165
Proline	Pro	P	115
Serine	Ser	S	105
Threonine	Thr	T	119
Tryptophan	Trp	W	204
Tyrosine	Tyr	Y	181
Valine	Val	V	117

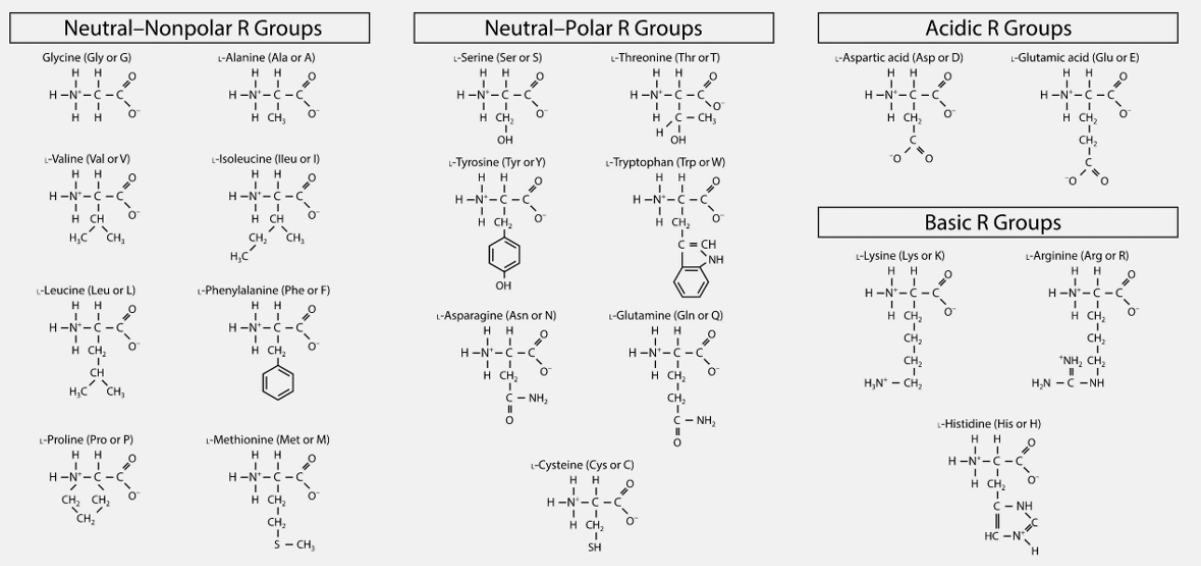


Figure 12. Amino acid structures. There are 20 amino acids each defined by their side chains (R), which may be nonpolar, polar, acidic or basic. The side chains also differ in terms of how bulky they are (their

space filling properties). These characteristics affect their interactions with other amino acids and molecules, which in turn may affect protein structure and function. Reproduced from promega.co.uk/resources (184)

3.6.2 Familial Hypocalciuric Hypercalcaemia (FHH)

Familial Hypocalciuric Hypercalcaemia (FHH) is a condition characterized by lifelong elevations of serum calcium concentrations, elevated or inappropriately normal plasma PTH concentrations, and low urinary calcium excretion resulting from PTH–independent reduced calcium excretion in the kidneys (185). In contrast to the low / low-normal magnesium concentrations typically seen in Primary Hyperparathyroidism, magnesium concentrations may be elevated in patients with FHH. PTH stimulates an increase in tubular reabsorption in patients with PHPT, however the direct effect of hypercalcaemia on the tubules is to reduce reabsorption of magnesium. In PHPT this results in low / low-normal magnesium concentrations. However, in FHH, the loss-of-function mutations affecting the CaSR lead to an increase in tubular calcium and magnesium reabsorption, resulting in normal / high concentrations of magnesium. It is an autosomal dominant, genetically heterogeneous disorder with 3 known clinical variants (FHH1-3) (20, 155), however 20-25% of FHH patients do not have a mutation in the genes known to cause FHH suggesting that other genetic causes remain to be elucidated.

3.6.2.1 FHH1

FHH type 1 (FHH1) is caused by loss-of-function CaSR mutations and accounts for 65% of cases of FHH (186). It is classically caused by heterozygous mutations of *CASR* (calcium sensing receptor), the gene encoding CaSR, with biallelic, i.e. homozygous or compound heterozygous, mutations typically causing the more severe neonatal severe hyperparathyroidism (NSHPT). However, occasionally patients with biallelic *CASR* mutations

can present as Primary Hyperparathyroidism in adulthood (187), and a patient with a heterozygous mutation acting in a dominant negative manner who presented with clinical NHSPT has been reported (188). Where FHH1 is classically well-tolerated, and often diagnosed as an incidental finding, NSHPT is a potentially fatal condition that manifests in the first few days of life. Patients have severe hypercalcaemia with associated complications including respiratory distress from hypotonia and rib cage deformities, bone under-mineralisation and multiple fractures. As FHH1 is typically a mild disease, it is likely that many cases go unrecognised, making estimations of the prevalence of FHH1 difficult. However, the most accurate estimate is likely to come from a recent study by Dershem et al (2020) which used the Regeneron DiscovEHR large-population sequencing dataset containing paired genetic and phenotypic information from 51,298 individuals to estimate the prevalence of FHH1 and ADH1 (189). *CASR* variants within this cohort were identified and classified using a bioinformatics pathogenicity triage. This triage resulted in a small number of previously unreported rare *CASR* variants predicted to be pathogenic by bioinformatic analysis which were then functionally characterised. Using this method, 38 unrelated individuals were identified giving an estimate of prevalence of 74.1 patients per 100,000 individuals (189). The identification of related individuals with genetically confirmed FHH1 within this cohort in combination with their phenotypic data allowed for an estimate of the penetrance of the disease. 23 of 25 related individuals had an elevated serum calcium (classified as 10.2mg/dl (NR 8.5-10.2) or over in this study), giving an estimated penetrance of 92% (189).

3.6.2.2 FHH2

FHH type 2 (FHH2) is the rarest form of FHH, accounting for <5% of cases, and is caused by loss-of-function mutations of *GNA11* (G-protein subunit alpha 11) encoding the G-protein G-

α_{11} (155). 4 probands have been reported to date (155, 190, 191), but this may reflect under-reporting as a result of the mild clinical course associated with the condition. Reported *GNA11* mutations are predicted to disrupt G-protein activation and impair CaSR signal transduction and consist of three missense substitutions (Thr54Met, Leu135Gln, Phe220Ser) and an in-frame isoleucine deletion (Ile200del) (155, 190, 191).

3.6.2.3 FHH3

FHH type 3 (FHH3) accounts for 10-15% of cases and is caused by loss-of-function mutations of *AP2S1* (adaptor-related protein complex 2, sigma 1 subunit) encoding AP2σ (20). FHH3 is distinct from FHH1 and FHH2, in that it is associated with a more severe phenotype (192). Rather than the benign lifelong, mild elevation in serum calcium classically associated with FHH, FHH3 patients more frequently have a marked symptomatic hypercalcaemia and hypercalcaemic complications including low bone mineral density and pancreatitis. Additionally FHH3 is associated with a significantly reduced urinary calcium excretion compared to FHH1. FHH3 demonstrates a genotype-phenotype correlation at the Arg15 codon. Of the three known FHH3-causing mutations at Arg15, namely Arg15His, Arg15Cys and Arg15Leu, patients with Arg15Leu mutations have significantly greater elevations of serum adjusted-calcium concentrations than those with Arg15Cys or Arg15His mutations (Figure 14) (192). Furthermore, individuals with Arg15Cys mutations are significantly more hypercalcaemic than those with Arg15His mutations (Figure 14). No significant differences in serum concentrations of phosphate, magnesium, ALP activity, PTH or urinary CCCR has been demonstrated between patients (192). Such Arg15 AP2σ mutations are predicted to affect key dileucine-based motifs on the CaSR cargo of CCVs reducing CaSR endocytosis and intracellular signalling (20) (Figure 13). Moreover, FHH3 appears to be associated with non-

calcitropic disorders including cognitive dysfunction and short stature (192) which is discussed in more detail below (Table 6). Additionally, age-related increases in PTH concentrations have been demonstrated in one large FHH3 kindred with the Arg15Cys mutation (20, 193, 194). The observation that FHH3 can be clinically severe and has both calcitropic and non-calcitropic phenotypes led to a focus on understanding more about AP2 complex biology and investigating potential therapies that form the basis of this thesis.

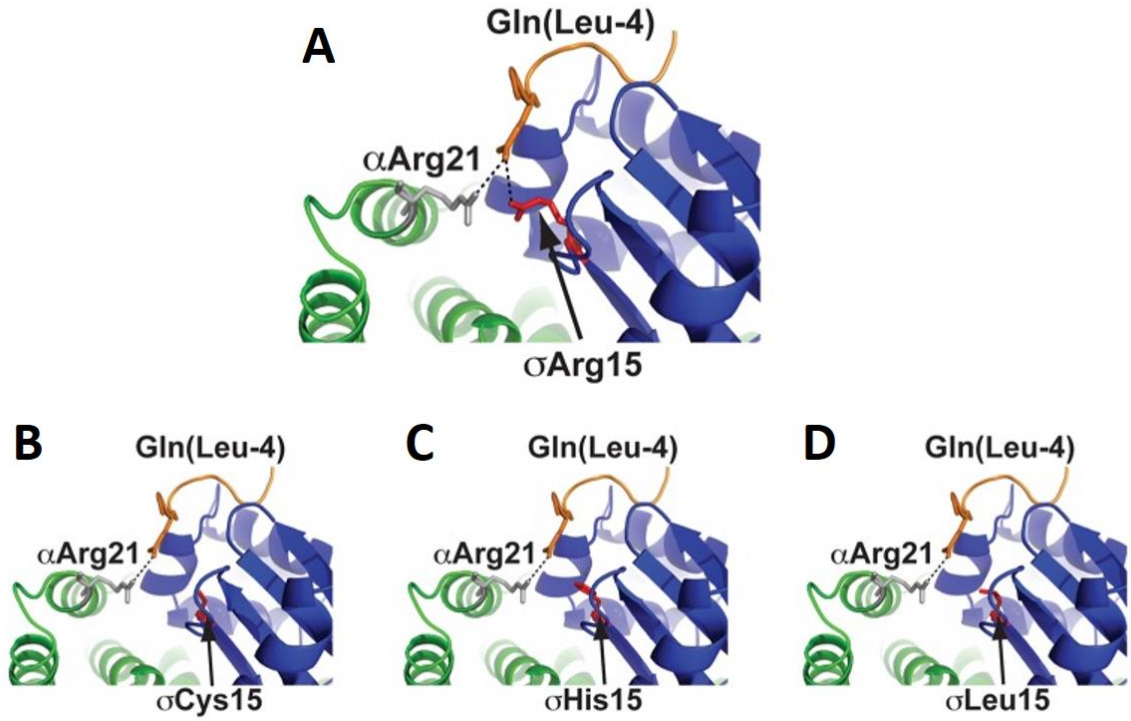


Figure 13. Figure adapted and reproduced from Hannan et al, HMG (2015)(192). (A) Crystal structure of the α-subunit (green) and σ2-subunit (blue) of the AP2 heterotetrameric complex bound to an acidic (Gln-containing) dileucine cargo protein motif (orange) [PDB file 2JKR]. The key polar contacts (black dashed lines) between the σ2-subunit Arg15 residue (σArg15, red) and α-subunit Arg21 residue (αArg21, grey), and a polar Gln residue located four residues from the first Leu residue of the acidic dileucine motif [Gln(Leu-4), orange], are shown. (B-D) Structural analysis of the observed Arg15 mutants (Arg15Cys, a basic to polar amino acid change (B), Arg15His, both basic amino acids (C) and

Arg15Leu, a basic to non-polar amino acid change (D)) are all predicted to result in the loss of the key polar contact with the polar cargo protein Gln (Leu-4) residue.

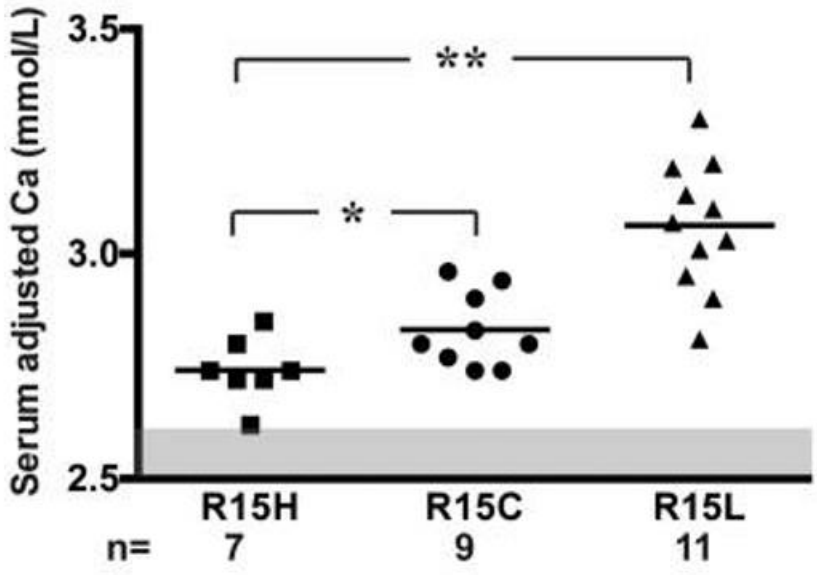


Figure 14. Figure adapted and reproduced from Hannan et al, HMG (2015)(192). Assessment of genotype–phenotype correlations between probands harbouring Arg15His (R15H), Arg15Cys (R15C) or Arg15Leu (R15L) *AP2S1* mutations. Serum biochemical values are shown as scatter plots. Probands with R15L mutations had significantly greater elevations of serum adjusted-calcium concentrations than probands with R15C or R15H mutations. Probands with R15C mutations were significantly more hypercalcaemic than probands with R15H mutations. The normal ranges [mean ± 2 standard deviations (SDs)] for serum calcium is indicated by the grey area. *$P < 0.05$, **$P < 0.01$. Mean values for the respective groups are indicated by horizontal solid lines. Kruskal-Wallis test used to compare multiple groups.

3.6.3 Autosomal Dominant Hypocalcaemia

Autosomal dominant hypocalcaemia (ADH) is a rare cause of genetic hypoparathyroidism characterised by hypocalcemia, which is often mild and increased fractional excretion of urinary calcium with a tendency to overt hypercalciuria. It may also be associated with hypomagnesaemia and hyperphosphataemia. Although these features are similar to those

seen in other causes of hypoparathyroidism, affected individuals generally have PTH concentrations that are inappropriately low rather than absolutely low, i.e. PTH concentrations are often detectable and within the reference range. This helps to differentiate ADH from other causes of genetic hypoparathyroidism. In ADH, the mild hypocalcaemia may be asymptomatic, but can sometimes produce symptoms attributable to muscle hyperexcitability, particularly if serum magnesium concentrations are also low. Additionally, affected individuals may develop nephrolithiasis as a result of increased urinary calcium, which can be exacerbated by injudicious use of calcium supplementation or activated vitamin D compounds (155, 186).

ADH is genetically heterogeneous with ADH type 1 (ADH1), the predominant form, caused by germline gain-of-function mutations of the CaSR (42) and ADH type 2 (ADH2) caused by germline gain-of-function mutations of $G\alpha_{11}$ (155). As ADH1-causing CaSR mutations are analogous to FHH1-causing CaSR mutations, and ADH2-causing G-protein mutations analogous to those G-protein mutations that cause FHH2, it was proposed that there may be an "ADH3" caused by gain-of-function mutations in AP2σ, analogous to FHH3. A study by Rogers et al (2014) investigated this hypothesis (195). 19 patients were identified who had the ADH phenotype of hypocalcaemia associated with normal or low PTH concentrations, but who not have a mutation identified in either *CASR* or *GNA11*. This samples size of 19 was predicted to identify at least one patient with an *AP2S1* mutation with a 98% probability, assuming that the prevalence of "ADH3" in patients with an ADH-phenotype was similar to the prevalence of FHH3 in patients with an FHH-phenotype, at 20%. Screening *AP2S1* in these ADH-phenotype patients did not reveal any abnormalities in the gene, suggesting that ADH3 may not occur, or if it does, represents a very rare cause of hypocalcaemia (195).

3.6.3.1 ADH1 and Bartter syndrome occurring in association with ADH

The recent study by Dershem et al (2020) using the Regeneron large-population sequencing dataset identified 2 unrelated individuals with a genetic diagnosis of ADH1 within the cohort of 51,289 individuals, giving a prevalence in this population of 3.9 per 100,000 (189). 2 related individuals with ADH1 were identified and both were found to be hypocalcaemic, suggesting a penetrance of 100% (189). ADH1 patients tend to exhibit the "classic" features of ADH characterised by mild hypocalcaemia and increased fractional excretion of urinary calcium with~10% having absolute hypercalciuria (155). Some patients with ADH1 may also have ectopic calcifications and/or elevations in bone mineral density (BMD) (44).

The vast majority of reported cases of ADH1 are caused by heterozygous gain-of-function mutations of the *CASR*, although there are reports of ADH1 patients with homozygous *CASR* mutations (196, 197). As described, there is an ADH1 mutation hot spot within the second loop of the VFT domain, which contributes to the CaSR homodimer interface (48, 123, 146). (130). Activating-ADH1 mutations have also been shown to cluster at the extracellular side of TM6–ECL3–TM7 interface suggesting that they favour receptor activation (48, 123, 132).

A certain subset of ADH1 patients have a more severe phenotype, with severe and symptomatic hypocalcaemia, significant hypercalciuria, and the additional finding of Bartter syndrome, that is, hypokalaemic metabolic alkalosis, hyperreninaemia and hyperaldosteronism, a condition referred to as Bartter syndrome occurring in association with ADH. Untreated patients frequently develop complications such as carpopedal spasm and nephrolithiasis. *In vitro* analysis of *CASR* mutations associated with Bartter syndrome occurring in association with ADH have demonstrated a more severe set-point abnormality

abnormality than is seen in ADH1, with some mutations appearing to cause constitutive activation of the CaSR (198, 199).

3.6.3.2 ADH2

To date 8 *GNA11* mutations resulting in ADH2 have been identified (200). Affected individuals tend to have a milder phenotype than those with ADH1 (200), although only small numbers have been reported, therefore the phenotypic spectrum remains to be fully elucidated (201). In addition to the biochemical features, short stature has been observed in 2 kindreds (202, 203).

3.6.4 Role of drug treatments in calcitropic and non-calcitropic disorders

Before the advent of targeted pharmacological therapies, the management of NSHPT and severe hypercalcaemia due to FHH would typically involve surgical neck exploration and parathyroidectomy. Even when parathyroid autotransplantation was used, patients would often end managing complete post-surgical hypoparathyroidism in the long term (204), which comes with its own morbidity and mortality (205). Similarly, symptomatic ADH patients have conventionally been managed in the same way as patients with hypoparathyroidism from other causes, with calcium and active vitamin D preparations. However, due to the difference in underlying physiology, ADH patients are particularly predisposed to developing hypercalciuria, nephrolithiasis and renal impairment from this management (155, 206), which can be a problem even in patients with post-surgical hypoparathyroidism. More recently recombinant PTH (1–34) (teriparatide) has been used to treat ADH, however, this therapy is not always enough to overcome the effect of the ADH1-mutation in the kidney CaSR and hypercalciuric complications may still occur (207).

Calcimimetic and calcilytic compounds are positive and negative modulators of the CaSR receptor (PAMS and NAMs), respectively (140) and therefore represent therapies that are more targeted towards correcting the underlying pathophysiological alterations in parathyroid and kidney function caused by loss-of-function or gain-of-function mutations affecting CaSR signalling.

Recent work by Gao et al (2021) using cryo-EM has uncovered the mechanism by which calcimimetics and calcilytics act on the CaSR (139). As stated, upon activation the CaSR homodimer adopts an asymmetric 7TM configuration that primes one protomer for G-protein coupling (139). Calcimimetics act to stabilise this asymmetry by targeting the 7TMDs and stabilising them in distinctly different poses in the two protomers. Calcilytics also target the TMDs and act to lock them in an inactive symmetrical configuration (139).

3.6.4.1 Calcimimetics (PAMs)

Calcimimetics are ligands that either mimic the effects of Ca^{2+} on the CaSR, or potentiate its effects and may be classified as type I or type II. Type I calcimimetics are agonists and include naturally occurring ligands. Type II calcimimetics are PAMs that enhance the effect of Ca^{2+} on the CaSR, producing a stronger intracellular signal than would otherwise be expected for the prevailing $[Ca^{2+}]_e$. Cinacalcet and evocalcet are two clinically approved chemically and structurally related small molecule PAMs that act as type II calcimimetics (Table 5). They belong to the arylalkylamine family of PAMs, which were derived from the nonselective calcium channel blocker, fendiline, and act allosterically by binding the CaSR in the 7TMD. In 2004 cinacalcet became the first GPCR allosteric modulator to be approved for clinical use and has FDA approval for the treatment of primary hyperparathyroidism where parathyroidectomy is contraindicated, for hypercalcemia in adults with parathyroid

carcinoma and for secondary hyperparathyroidism in patients on renal replacement therapy. Evocalcet was approved for the treatment of secondary hyperparathyroidism in patients on dialysis in Japan in 2018.

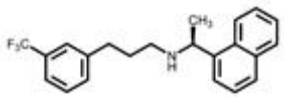
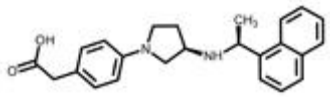
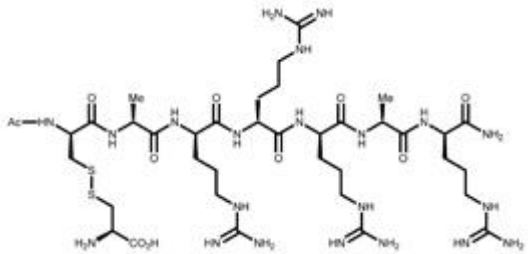
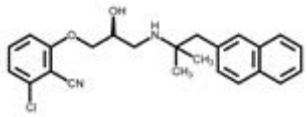
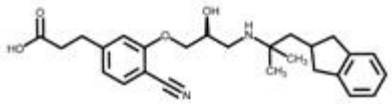
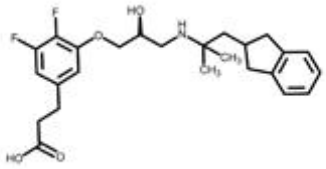
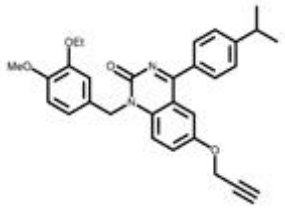
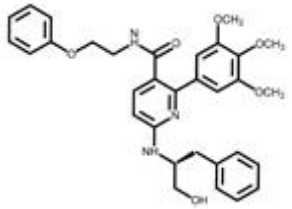
After FHH was discovered and its pathophysiology elucidated, *in vivo* experiments went on to demonstrate that cinacalcet rectified the signalling abnormalities seen in CaSR-expressing HEK293 cells transfected with inactivating FHH-causing mutations *in vitro* (208-210). This led to further trials demonstrating that cinacalcet can reduce serum calcium concentrations and alleviate symptomatic hypercalcaemia in FHH1 (208), FHH2 (209) and FHH3 patients (210). Cinacalcet is now not uncommonly used to treat patients with symptomatic FHH, and has also been used successfully to treat NSHPT (211), although, not surprisingly, it is ineffective if both CASR alleles have mutations whereby the CaSR is not expressed (212). The CaSR has also been shown to have an important physiological role in non-calcitropic tissues (Table 3), and, unsurprisingly, disorders of calcium signalling have been implicated in a wide variety of non-calcitropic diseases. Evidence is now emerging for a role for cinacalcet in treating these non-calcitropic disorders (213) and calcimimetics have recently been proven efficacious as a novel therapy for secretory diarrhoea (214), to inhibit growth of human lung adenocarcinomas in cell lines (215), and to reduce inflammation in mouse models of inflammatory bowel disease (216). However, the effect of calcimimetics on the non-calcitropic phenotypes associated with loss-of-function mutations of AP2σ remains to be elucidated.

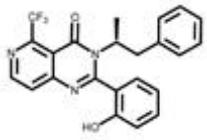
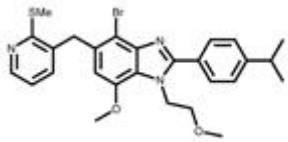
Etalcalcitide is a novel CaSR PAM comprised of 7 D-amino acids linked via a disulfide bond to L-cysteine that acts by binding to the CaSR via disulfide bond formation (217). It received FDA approval for the treatment of secondary hyperparathyroidism in patients with CKD on dialysis in 2017 and is administered intravenously at the end of dialysis.

3.6.4.2 Calcilytics (NAMs)

Calcilytics are negative allosteric modulators that reduce the sensitivity of the CaSR to Ca^{2+} and comprise two main classes of orally active compounds, the amino alcohols, which includes NPS2143, ronacaleret and NPS795, and the quinazolinones, which includes ATF 936 (Table 5). Calcilytics were originally investigated as potential therapies for osteoporosis, due to their ability to stimulate PTH secretion which could potentially lead to anabolic effects on bone mass. NPS 2143, which is structurally and chemically related to cinacalcet and other arylalkylamines, was the first calcilytic to be identified and investigated, however, whilst it was shown to lead to sustained increases in PTH secretion, it did not alter bone mass. Ronacaleret was generated through modifying the compound NPS 2143, and was also investigated, however, it was not shown to be efficacious in postmenopausal osteoporosis (218). Further efforts to identify NAMs as potential treatments for osteoporosis lead to the discovery of four chemically distinct NAM series (106): the quinazolinones ATF936 and AXT914; the pyridine BMS compound 1; a series of 3*H*-quinazoline-4-ones and 3*H*-pyrimidine-4-ones; and benzimidazoles. Despite this interest, none of these drugs have been demonstrated to be efficacious against osteoporosis (106) and until recently, no further research was undertaken. However, there has been recent interest in repurposing these NAMs for the treatment of ADH1 and an open label dose escalation study evaluating the safety, tolerability, pharmacodynamics and pharmacokinetics of intravenous NPSP795 in ADH1 has been completed (ClinicalTrials gov Identifier: NCT02204579, URL https://clinicaltrials.gov/ct2/show/NCT02204579, last accessed 02.05.22).

Table 5. Representative CaSR PAMs and NAMs and their chemical structures. Adapted from Leach et al 2020 (106).

Ligand	Structure
PAMs	
Cinacalcet	
Evocalcet	
Etelcalcetide	
NAMs	
NPS 2143	
NPSP795	
Ronacaleret	
ATF936	
BMS compound 1	

3H-pyrimidine-4-one compound (R)-2h	
Benzimidazole compound 40	

3.7 The role of Ap2σ mutations in FHH3

The *AP2S1* gene encoding AP2σ contains 5 coding exons, together with a 5' untranslated region (UTR) and 3'UTR (Figure 9). The start codon (ATG) is located in exon 1, and the stop codon (TGA) is located in exon 5. The canonical AP2σ isoform is comprised of 142 amino acids which are divided into 7 β-strands (β1-7) and 5 α-helices (α1-5) (Figure 16). It has 2 hydrophobic pockets that recognise and bind dileucine motifs, located near the interface with AP2α (32). AP2σ is ubiquitously expressed in all human tissues (46) and the amino acid sequence is highly evolutionarily conserved. Of the 142 amino acids, all are conserved in mice (*M. musculus*), clawed frogs (*X. tropicalis*) and zebrafish (*D. rerio*) (Figure 10). There are only 3 differences between the human protein and that of fruit flies (*D. melanogaster*), and only 4 differences between the human protein and that of nematodes (*C. elegans*) (Figure 16). That AP2σ has remained largely unchanged throughout evolution suggests that changes are detrimental to fitness and that its function is unique and essential to higher organisms.



Figure 15. Schematic representation of the genomic organisation of the *AP2S1* gene. The gene consists of 5 exons (dark grey boxes), with a 5' untranslated region (UTR) and 3'UTR (light grey boxes). The start codon (ATG) is located in exon 1, and the stop codon (TGA) is located in exon 5. The position of the known FHH3-causing Arg15 mutations, Arg15Cys, Arg15His and Arg15Leu, are shown in red.

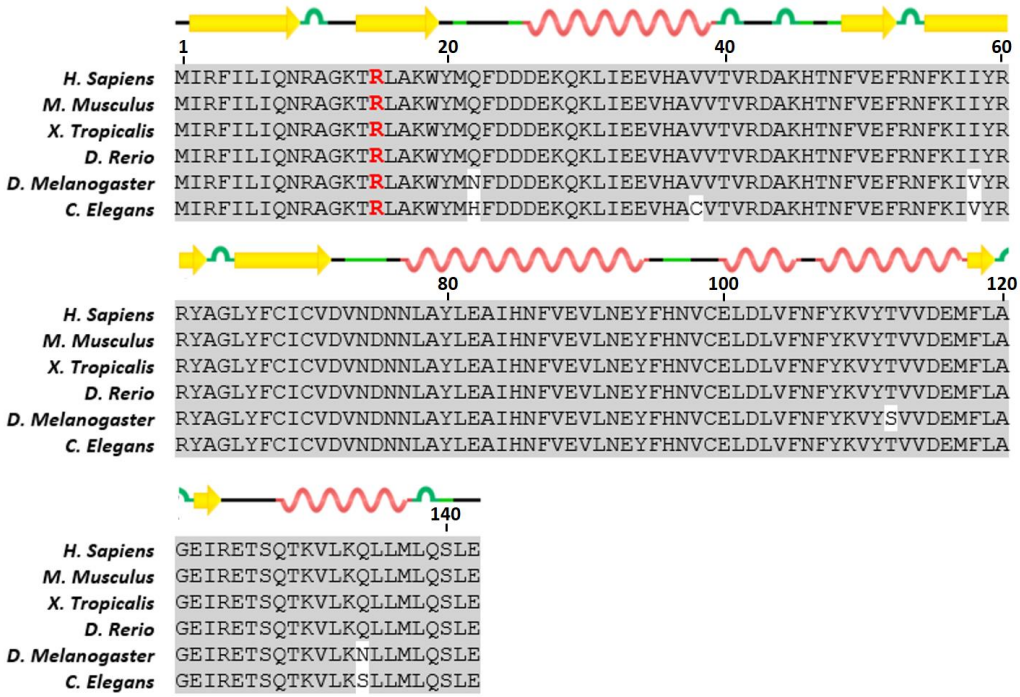


Figure 16. Multiple protein sequence alignment of AP2σ-subunit orthologs. The secondary structure of the protein is shown above (adapted from *Jackson et al*, Cell. 2010 (219)). Conserved residues are shaded grey. Codon 15, the site of all known FHH3-causing mutations, is shown in red. Codon numbers are indicated every 20 residues in black. β-strands are indicated by yellow arrows; α-helices are indicated by red wavy lines; non-repetitive loops are in green.

When I started my DPhil in October 2016, all reported AP2σ mutations had been found on one codon, Arg15, and shown to cause FHH3 (20). Arg15 encoded from exon 2, forms part of the β2-strand (Figure 15 and 10) and is involved in the interaction between the AP2 complex and the dileucine motif of the CaSR (20). Mutations of Arg15 have been shown to have dominant negative effects on the function of the AP2 complex (192), to impair endocytosis of the calcium-sensing receptor (CaSR) (20) and to result in impaired intracellular calcium signalling. According to the traditional model of CME, where endocytosis is the mechanism by which a receptor is deactivated, impairment of CaSR endocytosis alone would not explain how AP2σ mutations result in impaired CaSR signalling (192). These observations add weight to the experimental evidence that the CaSR is able to continue signalling after endocytosis

(178), and that impairment of this intracellular signalling pathway is significant enough to result in a clinical phenotype.

The arginine 15 residue is encoded by the CGC nucleotide triplet. Single nucleotide changes to this codon would generate 6 alternative residues, namely cysteine (TGC), serine (AGC), glycine (GGC), leucine (CTC), proline (CCC) and histidine (CCA). However, of the 6 possible variants, only Arg15Cys, Arg15His and Arg15Leu have been found in humans (20, 192), with no other variants of Arg15 present on the gnomaAD browser (last accessed 02.05.22) (220). Furthermore, there appears to be genotype-phenotype correlations between these FHH3-causing mutations, with Arg15Leu mutations associated with the most marked hypercalcaemia, and Arg15His associated with the mildest (192) (Figure 14). The other potential mutations of Arg15, namely Arg15Gly, Arg15Pro and Arg15Ser, have not been observed in humans, and have been shown to impair cell growth *in vitro* (192), suggesting that they may be incompatible with cell viability (Figure 17).

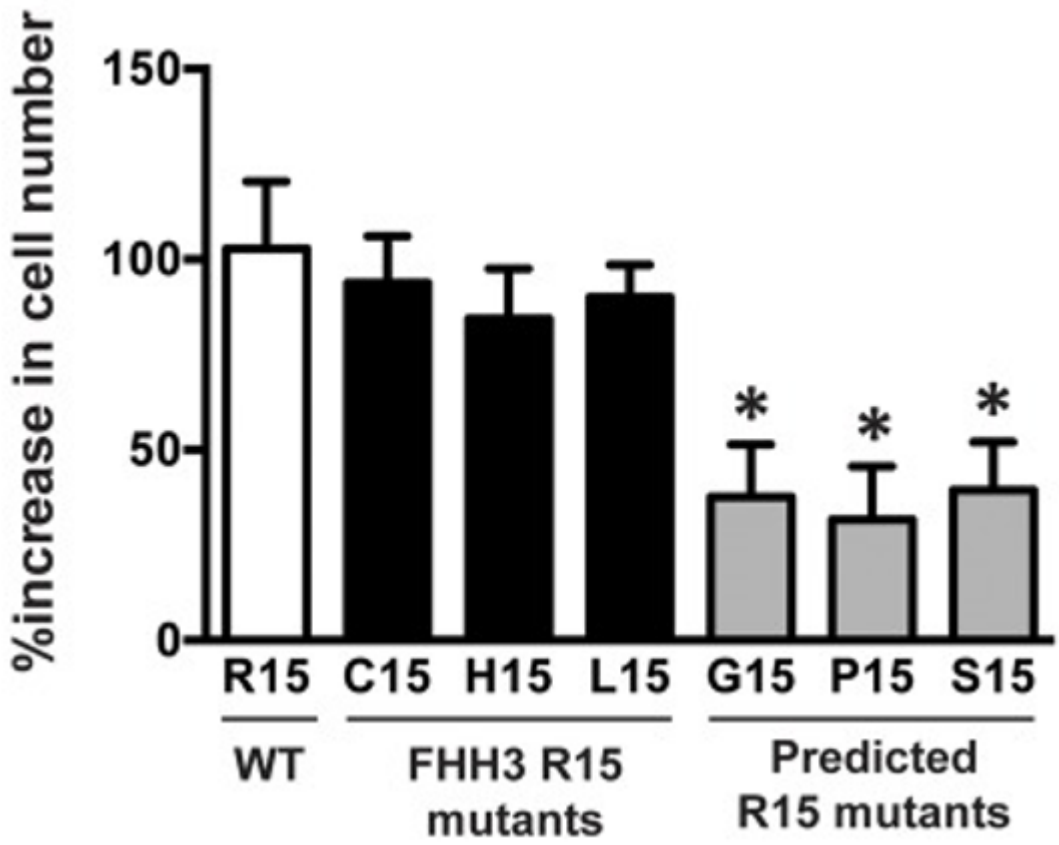


Figure 17. Adapted from Hannan et al (2015) (192). "Growth of cells expressing WT or mutant AP2σ2 proteins. Cells expressing the non-observed possible R15 mutants showed a significantly reduced percentage increase in cell numbers over a 24-h period when compared with cells expressing WT or FHH3-associated mutant AP2σ2 proteins, consistent with an impairment of proliferation. Results are from 11 to 18 assays and 4 independent transfections. *P < 0.05"

3.7.1 Bone and non-calcitropic effects of AP2σ mutations

To date, *AP2S1* mutations have only been implicated in one disorder, FHH3, a specific disorder of calcium homeostasis. However, multiple case reports exist of FHH3 patients with co-existing non-calcitropic conditions and/or a reduced bone mineral density (BMD) that are not typically seen in patients with FHH1 and FHH2 (192, 210, 221-229). Analysis of 11 peer-reviewed publications containing phenotypic data on 49 FHH3 patients with a confirmed *AP2S1* mutation revealed that co-existing reduced bone mineral density and/or non-

calcitropic disorders were observed in ~65% cases where data was available (30 out of 47), with Arg15Leu mutations being most frequent (Table 6). This adds further support to the findings by Hannan *et al*. that FHH3 shows genotype-phenotype correlations with Arg15Leu associated with the most severe phenotype (192) (Table 6).

The occurrence of non-calcitropic disorders in patients with FHH3-associated mutations is not surprising given that these mutations have been shown to impair CaSR signalling, and the CaSR plays an important role in the physiology of non-calcitropic tissues (Table 3). The AP2 complex is also ubiquitously expressed and facilitates CME of a wide range of proteins, including but not limited to the CaSR, in most tissues of the body. A p.Arg170Trp mutation in *AP2M1*, encoding the μ-subunit of AP2, has recently been identified in 4 individuals with neurodevelopmental disorders and epileptic seizures with functional analysis demonstrating significant impairment of CME, using transferrin uptake as a model (19). It is thus likely that mutations in AP2σ similarly exert their non-calcitropic effects by impairing endocytosis of cargo, such as receptors and adhesion molecules.

Table 6. Summary of the reported bone and non-calcitropic phenotypes in FHH3 patients in selected publications. All reports in peer-reviewed publications which contained both clinical and genetic details of FHH3 patients with a confirmed *AP2S1* mutation included. Each individual is described on a new line. *This paper also describes individuals with R15H mutations described in Hovden 2016, data only included once in the first publication. **In this cohort the BMD measurement may be falsely decreased due to the co-existent SS. OP = osteoporosis, LD = learning disabilities, ADHD = Attention Deficit Hyperactivity Disorder, CHD = Congenital Heart Disease, Panc = pancreatitis, MNG = multinodular goitre, Dep = depression, Psych = psychiatric problems, T1DM = type diabetes, NA = details not available, BMD = bone mineral density, NET = neuroendocrine tumour, IBS = Irritable Bowel Syndrome, Nil = no evidence of non-calcitropic phenotype, SS = short stature, Down's syndrome, KS = Klinefelter's syndrome, CP = Cerebral Palsy, FTT = failure to thrive

Publication	Arg15Cys	Arg15His	Arg15Leu
Kerut S et al, BMJ Case Rep (2020)(221)	OP		
Aashiq M et al, Case Rep Pediatr (2020)(222)		LD, ADHD CHD	
Wong FCK et al, F1000Res (2019)(223)	Panc MNG Nil		
Szalat A et al, Endocrine (2017)(224)			LD LD, Dep LD LD LD LD, Dep, ADHD LD, ADHD
Hovden S et al, EJE (2017)(226)*			Psych, LD Psych, LD, T1DM Nil Nil NA
Howles et al, Letter to Ed, NEJM (2016)(210)	Nil	 Nil	 Nil
Hovden S et al, Clin Case Rep (2016)(225)		Low BMD, NET Nil Nil	
Hannan et al, HMG (2015)(192)	Nil Nil LD LD IBS	 Nil Nil Nil NA	 CHD, LD, SS LD LD, Panc, SS LD

			NA LD Nil Nil
Tenhola S et al, J Clin Endocrinol Metab (2015)(227)			Low BMD, DS
Hendy et al, JCEM (2014)(228)	Dep Nil	 Low BMD, SS** Low BMD, SS**	 Psych, KS LD, CP
Fujisawa Y et al, JCEM (2013)(229)			FTT

3.8 *In vivo* models of disorders of calcium homeostasis

The mouse is the most common species used as an animal model for studying human genetic disease when investigations are impossible, impractical or inappropriate in human subjects. They are a cost-effective and efficient research tool and are well understood as they have been used in biomedical research for nearly a century. Recent advances in genetic engineering such as CRISPR-Cas technology which enables "editing" of the genome by deleting, inserting or mutating sections of the DNA sequence, have allowed manipulation of the mouse genome to the extent that mutations can be introduced with relative efficiency and a high degree of accuracy. As stated above, the amino acid sequence of mouse and human *AP2S1* is 100% homologous (Figure 10) suggesting functional conservation between species. Furthermore, mouse models have previously been developed for studying defects in calcium homeostasis.

3.8.1.1 FHH1

Mouse models for FHH1 exist and have helped to elucidate the condition and to test potential therapies (74, 230, 231). There are 3 mouse models available with mutations affecting the CaSR. Mice lacking the CaSR have been shown to recapitulate the human calcitropic

phenotype of FHH1 (230). Thus, mice with deletion of both alleles of *Casr* replicate the NSHPT phenotypes of failure-to-thrive and bone abnormalities; whilst heterozygous mice have milder hypercalcaemia as seen in FHH1 (230). As mice with a global *Casr* knockout die very young, 2 other mouse models are available to investigate the role of CaSR further. Mouse models with inducible CaSR deletion have demonstrated a critical role of the CaSR in early embryogenesis and skeletal development (74). In order to investigate the role of CaSR function independently of PTH stimulation, mice lacking both the CaSR and PTH have been also generated (231). These mice have demonstrated that the CaSR has effects on the fine regulation of serum calcium concentrations and renal calcium excretion beyond its effect on PTH secretion.

3.8.1.2 FHH2

A mouse model of FHH2 with a germline loss-of-function *Gna11* mutation (Asp195Gly), established by N-ethyl-N-nitrosourea (ENU) mutagenesis (232) has also been described and has allowed further investigation of the FHH2 phenotype. Additionally, mice with parathyroid-specific ablations of both the *Gna11* and *Gnaq* (encoding $G\alpha_q$) genes have been reported to develop marked hypercalcemia and hyperparathyroidism (233).

3.8.1.3 FHH3

At the start of my DPhil in October 2016, a mouse model of FHH3 remained to be established. Mouse models with mutations affecting AP2σ had been generated and had provided some insight into the protein function, however, they had not recapitulated the FHH3 phenotype. Mice with heterozygous mutations of AP2σ that result in the deletion of 17 evolutionarily conserved amino acids (del17), $AP2\sigma^{+/del17}$, generated by ENU, appear normal and have normal biochemistry. However, homozygous $AP2\sigma^{del17/del17}$ mice die between embryonic days

3.5 and 9.5, indicating that AP2σ has a role at the embryonic patterning stages and organogenesis (234). The need for a biological model of FHH3 is addressed in Chapter 7 of my thesis.

3.8.1.4 ADH1

Three different ADH1 mouse models have been reported: the *Nuf* mouse generated by chemical mutagenesis which harbours the germline gain-of-function CaSR mutation Leu723Gln (235); and two *knock-in* mouse models with ADH1-causing germline Cys129Ser or Ala843Glu gain-of-function CaSR mutations (236).

The Leu723Gln *Nuf* mouse model was generated in 2004 using the chemical mutagenesis agent isopropyl methane sulfonate (iPMS) alkylating agent. Both heterozygous and homozygous *Nuf* mice demonstrate the ADH1 phenotype of hypocalcemia, hyperphosphatemia, lowered plasma PTH concentrations, and ectopic calcifications (235). The calcilytic NSPSP795 was shown to elicit dose-dependent increases in PTH and ameliorate the hypocalcemia seen in the *Nuf* mouse (237).

The two knock-in ADH1 mouse models, which harboured Cys129Ser or Ala843Glu gain-of-function CaSR mutations, were generated in 2015 (236). The heterozygous mice exhibited hypocalcemia, hyperphosphatemia, reduced plasma PTH, hypercalciuria and renal calcifications, consistent with the phenotype of ADH1 patients. Interestingly, the homozygous mutant knock-in mice exhibited embryonic or perinatal lethality (236). The heterozygous mice were treated with the calcilytic JTT-305/MK-5442, which was shown to improve serum and urinary calcium and phosphate levels, and prevent renal calcification. It was shown to represent a superior treatment for ADH1 than recombinant PTH, which could not reduce hypercalciuria or renal calcification (236).

3.8.1.5 ADH2

Two mouse models for ADH2 have been described: one generated by ENU chemical mutagenesis to harbour a germline gain-of-function $G\alpha_{11}$ mutation, Ile62Val (238); and the other was generated by CRISPR-Cas9 gene editing and harbours a human ADH2-causing germline $G\alpha_{11}$ mutation, Arg60Cys (239). Both the Ile62Val mouse generated by ENU chemical mutagenesis, known as *Dark skin 7* (*Dsk7*), and the mouse harbouring the human ADH2-causing Arg60Cys exhibited hypocalcemia, hyperphosphatemia, reduced plasma PTH and normocalciuria, with the additional finding of increased skin pigmentation, not reported in patients with ADH2 (238, 239). Studies of the effect of the calcilytic NPS-2143 demonstrated that it induced a rapid and marked rise in plasma PTH and calcium concentrations in mice both heterozygous and homozygous for the *Dsk7* gene (209). The Arg60Cys mouse was treated with two different drugs, NPS-2143 as in the *Dsk7* mouse, and also the cyclic depsipeptide YM-254890 which acts as a competitive inhibitor of $G\alpha_{11/q}$ (239). As in the *Dsk7* mouse, NPS-2143 demonstrated a rapid and marked rise in plasma PTH and calcium concentrations in the Arg60Cys mouse (239). YM-254890 was also demonstrated to significantly increase blood calcium levels through direct inhibition of $G\alpha_{11/q}$ (239).

4 AIMS

The aims of my DPhil thesis are:

i. <u>To use large population datasets to search for novel *AP2S1* variants in human subjects</u>

When I started my DPhil in October 2016, all reported *AP2S1* mutations had been found on one codon, Arg15, and shown to cause Familial Hypocalciuric Hypercalcaemia type 3 (FHH3) (20). The presence or absence of AP2σ variants outside Arg15, and their frequency within populations could provide important information on how well changes to the protein are tolerated. Novel variants associated with disturbances of calcium signalling could provide additional insight into the structural-functional role of AP2σ within this pathway. It may be possible to elucidate non-calcitropic effects of AP2σ variants where phenotypic data is available, providing insight into the role of AP2 in other signalling pathways. Variants that do not appear to have phenotype effects could also indicate residues of AP2σ that are tolerant to change and therefore provide more information about the function of the protein.

ii. <u>To address the need for a biological model of FHH3</u>

At the start of my DPhil in October 2016, a mouse model of FHH3 remained to be established. Mouse models with mutations affecting AP2σ had been generated and had provided some insight into the protein function, however, they had not recapitulated the FHH3 phenotype. The generation of a mouse model of FHH3 would enable further characterisation of the non-calcitropic phenotype that appears to be associated with FHH3. It would also enable the evaluation of the roles of AP2σ in calcium homeostasis and endosomal trafficking of the CaSR through pathophysiological studies that are difficult to undertake in patients.

iii. <u>To explore the link between AP2σ mutations and developmental disorders, and the mechanism by which AP2σ mutations exert these effects.</u>

Patients with FHH3-associated mutations have been shown to have an increased frequency of non-calcitropic disorders, including neurodevelopmental disorders. This is not surprising given that these mutations impair CaSR signalling, the CaSR plays an important role in the physiology of non-calcitropic tissues, and the AP2 complex is also ubiquitously expressed and facilitates CME of a wide range of proteins, including but not limited to the CaSR, in most tissues of the body. Further understanding the relationship between AP2σ mutations and neurodevelopmental disorders would provide insight into both the function of the protein and the aetiology of these diseases, which may in the future provide an important therapeutic target.

5 METHODS

5.1 Patients

5.1.1 Informed consent

Informed consent was obtained from patients using protocols approved by the Multicentre Research Ethics Committee (UK) (MREC/02/2/93). For patients from the DiscovEHR dataset all clinical data and International Classification of Disease-9 codes were obtained from the electronic health records in accordance with Institutional Review Board approvals, in a de-identified manner through an approved data broker (240, 241).

5.2 Generation of plasmid expression constructs

AP2S1 variants (Arg3His, Arg15His, Ala44Thr, Phe52Tyr, Arg61His, Thr112Met, Met117Ile, Glu122Gly and Glu142Lys) were generated by site-directed mutagenesis (QuikChange Lightning, Agilent Technologies) using a human *AP2S1* cDNA expression construct (Clontech Laboratories Ltd) previously subcloned into pBI-CMV4-RFP (Clontech Laboratories Ltd) and gene-specific primers (SigmaAldrich), as described (192) to generate pBI-CMV4-RFP-*AP2S1*-WT and the nine variants (Arg3His Forward CTGGATGAGGATAAAGTGGATCATGGCGACCCC, Reverse GGGGTCGCCATGATCCACTTTA TCCTCATCCAG; Arg15His Forward ACCACTTGGCCAGACGCGTCTTGCCTG, Reverse CAGGCAAGACGCGTCTGGCCAAGTGG; Arg44Thr Forward CAAAGTTGGTGTGTTTGACGTCTCG GACGGTGAC, Reverse GTCACCGTCCGAGACGTCAAACACACCAACTTTG; Phe52Tyr Forward CTTAAAGTTCCGGTACTCCACAAAGTTGGTGTGTTTGG, Reverse CCAAACACACCAACTTTGT GGAGTACCGGAACTTTAAG; Arg61His Forward AGTAGAGGCCAGCATAGTGGCGG TAAATGATCTTA, Reverse TAAGATCATTTACCGCCACTATGCTGGCCTCTACT; Thr112Met Forward AAGGTTTACATGGTCGTGGAC, Reverse GTAGAAGTTGAACACCAGG; Met117Ile Forward TGGACGAGATTTTCCTGGCTG, Reverse CGACCGTGTAAACCTTGTAG; Glu122Gly Forward

TGGTCTCTCGGATTCCGCCAGCCAGGAAC, Reverse GTTCCTGGCTGGCGGAATCCGAGAG ACCA; Glu142Gly Forward ACAGTCCCTGAAGTGAATGATC, Reverse AGCATCAGCAGCTGTTTC). The bidirectional pBI-CMV4-RFP vector was used as it allowed the co-expression of AP2σ and red fluorescent protein (RFP) to facilitate an estimation of transfection efficiency. Sanger DNA sequence analysis of plasmid DNA (pBI-CMV4-RFP-*AP2S1*-WT and the nine variants) was performed using PCR amplification with *AP2S1* gene-specific primers (Sigma-Aldrich) (Forward AGAGTTGCCCTGAAAGGTTTT, Reverse CTGATTATGATCCTCTGGAG) as previously described (20). DNA sequence analysis of the PCR products was performed using the BigDye Terminator version 3.1 cycle sequencing kit (Life Technologies) and an ABI automated capillary sequencer (Applied Biosystems), as reported (242). DNA sequences were aligned to the consensus AP2S1 genomic sequence to confirm the correct wild-type (WT) or variant *AP2S1* sequences were present.

The *AP2S1* Arg15Leu and Arg10Trp variants were generated by site-directed mutagenesis (Q5 Site-Directed Mutagenesis kit, New England Biolabs) using a human *AP2S1* cDNA construct (Clontech Laboratories Ltd) previously subcloned into pcDNA5/TO construct (Thermo Fisher Scientific) using *AP2S1* specific primers (Thermo Fisher Scientific) (Arg15Leu Forward ACCA CTTGGCCAGTCGCGTCTTGCCTG, Reverse CAGGCAAGACGCGACTGGCCAAGTGGT; Arg10Trp Forward CATCCAGAACTGGGCAGGCAA, Reverse AGGATAAAGCGGATCATTCACTC) (243). A hemagglutinin (HA) tag (YPYDVPDYA), was cloned in frame at the C-terminal end of the protein to facilitate analysis of expression. These plasmids, pcDNA5/TO-*AP2S1*-WT, pcDNA5/TO-*AP2S1*-Arg15Leu and pcDNA5/TO-*AP2S1*-Arg10Trp, were Sanger sequenced as above.

XL 10-Gold ultracompetent cells (Agilent) were transformed with either 50ng of the pBI-CMV4-RFP-*AP2S1*-WT or nine variants, or pcDNA5/TO-*AP2S1*-WT or variant constructs for 30

min on ice, followed by heat-shock at 42°C. Transformed cells were plated on lysogeny broth (LB) agar plates with 50 µg/ml ampicillin and incubated at 37°C, overnight. Individual colonies were then harvested and cultured overnight in 3-7ml culture media containing 50 µg/ml ampicillin at 37°C. The culture media was then centrifuged to pellet bacterial cells and plasmid DNA recovered using the Wizard Plus SV Miniprep Purification System (Promega, USA) on spin columns according to the manufacturer's instructions. DNA was resuspended in water and the plasmid concentration determined using a NanoDrop ND-100 Spectrophotometer (Thermo Fisher Scientific).

5.3 Cells

Human embryonic kidney 293 (HEK293) cells were used because they have previously been established as models for studies involving CASR signalling and internalisation (20, 155). HEK293 cell lines stably expressing CaSR (termed HEK293-CASR) or FLAG-tagged CASR (termed Flac2, in which the FLAG tag is on the N-terminal of the CASR) were maintained in DMEM-Glutamax media (Thermo Fisher Scientific) supplemented with 10% Fetal Bovine Serum (Gibco) and 400µg/ml geneticin (Thermo Fisher Scientific)) (155). HEK293 cell lines stably expressing a FLAG tagged-CASR and a HA-tagged WT or mutant AP2σ (termed Flac2-Ap2σ-WT, Flac2-Ap2σ-Arg15Leu or Flac2-Ap2σ-Arg10Trp) were maintained in DMEM-Glutamax supplemented with 10% Fetal Bovine Serum, 100µg/ml hygromycin B and 400µg/ml geneticin (Thermo Fisher Scientific)) (243). All cells were maintained at 37°C, 5% CO_2 in a humidified incubator.

5.3.1 Transient transfection of cells

Transient transfections were performed using the pBI-CMV4-RFP-*AP2S1*-WT or mutant plasmids into HEK293-CASR cells using Lipofectamine 2000 (Life Technologies), as previously described (20, 190). Expression of RFP, which is expressed at equivalent levels to AP2σ from the pBI-CMV4-RFP-*AP2S1* bidirectional vector, was used to assess the efficiency of transfection. RFP fluorescence was detected using an Eclipse E400 fluorescence microscope with a Y-FL Epifluorescence filter, and images captured using a DXM1200C digital camera and NIS Elements software (Nikon) (20, 155).

5.3.2 Western blotting

In HEK293-CaSR cells transiently transfected with pBI-CMV4-RFP-*AP2S1*-WT or pBI-CMV4-RFP-*AP2S1*-variants, Ap2σ expression was analysed by Western blot analysis of whole-cell protein extract. Briefly cells were lysed using ice-cold lysis buffer (1% NP-40, 150mM sodium chloride, 50mM Tris pH 7.4, 1mM EDTA, 1× protease inhibitor (Sigma-Aldrich) and 2 mM sodium orthovanadate) for 15 minutes at 4^{o}C, and centrifugated at 12000xg at 4^{o}C. Protein concentration in the supernatant was determined by Bradford assay using a set of albumin standards and Coomassie blue. Each of the standards and samples were read on the Pherastar spectrophotometer (BMG Labtech) at a wavelength of 595nm. Cell lysates were prepared in 4× Laemmli loading dye (BioRad) containing mercaptoethanol then resolved using 10% SDS-PAGE gel electrophoresis at 100V. The proteins were then transferred to polyvinylidene difluoride membrane, blocked with 5% dry non-fat milk/TBS-t and probed for AP2σ (ab92380, Abcam) and calnexin (AB2301, Merck), which was used as a loading control. An HRP-conjugated secondary antibody (715-035-152, Jackson ImmunoResearch) was used for both AP2σ and calnexin prior to visualization using Pierce ECL Western blotting substrate. The

Western blots were visualized using an Immuno-Star WesternC kit (BioRad) on a BioRad Chemidoc XRS+ system.

In Flac2 cells CASR expression was analysed by Western blot analysis of whole-cell protein extract. Again, cells were lysed using ice-cold lysis buffer (0.5% NP-40, 135 mM sodium chloride, 20 mM Tris pH 7.5, 1 mM EDTA, 1× protease inhibitor (Sigma-Aldrich) 2 mM sodium orthovanadate and 10 mM sodium fluoride) for 15 minutes at 4°C, and centrifugated at 12000xg at 4°C. Protein concentration in the supernatant was determined by Bradford assay as described above. Cell lysates were prepared in 4× Laemmli loading dye (BioRad) containing mercaptoethanol then resolved using 10% SDS-PAGE gel electrophoresis at 100V. The proteins were then transferred to polyvinylidene difluoride membrane, blocked with 5% dry non-fat milk/TBS-t and probed using anti-FLAG antibodies (ab49763, Abcam), with tubulin (ab15246), protein expression used as a loading control. The HRP-conjugated secondary antibodies, 715-035-150 and 715-035-152, (Jackson ImmunoResearch) were used for FLAG and tubulin, respectively, prior to visualization using Pierce ECL Western blotting substrate. The western blots were visualized using an Immuno-Star WesternC kit (BioRad) on a BioRad Chemidoc XRS+ system. Densitometry analysis was performed using ImageJ software to calculate the number of pixels per band.

In Flac2-Ap2σ-WT and variant cells, AP2σ expression was analysed by Western blot analysis as described for CASR expression in Flac2 cells, but using anti-HA antibodies (CST3724, Cell Signaling Technologies) and the HRP-conjugated secondary antibody 715-035-152 (Jackson ImmunoResearch).

5.3.3 CASR signalling response assays

Flow cytometry was used to detect transient changes in Ca^{2+}_i in response to varying concentrations of $[Ca^{2+}]_e$ as described (20). In brief, cells were harvested 48 hours post-transfection and washed in calcium- and magnesium-free Hank's balanced salt solution (HBSS) (Invitrogen). They were then loaded with 1 μg/ml indo-1-acetoxymethylester (Indo-1-am) (Molecular Probes) and incubated for 1 hour at 37 °C. Free dye was removed by washing the cells in a buffered solution and the cells were resuspended in the calcium- and magnesium-free HBSS and maintained at 37°C. They were then stimulated by sequentially adding calcium to the solution to incrementally raise the $[Ca^{2+}]_o$ from 0 to 15 mM. Flow cytometry was performed with a Beckman Coulter MoFlo XDP equipped with JDSUY Xcyte UV Laser and a Coherent Sapphire 488 Laser using a 550LP dichroic mirror and 580/30 bandpass filter and peak mean fluorescence ratios were measured using Cytomation Summit software and expressed as a normalised response as described (20).

5.3.4 Drug compound studies

Cinacalcet (AMG-073 HCL; Cambridge Bioscience) was resuspended at 20 mg/ml in dimethyl sulfoxide (DMSO). Flac2+AP2σ-WT and Flac2+AP2σ-Arg15Leu cells were incubated with 10 nM cinacalcet, or DMSO for 15 min before being washed with phosphate buffered saline (PBS) and lysed with ice-cold lysis buffer (0.5% NP-40, 135 mM sodium chloride, 20 mM Tris pH 7.5, 1 mM ethylenediaminetetraacetic acid (EDTA), 1× protease inhibitor (Sigma-Aldrich) 2 mM sodium orthovanadate and 10 mM sodium fluoride) for 15 minutes at 4°C, and centrifugated at 12000xg at 4°C. The supernatant was then used in co-immunoprecipitation studies as described below.

5.3.5 Co-immunoprecipitation of FLAC2 cells

Cell lysates were mixed with 5µg anti-CASR antibody for 30 minutes at 4°C on a rotator before being added to 20µl protein G agarose beads (Cell Signalling Technology) and mixed for a further 2 hours. The beads were then washed 5× with lysis buffer and the protein prepared in 4x Laemmli loading dye. Immunoprecipitated proteins as well as total input proteins were analysed by Western blot as described above using the primary antibodies to FLAG (ab49763, Abcam) and HA (CST3724, Cell Signalling Technologies).

5.4 Mouse studies

5.4.1 Ethical approval

Animal studies were licensed under the Animal (Scientific Procedures) Act 1986, issued by the UK Government Home Office Department (PPL30/3271), and approved by the MRC Harwell Institute Ethical Review Committee.

5.4.2 Maintenance of mouse colonies

All mice were kept in accordance with Home Office welfare guidance at the Medical Research Council (MRC) Harwell Centre. Mice had free access to water and were fed *ad libitum* on a commercial diet (RM3, Special Diet Services) containing 1.24% calcium, 0.83% phosphorus and 2948 IU/kg of vitamin D. The environment had a 12 hour light and dark cycle, temperature was maintained at 21 ± 2°C and humidity maintained at 55 ± 10%.

5.4.3 CRISPR-Cas induced mutations in mice

The *knock-in* mouse models, *Ap2s1-Arg15Leu, Ap2s1-Arg15Cys* and *Ap2s1-Met117Ile* mouse were generated by introducing a precise single nucleotide change in the *AP2S1* gene using a Class 2 Clustered Regularly Interspaced Short Palindromic Repeat (CRISPR) –Cas9 system as described (243). The engineered CRISPR systems require a guide RNA (gRNA), a suitable

endonuclease and, in this case, a donor oligonucleotide repair template containing the desired single point mutation to introduce the mutation via homology directed repair (HDR). The gRNA was composed of a Protospacer Adjacent Motif (PAM), which serves as a binding sequence for SpCas9, and a nucleotide spacer that targeted the sequence proximal to the codon to be mutated and was designed at http://crispr.mit.edu/. The endonuclease used was *S. Pyogenes* Cas9 (SpCas9). This undergoes a conformational change upon gRNA binding from an inactive, non-DNA binding conformation into an active DNA-binding conformation. As the SpCas9-gRNA complex binds the target DNA, SpCas9 undergoes a second conformational change that allows the nuclease domains (RuvC and HNH) to cleave opposite strands of the target DNA and induce a double stranded break (DSB) ~3-4 nucleotides upstream of the PAM sequence in the target DNA. The donor oligonucleotide repair template was purchased as an Ultramer™ DNA oligonucleotide (IDT). It carried the target nucleotide change, had additional homologous sequence upstream and downstream of the target, and additional silent mutations to prevent the gRNA binding to the "repaired" mutant allele and cutting the engineered allele.

The Cas9 mRNA (Tebu-Bio), gRNA and donor oligonucleotide repair template were diluted and mixed in microinjection buffer (MIB; 10 mM Tris-HCl, 0.1 mM EDTA, 100 mM sodium chloride, pH 7.5) and micro-injected into the pronucleus of C57BL/6J zygotes. The single cell embryo containing the CRISPR-Cas9 system was then transferred into a pseudo-pregnant mouse. Founder mice harbouring the targeted allele were identified by analysing ear biopsy DNA. One mosaic founder mouse harbouring the desired mutation, either Arg15Leu, Arge15Cys or Met117Ile, was mated with WT C57BL/6J mice to produce the F1 generation of *Ap2s1*$^{+/mutant}$ heterozygous mice. The F1 *Ap2s1*$^{+/mutant}$ mice were then inter-crossed to generate the initial litters of WT, *Ap2s1*$^{+/mutant}$ and *Ap2s1*$^{mutant/mutant}$ mice for assessment of

viability. The F1 generation was genotyped using PCR, Sanger DNA sequencing and ddPCR copy counting using both a universal and mutant-specific assay to confirm that random donor integrations had not occurred, as described (243) (Figure 18).

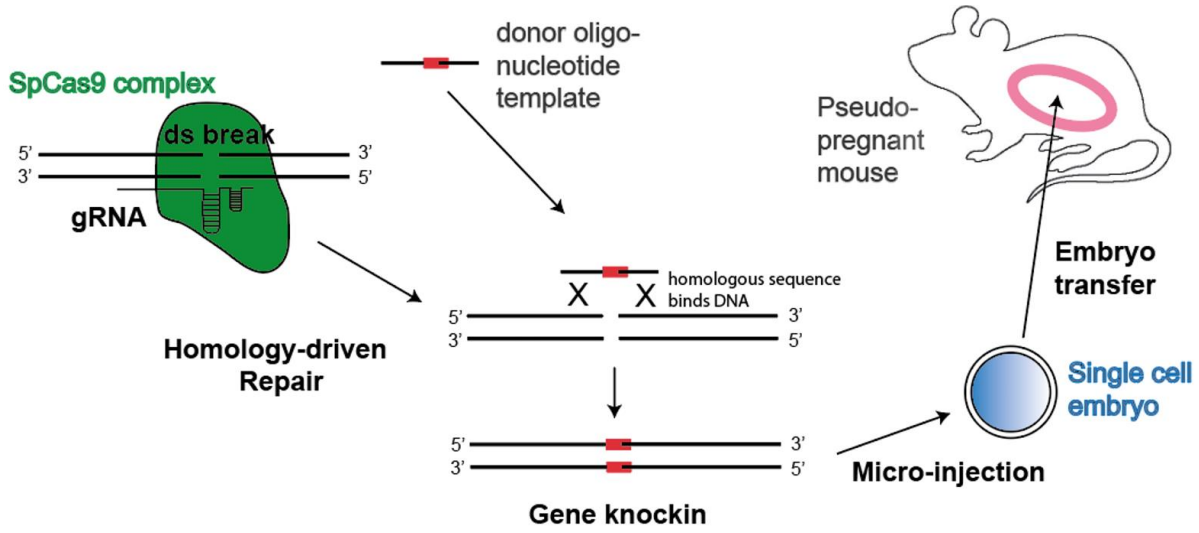


Figure 18. Generation of mutant *Ap2s1 knock-in* mouse models using a CRISPR–Cas9 system. The engineered CRISPR systems require a guide RNA (gRNA), a suitable endonuclease and, in this case, a donor oligonucleotide repair template containing the desired single point mutation (shown as a red dash on the donor oligo-nucleotide template) to introduce the mutation via homology directed repair (HDR). gRNA composed of a Protospacer Adjacent Motif (PAM) serves as a binding sequence for SpCas9, and a nucleotide spacer targets the sequence proximal to the desired codon. The endonuclease used was *S. Pyogenes* Cas9 (SpCas9). This undergoes a conformational change upon gRNA binding from an inactive, non-DNA binding conformation into an active DNA-binding conformation. As the SpCas9-gRNA complex binds the target DNA, SpCas9 undergoes a second conformational change that allows the nuclease domains to cleave opposite strands of the target DNA and induce a double stranded break (DSB) ~3-4 nucleotides upstream of the PAM sequence in the target DNA. The donor oligonucleotide repair template carries the target nucleotide change and has additional homologous sequence upstream and downstream of the target, and additional silent mutations to prevent the gRNA binding to the "repaired" mutant allele and cutting the engineered allele. It is incorporated into the cleaved DNA using Homology Directed Repair (HDR) resulting in a population of cells expressing the desired *Ap2s1* mutation. The single cell embryo containing the CRISPR-Cas9 system is transferred into a pseudo-pregnant mouse. Successful gene *knock-in* results in mice born harboring the desired *Ap2s1* mutation.

One mosaic founder mouse was then mated with a wild type (WT) mouse to produce the F1 generation of mice heterozygous for the desired mutation, i.e. Arg15Cys, Arg15Leu or Met117Ile. The F1 *Ap2s1*$^{+/mutant5}$ mice were then inter-crossed to generate the initial litters of WT, *Ap2s1*$^{+/mutant}$ and *Ap2s1*$^{mutant/mutant}$ mice and genotypes confirmed by DNA sequence analysis. The numbers of WT, *Ap2s1*$^{+/mutant}$ and *Ap2s1*$^{mutant/mutant}$ mice in the F2 generation were counted to assess the viability of the genotypes (Figure 19).

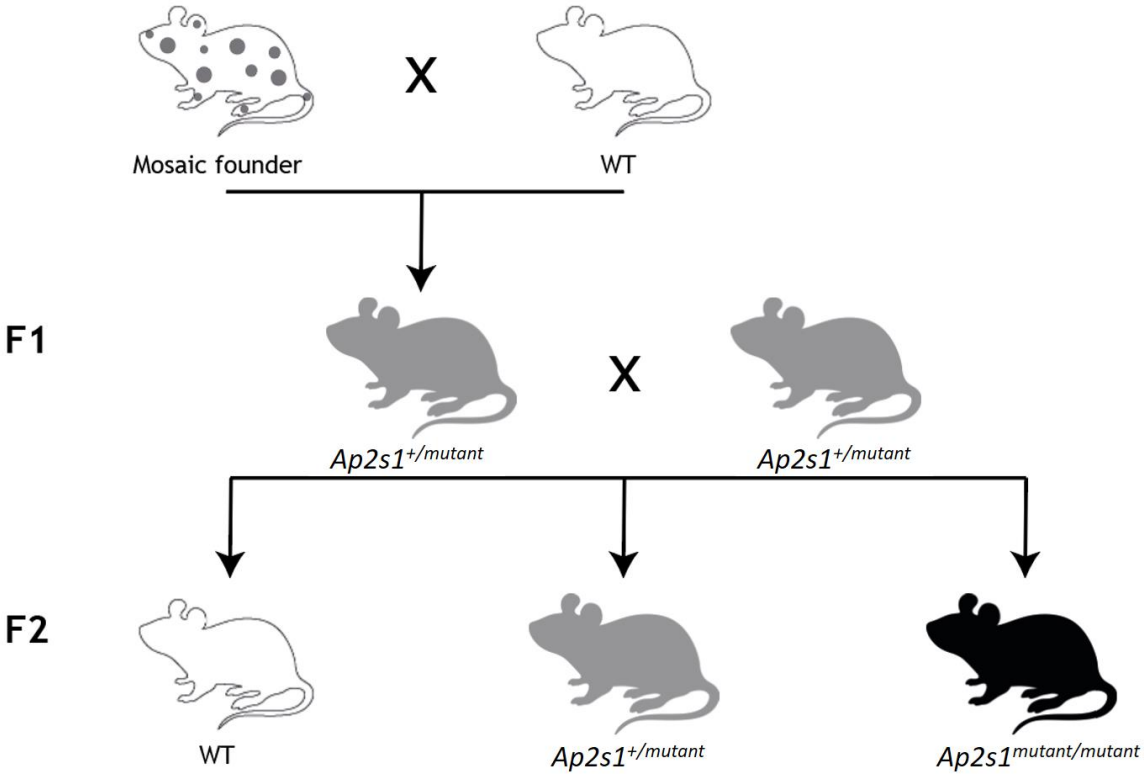


Figure 19. Generation of WT mice, and mice heterozygous (*Ap2s1*$^{+/mutant}$) and homozygous (*Ap2s1*$^{mutant/mutant}$) for the desired mutation, i.e. Arh15Cys, Arg15Leu and Met117Ile. A mosaic founder mouse was mated with a WT C57BL/BJ mouse to produce the F1 generation of mice heterozygous for the desired mutation. These F1 heterozygous mice were then inter-crossed to generate the WT, *Ap2s1*$^{+/mutant}$ and *Ap2s1*$^{mutant/mutant}$ mice (F2).

5.4.4 Methods of genotyping mice

Genotyping was performed by MRC Harwell Centre. Real time quantitative PCR was used to genotype the *Ap2s1-Met117Ile* mouse. This is the preferred method wherever possible as it is quantitative, and semi-automated so can be high throughput (244).

However, real time quantitative PCR could not accurately distinguish between WT and mutants in the *Ap2s1-Arg15Cys* and *Ap2s1-Arg15Leu* mouse models, as one of its limitations is that it can give false positive results with point mutations. For this reason allelic discrimination assays were used in these mouse models, as described (245).

5.4.5 Characterisation of Arg15Leu, Arg15Cys and Met117Ile mice

All blood samples were collected under isoflurane terminal anaesthesia from the retro-orbital vein, except for PTH which was collected from the lateral tail vein following application of topical local anaesthesia (118). PTH was collected using this protocol as some anaesthetic agents have been shown to significantly increase serum PTH (246, 247).

For sodium, potassium, calcium, albumin, phosphate, magnesium, ALP activity, glucose, lipids, liver function tests, urea and creatinine tests, plasma was separated by centrifugation at 5000*g* for 10 min at 8°C, and samples were analysed on a Beckman Coulter AU680 analyser. The formula: plasma calcium (mmol/l) − [(plasma albumin (g/l) − 30) × 0.02] was used to adjust plasma calcium for albumin concentrations (118).

1,25-dihydroxyvitamin D was quantified using a two-step process involving purification by immune-extraction and quantification by enzyme immunoassay (Immunodiagnostic Systems). PTH was measured using a two-site ELISA specific for mouse intact PTH (Immutopics, San Clemente, USA). FGF23 was measured using a two-site ELISA kit (Kainos Laboratories) (19). A mouse-specific ELISA (Biorbyt Ltd) was used to measure C-terminal

cross-linking telopeptide of type 1 collagen (CTX-1). An enzyme immunoassay (EIA) (Immunodiagnostic Systems) was used to measure procollagen type 1 N-terminal propeptide (P1NP).

Metabolic cages (Techniplast) were used to allow collection of urine. Mice aged 15–17 weeks were individually housed and fed *ad libitum* on water and powdered chow. They were allowed to acclimatize to their environment over a 72 h period prior to sample collection (232). A Beckman Coulter AU680 analyser was used to analyse urine for calcium, phosphate and creatinine (118, 232). The formula $U_x/P_x{}^*P_{Cr}/U_{Cr}$, (where U_x is the urinary concentration of the filtered substance in mmol/l, P_x is the plasma concentration of a substance in mmol/l, U_{Cr} is the urinary concentration of creatinine in mmol/l and P_{Cr} is the plasma concentration of creatinine in mmol/l) was used to calculate the fractional excretion of calcium and phosphate (232).

Whole body DXA scanning was performed on anesthetized Arg15Leu and Arg15Cys mice using a Lunar Piximus densitometer (GE Medical Systems) (232). DXA images were analysed using Piximus software (232).

5.4.6 Administration of cinacalcet to Arg15Leu mice

Cinacalcet (AMG-073 HCL) from Cambridge Bioscience (catalog no. CAY16042) was dissolved in a 20% aqueous solution of 2-hydroxypropyl-β-cyclodextrin (Sigma-Aldrich, catalog no. H107) (232). It was administered to mice randomly allocated to receive either 60 mg/kg cinacalcet or vehicle as a single oral gavage bolus (232). None of the mice had undergone any experimental procedures prior to dosing. Study investigators were blinded during animal handling and when measuring the biochemical endpoints derived from plasma and urine analysis.

5.4.7 Three-dimensional micro-computerised tomography (micro-CT) imaging of *Ap2s1-Arg15Leu* mouse embryos

Iodine-contrast three-dimensional micro-CT imaging was performed and analysed at MRC Harwell according to their standard protocol of morphological analysis for mutant mouse line embryos. 39 mouse embryos from 5 different *Ap2s1-Arg15Leu* litters, comprising WT, heterozygous and homozygous mouse embryos, were assessed for analysis at developmental stage E18.5, i.e. 18.5 days post-coitum with full term being approximately 21 days post-coitum.

5.5 Bioinformatic analysis

The large-scale sequencing datasets, Regeneron DiscovEHR dataset, dbSNP (248), the Exome Aggregation Consortium (ExAC) (249), (240), Genome Aggregation Database (GnomAD v2.1.1)(250) and ClinVar, (251) were used in these studies.

The DiscovEHR exome sequencing dataset has arisen from a collaboration between the Regeneron Genetics Center and Geisinger Health System and contains matched genotype and phenotype information from 51289 patient-participants (240). dbSNP is comprised of a large cluster of species-specific databases and contains over 12 million non-redundant sequence variations and over 1 billion individual genotypes from large-scale genotyping activities (248). The ExAc dataset is comprised of pooled exome sequencing data from 60,706 volunteers made available by international investigators (249) and was the predecessor of Genome Aggregation Database (250), used in my later studies, which encompasses data from 15,708 whole genomes and 125,748 exomes. ClinVar is a public archive of human genetic variants and interpretations of their relationships to diseases and other conditions (251).

The pathogenicity of variants was inferred from several criteria: allele frequency within the large sequencing datasets described, Exome Aggregation Consortium (ExAC) (249), Regeneron DiscovEHR dataset (240), Genome Aggregation Database (GnomAD v2.1.1)(250) and ClinVar, (251), amino acid conservation, predicted effect on protein function using the programs MutationTaster (www.mutationtaster.org/) (252), SIFT (sift.jcvi.org/)(253) and Polyphen-2 (genetics.bwh.harvard.edu/pph2/) (254), and literature review. SIFT predicts the effect of amino acid substitutions based on sequence homology and physicochemical properties. It gives a qualitative (tolerated or deleterious) and quantitative (the nearer to 0 the more likely deleterious) score (32). Polyphen-2 predicts effects based on sequence homology, protein databank structures, and pfam annotations (255). It gives a qualitative (probably damaging, possibly damaging, benign, or unknown) and quantitative score (the nearer to 0 the more benign, with a score >0.85 classified as probably damaging, and >0.15 classified as possibly damaging. Protein sequences of AP2σ orthologs were aligned using ClustalOmega (http://www.ebi.ac.uk/Tools/msa/clustalo/) (35).

5.6 Crystal structure modelling of variants and mutations

The crystal structure of AP2σ was modelled using reported AP2 structures (Protein Data Bank accession numbers 2XA7 and 2JKR) (32, 219) and the PyMOL Molecular Graphics System (Version1.2r3pre, Schrödinger, LL Pymol) (256).

5.7 Statistical analysis

A value of $P < 0.05$ was considered significant for all analyses and all calculations were performed using GraphPad Prism (GraphPad).

For *in vitro* functional expression studies, nonlinear regression was performed. The mean EC_{50} was used for statistical comparison by using the *F*-test. Sample sizes were determined by binomial probability analysis (Microsoft Excel) as previously reported (195). The mean EC_{50} and Hill coefficients were used for statistical comparison by using the *F*-test, and alterations in maximal signalling responses assessed using the Mann-Whitney *U* test.

One-way ANOVA followed by Sidak's test for pairwise multiple comparisons were used for all *in vivo* analyses. To ensure that ANOVA was the appropriate test for the data, the Brown-Forsythe test and, for groups of 5 or more variables, a corrected Bartlett's test were used to test the assumption that the data were from populations with the same standard deviations (257). Sidak's test was used to counteract the problem of multiple comparisons. It was used in preference to the more commonly used Bonferroni test as it assumes that each comparison made is independent of the others and is therefore more appropriate in this situation (258, 259). Chi-squared analysis was used to assess mouse viability.

6 RESULTS - INVESTIGATION OF AP2σ VARIANTS IN LARGE POPULATION DATASETS

6.1 Identification of AP2σ variants in the Regeneron DiscovEHR, ExAC and dbSNP Datasets

Reported variants in *AP2S1* in the literature have so far been restricted to codon 15. In order to determine whether additional variants could be identified, I examined three large population datasets including the Exome Aggregation Consortium (ExAC) (249), dbSNP (248), and the DiscovEHR dataset, with the latter having the advantage of detailed matched genotype and phenotype information. This analysis identified a number of *AP2S1* variants that were subsequently examined using bioinformatic tools to predict effects on protein function. To functionally characterise these variants, *AP2S1* expression constructs were generated and used to transfect HEK293 cell models expressing the CaSR in order to assess relative AP2σ expression levels and effects on CaSR signalling. This work has been included in the publication Gorvin et al (2018)(260) and is referenced throughout.

An analysis of the DiscovEHR dataset (last accessed November 2017) revealed five individuals with heterozygous coding *AP2S1* variants, which were all female, ranging in age from 34 to 73, with various co-existing medical conditions (Table 7). This group included three patients with the previously reported Arg15His mutations (patients 1-3) (20) and two patients with novel *AP2S1* variants (patients 4 and 5). The first novel variant (patient 4) was a G-to-A transition at nucleotide c.155 resulting in a missense substitution of the wild-type phenylalanine (Phe) to a mutant tyrosine (Tyr) at codon 52, and the second (patient 5) was a heterozygous G-to-T transversion at nucleotide c.350, resulting in a missense mutation of methionine (Met) to isoleucine (Ile) at codon 117 (Table 7)(261). Examination of the serum

calcium concentrations revealed that patients 1 and 2, both with the Arg15His mutation, together with patient 5, with the novel Met117Ile variant, were mildly hypercalcaemic (the normal range for albumin-adjusted calcium is 8.30-10.00mg/dl) (Table 7).

Table 7. Details of patients with AP2σ variants located on the DiscovEHR exome sequencing dataset. P=patient; Nt=nucleotide; Fr=frequency; F= female. Adj-calcium=albumin-adjusted calcium; PCKD=polycystic kidney disease; T2DM=type 2 diabetes; vit D def=vitamin D deficiency; OP=osteoporosis; MS=Multiple Sclerosis; NA=information not available. Mutations associated with hypercalcaemia are shown in red. [a]Normal range 8.30-10.00mg/dl, [b]albumin not available on this patient therefore uncorrected serum calcium concentration shown, normal range 8.8-10.3 mg/dl. Data published in Gorvin et al (2018) (262)

P	Nt change	Amino acid change	Type of variant	Allele Fr ($x10^{-6}$)	Sex	Age (years)	Adj-calcium (mg/dl)[a]	Co-existing medical conditions
1	c.44G>A	Arg15His	Missense	9.78	F	72	10.92	PCKD, hypothyroidism, hypertension, T2DM, vit D def, OP
2	c.44G>A	Arg15His	Missense	9.78	F	68	10.88	MS, vit D def, OP, obesity
3	c.44G>A	Arg15His	Missense	9.78	F	73	9.80	Pituitary tumour, asthma
4	c.155G>A	Phe52Tyr	Missense	9.78	F	53	9.62	Obesity, vit D def, hypothyroidism
5	c.350G>T	Met117Ile	Missense	9.78	F	34	10.10[b]	NA

The identification of a novel *AP2S1* Met117Ile variant associated with hypercalcaemia in the DiscovEHR dataset prompted us to search for additional *AP2S1* variants in other datasets, namely the ExAc (249) and dbSNP (248) datasets (databases last accessed November 2017). From the analysis of these datasets, 27 *AP2S1* variants comprising 6 non-synonymous variants (Table 8) and 21 synonymous variants (Table 9) were identified, all of which were heterozygous. Only one of these variants, the missense variant Ala44Thr, was identified from dbSNP, with the remainder all being found in ExAC. We then performed an additional analysis to determine whether the number of observed variants was below the expected number of

variants for a protein of 142 amino acids. This showed a significantly lower number of missense and nonsense variants than the frequency expected for a protein of this size (observed *Ap2s1* variants vs ExAc gene variants: missense = 0.008% vs 0.1%; nonsense = 0% vs 0.01%, χ^2=p<0.0001)(261) suggesting that *AP2S1* is intolerant to variation with residue changes likely to detrimentally affect function and fitness.

Table 8. Details of the non-synonymous *AP2S1* variants reported in the ExAc and dbSNP datasets. [a]allele count rather than frequency. Data published in Gorvin et al (2018) (260).

Nucleotide change	Amino acid change	Database	Type of variant	Allele frequency (x10^{-6})
c.8G>A	p.Arg3His	ExAC	missense	8.24
c.130C>T	p.Ala44Thr	dbSNP	missense	[a]1
c.182T>C	p.Arg61His	ExAC	missense	8.24
c.335C>T	p.Thr112Met	ExAC	missense	8.24
c.365A>G	p.Glu122Gly	ExAC	missense	8.24
c.424G>A	p.Glu142Lys	ExAC	missense	8.24

Table 9. Details of the synonymous *AP2S1* variants reported in the ExAc dataset. Data published in Gorvin et al (2018) (260)

Nucleotide change	Amino acid change	Allele frequency (x10^{-6})
c.15C>T	p.Ile5Ile	8.24
c.18C>T	p.Leu6Leu	16.5
c.30G>A	p.Arg10Arg	8.24
c.39G>A	p.Lys13Lys	8.24
c.42G>T	p.Thr14Thr	24.7
c.42G>A	p.Thr14Thr	98.9
c.75T>C	p.Asp25Asp	692.2
c.90G>A	p.Lys30Lys	8.24
c.96C>T	p.Ile32Ile	16.5
c.111C>T	p.Ala37Ala	189.5
c.129C>T	p.Asp43Asp	32.9
c.201C>T	p.Phe67Phe	8.24
c.241C>T	p.Leu81Leu	24.7
C.261C>T	p.Phe87Phe	148.3
c.276C>T	p.Asn92Asn	16.5
c.294C>T	p.Val98Val	16.5
c.345C>T	p.Asp115Asp	8.24
c.357G>A	p.Leu119Leu	8.24
c.378C>T	p.Thr126Thr	8.24
c.387G>A	pThr129Thr	32.9
c.396G>T	p.Leu132Leu	8.24

6.2 Bioinformatic and experimental assessment of AP2σ variants identified in the DiscovEHR, ExAC and dbSNP datasets

6.2.1 Examination of residue conservation and secondary structure of AP2σ variants

To date all the reported FHH3-causing AP2σ mutations have been restricted to a single codon, namely codon15, located in exon 2 of the *AP2S1* gene. The novel *AP2S1* variants found in the DiscovEHR (p.Phe52Tyr and p.Met117Ile), ExAc (p.Arg3His, pArg61His, p.Thr112Met, p.Glu122Gly and p.Glu142Lys) and dbSNP (p.Ala44Thr) datasets were distributed throughout exons 2, 3 and 5 of the *AP2S1* gene (Figure 20). The residues in which the variants occur are all highly evolutionarily conserved (Figure 21). Thr112Met and Met117Ile are located in α-helices; Arg3His, Arg15His, Phe52Tyr, Arg61His and Glu122Gly are located in β -sheets; Ala44Thr is located in a non-repetitive loop; and Glu142Lys is the last codon of AP2σ. This would suggest all residues affected are likely to have important structure-function roles in the AP2σ protein.

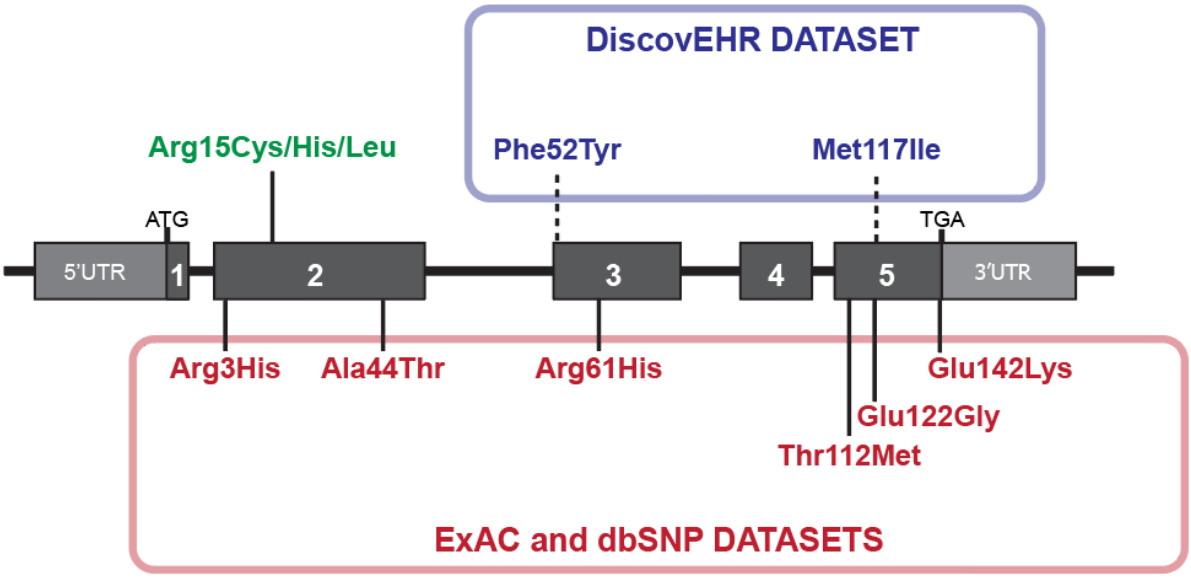


Figure 20. Schematic representation of the genomic organisation of the AP2S1 gene. The gene consists of 5 exons (dark grey boxes), with a 5' untranslated region (UTR) and 3'UTR (light grey

boxes). The start codon (ATG) is located in exon 1, and the stop codon (TGA) is located in exon 5. The distribution of the known FHH3-causing Arg15 mutations, Arg15Cys, Arg15His and Arg15Leu, are shown in green. The novel variants found in the DiscovEHR dataset, Phe52Tyr and Met117Ile, are shown above the gene in blue. The novel variants found in the ExAc and dbSNP datasets, Arg3His, Ala44Thr, Arg61His, Thr112Met, Glu122Gly and Glu142Lys, are shown below the gene in red. Data published in Gorvin et al (2018) (260).

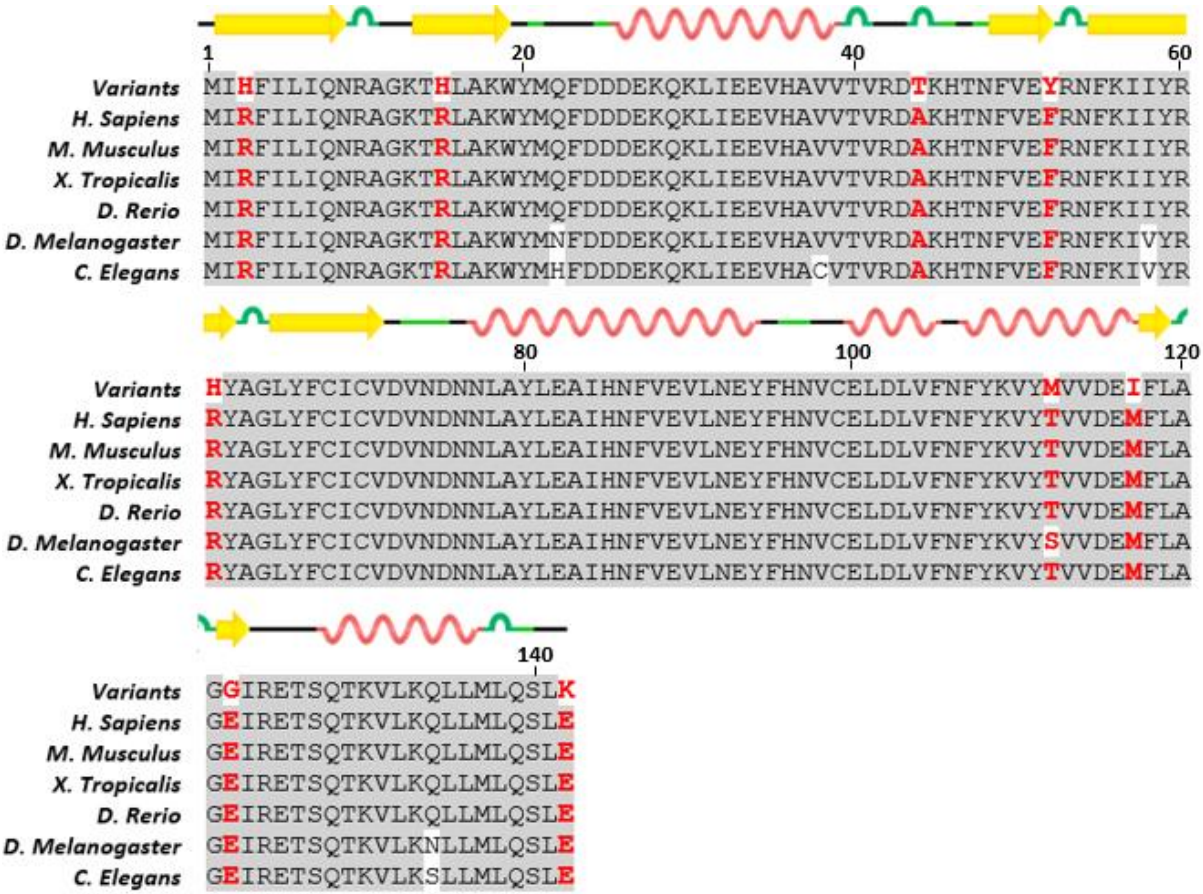


Figure 21. Multiple protein sequence alignment of AP2σ-subunit orthologs. The secondary structure of the protein is shown above (adapted from Jackson et al, Cell. 2010 (219)). Conserved residues are shaded grey, WT and variant residues are shown in red. Codon numbers are indicated every 20 residues in black. α-helices are indicated by red wavy lines; β-strands are indicated by yellow arrows; non-repetitive loops are in green. Data published in Gorvin et al (2018) (262).

6.2.2 PyMOL analysis of AP2σ variants

The effects of the FHH3-causing mutations, Arg15Cys, Arg15His (seen in our cohort) and Arg15Leu, have been predicted to result in loss or weakening of a key polar contact with Arg21 of AP2α1 with potential effects on dileucine motif binding (Figure 13) (192). The effect of the

remaining variants found in our datasets on the AP2σ structure was also assessed using the PyMOL molecular visualization system (256) and the previously published crystal structure of the AP2 heterotetramer (Protein Data Bank accession numbers 2XA7 and 2JKR) (32, 219). Neither of the novel DiscovEHR variants (Phe52Tyr and Met117Ile) were predicted to change the number of polar contacts (Figure 22A-B, Table 10). However, of the variants identified in the ExAC (Arg3His, Arg61His, Thr112Met, Glu122Gly and Glu142Lys) and dbSNP (Ala44Thr) databases, only Ala44Thr was not associated with a change in the predicted number of polar contacts (Figure 23A-B, Table 10). Thus, the variants identified in the ExAC database are all predicted to affect the protein structure.

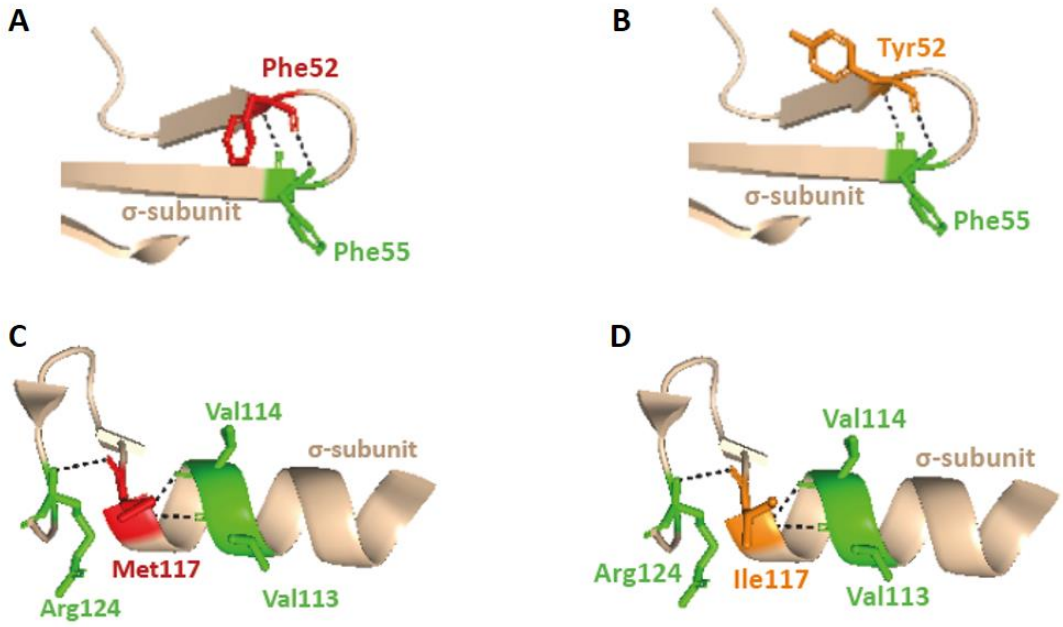


Figure 22 PyMOL analysis of the structural effects of the AP2σ variants identified in the DiscovEHR dataset. (A) Phe52 (red sticks) forms two polar contacts with Phe55 (green sticks). (B) Alteration of Phe52 to Tyr52 (orange sticks) is not predicted to disrupt these contacts. (C) Met117 (red sticks) forms polar contacts with Val113, Val114 and Arg124 (green sticks). (D) Alteration of Met117 to Ile117 (orange sticks) is not predicted to disrupt these contacts. The AP2σ subunit is shown in brown; polar contacts are denoted by a black dashed line. Data published in Gorvin et al (2018)(260).

Arg3 forms part of the β1-strand of AP2σ, and has two polar contacts with Asp72 located immediately after the β5-strand (**Error! Reference source not found.**B) and a polar contact with Cys70. The Arg3His variant is predicted to be associated with the complete loss of the polar contacts with Asp72 (**Error! Reference source not found.**C, Table 10); but not with the polar contact with Cys70. Arg61 forms part of the β4-strand of AP2σ (**Error! Reference source not found.**E), and is a basic amino acid predicted to interact with the acidic dileucine motif present on cargo proteins, including the CaSR (**Error! Reference source not found.**F). The interaction between the AP2 complex and the dileucine motif is one of the first critical steps in CME. Alteration of Arg61 to His61 (also basic) is predicted to result in the loss of 5 out of 6 possible polar contacts (Figure 23G), which could affect the interaction with the dileucine motif (**Error! Reference source not found.**H, Table 10). Arg 61 is proximal to the acidic LL moiety at position L(L0) and L(L+1) (32). The interaction of the dileucine motif with AP2σ has been shown to be affected by mutating Arg63 to Trp63, a much bulkier amino acid side chain (32). It could be that the change in space filling properties when Arg61 mutates to His61 affects the interaction with the dileucine motif in a similar way.

Thr112Met, Glu122Gly and Glu142Lys were all predicted to result in loss of polar contacts between adjacent residues on AP2σ and also with residues located within the AP2α subunit, and thus may disrupt stability between the two subunits within the AP2 complex (Figure 24 **Error! Reference source not found.**, Table 10). Thr112 on the AP2σ α4-helix forms 4 polar contacts, 3 within the α4-helix of AP2σ (with Tyr108, Lys109 and Glu116), and one with Gln92 on AP2α (Figure 5A). Alteration of AP2σ Thr112 to methionine is predicted to result in the loss of the polar contact with AP2α Gln92 (**Error! Reference source not found.**B, Table 10). Glu122 forms polar contacts with Leu119 on AP2σ, which appears to stabilize a non-repetitive loop, and Ser209 on AP2α (Figure 5C). Alteration of AP2σ Glu122 to glycine is predicted to result in

the loss of the polar contact with AP2α Ser209, (**Error! Reference source not found.**D, Table 10). Glu142 is the final coding residue of the AP2σ-subunit and forms a polar contact with both Arg87 and Thr89 on AP2α, and 2 polar contacts with Tyr88 on the AP2α-subunit (**Error! Reference source not found.**E). Alteration of AP2σ Glu142 (an acidic amino acid) to a lysine, a basic amino acid, is predicted to abolish the polar contact with Arg87 on the AP2α-subunit, and one of the contacts with Tyr88 on the AP2α subunit (Figure 24F, Table 10) (260) Mutation from an acidic amino acid to a basic amino acid is also likely to affect the protein structure and function through the change in the chemical property of this residue.

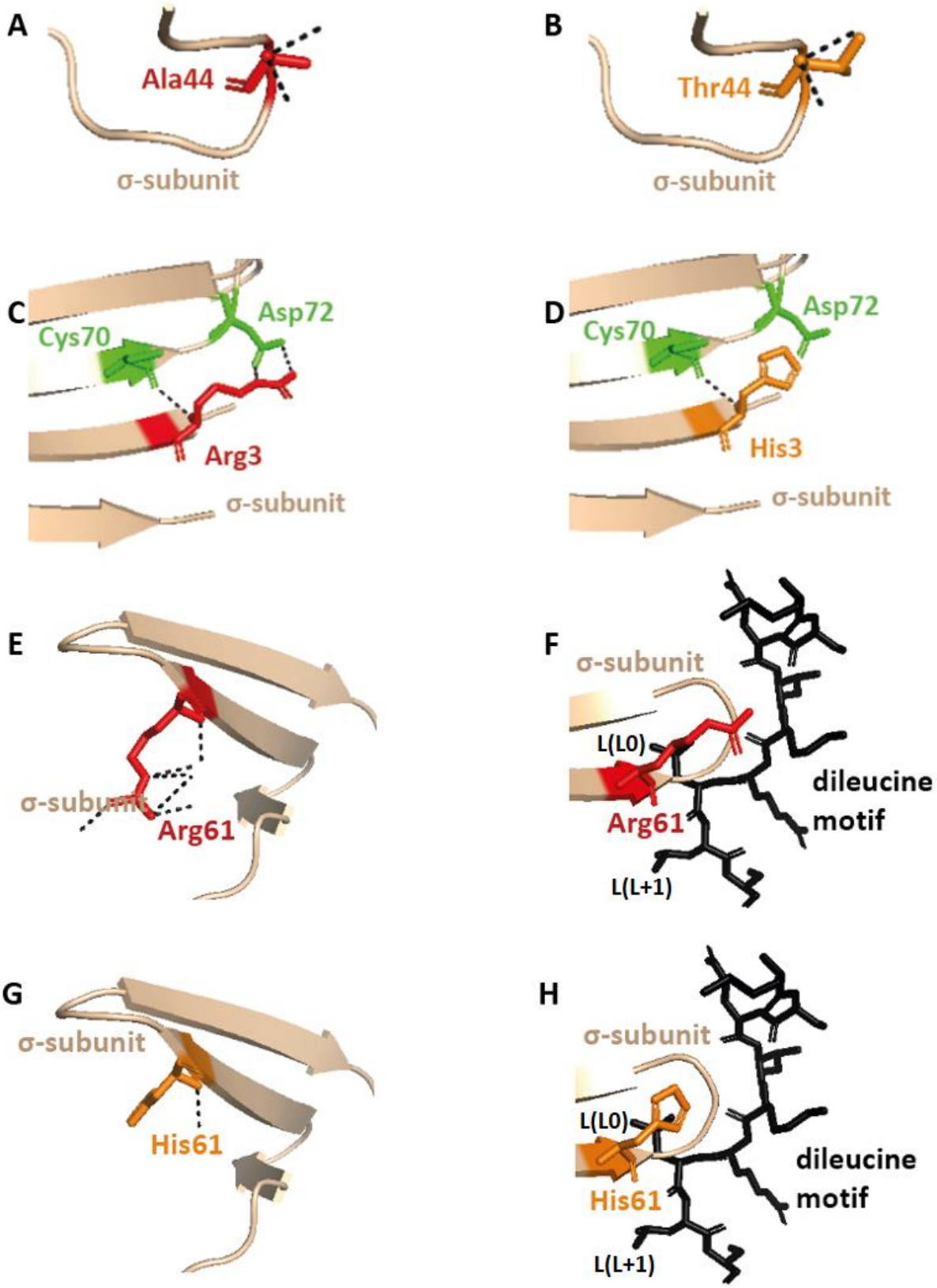


Figure 23. PyMOL analysis of the structural effects of 3 of the AP2σ variants (Arg3His, Ala44Thr and Arg61His) identified in the dbSNP and ExAc datasets. (A) Ala44 (red sticks) has the potential to form two polar contacts. (B) Alteration of Ala44 to Thr44 (orange sticks) is not predicted to disrupt these

potential contacts. (C) Arg3 (red sticks) forms one polar contact with Cys70 (green sticks) and two polar contacts with Asp72 (green sticks) on AP2σ-subunit. (D) Alteration of Arg3 to His3 (orange sticks) results in loss of both polar contacts with Asp72. (E and F) Arg61 (red sticks) forms 6 polar contacts and is a basic amino acid that is likely to interact with the acidic dileucine motif of cargo proteins, including the CaSR. It is shown to be proximal to the acidic LL moiety at position L(L0) and L(L+1) (32) (G and H) Alteration of Arg61 to His61 (orange sticks) is predicted to disrupt 5 out of 6 of these contacts. The change in space filling properties when Arg63 is substituted by His63 may also affect dileucine motif binding. The AP2σ subunit is shown in brown; polar contacts are denoted by a black dashed line; the dileucine motif of a model GPCR is shown as black sticks. Data published in Gorvin et al (2018) (260).

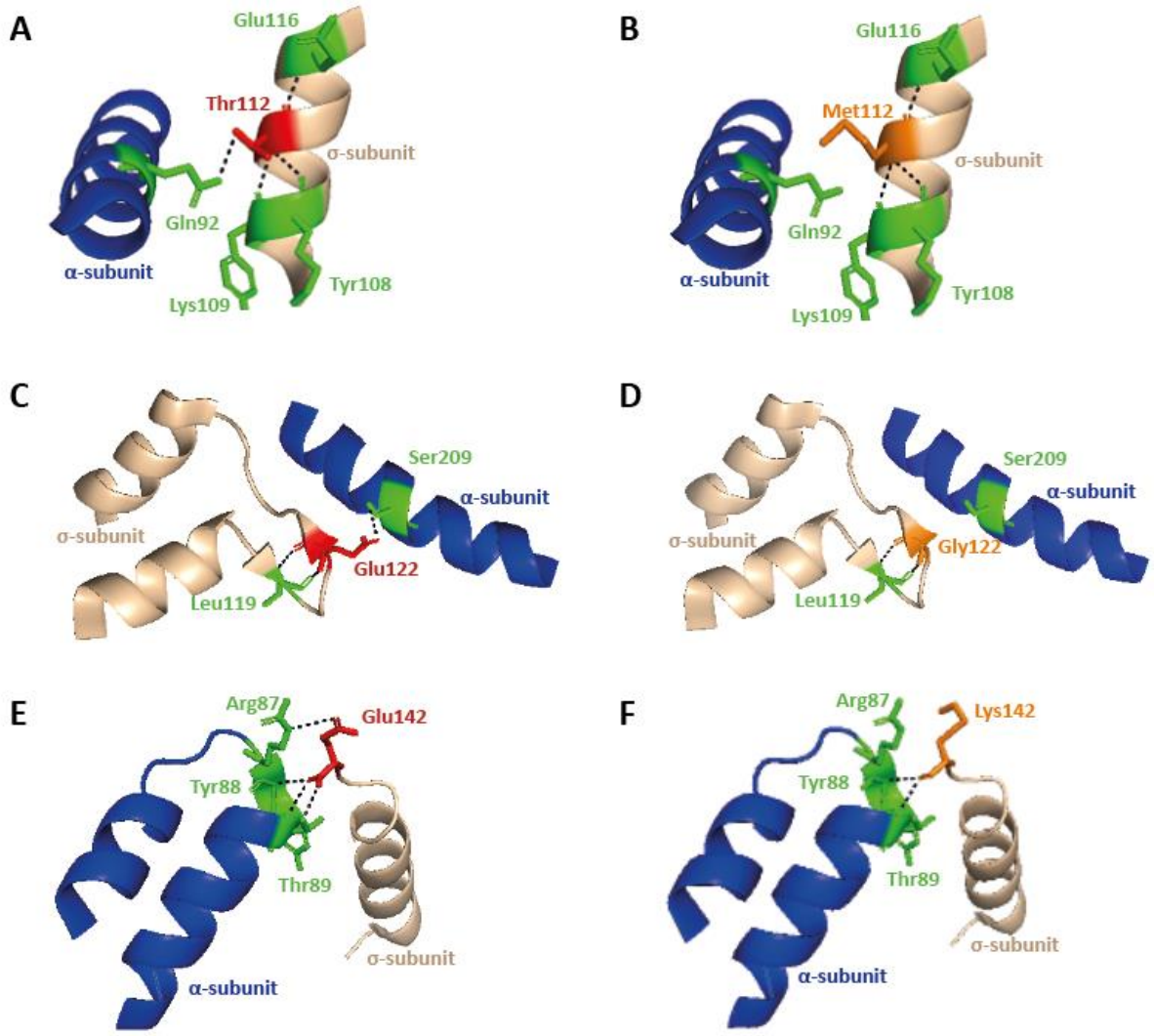


Figure 24. PyMOL analysis of the structural effects of 3 of the AP2σ variants (Thr112Met, Glu122Gly and Glu142Lys) identified in the dbSNP and ExAc datasets. (A) AP2σ Thr112 (red sticks) forms polar contacts with Tyr108, Lys109 and Glu116 (green sticks) on the AP2σ-subunit, and with Gln92 (green sticks) on the AP2α-subunit. (B) Alteration of Thr112 to Met112 (orange sticks) leads to loss of the polar contact with Gln92 on the AP2α-subunit. (C) AP2σ Glu122 (red sticks) forms one polar contact with Ser209 (green sticks) on the AP2α-subunit (blue), and two polar contacts with Leu119 (green sticks) on the AP2σ-subunit (brown). (D) Alteration of Glu122 to Gly122 (orange sticks) results in the loss of the polar contact with Ser209 on the AP2α-subunit. (E) AP2σ Glu142 (red sticks) is predicted to form one polar contact with Arg87 and Thr89, and 2 polar contacts with Tyr88 (green sticks) all on the AP2α-subunit. (F) Alteration of acidic Glu142 to basic Lys142 (orange sticks) is predicted to disrupt the polar contact with Arg87, and one of the contacts with Tyr88, both on the AP2α subunit and will also have an effect on the chemical properties of the protein. The AP2σ-subunit is shown in

brown; the AP2α-subunit is shown in blue; polar contacts are denoted by a black dashed line. Data published in Gorvin et al (2018)(260).

6.2.3 SIFT and PolyPhen-2 analysis of AP2σ variants

As discussed, Arg15His (found in the DiscovEHR dataset) and 2 other Arg15 mutations: Arg15Cys and Ar15Leu; have been reported to pathological mutations that result in FHH3, (192). Pymol analysis of these variants has demonstrated that they are all predicted to result in the loss or weakening of a polar contact with Arg21 of AP2α1 (Figure 13) (192) and they were all predicted to be deleterious and damaging/possibly damaging by SIFT and PolyPhen-2 respectively.

The predicted effect of the novel variants on protein function was also assessed using the prediction software SIFT and Polyphen-2 (253, 263). Of the remaining 8 non-synonymous variants (Ala44Thr, Phe52Tyr, Thr112Met, Met117Ile, Glu122Gly and Glu142Lys) SIFT predicted that 6 would be deleterious (Ala44Thr, Phe52Tyr, Thr112Met, Met117Ile, Glu122Gly and Glu142Lys), whilst Polyphen-2 predicted that 7 would be damaging or possibly damaging (Arg3His, Arg15His, Phe52Tyr, Arg61His, Thr112Met, Met117Ile, Glu122Gly and Glu142Lys) (Table 10). Thus, the SIFT and PolyPhen-2 prediction analyses suggested that 5 of the variants (Phe52Tyr, Thr112Met, Met117Ile, Glu122Gly and Glu142Lys) were deleterious and damaging/possibly damaging. However, SIFT predicted that Arg3His and Arg61His were likely to be tolerated, whereas PolyPhen-2 predicted that they would be possibly damaging or damaging, respectively. SIFT predicted that Ala44Thr would be deleterious, whereas PolyPhen-2 predicted that it would be benign. Additionally, there did not appear to be a consistent relationship between the predicted effects of the variants on AP2σ structure and their predicted effects on AP2σ function (Table 10). Crystal structural modelling of the 5 variants where SIFT and PolyPhen-2 concur (Phe52Tyr, Thr112Met, Met117Ile, Glu122Gly and

Glu142Lys) did not produce consistent results. Phe52Tyr and Met117Ile were not predicted to have an effect on the protein structure, whereas Thr112Met, Glu122Gly and Glu142Lys were all predicted to result in loss of a polar contact between AP2σ and AP2α. The 3 variants where SIFT and PolyPhen-2 did not agree (Arg3His, Ala44Thr and Arg61His) had varying predicted effects on AP2σ structure, including loss of 1 polar contact within AP2σ for Arg3His, no change for Ala44Thr and loss of 5 potential polar contacts predicted to affect dileucine motif binding for Arg61His. Met117Ile is associated with hypercalcaemia in a patient and SIFT and PolyPhen-2 agree that it is likely to be deleterious and possibly damaging. However, structural modelling did not predict a resultant structural alteration in Met117Ile. This may suggest that an absence of change in the overall number of polar contacts does not necessarily mean there will be no effect on function. Evidence from multiple sources including prediction software tools and structural modelling can aid in predicting functional effects. In order to better understand the effects of these variants on AP2σ function, expression constructs for AP2σ WT and the variants were generated and transfected into HEK293-based cells models.

Table 10. Summary of the *in silico* assessment of the non-synonymous AP2S1 variants. SIFT and PolyPhen-2 prediction tools were used to assess the predicted effects of the variants on the function of AP2σ. The predicted structural effect of each variant on polar contacts assessed using PyMOL is also summarised. [A]Variant associated with hypercalcaemia in a patient; [B]Variant known to be an FHH3-causing mutation; [C]As reported by Hannan et al 2015 (192). - =no effect on the number of polar contacts predicted by PyMOL. Data published in Gorvin et al (2018) (262).

Variant	SIFT	PolyPhen-2	Loss of polar contacts predicted by PyMOL	
			within AP2σ	**between AP2σ and other structure**
Previously reported FHH3-causing mutations:				
Arg15Cys[A,B]	Deleterious	Possibly damaging	-	1 polar contact with AP2α[C]
Arg15His[A,B]	Deleterious	Possibly damaging	-	1 polar contact with AP2α[C]
Arg15Leu[A,B]	Deleterious	Possibly damaging	-	1 polar contact with AP2α[C]
DiscovEHR dataset:				
Phe52Tyr	Deleterious	Possibly damaging	-	-
Met117Ile[A]	Deleterious	Possibly damaging	-	-
dbSNP and ExAC datasets:				
Arg3His	Tolerated	Possibly damaging	1 polar contact	-
Ala44Thr	Deleterious	Benign	-	-
Arg61His	Tolerated	Damaging	-	5 potential polar contacts that may affect dileucine motif binding
Thr112Met	Deleterious	Possibly damaging	-	1 polar contact with AP2α
Glu122Gly	Deleterious	Damaging	-	1 polar contact with AP2α
Glu142Lys	Deleterious	Possibly damaging	1 polar contact	1 polar contact with AP2α (also a change from an acidic to a basic residue)

6.2.4 Assessment of the effect of the AP2σ variants on CaSR-mediated Ca^{2+}_i signalling

We performed functional experimental studies to evaluate the effect of the variants and compare results with the predicted effects generated by the *in silico* prediction tools. The CaSR was used as a model signalling receptor system as the patients in the DiscovEHR dataset with the Arg15His and Met117Ile variants appeared to have a calcium phenotype. A pBI-CMV4-RFP construct containing full length *AP2S1* was mutated to generate nine constructs each containing one of the variants - Arg3His, Arg15His, Ala44Thr, Phe52Tyr, Arg61His, Thr112Met, Met117Ile, Glu122Gly and Glu142Lys (192). The construct has a bi-directional promoter to allow simultaneous expression of *AP2S1* cDNA and red-fluorescent protein (RFP) cDNA at equivalent levels. The constructs containing either WT or variant *AP2S1* (pBI-CMV4-RFP-*AP2S1*-WT/variant) were then transiently transfected into HEK293 cells stably

expressing the CaSR (HEK293-CaSR) (20). Western blot analysis demonstrated that the AP2σ protein was overexpressed in transfected cells at higher levels compared to the endogenous AP2σ in untransfected cells, and was expressed at similar levels between the WT and nine variants (Figure 25). In addition, fluorescent microscopy used to detect RFP, also confirmed successful transfection of the plasmids (Figure 26), and thus exogenous AP2σ, in a high percentage of cells.

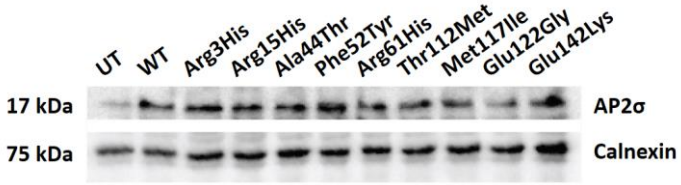


Figure 25. Western blot demonstrating AP2σ expression in untransfected (UT) HEK293-CaSR cells, and HEK293-CaSR cells transiently transfected with pBI-CMV4-RFP-*AP2S1*-WT or pBI-CMV4-RFP-*AP2S1*-variants. Cell lysates were probed for AP2σ (17kDa) and calnexin (75kDa) control. Transfected cells expressed increased levels of AP2σ compared to UT cells. Levels of AP2σ expression were generally similar for all variants. Data published in Gorvin et al (2018) (260).

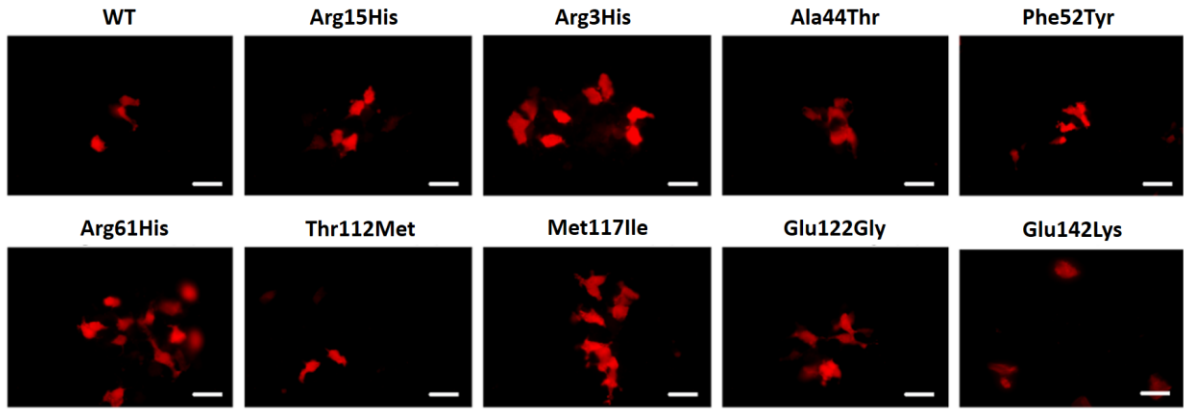


Figure 26. Fluorescence microscopy of HEK293-CaSR cells transiently transfected with pBI-CMV4-RFP-*AP2S1*-WT or pBI-CMV4-RFP-*AP2S1*-variants. RFP expression within the transfected HEK293-CaSR cells was visualised confirming successful transfection of *AP2S1* expression constructs. Untransfected not shown (plain black square). The scale bar indicates 10μm. Data published in Gorvin et al (2018) (260).

In parallel, Fluorescence-Activated Cell Sorting (FACS) assays were used to assess the effect of the AP2σ variants on intracellular calcium signalling, with the previously characterised FHH3-causing Arg15His mutation (20) used as a control loss-of-function mutant. Transfected cells were labelled with the UV light-excitable cell-permeant ratiometric calcium indicator, Indo-1AM, and exposed to different $[Ca^{2+}]_e$. Transfected cells expressing RFP were isolated by FACS and used to detect shifts in the light emission from Indo-1AM occurring in response to changes in intracellular calcium concentration ($[Ca^{2+}]_i$) (42).

The isolated HEK293-CaSR cells expressing either AP2σ WT, Arg15His or the 8 novel variants showed a dose-dependent increase in $[Ca^{2+}]_i$ in response to increasing $[Ca^{2+}]_e$ (Figure 27A-H). Cells expressing the previously characterised FHH3-causing Arg15His mutation demonstrated a reduced $[Ca^{2+}]_i$ response compared to cells expressing WT AP2σ, which resulted in a rightward shift of the Ca^{2+}_i concentration-response curve and significantly elevated half-maximal (EC_{50}) value from 2.87 to 3.66, as expected for the loss-of-function control mutation (Figure 27A-H, Figure 28, Table 11).

The dose response curves for Arg3His, Ala44Thr, Phe52Tyr, Arg61His and Glu122Gly AP2σ variant expressing cells followed the WT curves closely and did not demonstrate a rightward shift of the Ca^{2+}_i concentration-response curve (Figure 27A, B, C, D and E). The half-maximal (EC_{50}) value of these cells again did not differ significantly from cells expressing WT AP2σ (Figure 28, Table 11). However, in contrast Thr112Met, Met117Ile and Glu142Lys AP2σ variant expressing cells were significantly different from cells expressing WT AP2σ. Thr112Met expressing cells demonstrated a rightward shift of the Ca^{2+}_i concentration-response curve similar to Arg15His (Figure 27F). The half-maximal (EC_{50}) value was significantly elevated at 3.39 (95% confidence interval 3.26-3.53) (Figure 28, Table 11). Met117Ile

expressing cells also demonstrated a rightward shift of the Ca^{2+}_i concentration-response curve similar to Arg15His (Figure 27G) and the half-maximal (EC_{50}) value was significantly elevated at 3.41 (95% confidence interval 3.29-3.54) (Figure 28, Table 11). Glu142Lys expressing cells also demonstrated a rightward shift of the Ca^{2+}_i concentration-response curve similar to Arg15His (Figure 27H) and a significantly elevated half-maximal (EC_{50}) value at 3.63 (95% confidence interval 3.49-3.78) (Figure 28, Table 11). This suggests that the Thr112Met, Met117Ile and Glu142Lys variants also result in a loss-of-function of AP2σ, as seen in the FHH3-causing mutations (192, 260). Furthermore the CaSR signalling data for the Phe52Tyr and variants Met117Ile indicating no effect and loss-of-function respectively, is in agreement with the patient phenotypic data in the DiscovEHR dataset in which the patient with the Phe52Tyr variant is normocalcaemic and the patient with the Met117Ile variant is mildly hypercalcaemic.

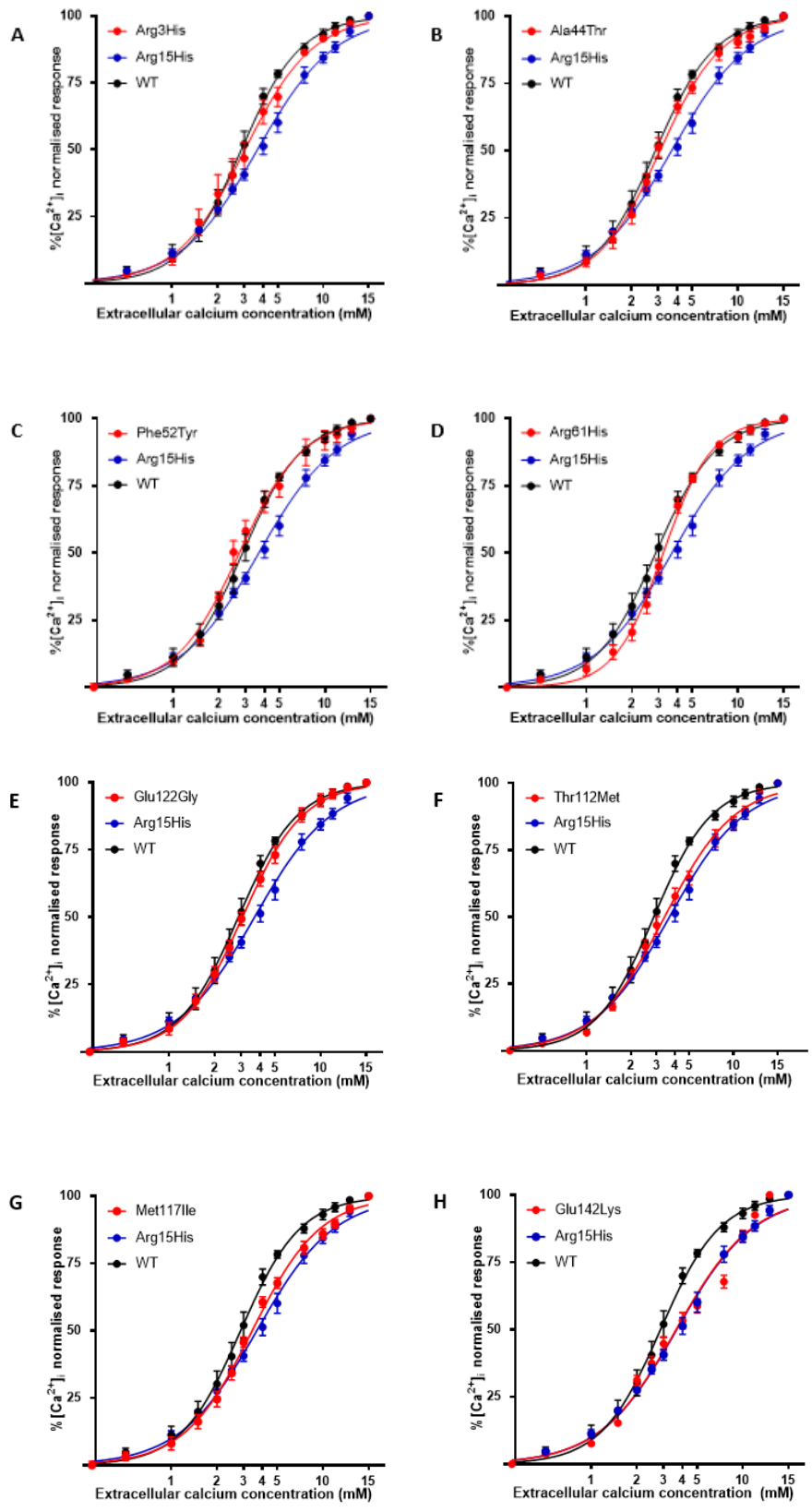


Figure 27. Dose-response curves showing the $Ca^{2+}{}_i$ response to increasing $[Ca^{2+}]_e$ expressed as a percentage of the maximum normalised response of HEK293-CaSR cells expressing the AP2σ WT (shown in black), , compared to HEK293-CaSR cells expressing either Arg15His loss-of-function control

(shown in blue) or AP2σ variants (shown in red). Results shown as the mean+/-SEM of 4-8 independent transfections. Arg15His shows a rightward shift in the curve compared to WT. (A) Arg3His (B) Ala44Thr (C) Phe52Tyr (D) Arg61His (E) Glu122Gly (F) Thr112Met (G) Met117Ile (H) Glu142Lys. Data published in Gorvin et al (2018) (260).

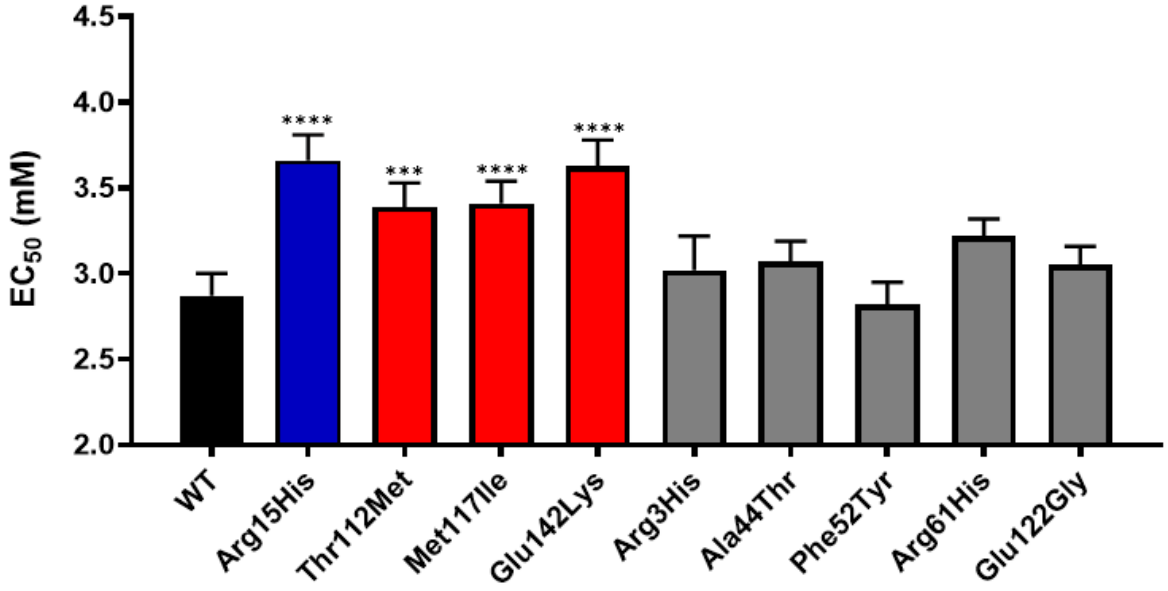


Figure 28. Histograms showing the half-maximal concentration (EC_{50}) with 95% confidence intervals and p-values of HEK293-CaSR cells expressing the AP2σ WT (shown in black), compared to HEK293-CaSR cells expressing either Arg15His loss-of-function control (shown in blue) or AP2σ variants (variants with a significantly different EC_{50} compared to WT shown in red, variants with no significant difference in their EC_{50} when compared to WT shown in grey). Statistical analysis performed using the F-test. Arg15His has a significantly higher EC_{50} compared to WT. Comparison of the EC_{50}s of Thr112Met, Met117Ile and Glu142Lys with WT showed they were significantly elevated, similar to Arg15His. Comparison of the EC_{50}s of Arg3His, Ala44Thr, Phe52Tyr, Arg61His and Glu122Gly with WT showed no significant difference. ***p<0.001 ****p<0.0001. Data published in Gorvin et al (2018) (260).

Table 11. Summary of the half-maximal concentration (EC_{50}), with 95% confidence intervals and p-values, of cells expressing either WT, loss-of-function control Arg15His or variant AP2σ. [A]FHH3-causing, loss-of-function control mutation Arg15His, also seen in the DiscovEHR dataset. Statistical analysis performed using the F-test. ns=not significant; ***p<0.001; ****p<0.0001. Data published in Gorvin et al (2018) (260). Variants associated with a significant change in EC_{50} are shown in red.

Variant	EC_{50}	95% confidence interval	p-value
Controls:			
WT	2.87	2.74-3.00	
Arg15His[A]	3.66	3.52-3.81	****
DiscovEHR dataset:			
Phe52Tyr	2.82	2.70-2.95	ns
Met117Ile	3.41	3.29-3.54	****
dbSNP and ExAC datasets:			
Arg3His	3.02	2.84-3.22	ns
Ala44Thr	3.07	2.96-3.19	ns
Arg61His	3.22	3.13-3.32	ns
Thr112Met	3.39	3.26-3.53	***
Glu122Gly	3.05	2.94-3.16	ns
Glu142Lys	3.63	3.49-3.78	****

7 RESULTS – ESTABLISHING MOUSE MODELS OF FHH3

FHH1, which is the most prevalent type of FHH, has a well characterized calcitropic phenotype (42, 186, 206, 264, 265) facilitated by the development of a mouse model that allows further phenotypic investigations and preliminary testing of drug treatments (230). FHH2, the rarest form of FHH accounting for <5% of cases, also has a mouse model with a germline loss-of-function *Gna11* mutation (232) available to aid its characterisation. As described in the introduction, FHH3 is associated with a more severe phenotype than FHH1 and FHH2 (192) and appears to be associated with non-calcitropic phenotypes including skeletal disease (192, 194), cognitive dysfunction, short stature, and atrial septal defect (192) (Table 6). One large FHH3 kindred with the Arg15Cys mutation (the Oklahoma kindred) has also been found to have age-related increases in PTH concentrations (20, 193, 194). FHH3 appears to demonstrate genotype-phenotype correlation at the Arg15 codon. Of the three known FHH3-causing mutations at Arg15, namely Arg15His, Arg15Cys and Arg15Leu, patients with Arg15Leu mutations have the most severe phenotype with significantly greater elevations of serum adjusted-calcium concentrations than probands with Arg15Cys or Arg15His mutations and patients with Arg15Cys mutations are significantly more hypercalcaemic than those with Arg15His mutations (Figure 14). However, despite this apparently more severe phenotype, until now no mouse model of FHH3 has existed to enable its further characterisation.

In chapter 6 I used large sequencing datasets to search for novel causes of FHH3. As previously described, they provide an important resource of genetic information on what may be considered to be the “normal” population, however it is important that results are interpreted in the context of the populations whose data has been submitted. The Genome Aggregation Database (gnomAD) (220) is an aggregation of exome and genome sequencing data from a

wide variety of large scale sequencing projects. It includes the analysis of groups of patients with conditions such as atrial fibrillation, chronic obstructive pulmonary disorder, various cancers and psychiatric conditions, from a variety of countries including the UK, Finland, Pakistan and Japan. It spans 125,748 exome sequences and 15,708 whole genome sequences from unrelated individuals. Interrogating the *AP2S1* gene in the gnomAD v2.1.1 dataset revealed fewer observed missense and predicted loss-of-function single nucleotide variants (SNVs) than would be expected (Table 12). The number of observed synonymous variants deviated only slightly from the number that would be expected (39.5 vs 39). The ratio of observed SNVs to expected SNVs (o/e) is close to 1.0 for the synonymous variants, and the 90% confidence interval (90% C.I.) crosses 1.0, suggesting that the gene is tolerant of this type of variant. The Z-score (or distance from the mean value when measured in standard deviations) is close to zero, in support of this (Table 12). In contrast, the number of observed missense variants deviates widely from the number that would be expected (92.4 vs 15). The o/e ratio is low at 0.16 (90% C.I. 0.11-0.25) suggesting that the gene is intolerant of this type of variant. The Z-score is strongly positive at 2.86, supporting the observation that these mutations are subject to more constraint (Table 12). The observed number of variants predicted to result in a loss of function of the gene (pLOF) was also much lower than the number expected to occur (1 vs 9.4). Again, the o/e ratio was low at 0.11 (90% C.I. 0.0.4-0.50) suggesting that the gene is intolerant of loss-of-function mutations. A probability of loss-of-function mutation intolerance score (pLI) is derived from a comparison of the observed number of variants in a sample, to the number expected in the absence of fitness effects given an estimated mutation rate for the gene. A value closer to 1.0, suggests that a gene is more intolerant of protein truncating variation, with pLI>0.9 indicating extreme intolerance. The

pLI score for *AP2S1* is 0.79 suggesting that the gene may be intolerant of truncation (Table 12).

Table 12. Table of constraint metrics for *AP2S1* using data available on gnomAD v2.1.1 (220). SNV=single nucleotide variant; pLOF=predicted loss-of-function; o/e=ratio of the observed number of SNVs to the expected number of SNVs for this gene (shown with 90% confidence intervals). [A]Z-score; [B]predicted loss-of-function intolerance (pLI) score.

Category	Expected SNVs	Observed SNVs	o/e	Measure of intolerance
Synonymous	39.5	39	0.99 (0.76-1.29)	0.06[A]
Missense	92.4	15	0.16 (0.11-0.25)	2.86[A]
pLOF	9.4	1	0.11 (0.04-0.50)	0.79[B]

Experimental evidence derived from mice with *N*-ethyl-*N*-nitrosourea (ENU) induced AP2σ mutations is not in complete agreement with these observations. Mice with the missense variants, Tyr20Asn and Ile123Asn, were viable and, in addition, the variants were found to have no effect on CaSR signalling *in vitro*. Mice with an in-frame deletion of 17 amino acids did not have a calcitropic phenotype, despite a >50% reduction in AP2σ protein expression (234). These results demonstrate the need for *in vitro* and *in vivo* functional assessments of the AP2σ variants observed in humans to determine their potential role in the pathophysiology of calcium homeostasis.

The development of 2 murine FHH3 models based on Arg15 mutations will be described in this chapter. The generation of these mouse models will facilitate further investigations of calcitropic and non-calcitropic phenotypes, as well as allowing the testing of drug treatments, which will also be described. In chapter 6, I described findings that demonstrated that the novel AP2σ variant, Met117Ile, was associated with reduced intracellular calcium signalling *in vitro*, and with mild hypercalcaemia in a patient (260). Therefore, I have also generated an *Ap2s1* Met117Ile mouse model that will be described to assess the effect of this variant on calcitropic phenotypes.

In total I have generated 3 *knock-in* mouse models of FHH3 using CRISPR-Cas technology (266) to: facilitate investigation of the *in vivo* roles of the AP2σ protein; further characterise the calcitropic and non-calcitropic phenotype and pathophysiology of FHH3; and to evaluate CaSR-targeted therapy for this disorder. The models generated were firstly *Ap2s1-Arg15Leu* as this is associated with the clinically most severe phenotype in FHH3 patients, secondly *Ap2s1-Arg15Cys* to allow investigation of the genotype-phenotype correlation at the Arg15 codon, and thirdly *Ap2s1-Met117Ile* as this represents another potential class of FHH3-causing AP2σ mutations.

7.1 CRISPR-Cas-induced *Ap2s1* mutant Arg15Leu mice

7.1.1 Generation of *Ap2s1-Arg15Leu* mice

Mutant mice harbouring c.G44T p.Arg15Leu in the *Ap2s1* gene were generated on a C57BL/6J strain background using a Class 2 Clustered Regularly Interspaced Short Palindromic Repeat (CRISPR) –Cas9 system system, as reported (239, 267) and described in the Methods (Figure 18). The c.G44T mutation was chosen as this is the only nucleotide change found in Arg15Leu patients. Where indicated, this work has been published in the paper Hannan et al (2021) (243).

Founder mice harbouring the targeted allele were identified by analysing ear biopsy DNA using allelic discrimination (245). One mosaic founder mouse was then mated with a wild type (WT) mouse to produce the F1 generation of $Ap2s1^{+/L15}$ heterozygous mice. The F1 $Ap2s1^{+/L15}$ mice were then inter-crossed to generate the initial litters of WT, $Ap2s1^{+/L15}$ and $Ap2s1^{L15/L15}$ mice (Figure 19). The numbers of WT, $Ap2s1^{+/L15}$ and $Ap2s1^{L15/L15}$ mice in the F2 generation were counted to assess the viability of the genotypes.

At birth, the numbers of WT, *Ap2s1*$^{+/L15}$ and *Ap2s1*$^{R15L/R15L}$ mice did not deviate from the expected 1:2:1 Mendelian ratio when tested by Chi-squared analysis. WT and *Ap2s1*$^{+/L15}$ mice were viable and survived into adulthood (Table 13). However, >75% (13/17) *Ap2s1*$^{R15L/R15L}$ mice died within 48 hours after birth. Due to this homozygote mortality within 48 hours of birth, the numbers of WT, *Ap2s1*$^{+/L15}$ and *Ap2s1*$^{R15L/R15L}$ mice significantly deviated from the Mendelian ratio at 3 weeks of age (χ^2=10.55, p=0.005). Of the surviving *Ap2s1*$^{R15L/R15L}$ mice, one female and three males survived past 48h. The female was culled at 36 days for hydrocephalus and one male was culled at 56 days for poor condition. The remaining two males survived to 16 weeks of age for biochemical analysis. The Mendelian ratio of mice surviving to adulthood therefore deviated further from expected (χ^2=17.81, p=0.0001). Because of the high rate of homozygote neonatal lethality, WT and *Ap2s1*$^{+/L15}$ mice were generated for subsequent studies by backcrossing *Ap2s1*$^{+/L15}$ mice onto the WT background.

Table 13. Proportion of offspring bred from crosses of *Ap2s1*$^{+/L15}$ x *Ap2s1*$^{+/L15}$ mice. Heterozygous crosses led to the expected Mendelian inheritance ratio of 1:2:1 for WT : *Ap2s1*$^{+/L15}$: *Ap2s1*$^{L15/L15}$ offspring at birth. However, the homozygote mice had reduced viability beyond the first few days, leading to a significantly different ratio of offspring genotypes at weaning and at adulthood. Blue denotes a lower than expected value. **p<0.01, *** p<0.001 (by Chi-squared analysis). Data published in Hannan et al (2021) (243).

Genotype	Number of offspring observed at birth (n=72)	Number of offspring observed at weaning (~3 weeks old) (n=48)	Number of offspring observed at adulthood (>10 weeks old) (n=46)
WT	17 (24%)	14 (29%)	14 (31%)
Ap2s1$^{+/L15}$	38 (52%)	30 (63%)	30 (65%)
Ap2s1$^{L15/L15}$	17 (24%)	4 (8%)**	2 (4%)***

Adult *Ap2s1*$^{+/L15}$ mice showed no gross morphological abnormalities, and behaviours such as eating, drinking, grooming, activity levels and interacting with cage-mates were observed to be similar between *Ap2s1*$^{+/L15}$ and WT mice. However, male *Ap2s1*$^{+/L15}$ mice had a significantly reduced body weight compared to age-matched WT male mice (Table 14).

7.1.2 *Ap2s1-Arg15Leu* mouse biochemical phenotyping

Male and female *Ap2s1*$^{+/R15L}$ mice exhibited abnormalities of their calcitropic biochemistry consistent with the human FHH3 phenotype (Figure 29, Table 14). They had a marked hypercalcaemia and elevation of PTH concentrations when compared to WT mice. This was associated with increased plasma ALP and plasma magnesium concentrations, but decreased inorganic phosphate when compared to WT mice (Figure 29, Table 14). Female, but not male, *Ap2s1*$^{+/R15L}$ mice have significantly lower 24 hour urinary calcium excretion values than female WT mice, again, consistent with the human FHH3 phenotype, although differences in urinary CCCR were not significantly different between *Ap2s1*$^{+/R15L}$ and WT mice (Figure 30, Table 14).

Table 14. Age, body weight and calcitropic biochemistry of adult WT and *Ap2s1*$^{+L15}$ mice, aged 16-17 weeks. [A]plasma adjusted calcium; PTH=plasma parathyroid hormone; ALP=alkaline phosphatase; 1,25 vit D=1,25-hydroxyvitamin D; FGF23=Fibroblast Growth Factor 23; P1NP= pro-collagen type 1 N-terminal pro-peptide; CCCR=24 hour urine calcium:creatinine clearance ratio. Red denotes a higher than expected value; blue denotes a lower than expected value. All values are expressed as mean ± SEM. *p<0.05, **p<0.01; ***p<0.001, ****p<0.0001 for *Ap2s1*$^{+/L15}$ mice versus respective WT mice. One-way ANOVA followed by Sidak's test for pairwise multiple comparisons were used for all analyses. Data published in Hannan et al (2021) (243).

	Male		**Female**	
	WT	***Ap2s1*$^{+/L15}$**	**WT**	***Ap2s1*$^{+/L15}$**
Age (weeks)	16.5±0.07 (n=12)	16.4±0.1 (n=12)	16.4±0.1 (n=12)	16.3±0.1 (n=12)
Weight (g)	30.0±0.3 (n=12)	28.4±0.5 (n=12)*	23.9±0.4 (n=12)	22.7±0.5 (n=12)
Plasma biochemistry:				
Adj-calcium (mmol/l)[A]	2.36±0.01 (n=12)	2.91±0.02 (n=12)****	2.31±0.01 (n=12)	2.93±0.02 (n=12)****
PTH (ng/l)	74.4±12.2 (n=12)	148.8±15.6 (n=12)**	29.9±2.4 (n=9)	161.3±24.1 (n=12)****
Phosphate (mmol/l)	1.81±0.07 (n=12)	1.41±0.07 (n=12)**	1.67±0.09 (n=12)	1.26±0.08 (n=12)**
Magnesium (mmol/l)	0.95±0.02 (n=11)	1.10±0.02 (n=11)***	1.08±0.02 (n=12)	1.24±0.04 (n=9)***
ALP (U/l)	87.8±3.3 (n=12)	107.3±3.1 (n=12)***	118.3±4.2 (n=12)	143.0±3.7 (n=10)****
1,25 vit D (pmol/l)	100.8±11.1 (n=12)	113.3±7.3 (n=12)	76.1±6.5 (n=8)	105.5±11.5 (n=7)
FGF23 (ng/l)	301±26 (n=11)	691±53 (n=12)****	332±14 (n=11)	912±75 (n=12)****
P1NP (μg/l)	60.7±4.8 (n=11)	63.7±5.9 (n=11)	36.4±1.6 (n=12)	41.0±2.2 (n=12)
Urine biochemistry:				
24hr urine volume (ml)	5.3±0.2 (n=12)	5.5±0.2 (n=12)	5.2±0.3 (n=12)	5.8±0.2 (n=12)
24hr calcium excretion (μmol/24hr)	6.68±0.6 (n=12)	4.51±0.6 (n=11)	9.67±0.8 (n=12)	6.34±0.7 (n=11)**
CCCR x10^3	1.3±0.1 (n=12)	0.8±0.2 (n=11)	2.0±0.2 (n=12)	1.5±0.2 (n=11)

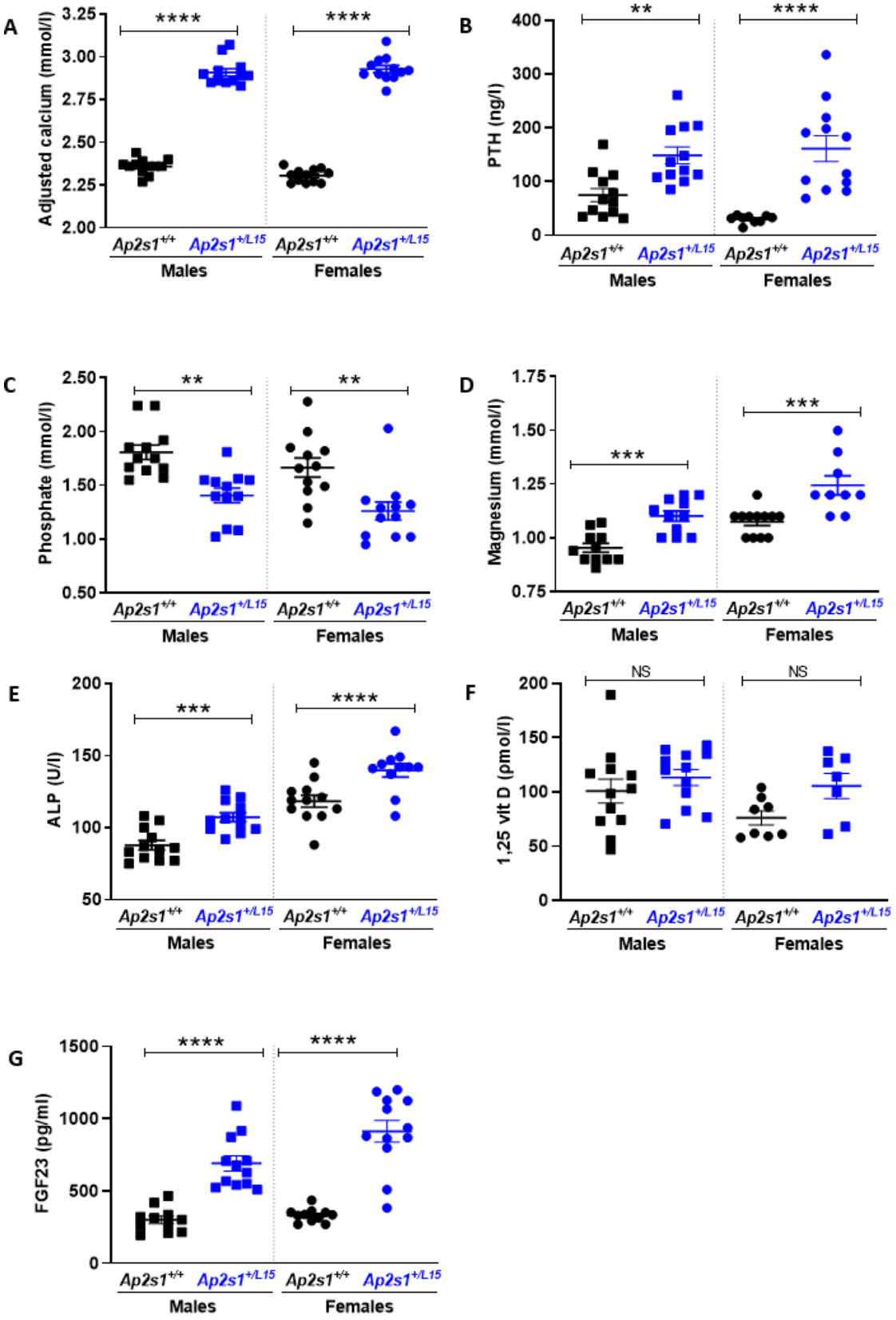


Figure 29. Calcitropic plasma biochemistry of adult WT and *Ap2s1*$^{+/L15}$ mice, aged 16-17 weeks. (A) Adjusted calcium; (B) Parathyroid hormone (PTH); (C) Phosphate; (D) Magnesium; (E) Alkaline

phosphatase (ALP); (F) 1,25-hydroxyvitamin D (1,25 vit D); and (G) Fibroblast growth factor 23 (FGF23). Males are denoted by squares, females by circles. WT *Ap2s1*$^{+/+}$ mice are in black, heterozygous *Ap2s1*$^{+/L15}$ mice are in blue. Mean±SEM values for respective groups (n=7-12 mice per group) are indicated. NS=non-significant; *p<0.05, **p<0.01; ***p<0.001, ****p<0.0001 for *Ap2s1*$^{+/L15}$ mice versus respective WT mice. One-way ANOVA followed by Sidak's test for pairwise multiple comparisons were used for all analyses. Data published in Hannan et al (2021) (243).

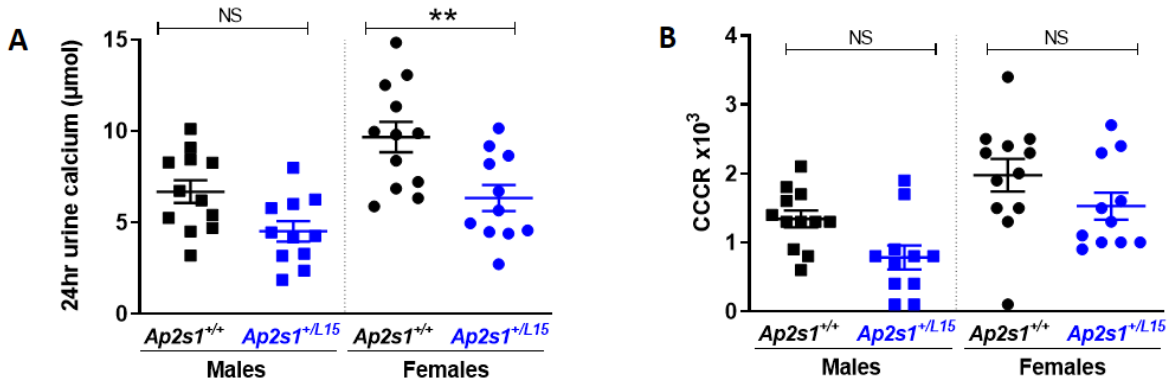


Figure 30. Calcitropic urine biochemistry of adult WT and *Ap2s1*$^{+/L15}$ mice, aged 16-17 weeks. (A) 24 hour urine calcium; and (B) calcium:creatinine clearance ratio (CCCR) x10^3. Males are denoted by squares, females by circles. WT *Ap2s1*$^{+/*}$ mice are in black, heterozygous *Ap2s1*$^{+/L15}$ mice are in blue. Mean±SEM values for respective groups (n=7-12 mice per group) are indicated. NS=non-significant for *Ap2s1*$^{+/L15}$ mice versus respective WT mice. One-way ANOVA followed by Sidak's test for pairwise multiple comparisons were used for all analyses. Data published in Hannan et al (2021) (243).

Our investigations also revealed abnormalities that have not been recorded in reports of human FHH3 patients. Male and female *Ap2s1*$^{+/R15L}$ mice had elevated plasma fibroblast growth factor 23 (FGF23), which was not associated with alterations in plasma 1,25-dihydroxyvitamin D concentrations (Figure 29, Table 14). In addition, we were able to investigate the *Ap2s1*$^{+/R15L}$ mice for a non-calcitropic biochemical phenotype. As the CaSR is widely expressed in the kidneys, myocardium, pancreatic islets, enteroendocrine cells and adipose tissue (Table 3) and AP2 is ubiquitously expressed we decided to perform a comprehensive biochemical screen measuring electrolytes and renal function, liver function,

glucose and lipids. Female *Ap2s1*$^{+/R15L}$ mice had significantly lower plasma urea, total cholesterol, HDL cholesterol, and significantly higher plasma bilirubin compared to female WT mice. These changes were not seen in the male *Ap2s1*$^{+/R15L}$ mice (Figure 31, Table 15).

Table 15. Non-calcitropic biochemistry of adult WT and *Ap2s1*$^{+/L15}$ mice, aged 16-17 weeks. [A]Glucose and lipid concentrations were measured in non-fasting mice. HDL-c=HDL cholesterol; LDL-c=LDL cholesterol; ALT=alanine aminotransferase; AST=aspartate aminotransferase. All values are expressed as mean ± SEM. [¥]p=0.0522; *p<0.05; **p<0.01 for *Ap2s1*$^{+/L15}$ mice versus respective WT mice. Red denotes a higher than expected value; blue denotes a lower than expected value. One-way ANOVA followed by Sidak's test for pairwise multiple comparisons were used for all analyses. Data published in Hannan et al (2021) (243).

	Male		**Female**	
	WT	***Ap2s1*$^{+/L15}$**	**WT**	***Ap2s1*$^{+/L15}$**
Electrolytes and renal:				
Sodium (mmol/l)	147±0.4 (n=12)	147±0.4 (n=11)	145±0.3 (n=12)	144±0.5 (n=12)
Potassium (mmol/l)	4.4±0.1 (n=12)	4.6±0.1 (n=11)	4.8±0.1 (n=12)	4.9±0.1 (n=12)
Urea (mmol/l)	10.8±0.4 (n=12)	9.6±0.2 (n=12)	10.6±0.4 (n=12)	8.7±0.5 (n=12)**
Creatinine (mmol/l)	9.8±0.3 (n=12)	10.5±0.4 (n=12)	10.2±0.4 (n=12)	10.8±0.5 (n=12)
Glucose and lipids[A]*:*				
Glucose (mmol/l)	13.3±0.4 (n=12)	13.1±0.7 (n=12)	12.1±0.4 (n=12)	11.8±0.8 (n=12)
Total cholesterol (mmol/l)	2.27±0.11 (n=12)	2.17±0.04 (n=11)	1.95±0.06 (n=12)	1.55±0.12 (n=12)**
LDL-c (mmol/l)	0.49±0.03 (n=12)	0.45±0.01 (n=12)	0.39±0.01(n=12)	0.34±0.01 (n=12)[¥]
HDL-c (mmol/l)	1.54±0.07 (n=12)	1.47±0.03 (n=11)	1.10±0.04 (n=12)	0.85±0.08 (n=12)*
Triglycerides (mmol/l)	1.33±0.10 (n=12)	1.33±0.09 (n=12)	0.90±0.06 (n=12)	0.86±0.06 (n=12)
Liver:				
Total bilirubin (μmol/l)	1.9±0.2 (n=12)	1.5±0.1 (n=11)	2.8±0.2 (n=12)	3.5±0.2 (n=12)*
ALT (U/l)	39.7±2.3 (n=10)	38.2±1.7 (n=11)	31.7±2.3 (n=12)	30.5±1.2 (n=12)
AST (U/l)	57.0±4.7 (n=12)	57.6±5.2 (n=12)	54.8±3.6 (n=12)	59.8±4.4 (n=12)

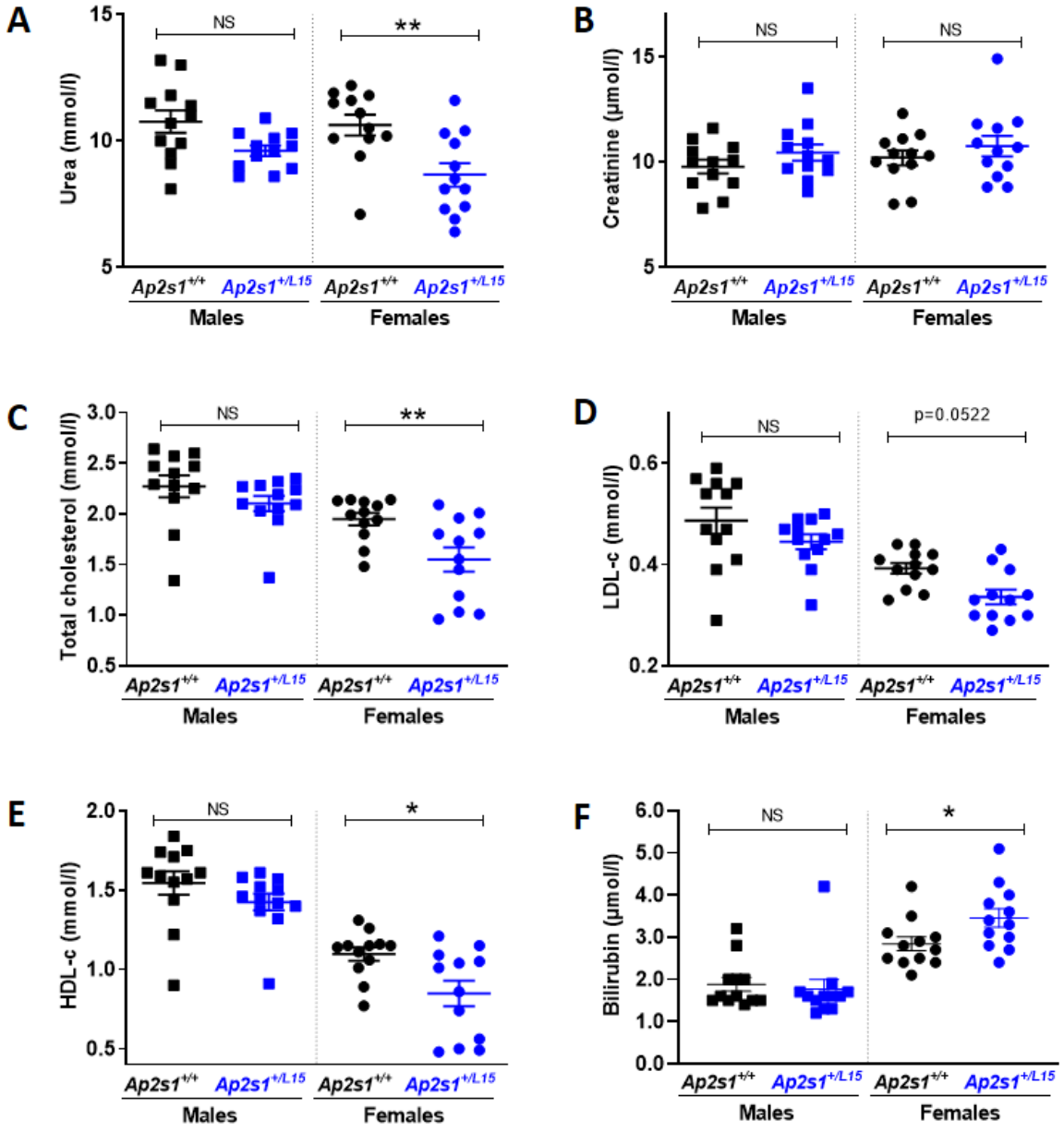


Figure 31. Non-calcitropic plasma biochemistry of adult WT and *Ap2s1*$^{+/L15}$ mice, aged 16-17 weeks. (A) Urea; (B) Creatinine; (C) Total cholesterol; (D) Low density lipoprotein (LDL) cholesterol; (E) High density lipoprotein (HDL) cholesterol; and (F) Bilirubin. Mean±SEM values for respective groups (n=7-12 mice per group) are indicated. Males are denoted by squares, females by circles. WT *Ap2s1*$^{+/+}$ mice are in black, heterozygous *Ap2s1*$^{+/L15}$ mice are in blue. NS=non-significant; *p<0.05, **p<0.01 for *Ap2s1*$^{+/L15}$ mice versus respective WT mice. One-way ANOVA followed by Sidak's test for pairwise multiple comparisons were used for all analyses. Data published in Hannan et al (2021) (243).

7.1.3 *Ap2s1-Arg15Leu* mouse bone phenotyping

Bone metabolism was assessed by whole body dual-energy X-ray absorptiometry (DXA), and by measurement of the pro-collagen type 1 N-terminal pro-peptide (P1NP) bone turnover marker. There was no difference found in Bone Mineral Content (BMC) corrected for body weight, Bone Mineral Density (BMD) or P1NP concentrations between the *Ap2s1*$^{+/R15L}$ and WT mice (Table 32, Figure 32).

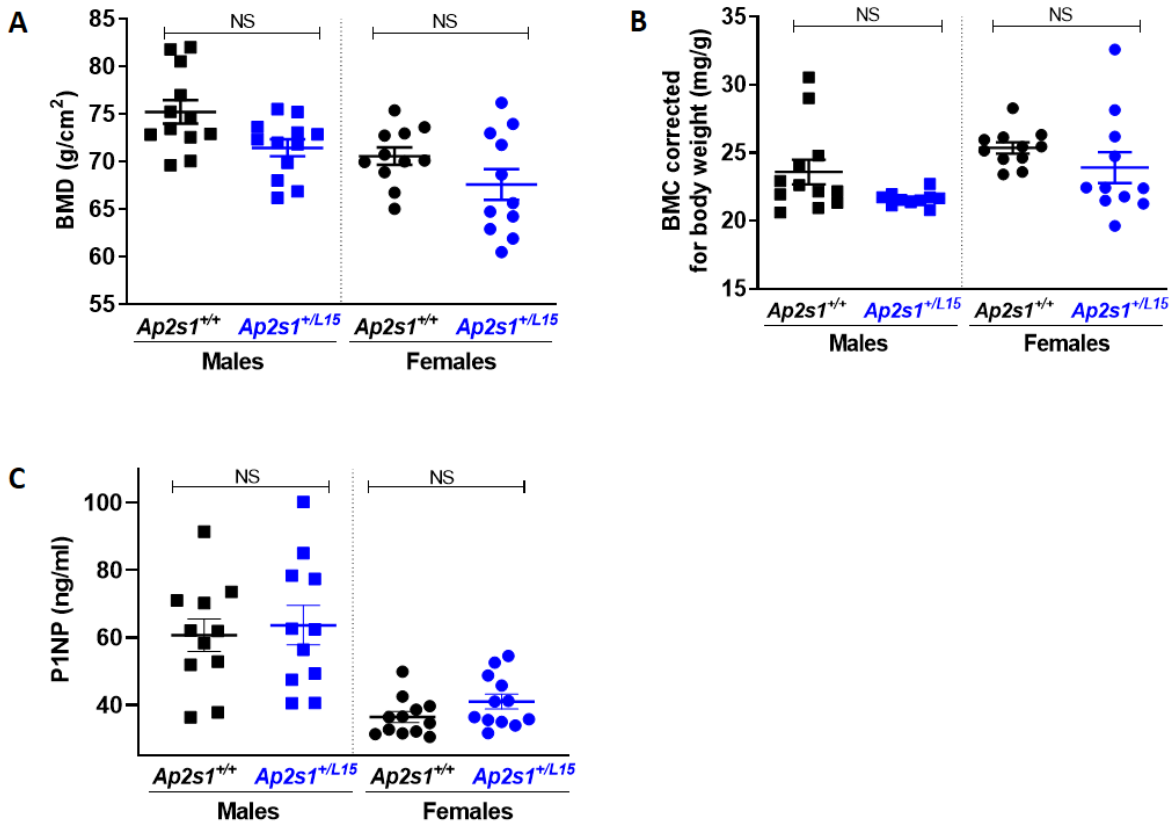


Figure 32. Bone phenotype of adult WT and *Ap2s1*$^{+/L15}$ mice, aged 16-17 weeks. (A) Bone mineral density (BMD); (B) Bone mineral content (BMC) corrected for body weight; and (C) pro-collagen type 1 N-terminal pro-peptide (P1NP) bone turnover marker. Mean±SEM values for respective groups (n=7-12 mice per group) are indicated. Males are denoted by squares, females by circles. WT *Ap2s1*$^{+/+}$ mice are in black, heterozygous *Ap2s1*$^{+/L15}$ mice are in blue. NS=non-significant for *Ap2s1*$^{+/L15}$ mice versus respective WT mice. One-way ANOVA followed by Sidak's test for pairwise multiple comparisons were used for all analyses. Data published in Hannan et al (2021) (243).

7.1.4 Analysis of the 2 surviving *Ap2s1*$^{L15/L15}$ mice

As described, >75% (13/17) *Ap2s1*$^{L15/L15}$ mice died within 48 hours after birth. However, two males survived to 16 weeks of age for biochemical analysis. These mice had plasma adjusted calcium concentrations >10 standard deviations from the mean for WT mice, and >5 SD away from the mean for *Ap2s1*$^{+/L15}$ mice. The surviving *Ap2s1*$^{L15/L15}$ mice also had plasma PTH concentrations >5 and >3 standard deviations from the mean for WT mice and plasma phosphate concentrations >3 standard deviations lower than the mean for WT mice. One *Ap2s1*$^{L15/L15}$ mouse had an ALP value >10 standard deviations from the mean for WT mice, and >5 SD away from the mean for *Ap2s1*$^{+/L15}$ mice, and the other had an ALP value >3 standard deviations away from the mean for WT mice. One *Ap2s1*$^{L15/L15}$ mouse had a magnesium concentration >2 standard deviations from the mean for WT mice. In this all male group analysis, no significant differences were seen in urea and the lipid profile between the WT and *Ap2s1*$^{+/L15}$ mice, as before (Table 15, Figure 31). However, in this analysis, the male *Ap2s1*$^{+/L15}$ mice had significantly higher plasma creatinine values than the WT mice, and one *Ap2s1*$^{L15/L15}$ mouse had a plasma creatinine >2 standard deviations from the mean for WT mice. This finding was not seen in the previous analysis comparing WT and *Ap2s1*$^{+/L15}$ mice (Table 15, Figure 31).

Table 16. Age, body weight, calcitropic biochemistry and non-calcitropic biochemistry of adult male WT, *Ap2s1*$^{+/L15}$, and *Ap2s1*$^{L15/L15}$ mice. [A]plasma albumin--adjusted calcium; [B]Glucose and lipid concentrations were measured in non-fasting plasma samples; [C]Corrected for body weight. PTH=plasma parathyroid hormone; ALP=plasma alkaline phosphatase; ALT=alanine aminotransferase; HDL-c=HDL cholesterol; LDL-c=LDL cholesterol; BMC=bone mineral content; BMD=bone mineral density. Red denotes a higher than expected value; blue denotes a lower than expected value. All WT and *Ap2s1*$^{+/L15}$ values are expressed as mean ± SEM. *p<0.05; **p<0.01; ***p<0.001; ****p<0.0001. One-way ANOVA followed by Sidak's test for pairwise multiple comparisons were used to compare *Ap2s1*$^{+/L15}$ with WT mice. Values of individual *Ap2s1*$^{L15/L15}$ mice are: [a]>10 SD; [b]>3 SD; [c]>5 SD; and [d]>2 SD away from the respective mean WT value; and [e]>5 SD away from the respective mean *Ap2s1*$^{+/L15}$ value. Data published in Hannan et al (2021) (243).

	WT (n=3-4)	***Ap2s1*$^{+/L15}$ (n=5)**	***Ap2s1*$^{L15/L15}$ (n=2)**
Age (weeks)	17.9±1.1	18.4±0.5	18.1, 22.0
Calcitropic biochemistry - plasma:			
Adj-calcium (mmol/l)[A]	2.39±0.03	2.91±0.01****	3.12[a,e], 3.22[a,e]
PTH (ng/l)	42.0±11	94.3±24	134[b], 180[c]
Phosphate (mmol/l)	1.92±0.10	1.32±0.05***	1.17[b], 1.18[b]
Magnesium (mmol/l)	1.0±0.05	1.2±0.06	1.2, 1.3[d]
ALP (U/l)	75.8±1.9	93.6±3.3*	88[b], 150[a,e]
Calcitropic biochemistry - urine:			
Total urine volume (ml)	5.16±0.32	5.34±0.28	5.34, 6.47
24h calcium excretion (µmol/24h)	9.1±0.9	7.3±1.2	5.7, 8.2
Electrolytes and renal:			
Sodium (mmol/l)	146.0±0.58	146.0±0.55	147.0, 148.0
Potassium (mol/l)	4.57±0.23	4.49±0.10	4.13, 4.23
Urea (mmol/l)	10.7±0.66	10.4±0.63	9.6, 9.8
Creatinine (µmol/l)	7.70±0.44	10.14±0.65*	8.5, 9.9[d]
Glucose and lipids[B]:			
Glucose (mmol/L)	14.9±0.33	15.1±0.45	13.1, 14.0
Total cholesterol (mmol/l)	2.33±0.29	1.89±0.21	1.74, 1.86
LDL-c (mmol/l)	0.50±0.08	0.39±0.04	0.41, 0.42
HDL-c (mmol/l)	1.60±0.20	1.31±0.15	1.24, 1.27
Triglycerides (mmol/l)	1.11±0.23	0.90±0.11	0.70, 0.84
Total bilirubin (µmol/l)	2.40±0.67	2.10±0.79	1.60, 1.80
ALT (U/l)	46.3±16.0	32.4±2.6	30.0, 40.0
AST (U/l)	63.8±25.8	50.0±7.7	41.0, 44.0
Bone phenotyping:			
BMC (mg/g)[C]	20.6±1.15	22.38±1.29	20.31, 21.18
BMD (mg/cm^2)	69.4±2.6	72.5±2.8	69.3, 69.6
Fat mass (%)	16.9±4.06	17.1±2.38	12.36, 15.87

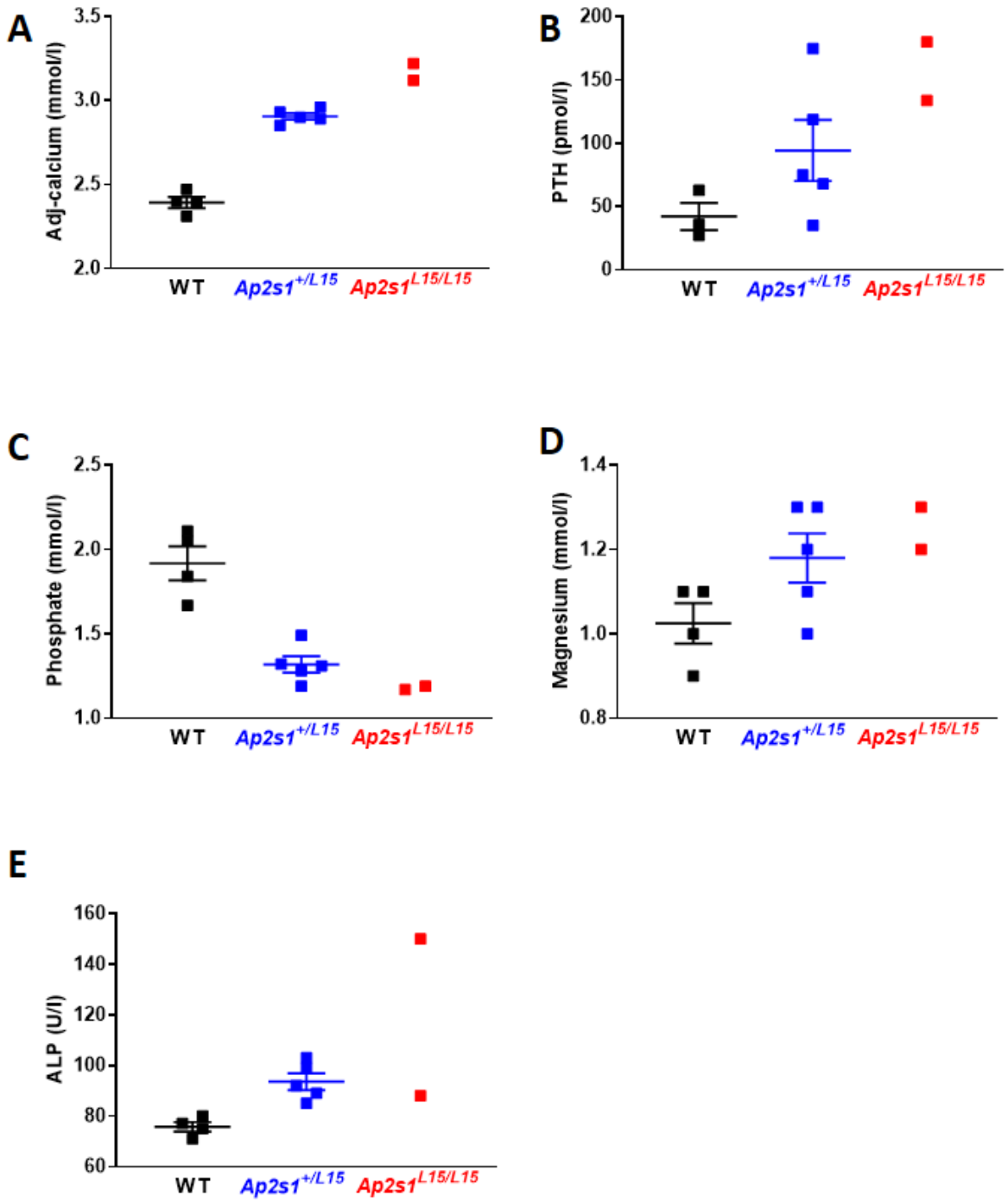


Figure 33. Comparison of calcitropic biochemistry between the male *Ap2s1*$^{L15/L15}$ mice that survived to adulthood (n=2), and age-matched male WT and *Ap2s1*$^{+/L15}$ mice. (A) Adjusted calcium; (B) Parathyroid hormone (PTH); (C) Phosphate; (D) Magnesium; and (E) Alkaline phosphatase (ALP). Mean±SEM values for respective groups are indicated. WT mice are in black, heterozygous *Ap2s1*$^{+/L15}$ mice are in blue, homozygous *Ap2s1*$^{L15/L15}$ mice are in red. Data published in Hannan et al (2021) (243).

7.1.5 Analysis of the effect of cinacalcet on serum calcium and PTH in the *Ap2s1-Arg15Leu* mouse

As described in previous chapters, cinacalcet is a calcimimetic that has been shown to rectify impaired CaSR signalling due to FHH3-causing *AP2S1* mutations *in vitro* (268), and to decrease serum calcium concentrations in three patients with FHH3 caused by *AP2S1*-Arg15Leu mutations (268-270). Preliminary investigations demonstrated that doses of 30, 60 and 120 mg/kg cinacalcet administered by oral gavage to $Ap2s1^{+/L15}$ mice all significantly decreased plasma concentrations of PTH and calcium compared to mice given drug vehicle alone, and dose-dependent effects were not observed (Figure 34).

A single 60mg/kg oral bolus of cinacalcet was then given to both $Ap2s1^{+/L15}$ and WT male and female mice and plasma adjusted-calcium and PTH concentrations were measured at 0, 1, 2 and 4 hours post-dose. Cinacalcet significantly lowered plasma adjusted calcium in both WT and $Ap2s1^{+/R15L}$ mice, and adjusted calcium concentrations in $Ap2s1^{+/R15L}$ mice were lowered to WT concentrations (Figure 35). PTH concentrations were much higher in the $Ap2s1^{+/R15L}$ mice compared to WT, and were transiently suppressed at 1-hour post-dose by cinacalcet (Figure 35).

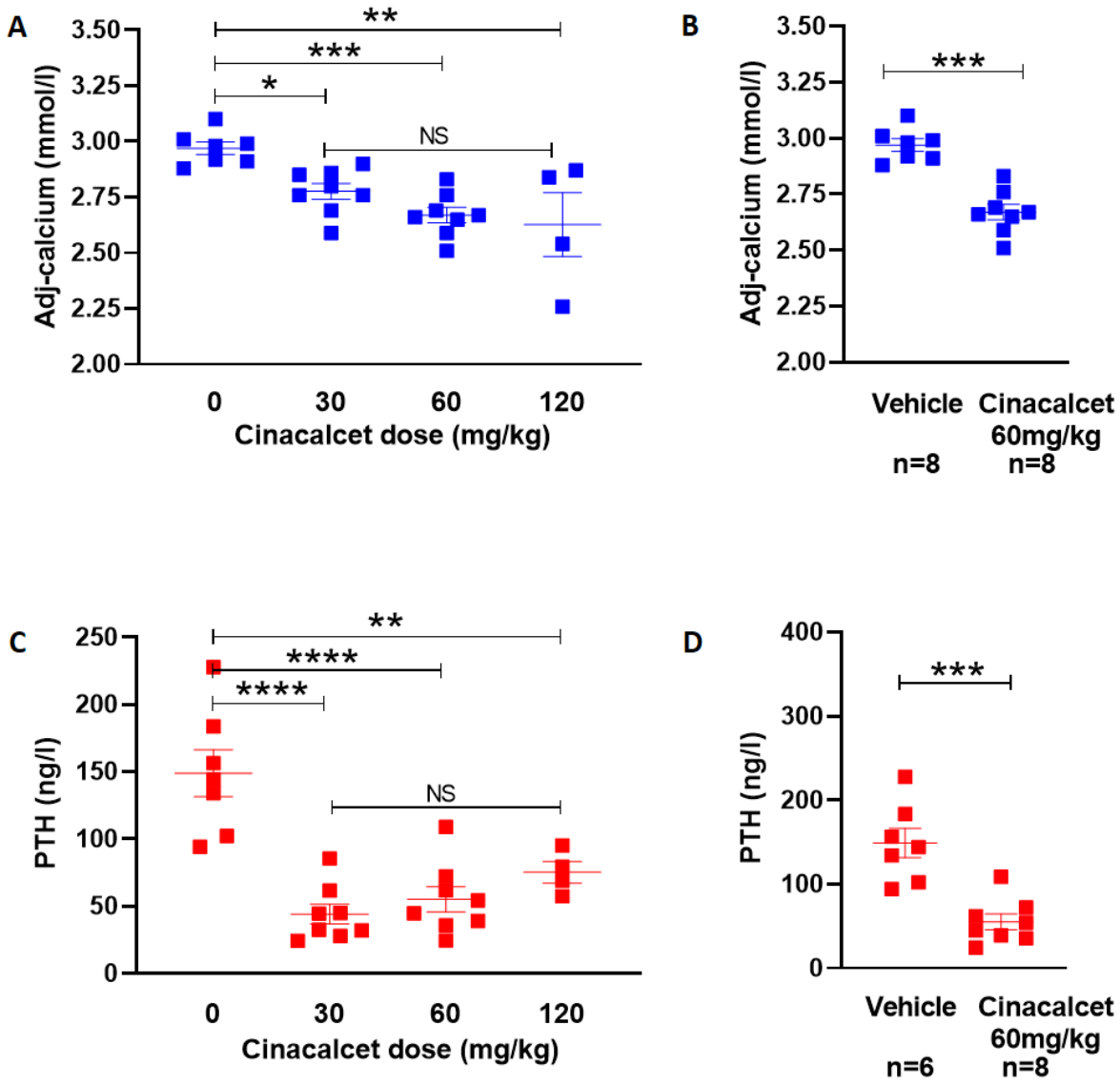


Figure 34. Cinacalcet dose ranging study in male and female *Ap2s1*$^{+/L15}$ mice aged 14-18 weeks. (A) Effect of 0, 30, 60 and 120mg/kg cinacalcet on plasma adjusted calcium (adj-calcium) measured at 120 minutes post-dose; (B) Effect of 60mg/kg cinacalcet compared to vehicle alone on plasma adjusted calcium (adj-calcium) measured at 120 minutes post-dose; (C) Effect of 0, 30, 60 and 120mg/kg cinacalcet on parathyroid hormone (PTH) measured at 30 minutes post-dose; (D) Effect of 60mg/kg cinacalcet compared to vehicle alone on parathyroid hormone (PTH) measured at 30 minutes post-dose; Mean±SEM values for respective groups NS=non-significant; *p<0.05, **p<0.01; ***p<0.001, ****p<0.0001. One-way ANOVA followed by Sidak's test for pairwise multiple comparisons were used for all analyses.

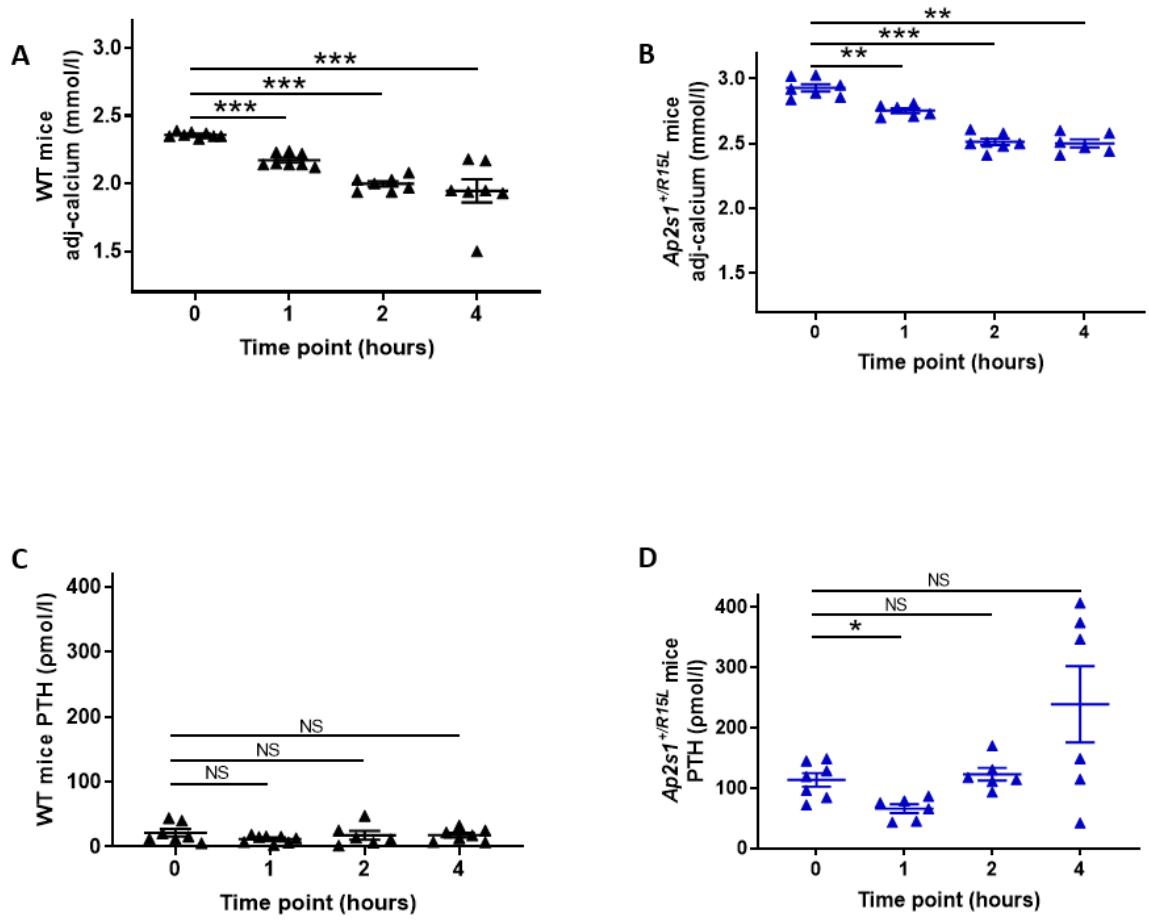


Figure 35. Effect of a single 60 mg/kg bolus of cinacalcet on plasma albumin-adjusted calcium (adj-calcium) and parathyroid hormone (PTH) concentrations at 0, 1, 2 and 4 hours post dose in adult WT (*Ap2s1*$^{+/+}$) and *Ap2s1*$^{+/L15}$ mice, aged 15-22 weeks. (A) plasma albumin-adjusted calcium in WT mice; (B) plasma albumin-adjusted calcium in *Ap2s1*$^{+L15}$ mice; (C) plasma parathyroid hormone (PTH) in WT mice; and (D) plasma parathyroid hormone (PTH) in *Ap2s1*$^{+/L15}$ mice. Mean±SEM values for respective groups (n=6-7 mice per group) are indicated. WT mice are in black, heterozygous *Ap2s1*$^{+/L15}$ mice are in blue. NS, non-significant; *p<0.05, **p<0.01; ***p<0.001, ****p<0.0001 for *Ap2s1*$^{+/L15}$ mice versus WT mice. One-way ANOVA followed by Sidak's test for pairwise multiple comparisons were used for all analyses. Data published in Hannan et al (2021) (243).

7.1.6 Assessment of serum PTH concentrations with increasing mouse age in the *Ap2s1-Arg15Leu* mouse

Plasma adjusted calcium and PTH concentrations were measured in *Ap2s1*$^{+/R15L}$ and WT mice at 8 weeks and 16 weeks old. PTH concentrations and were found to increase significantly

with ageing female *Ap2s1*$^{+/R15L}$ mice, but not the male *Ap2s1*$^{+/R15L}$ mice or WT mice. There was no change in plasma adjusted calcium concentrations with age (Figure 36).

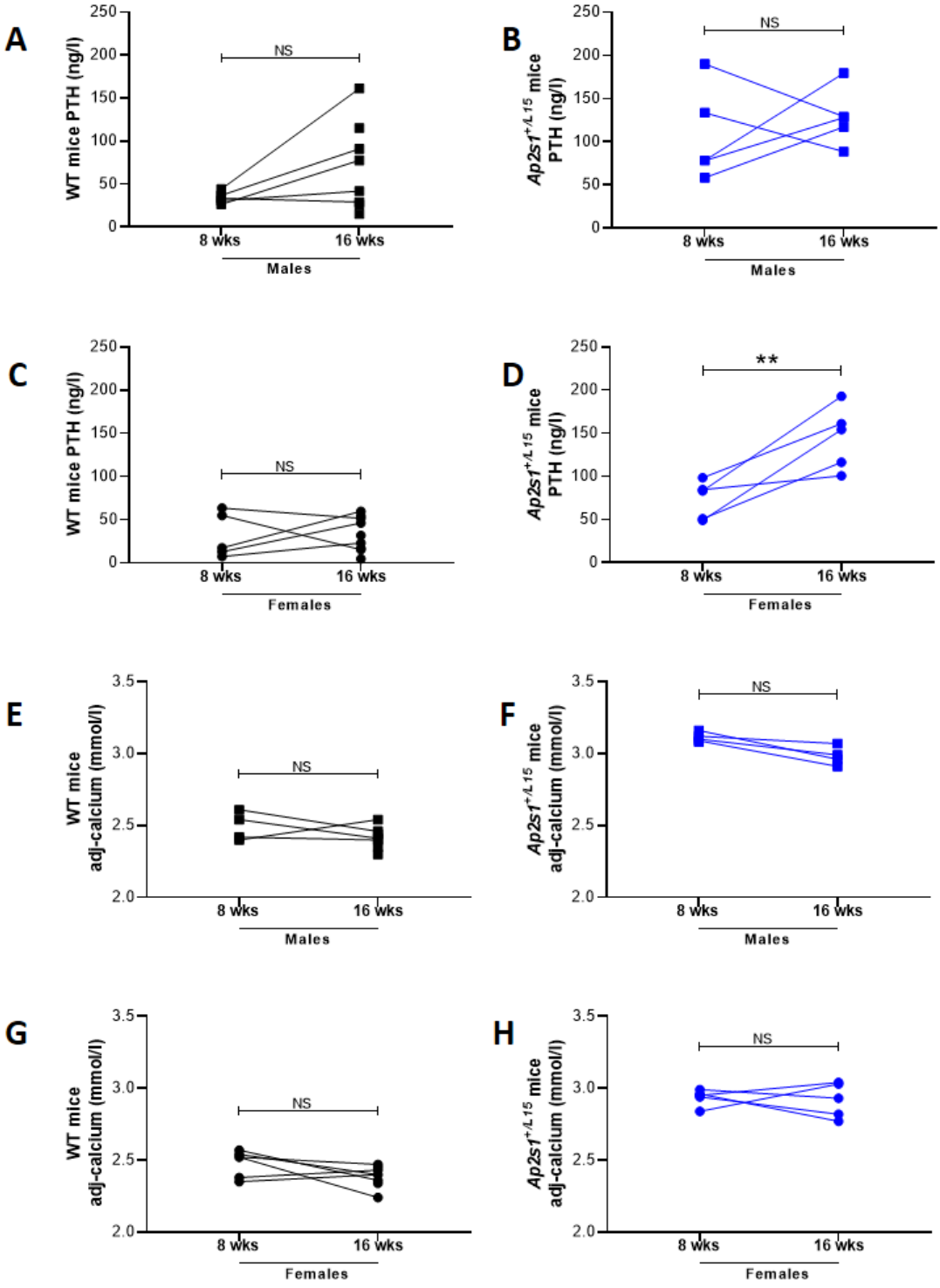


Figure 36. Age-related changes in plasma albumin-adjusted calcium (adj-calcium), and parathyroid hormone (PTH) of WT and *Ap2s1*$^{+/L15}$ mice, each mouse bled at 8 weeks and 16 weeks. Changes in plasma parathyroid hormone (PTH) in (A) male WT mice; (B) male *Ap2s1*$^{+/L15}$ mice; (C) female WT mice; (D) female *Ap2s1*$^{+/L15}$ mice.

Changes in plasma albumin-adjusted calcium in (E) male WT mice; (F) male *Ap2s1*$^{+/L15}$ mice; (G) female WT mice; (H) female *Ap2s1*$^{+/L15}$ mice. Mean±SEM values for respective groups (n=4-9 mice per group) are indicated. WT mice are in black, heterozygous *Ap2s1*$^{+/L15}$ mice are in blue. Males are denoted by squares, females by circles. NS=non-significant; **p<0.01; for *Ap2s1*$^{+/L15}$ mice versus WT mice. One-way ANOVA followed by Sidak's test for pairwise multiple comparisons were used for analysis. Data published in Hannan et al (2021) (243).

7.1.7 Structural analysis of *Ap2s1-Arg15Leu* mouse embryos using micro-CT

As discussed, non-calcitropic abnormalities, including learning difficulties, have been reported in FHH3 patients (Table 6). This is not surprising given that the AP2 complex is ubiquitously expressed and facilitates CME of a wide range of proteins, including but not limited to the CaSR, in most tissues of the body. In support of this, a p.Arg170Trp mutation in *AP2M1*, encoding the μ-subunit of AP2, has recently been identified in 4 individuals with neurodevelopmental disorders and epileptic seizures with functional analysis demonstrating significant impairment of CME (19). It is thus likely that mutations in AP2σ similarly exert their non-calcitropic effects by impairing endocytosis of cargo, such as receptors and adhesion molecules, and may cause physiological effects that have not yet been recognised. To further investigate this, we performed a structural analysis of the *Ap2s1-Arg15Leu* mouse. Only 2 mice with the *Ap2s1*$^{L15/L15}$ genotype survived to adulthood and were therefore not representative of the majority of mice with the homozygous mutation. However, iodine-contrast micro-CT of mouse embryos has been demonstrated to be an ideal method of high throughput analysis of mouse mutants with embryonic and early postnatal lethality (271) and can provide 3D morphological analysis of mouse embryos and neonates between embryonic day 8.5 and postnatal day 3, with high spatial resolution up to 3 μm/voxel (271). We therefore decided to use micro-CT of the *Ap2s1-Arg15Leu* mouse embryos to allow comparison of greater numbers of each genotype at the same developmental stage. 39 mouse embryos from 5 different litters were assessed for analysis at developmental stage E18.5, i.e. 18.5 days post-

coitum with full term being approximately 21 days post-coitum. Of these embryos, one was resorbed before analysis took place, 8 were WT, 20 heterozygous and 9 homozygous for the *Ap2s1-Arg15Leu* mutation (Table 17). A standard protocol to investigate for embryonic structural abnormalities was used in each genotype.

Table 17. Details of the *Ap2s1-Arg15Leu* mouse litters used for structural analysis. 5 litters were included: AP2S1-R15L-EM1-B6-IC/6.1, AP2S1-R15L-EM1-B6-IC/6.2, AP2S1-R15L-EM1-B6-IC/6.3, AP2S1-R15L-EM1-B6-IC/7.1 and AP2S1-R15L-EM1-B6-IC/7.2. These 5 litters produced between 6 and 9 embryos each, 39 mouse embryos in total. Of these, 38 embryos survived to E18.5 for analysis, and one embryo from litter AP2S1-R15L-EM1-B6-IC/6.2 was resorbed prior to analysis. Of the 38 surviving embryos, 8 were confirmed to be WT, 20 were *Ap2s1*$^{+/L15}$ and 9 were *Ap2s1*$^{L15/L15}$.

Litter	Total number of embryos	WT (n=8)	*Ap2s1*$^{+/L15}$ (n=20)	*Ap2s1*$^{L15/L15}$ (n=9)	Resorbant (n=1)
AP2S1-R15L-EM1-B6-IC/6.1	9	2	5	1	0
AP2S1-R15L-EM1-B6-IC/6.2	8	2	5	1	1
AP2S1-R15L-EM1-B6-IC/6.3	9	1	5	2	0
AP2S1-R15L-EM1-B6-IC/7.1	6	2	1	3	0
AP2S1-R15L-EM1-B6-IC/7.2	7	1	4	2	0

7.1.7.1 Embryo sizes

Embryo size can be determined by measuring crown-to-rump length and embryo volume. Embryonic development of inbred C57BL/6 mice has been well characterised and it is expected for there to be a degree of intra- and inter-litter variation in actual stages of embryos where days of gestation are used for staging (272). However, greater variability was seen within the homozygous embryos than within the WT and heterozygous embryos, such that 44% of homozygous mutant embryos were measured to be outside of the expected size range for their gestation (Figure 37). There was no clear difference in the mean embryo lengths or volumes, or the range of measurements, between the WT and *Ap2s1*$^{+/L15}$ embryos. However, there was one clear outlier in the *Ap2s1*$^{L15/L15}$ embryo group which was shorter and 2 that

appear longer than would be expected (Figure 37A). Similarly, when embryo volume was assessed, there was one clear outlier in the *Ap2s1*$^{L15/L15}$ embryo group which was smaller and 3 that appear larger than would be expected (Figure 37B).

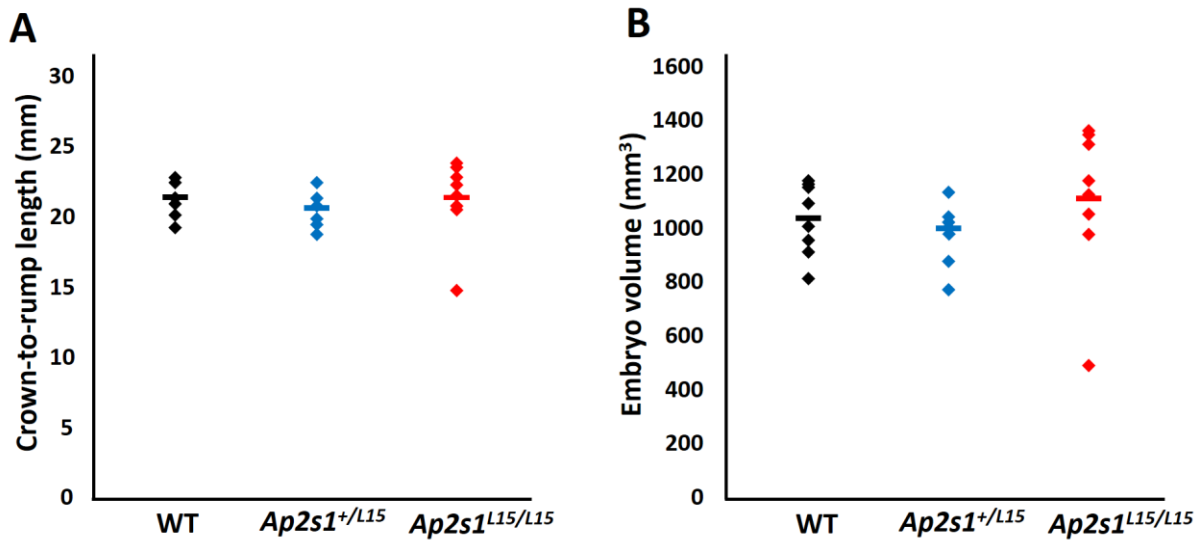


Figure 37. Analysis of WT (black), *Ap2s1*$^{+/L15}$ (blue) and *Ap2s1*$^{L15/L15}$ (red) mouse embryos at E18.5 gestation by micro-CT. Male and female embryos represented by a diamond, mean length shown by a horizontal bar. (A) Crown-to-rump length in millimeters (mm). There is no clear difference in the mean embryo lengths between the genotypes. The distribution of embryo lengths is similar between the genotypes, aside from one clear outlier in the *Ap2s1*$^{L15/L15}$ embryo group which is shorter. (B) Embryo volume in millimeters cubed (mm^3). There is no clear difference in the mean embryo lengths or distribution of lengths between the WT and *Ap2s1*$^{+/L15}$ embryos. Again, there is a clear outlier in the *Ap2s1*$^{L15/L15}$ embryo group which has a lower volume. Otherwise the *Ap2s1*$^{L15/L15}$ embryos have similar or slightly larger volumes than the WT and *Ap2s1*$^{+/L15}$ embryos.

7.1.7.2 Structural analysis of the kidneys in the *Ap2s1-Arg15Leu* mouse model

Cross-sectional imaging of the kidneys was obtained in WT, *Ap2s1*$^{+/L15}$ and *Ap2s1*$^{L15/L15}$ mice micro-CT. Abnormal kidney development was observed in 75% of heterozygous and 77% of homozygous mutant embryos. A representative example of kidney development in each genotype is shown below (Figure 38). The *Ap2s1*$^{+/L15}$ and *Ap2s1*$^{L15/L15}$ mice kidneys do not have

any clear difference in the overall size or shape of the kidneys when compared to the WT mouse kidney. However, the *Ap2s1*$^{+/L15}$ and *Ap2s1*$^{L15/L15}$ mice did have visibly dilated renal pelvises and calices when compared to the WT mouse, with this dilation more pronounced in the *Ap2s1*$^{L15/L15}$ mouse than the *Ap2s1*$^{+/L15}$ mouse (Figure 38).

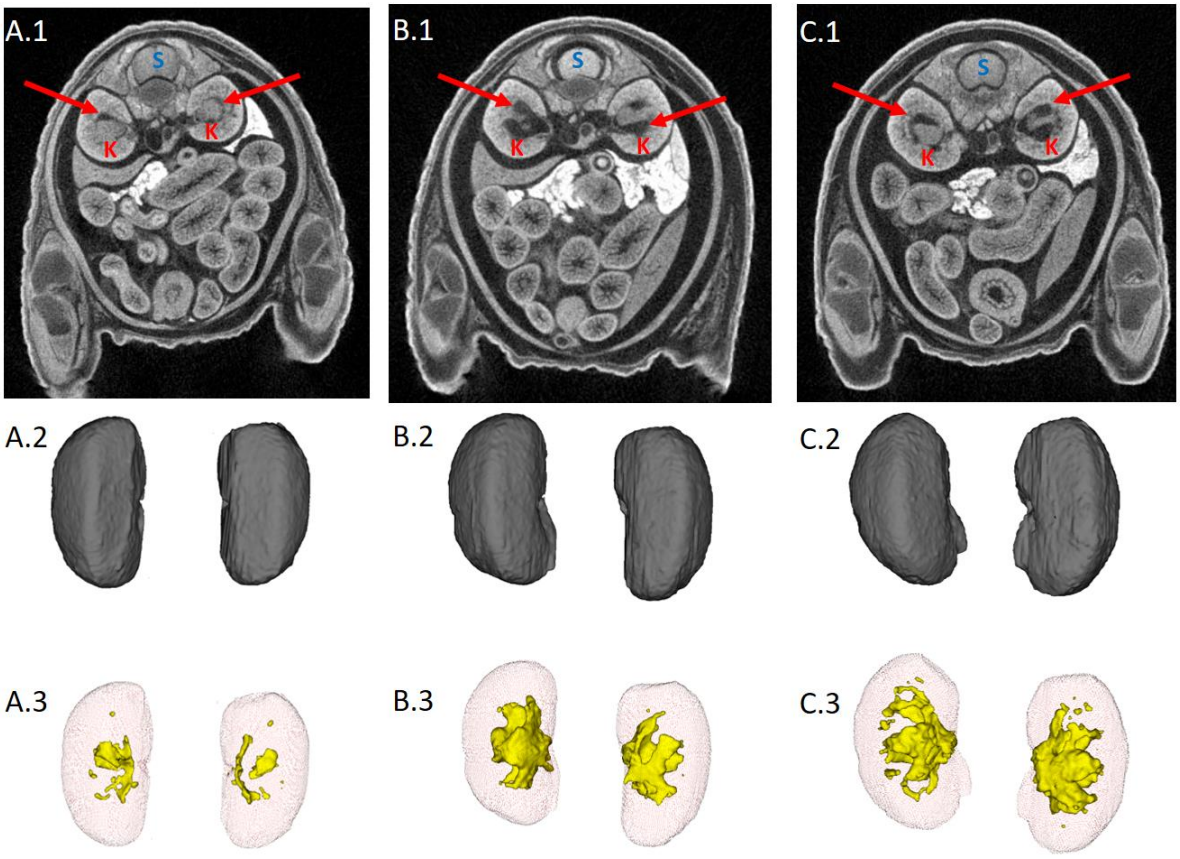


Figure 38. A representative example of cross-sectional imaging of a WT (A), *Ap2s1*$^{+/L15}$ (B), and *Ap2s1*$^{L15/L15}$ (C) mouse obtained through 3-dimensional micro-CT. K (red) =kidney, S (blue) =spine, red arrow=renal calices. Images A-C.1 are 2-dimensional axial views obtained through micro-CT. Images A-C.2 and A-C.3 are 3-dimensional reconstructions of the mouse kidneys in the coronal view obtained from 3-dimensional micro-CT. A-C.2 show the gross morphology of the kidney which allows computerised estimation of the total kidney volume. A-C.3 are 3-dimensional reconstructions of the renal pelvis and calices (yellow). Images A.1-3 show the normal appearance of the kidneys in WT mice. B.1 demonstrates visibly enlarged renal calices (red arrows) in the *Ap2s1*$^{+/L15}$ mice when compared to those in the WT mice. B.2 demonstrates no visible change in kidney size or shape in the *Ap2s1*$^{+/L15}$ mice when compared to those in the WT mice. B.3 demonstrates visibly enlarged renal calices (yellow) in the *Ap2s1*$^{+/L15}$ mice when compared to those in the WT mice. C.1 demonstrates visibly enlarged

renal calices (red arrows) in the *Ap2s1*$^{L15/L15}$ mice when compared to those in the WT mice. Comparison to the *Ap2s1*$^{+/L15}$ mice shows no clear difference. C.2 demonstrates no visible change in kidney size or shape in the *Ap2s1*$^{+/L15}$ mice when compared to those in the WT mice or the *Ap2s1*$^{+/L15}$ mice. C.3 demonstrates visibly enlarged renal calices (yellow) in the *Ap2s1*$^{L15/L15}$ mice when compared to those in the WT mice. They are also visibly larger than those seen in the *Ap2s1*$^{+/L15}$ mice. This difference is not as clear when comparing the image in C.2 to that in B.2, suggesting that the 2-dimensional appearance is affected by the particular plane of imaging.

7.1.7.3 Structural analysis of the brain in the *Ap2s1-Arg15Leu* mouse model

Cross-sectional imaging of the brain was obtained in WT, *Ap2s1*$^{+/L15}$ and *Ap2s1*$^{L15/L15}$ mice using 3-dimensional micro-CT. Abnormal brain ventricle development was observed in 37% of *Ap2s1*$^{+/L15}$ mice and 44% of *Ap2s1*$^{L15/L15}$ mice. An enlarged subarachnoid space was observed in 55% of homozygous embryos. A representative example of the brain development in each genotype is shown below (Figure 39). The *Ap2s1*$^{+/L15}$ mouse appears to have enlarged ventricles and interhemispheric CSF spaces and an increased posterior CSF space when compared to the WT mouse. The *Ap2s1*$^{L15/L15}$ mouse has grossly increased anterior, lateral and posterior CSF spaces when compared to the WT and *Ap2s1*$^{+/L15}$ mice. The volume of brain parenchyma appeared to be diminished making a direct comparison of the size of the ventricles and interhemispheric CSF spaces between the *Ap2s1*$^{L15/L15}$ mouse and the WT and *Ap2s1*$^{+/L15}$ mice difficult. However, the maintained / enlarged size of the ventricles and interhemispheric CSF spaces suggests that they are not affected by pressure from the grossly enlarged anterior, lateral and posterior CSF spaces (Figure 39).

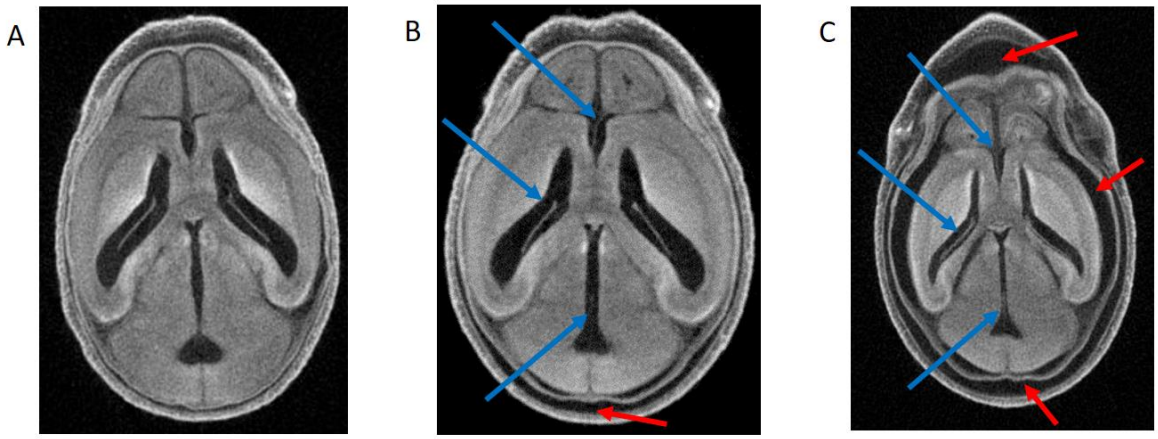


Figure 39. A representative example of coronal brain imaging in a WT (A), *Ap2s1*$^{+/L15}$ (B), and *Ap2s1*$^{L15/L15}$ (C) mouse obtained through 3-dimensional micro-CT. Image A shows the normal appearance of the brain, ventricles and CSF spaces in a WT mouse. Image B demonstrates visibly enlarged ventricles and interhemispheric CSF space (blue arrows) and an increased posterior CSF space (red arrow) in an *Ap2s1*$^{+/L15}$ mouse when compared to a WT mouse. Image C demonstrates grossly increased anterior, lateral and posterior CSF spaces (red arrows) in the *Ap2s1*$^{L15/L15}$ mouse when compared to the WT and *Ap2s1*$^{+/L15}$ mice. The volume of brain parenchyma appears to be diminished.

7.2 CRISPR-Cas-induced *Ap2s1* mutant Arg15Cys mice

7.2.1 Generation of Arg15Cys mice

Mutant mice harbouring p.Arg15Cys in the *Ap2s1* gene were generated on a C57BL/6J strain background using CRISPR–Cas9 system system, as reported (239, 267) and described in Figure 18 and Figure 19 with Arg15Cys being the mutation being introduced. Mice were genotyped by analysing ear biopsy DNA using allelic discrimination (245) to confirm their mutation carrying status. The observed number of offspring born did not differ from the expected Mendelian inheritance ratio of 1:2:1 for WT: *Ap2s1*$^{+/C15}$: *Ap2s1*$^{C15/C15}$ offspring (χ^2=4.82, p=0.090), however it did differ significantly at weaning (χ^2=6.48, p=0.039) and at adulthood (χ^2=7.64, p=0.022). Unlike the mice homozygous for the Arg15Leu mutation, sufficient

numbers of *Ap2s1*$^{C15/C15}$ mice reached adulthood to allow a complete phenotypic assessment (Table 18).

Table 18. The proportion of offspring bred from crosses of *Ap2s1*$^{+/C15}$ x *Ap2s1*$^{+/C15}$ mice observed at birth, weaning and adulthood, *p<0.05 (by Chi-squared analysis). Blue denotes a lower than expected value.

Genotype	Number of offspring observed at birth (n=180)	Number of offspring observed at weaning (~3 weeks old) (n=152)	Number of offspring observed at adulthood (>10 weeks old) (n=144)
WT	68 (38%)	58 (38%)	56 (39%)
Ap2s1$^{+/C15}$	83 (46%)	75 (49%)	70 (49%)
Ap2s1$^{C15/C15}$	29 (16%)	19 (13%)*	18 (12%)*

7.2.2 Arg15Cys mouse biochemical phenotype

Male and female *Ap2s1*$^{+/C15}$ mice exhibited abnormalities of their calcitropic biochemistry consistent with the human FHH3 phenotype, and the previously described *Ap2s1*$^{+/L15}$ mouse phenotype. They had a marked hypercalcaemia, elevated PTH (although this did not reach significance), increased plasma ALP and plasma magnesium (significant in males only) concentrations when compared to WT mice; plasma phosphate was decreased in mutant mice. As with the *Ap2s1*$^{+/R15L}$ mouse, only the females showed significantly lower urinary CCCR values, consistent with the human FHH3 phenotype, with no significant difference seen in 24 hour urinary calcium excretion values between *Ap2s1*$^{+/R1C}$ and WT mice (Figure 40, Table 19). The *Ap2s1*$^{C15/C15}$ mice showed a more severe phenotype than their *Ap2s1*$^{+/C15}$ counterparts. Plasma albumin-adjusted calcium was significantly higher in both sexes, with a significant difference also seen in phosphate, magnesium and ALP concentrations of male mice only (Figure 40, Table 19). Female *Ap2s1*$^{C15/C15}$ had higher total cholesterol concentrations than their WT littermates, and both *Ap2s1*$^{+/C15}$ and *Ap2s1*$^{C15/C15}$ mice had significantly higher plasma urea concentrations than WT mice (Table 19).

Table 19 . Age, body weight, calcitropic biochemistry and non-calcitropic biochemistry of adult WT, *Ap2s1*$^{+/C15}$, and *Ap2s1*$^{C15/C15}$ mice, aged 15-17 weeks. [A]plasma albumin--adjusted calcium; [B]Glucose and lipid concentrations were measured in non-fasting plasma samples; PTH=plasma parathyroid hormone; ALP=plasma alkaline phosphatase; CCCR=24 hour urine calcium:creatinine clearance ratio; ALT=alanine aminotransferase; AST=aspartate aminotransferase; HDL-c=HDL cholesterol; LDL-c=LDL cholesterol. Red denotes a higher than expected value; blue denotes a lower than expected value. All values are expressed as mean ± SEM. [a]mice vs respective WT mice, [b] *Ap2s1*$^{C15/C15}$ mice vs respective *Ap2s1*$^{+/C15}$ mice. *p<0.05; **p<0.01; ***p<0.001; ****p<0.0001. One-way ANOVA followed by Sidak's test for pairwise multiple comparisons were used for all analyses.

	Male			Female		
	WT	***Ap2s1*$^{+/C15}$**	***Ap2s1*$^{C15/C15}$**	**WT**	***Ap2s1*$^{+/C15}$**	***Ap2s1*$^{C15/C15}$**
Age (weeks)	16.1±0.5 (n=5)	15.3±0.3 (n=10)	15.1±0.8 (n=3)	16.8±0.9 (n=8)	15.8±0.4 (n=8)	16.4±0.4 (n=7)
Weight (g)	31.6±1.1 (n=5)	30.5±0.8 (n=10)	24.4±1.6 (n=3)[a**, b**]	24.3±0.4 (n=8)	23.0±0.4 (n=8)	21.2±0.8 (n=7)[a**]
Calcitropic biochemistry - plasma:						
Adj-calcium (mmol/L)[A]	2.32±0.03 (n=5)	2.72±0.02 (n=10)[a****]	3.20±0.01 (n=3)[a****, b****]	2.32±0.02 (n=8)	2.76±0.05 (n=8)[a****]	3.27±0.02 (n=7)[a****, b****]
PTH (ng/L)	92.9±0.8 (n=4)	147.6±55.5 (n=10)	359.6±195.2 (n=3)[a*]	47.21±14.5 (n=5)	120.0±21.6 (n=8)	157.1±38.5 (n=6)[a**]
Phosphate (mmol/L)	1.76±0.10 (n=5)	1.46±0.06 (n=10)[a*]	1.20±0.06 (n=3)[a**]	2.11±0.17 (n=8)	1.39±0.14 (n=8)[a**]	1.51±0.13 (n=7)[a*]
Magnesium (mmol/L)	0.94±0.03 (n=5)	1.08±0.02 (n=10)[a**]	1.23±0.04 (n=3)[a***, b*]	1.10±0.04 (n=8)	1.18±0.03 (n=8)	1.35±0.05 (n=7)[a***, b*]
ALP (U/L)	78.0±3.5 (n=5)	91.9±2.5 (n=10)[a*]	139.7±3.2 (n=3)[a****, b****]	113.3±7.4 (n=8)	133.3±5.1 (n=8)	146.6±6.0 (n=7)[a**]
Calcitropic biochemistry - urine:						
Total urine volume (ml)	3.5±0.6 (n=5)	2.9±0.3 (n=8)	3.1±1.0 (n=3)	4.0±0.6 (n=8)	3.9±0.8 (n=8)	4.7±0.6 (n=7)
Urine CCCRx10^3	2.9±0.7 (n=5)	2.3±0.3 (n=8)	1.9±0.4 (n=4)	4.3±0.7 (n=4)	2.2±0.3 (n=8)[a***]	1.6±0.2 (n=8)[a****]
24h calcium excretion (µmol/24h)	4.87±0.8 (n=5)	4.21±0.6 (n=8)	3.10±0.1 (n=3)	5.88±0.8 (n=8)	5.71±1.2 (n=8)	5.53±1.0 (n=7)
Electrolytes and renal:						
Sodium (mmol/l)	145.4±0.8 (n=5)	145.8±0.3 (n=10)	146.0±0 (n=3)	144.5±0.63 (n=8)	144.1±0.5 (n=8)	143.3±0.5 (n=7)
Potassium (mol/l)	4.8±0.2 (n=5)	5.0±0.1 (n=10)	4.8±0.3 (n=3)	4.6±0.1 (n=8)	4.6±0.1 (n=8)	4.5±0.1 (n=7)
Urea (mmol/l)	11.9±0.9 (n=5)	10.0±0.5 (n=10)	11.9±0.9 (n=3)	13.3±0.8 (n=8)	10.2±0.7 (n=8)[a**]	9.6±0.5 (n=7)[a**]
Creatinine (µmol/l)	11.1±1.2 (n=5)	18.9±0.5 (n=10)	13.5±1.0 (n=3)	13.7±0.9 (n=8)	12.8±0.5 (n=8)	13.7±0.4 (n=7)
Glucose and lipids[B]:						
Glucose (mmol/L)	15.3±1.2 (n=5)	14.21±0.6 (n=10)	15.7±0.2 (n=3)	14.5±0.6 (n=8)	15.7±0.6 (n=8)	16.9±0.8 (n=7)

Total cholesterol (mmol/L)	2.02±0.19 (n=5)	1.82±0.15 (n=10)	1.74±0.02 (n=3)	2.02±0.07 (n=7)	1.93±0.03 (n=7)	1.55±0.08 (n=7)[a***]
LDL-c (mmol/L)	0.4±0.0 (n=5)	0.3±0.0 (n=10)	0.3±0.0 (n=3)	0.4±0.0 (n=8)	0.4±0.0 (n=8)	0.4±0.0 (n=7)
HDL-c (mmol/L)	1.4±0.2 (n=5)	1.3±1.1 (n=10)	1.2±0.1 (n=3)	1.2±0.1 (n=8)	1.2±0.1 (n=8)	1.0±0.1 (n=7)
Triglycerides (mmol/L)	1.0±0.1 (n=5)	0.9±0.1 (n=10)	1.0±0.2 (n=3)	0.9±0.1 (n=8)	0.9±0.1 (n=8)	0.8±0.1 (n=7)
Liver:						
Total bilirubin (μmol/L)	2.4±0.4 (n=5)	3.4±0.3 (n=10)	2.7±1.0 (n=3)	2.1±0.1 (n=8)	2.9±0.3 (n=8)	2.2±0.3 (n=7)
ALT (U/L)	38.2±2.7 (n=5)	46.1±4.3 (n=10)	53.0±10.1 (n=3)	33.0±2.2 (n=8)	34.3±4.8 (n=7)	31.0±1.8 (n=6)
AST (U/L)	58.8±7.5 (n=5)	75.4±7.6 (n=10)	77.3±28.4 (n=3)	67.9±7.2 (n=7)	68.4±8.8 (n=8)	73.0±9.7 (n=7)

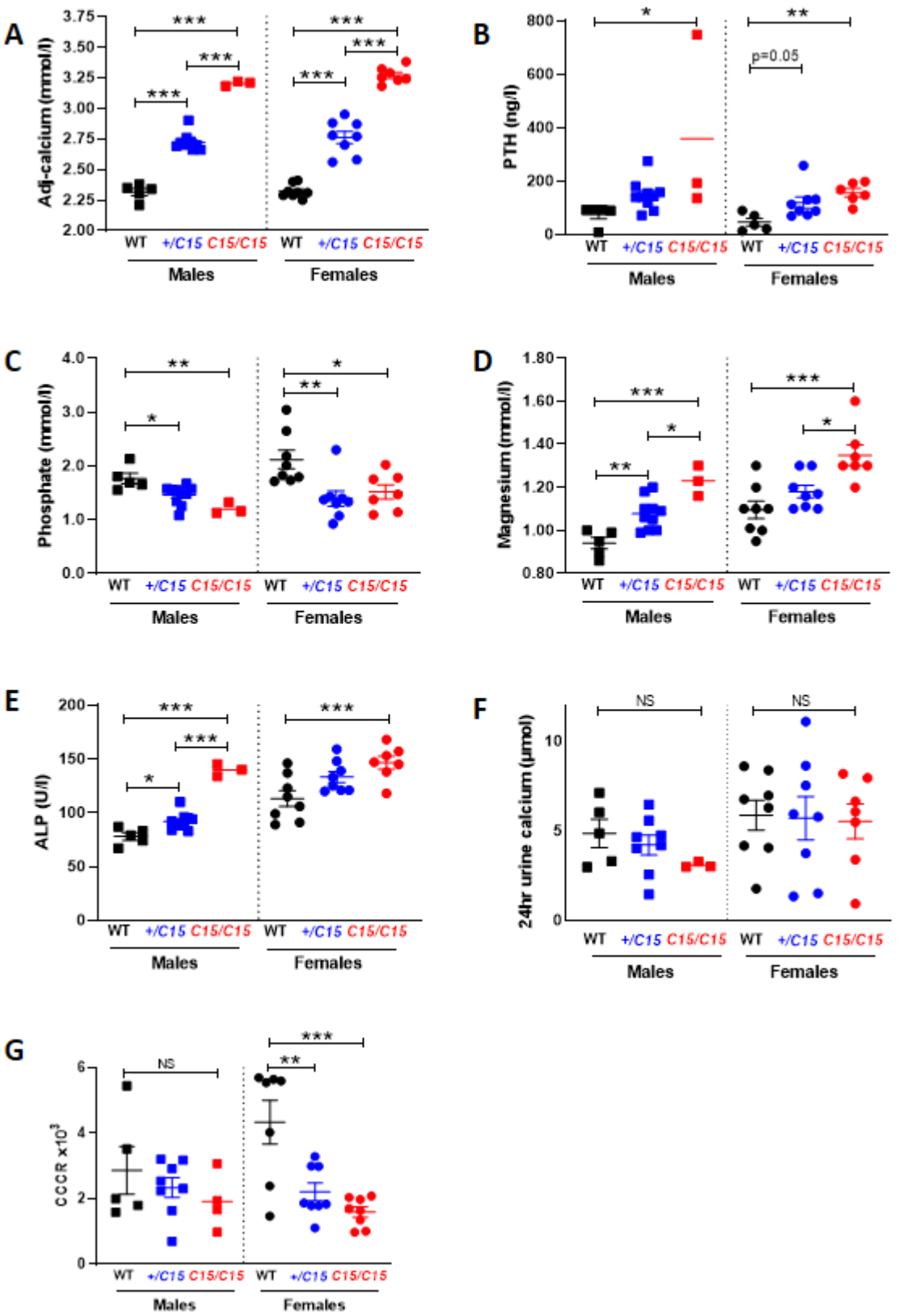


Figure 40. Calcitropic phenotype of adult WT, *Ap2s1*$^{+/C15}$ and *Ap2s1*$^{C15/C15}$ mice, aged 14-18 weeks. (A) plasma albumin-adjusted calcium (adj-calcium); (B) plasma parathyroid hormone (PTH); (C) plasma phosphate; (D) plasma magnesium; (E) plasma alkaline phosphatase (ALP); (F) 24 hour urine calcium;

and (G) calcium:creatinine clearance ratio (CCCR) x10^3. Males are denoted by squares, females by circles. WT *Ap2s1*$^{+/+}$ mice are in black, heterozygous *Ap2s1*$^{+/C15}$ (*C+/*C15) mice are in blue and homozygous *Ap2s1*$^{C15/C15}$ (*C15/*C15) mice are in red. Mean ±SEM values for respective groups (n=3-10 mice per group) are indicated. NS, non-significant; *p<0.05, **p<0.01; ***p<0.001, ***p<0.0001 for *Ap2s1*$^{+/C15}$ mice versus respective WT mice, *Ap2s1*$^{C15/C15}$ mice versus respective WT mice, and *Ap2s1*$^{C15/C15}$ mice versus respective *Ap2s1*$^{+/C15}$ mice. One-way ANOVA followed by Sidak's test for pairwise multiple comparisons were used for all analyses.

7.2.3 Arg15Cys mouse bone phenotyping

Bone metabolism was assessed by whole body dual-energy X-ray absorptiometry (DEXA), and by measurement of the pro-collagen type 1 N-terminal pro-peptide (P1NP) bone turnover marker. There was no difference found in Bone Mineral Content (BMC) corrected for body weight, Bone Mineral Density (BMD) or P1NP concentrations between the *Ap2s1*$^{+/C15}$ and WT mice (Table 20). However, male *Ap2s1*$^{C15/C15}$ mice had a significantly lower BMD than both *Ap2s1*$^{+/C15}$ and WT mice, and female *Ap2s1*$^{C15/C15}$ had a significantly lower BMD than WT littermates (Table 20).

Table 20. Whole body dual-energy X-ray absorptiometry (DXA) analysis of WT, *Ap2s1*$^{+/C15}$ mice and *Ap2s1*$^{C15/C15}$ mice, aged 15-17 weeks. BMC=bone mineral content; BMD=bone mineral density. [A]Corrected for body weight. Blue denotes a lower than expected value. All values are expressed as mean±SEM. [a]mice vs respective WT mice, [b] *Ap2s1*$^{C15/C15}$ mice vs respective *Ap2s1*$^{+/C15}$ mice. *p<0.05; **p<0.01. One-way ANOVA followed by Sidak's test for pairwise multiple comparisons were used for all analyses.

	Male			Female		
	WT	***Ap2s1*$^{+/C15}$**	***Ap2s1*$^{C15/C15}$**	**WT**	***Ap2s1*$^{+/C15}$**	***Ap2s1*$^{C15/C15}$**
BMC[A] (mg/g)	22.1±0.8 (n=5)	20.0±0.4 (n=9)	19.7±0.7 (n=3)	24.5±1.3 (n=7)	23.9±0.8 (n=8)	21.5±0.6 (n=7)
BMD (mg/cm^2)	72.7±2.0 (n=5)	71.3±0.8 (n=10)	64.4±3.5 (n=3)[a*b*]	71.6±1.7 (n=8)	67.1±1.3 (n=8)	63.9±0.9 (n=7)[a**]
Fat mass (%)	15.2±3.1 (n=5)	12.5±0.7 (n=9)	11.8±2.3 (n=3)	15.6±1.6 (n=7)	15.1±1.3 (n=8)	12.6±0.9 (n=7)

7.2.4 Assessment of serum PTH concentrations with increasing mouse age

Plasma adjusted calcium and PTH concentrations were measured twice in WT, *Ap2s1*$^{+/C15}$ and *Ap2s1*$^{C15/C15}$ mice, once at 8 weeks and once at 16 weeks old in each mouse. PTH concentrations and were found to be significantly increased with ageing in the *Ap2s1*$^{+/C15}$ and *Ap2s1*$^{C15/C15}$ mice, but not the WT mice (Figure 41). This is consistent with the findings in *Ap2s1*$^{+/C15}$ mice and recapitulates the human phenotype seen in one FHH3 kindred with an Arg15Cys mutation (20, 193, 194).

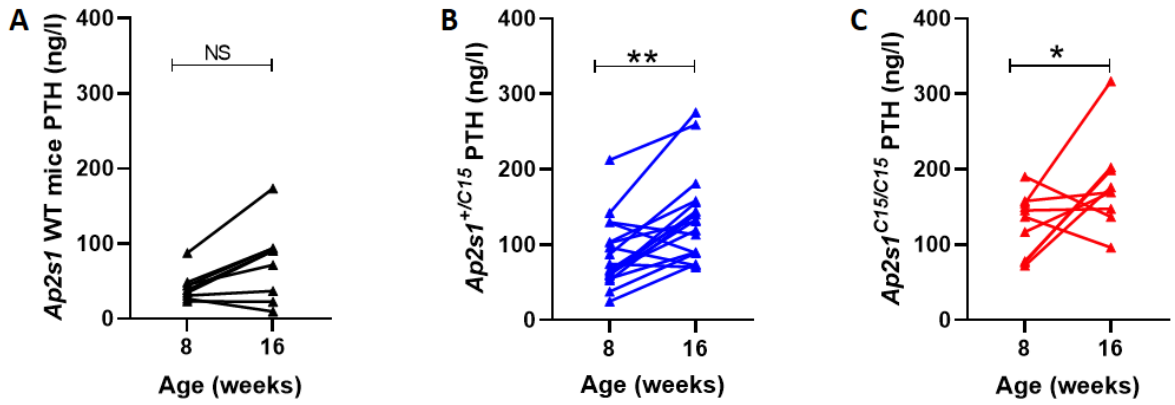


Figure 41. Age-related changes in serum parathyroid hormone (PTH) of (A) WT; (B) *Ap2s1*$^{+/C15}$ mice; and (C) *Ap2s1*$^{C15/C15}$ mice. Mean±SEM values for respective groups (n=8-18 male and female mice per group) are indicated. WT mice are in black; heterozygous *Ap2s1*$^{+/C15}$ mice are in blue; and homozygous *Ap2s1*$^{C15/C15}$ mice are in red. NS, non-significant; *p<0.05; **p<0.01; for mice at 16 weeks old versus 8 weeks old. One-way ANOVA followed by Sidak's test for pairwise multiple comparisons were used for analysis.

7.3 CRISPR-Cas-induced *Ap2s1* mutant Met117Ile mice

7.3.1 Generation of Met117Ile mice

We generated the *Ap2s1-Met117Ile* mouse model to further investigate the novel AP2σ variant, Met117Ile, associated with reduced intracellular calcium signalling *in vitro* and with

hypercalcaemia in a patient (260) described in chapter 6. Mutant mice harbouring c.350G>T p.Met117Ile in the *Ap2s1* gene were generated on a C57BL/6J strain background using CRISPR–Cas9 system, as reported (239, 267) and described in Figure 18 with Met117Ile as the mutation to be introduced. Once germ line transmission of *Ap2s1-Met117Ile* was achieved, a colony of 70 mice was established by crossing heterozygous affected (*Ap2s1*$^{+/I117I}$) mice as described in Figure 19. Mice were genotyped using real time quantitative PCR (273) to confirm their mutation carrying status.

The *Ap2s1*$^{+/I117}$ mice were healthy and fertile and the proportion of weaned offspring did not deviate significantly from the Mendelian inheritance expected ratio of 1:2:1 for the WT, *Ap2s1*$^{+/I117}$ and *Ap2s1*$^{I117/I117}$ genotypes (Table 21). All mice appeared phenotypically normal and there was no difference in the weights of the different genotypes (Table 24), which indicated that the homozygous *Ap2s1*$^{I117/I117}$ were viable with no embryonic or neonatal lethality.

Table 21. Proportion of offspring bred from crosses of *Ap2s1*$^{+/I117}$ x *Ap2s1*$^{+/I117}$ mice. Heterozygous crosses led to the expected Mendelian inheritance ratio of 1:2:1 for WT : *Ap2s1*$^{+/I117}$: *Ap2s1*$^{I117/I117}$ offspring at weaning. Chi-square analysis shows that the proportion of offspring do not differ from those expected (p=0.61).

Genotype	**Expected number of offspring (n=149 at weaning)**	**Observed number of offspring (n=149 at weaning)**
WT	37.25 (25%)	31 (21%)
Ap2s1$^{+/I117}$	74.5 (50%)	75 (50%)
Ap2s1$^{I117/I117}$	37.25 (25%)	43 (29%)

7.3.2 Met117Ile mouse biochemical phenotype

The mice underwent plasma biochemical analysis. This revealed that *Ap2s1*$^{+/I117}$ and *Ap2s1*$^{I117/I117}$ mice were not significantly hypercalcaemic when compared to WT mice. In addition, their plasma PTH and phosphate concentrations did not differ significantly, and there was no significant difference in the fractional excretion of calcium between the

genotypes (Table 22). Thus, *Ap2s1-Met117Ile* mutant mice do not recapitulate the human FHH3 calcitropic phenotype. In addition, no significant differences were seen in plasma ALP, magnesium, sodium, potassium, urea and creatinine between the groups, and there was no significant difference in bone mineral density (Table 22).

Table 22. Age, body weight, calcitropic phenotyping and non-calcitropic phenotyping of adult WT, *Ap2s1*$^{+/I117}$, and *Ap2s1*$^{I117/I117}$ mice, aged 15-17 weeks. [A]plasma adjusted calcium; PTH=plasma parathyroid hormone; ALP=plasma alkaline phosphatase; CCCR=24 hour urine calcium:creatinine clearance ratio; BMD=bone mineral density. All values are expressed as mean±SEM. There is no significant difference for any result between *Ap2s1*$^{+/I117}$ mice versus respective WT mice and *Ap2s1*$^{I117/I117}$mice versus respective WT mice. One-way ANOVA followed by Sidak's test for pairwise multiple comparisons were used for all analyses.

	Male			**Female**		
	WT (n=9)	***Ap2s1*$^{+/I117}$ (n=10)**	***Ap2s1*$^{I117I/I117}$ (n=10)**	**WT (n=7)**	***Ap2s1*$^{+/I117}$ (n=4)**	***Ap2s1*$^{I117I/I117}$ (n=8)**
Age (weeks)	16.5±0.6	15.76±0.08	15.7±0.1	15.8±0.1	15.6±0.1	15.7±0.1
Weight (g)	29.7±0.6	29.7±0.4	29.3±0.4	23.1±0.4	23.0±0.5	22.9±0.4
Calcitropic phenotyping:						
Adj-calcium (mmol/L)[A]	2.3±0	2.3±0	2.3±0	2.3±0	2.3±0	2.3±0
PTH (ng/L)	70.9±13.2	99.1±22.7	101.9±12.7	32.9±4.9	35.0±7.5	54.6±15.8
Phosphate (mmol/L)	1.75±0.1	2.0±0.1	88.2±2.9	1.8±0.1	1.7±0	1.8±0.1
Magnesium (mmol/L)	1.1±0	1.0±0	1.9±0.1	1.2±0	1.2±0.1	1.2±0.1
ALP (U/L)	87.3±4.3	93.3±3.7	88.2±2.9	122.7±4.7	133.3±3.4	130.6±2.1
Urine CCCRx10^3	1.7±0.26	2.0±0.2	1.8±0.3	3.5±0.5	3.5±0.7	2.8±0.3
BMD (g/cm^2)	0.07±0	0.07±0	0.07±0	0.07±0	0.07±0	0.07±0
Non-calcitropic phenotyping:						
Sodium (mmol/l)	146.4±1.0	146.6±0.9	147±0.9	145.6±0.5	146.8±0.6	143.1±1.8
Potassium (mol/l)	4.6±0.1	4.6±0.1	4.6±0.1	5.2±0.3	5.0±0.4	4.9±0.2
Urea (mmol/l)	11.7±0.6	12.1±0.6	12.1±0.4	9.8±0.5	11.7±0.8	10.5±0.3
Creatinine (µmol/l)	9.0±0.4	10.5±0.6	9.7±0.6	12.0±0.9	10.5±0.8	10.5±0.5

7.4 Evaluation of the Arg15Leu, Arg15Cys and Met117Ile mice as *in vivo* models of FHH3

In order to evaluate the mouse lines as models of FHH3, it would be useful to know how each line compares to the other, as the Arg15Leu mutation is associated with a more severe phenotype than the Arg15Cys mutation, and little is known about the phenotype of Met117Ile in humans. Clearly, results of a comparison between these groups should be interpreted with caution as the experiments were not set up to facilitate this. However, the mice were all from the same background (C57BL/6J) and results were obtained using standard protocols across the groups. For the purposes of this comparison, all mutant groups were compared against a single group of WT mice. This is not ideal as in usual circumstances the best comparator is WT littermates. The results of calcitropic testing from the WT littermates of each of the Ap2s1 mutant strains *Ap2s1-Met117Ile*, *Ap2s1-Arg15Cys* and *Ap2s1-Arg15Leu*, were compared with each other to look for significant differences between the groups. The results showed that there was no difference in mouse ages, plasma adjusted-calcium, PTH, phosphate, or ALP concentrations between the 3 strains. However, the *Ap2s1-Arg15Leu* WT mice were slightly smaller than the *Ap2s1-Arg15Cys* WT mice. Additionally, serum magnesium concentrations were higher in the *Ap2s1-Met117Ile* WT mice than the *Ap2s1-Arg15Leu* WT mice, and the *Ap2s1-Arg15Cys* WT mice had significantly higher urinary CCCR results than the *Ap2s1-Met117Ile* and *Ap2s1-Arg15Leu* WT mice. These differences are likely to reflect variation in experimental conditions.

Table 23. Comparison of the calcitropic phenotype of adult male and female WT mice from each of the 3 strains of *Ap2s1-mutant* mice generated: *Ap2s1-Met117Ile*, *Ap2s1-Arg15Cys*, *Ap2s1-Arg15Leu*. Adj-calcium=plasma albumin-adjusted calcium; PTH=parathyroid hormone; ALP= plasma alkaline phosphatase; CCCR= calcium:creatinine clearance ratio; DXA=whole body dual-energy X-ray absorptiometry; and BMD=bone mineral density. Mean±SEM values for respective groups (n=10-24 mice per group) are indicated.*p<0.05, **p<0.01; ****p<0.0001 for result versus [a]*Ap2s1-Met117Ile*, [b]*Ap2s1-Arg15Cys* [c]*Ap2s1-Arg15Leu*. One-way ANOVA followed by Sidak's test for pairwise multiple comparisons were used for all analyses.

	Mouse strain		
	Ap2s1-Met117Ile (n=16)	***Ap2s1-Arg15Cys*** (n=13)	***Ap2s1-Arg15Leu*** (n=23-24)
Age (weeks)	16.2±0.4	16.5±0.3	16.5±0.1
Weight (g)	26.8±0.9	27.1±1.1[c*]	26.9±0.7[b*]
Plasma biochemistry:			
Adj-calcium (mmol/l)	2.29±0.02	2.32±0.02	2.33±0.01
PTH (ng/l)	54.3±9.0	61.7±11.5	57.5±7.9
Phosphate (mmol/l)	1.76±0.06	1.98±0.12	1.74±0.06
Magnesium (mmol/l)	1.12±0.03[c*]	1.04±0.03	1.02±0.02[a*]
ALP (U/l)	102.8±5.5	99.7±6.8	103.1±4.1
Urine biochemistry:			
CCCR x10^3	2.3±0.3[b**]	3.7±0.5[a**, c****]	1.7±0.2[b****]
DXA:			
BMD (mg/cm^2)	-	72.0±1.2	73.0±0.9

Calcitropic phenotype data for male and female mice combined was compared between heterozygous and homozygous affected mouse mutants from each of the 3 mouse models, Arg15Leu, Arg15Cys and Met117Ile, against WT mouse data (Figure 42, Table 24). WT mouse data from the *Ap2s1-Arg15Leu* WT mice mouse strain was used for all plasma biochemistry as this dataset had the fewest outlying results when compared to the other groups, i.e. in the *Ap2s1-Met117Ile* WT mice the plasma magnesium was higher than in the *Ap2s1-Arg15Leu* WT mice only (and this only just reached significance); whereas in the *Ap2s1-Arg15Cys* WT mice the urinary CCCR was significantly higher than in both the *Ap2s1-Arg15Leu* WT mice and *Ap2s1-Met117Ile* WT mice; and the *Ap2s1-Arg15Leu* WT mice were significantly smaller than the *Ap2s1-Arg15Cys* WT mice. As BMD data was not available for the *Ap2s1-Met117Ile* mouse

strain, the data from the *Ap2s1-Arg15Leu* WT mice was used for comparison. Available data from the 2 male *Ap2s1*$^{L15/L15}$ mice surviving to adulthood was plotted for comparison.

Statistical comparison was made between the *Ap2s1*$^{+/C15}$, *Ap2s1*$^{+/L15}$ and *Ap2s1*$^{+/I117}$ mice. With the exception of the *Ap2s1*$^{+/I117}$ mouse, which was slightly older and heavier, there was no significant differences between the ages and weights of the mice at the time of sampling (Table 24). *Ap2s1*$^{+/L15}$ mice had significantly higher plasma calcium concentrations than *Ap2s1*$^{+/C15}$ mice and therefore demonstrated the same genotype:phenotype correlation seen in FHH3 patients. Both of the Arg15 mutant mice, *Ap2s1*$^{+/C15}$ and *Ap2s1*$^{+/L15}$, had higher plasma calcium concentrations than the *Ap2s1*$^{+/I117}$ mouse which did not differ from the WT.

The *Ap2s1*$^{+/L15}$ mice had significantly lower urine CCCR than the *Ap2s1*$^{+/C15}$ mice. This finding is not seen in FHH3 patients where there is no significant difference in urine CCCR between the different genotypes (192), and may be explained by the fact that the *Ap2s1-Arg15Cys* WT mice had significantly higher CCCR results than the WT mice from the other 2 strains, reflecting inconsistency in experimental conditions. Both of the Arg15 mutant mice, *Ap2s1*$^{+/C15}$ and *Ap2s1*$^{+/L15}$, had lower urine CCCR than the *Ap2s1*$^{+/I117}$ mouse which did not differ from the WT.

Comparison was made between the homozygous *Ap2s1*$^{C15/C15}$ and *Ap2s1*$^{I117/I117}$ mice, and the heterozygous *Ap2s1*$^{+/L15}$mice given the lack of homozygous *Ap2s1*$^{L15/L15}$ mice available for study. The *Ap2s1*$^{C15/C15}$ mice had higher plasma calcium, magnesium and ALP concentrations, and a lower body weight and BMD than the heterozygous *Ap2s1*$^{+/L15}$. This suggests that whilst the Arg15Leu phenotype is more severe than the Arg15Cys phenotype, the impact of a heterozygous Arg15Leu mutation does not outweigh the effect of homozygosity with an Arg15Cys mutation. The *Ap2s1*$^{C15/C15}$ also had higher plasma calcium, magnesium and ALP

concentrations, and a lower body weight and BMD than the *Ap2s1*$^{I117/I117}$ mouse, which again did not differ from WT.

The Arg15Leu and Arg15Cys mice best fit the patient FHH3 phenotype as they recapitulate the biochemical derangements and genotype:phenotype correlation seen in patients. The Arg15Cys mouse line exhibits increasing PTH with increasing mouse age as seen in one human Arg15Cys FHH3 kindred. Interestingly, this is also seen in the Arg15Leu mouse and could be an as yet unobserved phenomena in patients with the Arg15Leu genotype.

Table 24. Calcitropic phenotype of adult male and female WT, *Ap2s1*$^{+/I117}$ *(+/I117*), *Ap2s1*$^{I117/I117}$ (*I117/I117*), *Ap2s1*$^{+/C15}$ *(+/C15*), *Ap2s1*$^{C15/C15}$ (*C15/C15*) and *Ap2s1*$^{+/L15}$ *(+/L15*) mice, aged 15-17 weeks. [A]Individual values are shown for the two male homozygous mice. Adj-calcium=plasma albumin-adjusted calcium; PTH=parathyroid hormone; ALP= plasma alkaline phosphatase; CCCR= calcium:creatinine clearance ratio; DXA=whole body dual-energy X-ray absorptiometry; and BMD=bone mineral density. Mean±SEM values for respective groups (n=10-24 mice per group) are indicated.*p<0.05, **p<0.01; ****p<0.0001 for *Ap2s1*$^{+/L15}$ mice versus respective [a]*Ap2s1*$^{+/C15}$, and [b]*Ap2s1*$^{C15/C15}$ mice. One-way ANOVA followed by Sidak's test for pairwise multiple comparisons were used for all analyses.

	WT	***+/I117***	***I117/I117***	***+/C15***	***C15/C15***	***+/L15***	***[A]L15/L15***
Age (weeks)	16.2±0.4 (n=16)	15.7±0.1 (n=14)	15.7±0.2 (n=18)	15.5±0.2 (n=18)	16.0±0.4 (n=10)	16.4±0.1 (n=24)[a]*	18.0, 22.0
Weight (g)	26.8±0.9 (n=16)	27.8±0.9 (n=14)	26.5±0.8 (n=18)	27.2±1.0 (n=18)	22.2±0.8 (n=10)	25.6±0.7 (n=24)[b]*	-
Plasma biochemistry:							
Adj-calcium (mmol/l)	2.29±0.02 (n=16)	2.28±0.02 (n=14)	2.30±0.01 (n=18)	2.74±0.02 (n=18)	3.25±0.02 (n=10)	2.92±0.01 (n=24)[a]****, [b]****	3.12, 3.22
PTH (ng/l)	54.3±9.0 (n=16)	80.8±18.0 (n=14)	80.9±11.2 (n=18)	135.4±13.7 (n=18)	159.1±12.7 (n=8)	155.0±14.1 (n=24)	134, 180
Phosphate (mmol/l)	1.76±0.06 (n=16)	1.88±0.09 (n=14)	1.86±0.07 (n=18)	1.43±0.07 (n=18)	1.42±0.10 (n=10)	1.30±0.05 (n=23)	1.17, 1.18
Magnesium (mmol/l)	1.12±0.03 (n=16)	1.09±0.03 (n=14)	1.11±0.03 (n=18)	1.12±0.02 (n=18)	1.31±0.04 (n=10)	1.17±0.03 (n=20)[b]**	-
ALP (U/l)	102.8±5.5 (n=16)	104.7±5.7 (n=14)	107.1±5.4 (n=18)	110.3±5.6 (n=18)	144.5±4.3 (n=10)	122.8±4.4 (n=23)[b]*	-
Urine biochemistry:							
CCCR x10^3	2.3±0.3 (n=16)	2.5±0.3 (n=14)	2.2±0.2 (n=18)	2.3±0.2 (n=16)	1.7±0.2 (n=12)	1.2±0.2 (n=22)[a]**	-
DXA:							
BMD (mg/cm^2)	73.0±0.9 (n=23)	-	-	69.4±0.9 (n=18)	64.1±1.1 (n=10)	69.6±1.0 (n=23) [b]**	-

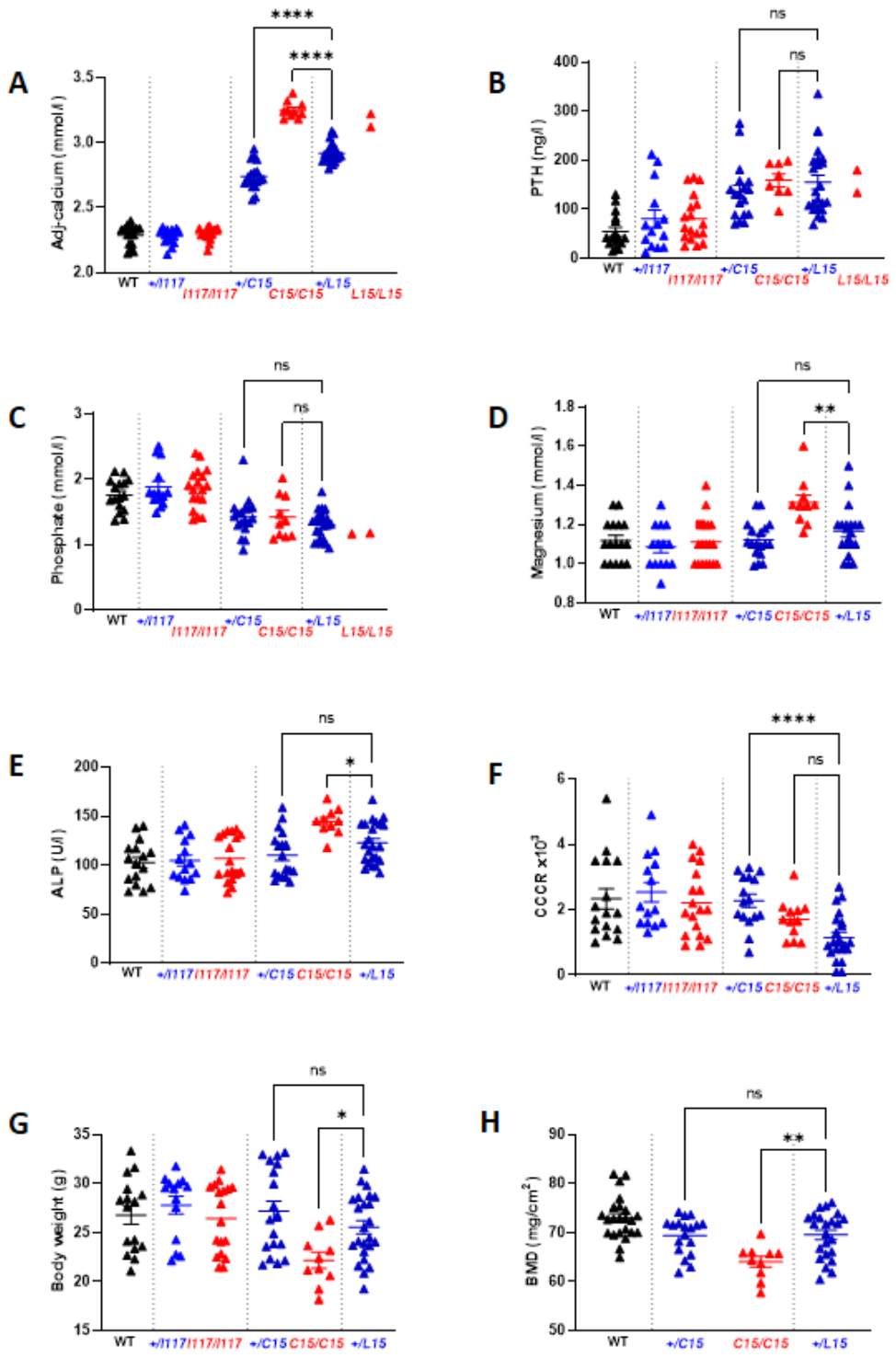


Figure 42. Calcitropic phenotype of adult male and female WT, *Ap2s1*$^{+/I117}$ *(+/I117)*, *Ap2s1*$^{I117/I117}$ (*I117/I117*), *Ap2s1*$^{+/C15}$ *(+/C15)*, *Ap2s1*$^{C15/C15}$ (*C15/C15*) and *Ap2s1*$^{+/L15}$ *(+/L15)* mice, aged 15-17 weeks. (A) plasma albumin-adjusted calcium (adj-calcium); (B) plasma parathyroid hormone (PTH); (C) plasma phosphate; (D) plasma magnesium; (E) plasma alkaline phosphatase (ALP); (F) calcium:creatinine clearance ratio (CCCR) x10^3; (G) body weight; and (H) bone mineral density (BMD). Male and female mice are denoted by triangles. WT *Ap2s1*$^{+/+}$ mice are in black, heterozygous *Ap2s1*$^{+/I117}$ *(+/I117)*,

Ap2s1$^{+/C15}$ (*+/*C15) and *Ap2s1*$^{+/L15}$ *(+/L15*) mice are in blue, and homozygous *Ap2s1*$^{M117I/M117I}$ (*I117/I117*), *Ap2s1*$^{C15/C15}$ (*C15/*C15), and *Ap2s1*$^{L15/L15}$ (*L15/L15*) mice are in red. Mean±SEM values for respective groups (n=10-24 mice per group) are indicated. ns=non-significant; *p<0.05, **p<0.01; ****p<0.0001 for *Ap2s1*$^{+/L15}$ mice versus respective *Ap2s1*$^{+/C15}$ and *Ap2s1*$^{C15/C15}$ mice. One-way ANOVA followed by Sidak's test for pairwise multiple comparisons were used for all analyses.

Human patients with FHH3 have been shown to have more severe hypercalcaemia, hypomagnesaemia and hypocalciuria than those with FHH1 (192). To investigate for this effect in the *Ap2s1*$^{+/C15}$ and *Ap2s1*$^{+/L15}$ mouse models, a comparison was made with the existing mouse model of FHH1 (230), and the published phenotypic data available on human patients with FHH1 and FHH3 (192) (Table 25).

In FHH1 patients, the mean albumin-adjusted calcium is ~6.2% above the upper limit of normal (2.76 vs 2.60 mmol/l), whereas for FHH3 patients it is considerably more elevated at ~10.4% above the upper limit of normal (2.87 vs 2.60 mmol/l). In the mouse model of FHH1, also generated on a background of the C57BL/6 mouse as in our mouse models, the mean total calcium was ~8% higher than that seen in WT mice (10.4 vs 9.6 mg/dl), similar to the elevations seen in FHH1 patients. In our *Ap2s1*$^{+/C15}$ and *Ap2s1*$^{+/L15}$ mouse models the mean albumin-adjusted calcium was ~19.7% and ~27.5% higher than that seen in WT mice, respectively (2.74 and 2.92 vs 2.29 mmol/l respectively) (Table 25). Our mouse models of FHH3 therefore demonstrate a more severe hypercalcaemia than that seen in the mouse model of FHH1, and this difference is more pronounced than that observed between FHH1 and FHH3 patients.

Our FHH3 mouse models have more significant elevations in their serum calcium concentrations than is seen in the human phenotype (~19.7% and ~27.5% higher than in WT mice, compared to ~10.4% above the upper limit of normal in FHH3 patients) (Table 25).

Analysing FHH3 patients by genotype reveals that those with the Arg15Cys mutation have serum albumin-adjusted calcium concentrations ~8.8% higher, and those with the Arg15Leu mutation have serum albumin-adjusted calcium concentrations ~17.7% higher than the upper limit of normal (2.83 and 3.06 vs 2.60 mmol/l respectively). The elevated serum calcium concentrations seen in the *Ap2s1*$^{+/C15}$ mouse is therefore comparable to that seen in patients harbouring the Arg15Leu mutation (~19.7% compared to ~17.7%). Our 2 mouse models of FHH3 demonstrate the genotype-phenotype correlation in serum calcium concentrations seen in FHH3 patients, but in a less pronounced way. Our *Ap2s1*$^{+/L15}$ mouse model has a serum calcium concentration that is less than 1.5 times higher than in the *Ap2s1*$^{+/C15}$ mice (~27.5% compared to ~19.7%), whereas patients with the Arg15Leu mutation have a serum calcium that is more than twice as high as that seen in patients with the Arg15Cys mutation (~17.7% compared to ~8.8%) (Table 25).

Patients with FHH3 have serum magnesium concentrations that are 4% above the upper limit of normal (1.04 vs 1.00 mmol/l) and urinary CCCRs that are 5 times lower than the lower limit of normal (0.004 vs 0.02), whereas FHH1 patients have serum magnesium concentrations within the normal range, and urinary CCCRs that are roughly one third of the lower limit of normal (0.007 vs 0.02) (Table 25). In our *Ap2s1*$^{+/C15}$ mouse model the combined serum magnesium concentrations and urinary CCCR for both sexes did not differ from that seen in the WT mice (1.12mmol/l and 0.0023 respectively, a significant difference can be seen in the female *Ap2s1*$^{+/C15}$ mice compared to WT). The *Ap2s1*$^{+/L15}$ mice had serum magnesium concentrations ~4.5% above that seen in WT mice respectively (1.17 vs 1.12mmol/l), and urinary CCCRs that are roughly half of the value seen in WT mice (0.0012 vs 0.0023). In comparison, the FHH1 mouse had a serum magnesium ~11% higher than the WT (2.74 vs 2.43 mEq/l) and a total urine calcium just over half of that seen in WT mice (11.73 vs 20.18mg/dl)

(Table 25). In contrast to the relationship seen between FHH1 and FHH3 patients, our FHH3 mouse models do not have more severe hypermagnesaemia and hypocalciuria than the existing FHH1 mouse model.

Table 25. Comparison of adult male and female mouse models of FHH1 (230) and FHH3 with the adult human phenotypes. Human FHH1 and FHH3 phenotypic data from Hannan et al (2018) (192). For the mouse models WT mice are shown as a comparator, for the human patients the normal ranges are given. Mean ±SEM values with number of probands (n) for respective groups are indicated. [*]Arg15Leu=3.06±0.04 mmol/l; Arg15Cys=2.83±0.03 mmol/l (192); PTH=parathyroid hormone; ALP= plasma alkaline phosphatase; [a]Total calcium (expressed as mmol/l, converted from mg/dl); [b]PTH (pg/l); [c]total magnesium (mEq/l); [d]urine total calcium (from aspirate) (mg/dl); [e]albumin-adjusted calcium (mmol/l); [f]PTH (ng/l); [g]magnesium (mmol/l); [h]calcium:creatinine clearance ratio x10^3; [i]normal range 2.10-2.60; [j]normal range 0.70-1.00; [k]normal range >0.02.

	Mouse					Human (192)	
	FHH1(230)		FHH3			FHH1	FHH3[*]
	WT	*+/-*	WT	*+/C15*	*+/L15*		
Calcium[a,e]	2.4±0.1[a] (n=31)	2.59±0.1[a] (n=29)	2.29±0.02[e] (n=16)	2.74±0.02[e] (n=18)	2.92±0.01[e] (n=24)	2.76±0.02[e,i] (n=43)	2.87±0.02[e,i] (n=51)
PTH[b,f]	25±6.4[b] (n=8)	39.1±14.7[b] (n=8)	54.3±9.0[f] (n=16)	135.4±13.7[f] (n=18)	155.0±14.1[f] (n=24)	-	
Phosphate (mmol/l)	-	-	1.76±0.06 (n=16)	1.43±0.07 (n=18)	1.30±0.05 (n=23)	-	
Magnesium[c,g]	2.43±0.24[c] (n=16)	2.74±0.53[c] (n=16)	1.12±0.03[g] (n=16)	1.12±0.02[g] (n=18)	1.17±0.03[g] (n=20)	0.95±0.02[g,j] (n=43)	1.04±0.02[g,,j] (n=51)
ALP (U/l)	-	-	102.8±5.5 (n=16)	110.3±5.6 (n=18)	122.8±4.4 (n=23)	-	-
Urinary calcium excretion[d,h]	20.18±9.6[d] (n=10)	11.73±9.3[d] (n=15)	2.3±0.3[h] (n=16)	2.3±0.2[h] (n=16)	1.2±0.2[h] (n=22)	7.0±1.0[h, k] (n=43)	4.0±1.0[h, k] (n=51)

8 RESULTS - INVESTIGATION OF *AP2S1* VARIANTS IN PATIENTS WITH NEUROCOGNITIVE DISORDERS

8.1 Neurocognitive disorders in patients with FHH3

As described in the introduction, non-calcitropic disorders are a common finding in patients with FHH3 (Table 6) (192, 210, 221-229). In particular, patients with Arg15Leu mutations appear to have a high incidence of concurrent neurocognitive disorders, such that ~60% (14/23) of reported cases have learning disabilities and ~30% (7/23) of reported cases have psychiatric disorders (Table 26).

Table 26. The frequency of co-existing non-calcitropic conditions and reduced bone mineral density in reported cases of FHH3 patients with confirmed Arg15Cys, Arg15His and Arg15Leu mutations. All reports in peer-reviewed publications which contained both clinical and genetic details of FHH3 patients with a confirmed *AP2S1* mutation included. LD = learning disabilities, Psych = psychiatric problems (including cases with unspecified psychiatric problems, depression and ADHD), Nil = no evidence of non-calcitropic phenotype or reduced bone mineral density.

Condition	Arg15Cys	Arg15His	Arg15Leu
LD	17%	8%	61%
Psych	8%	8%	30%
Nil	50%	77%	22%
Total no. of cases reported	12	13	23

As described, the σ-subunit of AP2 is thought to recognise the dileucine motif on GPCRs, including, but not limited to the CaSR, which then leads to CME of the receptor (20, 28). AP2-mediated CME has been shown to play an important role in numerous neurocognitive processes, including the recycling of synaptic vesicles at mammalian central synapses (274), the regulation of GABA and glutamate receptors at the neuron surface (275) and receptor trafficking in the hippocampus (276). Additionally, mutations affecting AP2 function have already been described in association with impaired neurocognition. A recent publication has demonstrated that a mutation in *AP2M1*, encoding the μ-subunit of AP2, appears to cause

learning difficulties by disrupting CME at an early stage, using transferrin as its model receptor, and does not affect calcium physiology (19).

It may also be that the disorders of neurocognition associated with FHH3 occur as a result of a disruption to CaSR signalling. CaSR signalling has been shown to be important in a wide variety of neuronal processes (Table 3). Experience from the CaSR knock out mouse model ($CaSR^{-/-}$)(230), and the CaSR and PTH knock out mouse model ($CaSR^{-/-}PTH^{-/-}$) (231), has provided insight into the role of the CaSR in the developing brain. As described in the introduction, the $CaSR^{-/-}$ mouse is subject to the effects of both CaSR knock-out, and the resulting hyperparathyroidism. Deletion of PTH in the $CaSR^{-/-}PTH^{-/-}$ mouse enables analysis of the effects of CaSR knock out in mice not subject to hyperparathyroidism, hypercalcaemia and hypophosphataemia (277). $CaSR^{-/-}$ mice exhibit reduced brain weight and size, a developmental delay in expression of proliferating nuclear antigen, and reduced neuronal and glial differentiation markers at 1 and 2 weeks when compared to WT littermates (230), whereas $CaSR^{-/-}PTH^{-/-}$ mice have normal brain cell proliferation, but not differentiation (231, 277). Importantly, this study reveals not only an involvement of the CaSR in brain differentiation, but also the effects of hyperparathyroidism on the developing brain. As FHH3 patients are likely to begin to develop hypercalcaemia, and possibly elevated PTH, *in utero*, which may be exacerbated if they are carried by mothers negative for the mutation, the existence of abnormal neurocognition may be at least partly attributed to this, in addition to the effects of the mutation itself.

The CaSR has also been demonstrated to have an important role in the adult nervous system, outside of the regulation of calcium homeostasis. For example, Arg898Glu is a rare variant of the CaSR identified in patients with idiopathic epilepsy. It is functionally consistent with a

gain-of-function phenotype (278), but subjects harbouring the variant have levels of serum calcium, phosphate, sodium, potassium, and parathyroid hormone within the reference range (279). The CaSR has been shown to form heterodimers with other GPCRs involved in neurotransmission, including metabotropic glutamate receptors (mGluRs) and γ-amino isobutyric acid B receptors (GABABRs). The functional consequences of these heterodimers remains to be fully elucidated, however they may feasibly affect ligand binding and sensitivity, the pharmacology of the receptor, and signalling and neurotransmission (280).

8.2 Identification of AP2σ-Arg10 variants associated with impaired neurocognition

Correspondence with collaborators in the USA identified a cohort of nine unrelated individuals with developmental delay of unknown aetiology who have been found to harbour heterozygous variants of *AP2S1* codon 10.

8.2.1 Genotypic and phenotypic characteristics of the *AP2S1* Arg10 variant cohort

The cohort of nine patients with AP2σ-Arg10 variants was made up of 3 females and 6 males, ranging in age at last assessment from 9 months to 18 years. None of the patients appeared to have a calcitropic phenotype as seen in patients with AP2σ-Arg15 and AP2σ-Met117 mutations (20, 192, 260) since all had serum calcium and PTH concentrations within the normal range. Detailed phenotypic data was available on 8 out of 9 patients and of these, all had developmental delay, 6 had seizures and 5 had autism, or possible autism. Genotyping analysis was performed by our collaborators. Eight patients were found to harbour a novel C-to-T transition at nucleotide c.28, resulting in a missense substitution of the wild-type arginine (Arg) encoded by codon 10 to a tryptophan (Trp), and one patient was found to have a novel

heterozygous G-to-A transition at nucleotide c.29, resulting in a missense substitution of the wild-type arginine encoded by codon 10 to a glutamine (Gln) (Table 27). All mutations were *de novo* (Table 27).

8.2.2 *In silico* assessment of the AP2σ-Arg10 variants

Arg10 is encoded by exon 2 of the *AP2S1* gene, 5 residues upstream of the Arg15 codon involved in FHH3. It forms part of a loop linking the β1- and β2-strands in the secondary structure of the protein. (Figure 43, Figure 44). As described in Chapter 6, the *AP2S1* gene is subject to a high degree of evolutionary conservation suggesting that it may have an important function shared across species (

Figure 16), and the AP2σ-Arg10 codon is fully conserved across 5 species (M. Musculus, X. Tropicalis, D. Rerio, D. Melanogaster and C. Elegans) (Figure 44).

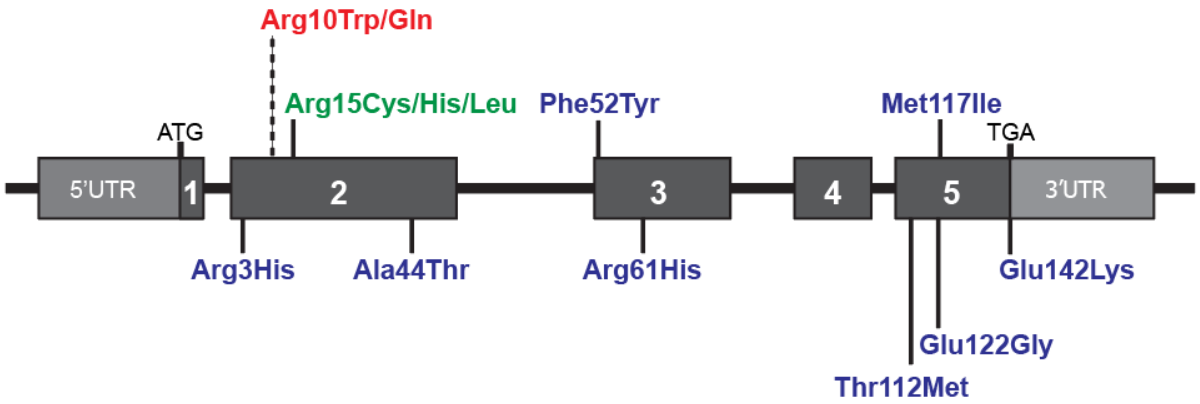


Figure 43. Schematic representation of the genomic organisation of the *AP2S1* gene (adapted from Figure 15). The gene consists of 5 exons (dark grey boxes), with a 5' untranslated region (UTR) and 3'UTR (light grey boxes). The start codon (ATG) is located in exon 1, and the stop codon (TGA) is located in exon 5. The distribution of the Arg10 variants found in our cohort, Arg10Trp and Arg10Gln, are shown in red. The known FHH3-causing Arg15 mutations, Arg15Cys, Arg15His and Arg15Leu, are shown in green. The novel variants found in the DiscovEHR dataset, Phe52Tyr and Met117Ile, and those found in the ExAc and dbSNP datasets, Arg3His, Ala44Thr, Arg61His, Thr112Met, Glu122Gly and Glu142Lys, are shown in blue.

Table 27. Genotypic and phenotypic characteristics of patients with neurocognitive disorders found to have AP2σ-Arg10 variants. F=female; M=male; Y=years; RR=within reference range; NA = not available; GDD = global developmental delay; DD = developmental delay; ADHD = Attention Deficit Hyperactivity Disorder

Case	**1**	**2**	**3**	**4**	**5**	**6**	**7**	**8**	**9**
Variant	c.28C>T, p.R10W	c.28C>T, p.R10W	c.28C>T, p.R10W	c.28C>T, p.R10W	c.28C>T, p.R10W	c.28C>T, p.R10W	c.28C>T, p.R10W	c.29G>A, p.R10Q	c.28C>T, p.R10W
Inheritance	de novo	de novo	de novo	de novo	de novo	de novo	de novo	de novo	de novo
Sex	F	M	F	M	M	F	M	M	M
Age at last assessment	7Y	12Y	18Y	9Y	16Y	9 months	1Y	6Y	6Y
Calcium and PTH	RR	RR	RR	RR	RR	RR	RR	RR	RR
Neurological findings	GDD, hypotonia, waddling gait	GDD, aphasic, hypotonia, jerky movements	NA	DD, speech delay	severe intellectual disability	gross motor DD	gross motor DD, hypotonia	GDD	GDD
Behavioural findings	autism, hyperactivity aggression, tantrums	autism, ADHD, tantrums	NA	possible autism	autism, violent and self injurous behaviour	otherwise normal	otherwise normal	autism	otherwise normal
Other findings	growth retardation, facial dysmorphism, clinodactyly, constipation, asthma	strabismus, microcephaly,	NA	microcephaly, 2 hypopigmented areas on shoulder, 1 café au lait macule	weight 7th centile, pyloric stenosis (treated), constipation, mild joint laxity	nil	nil	born at 34/40, jejenal atresia, subgaleal haemorrhage, 3x café au lait macules, asthma	born at 32/40
Seizures	1 febrile seizure	grand mal seizures	NA	grand mal seizures	grand mal seizures and drop attacks	grand mal seizures	petit mal seizures	nil	nil
Results of MRI brain	NA	NA	NA	within normal limits	features of mesial temporal sclerosis on the left	within normal limits	within normal limits	features of intracerebral haemorrhage at 1/12	white matter hypoplasia

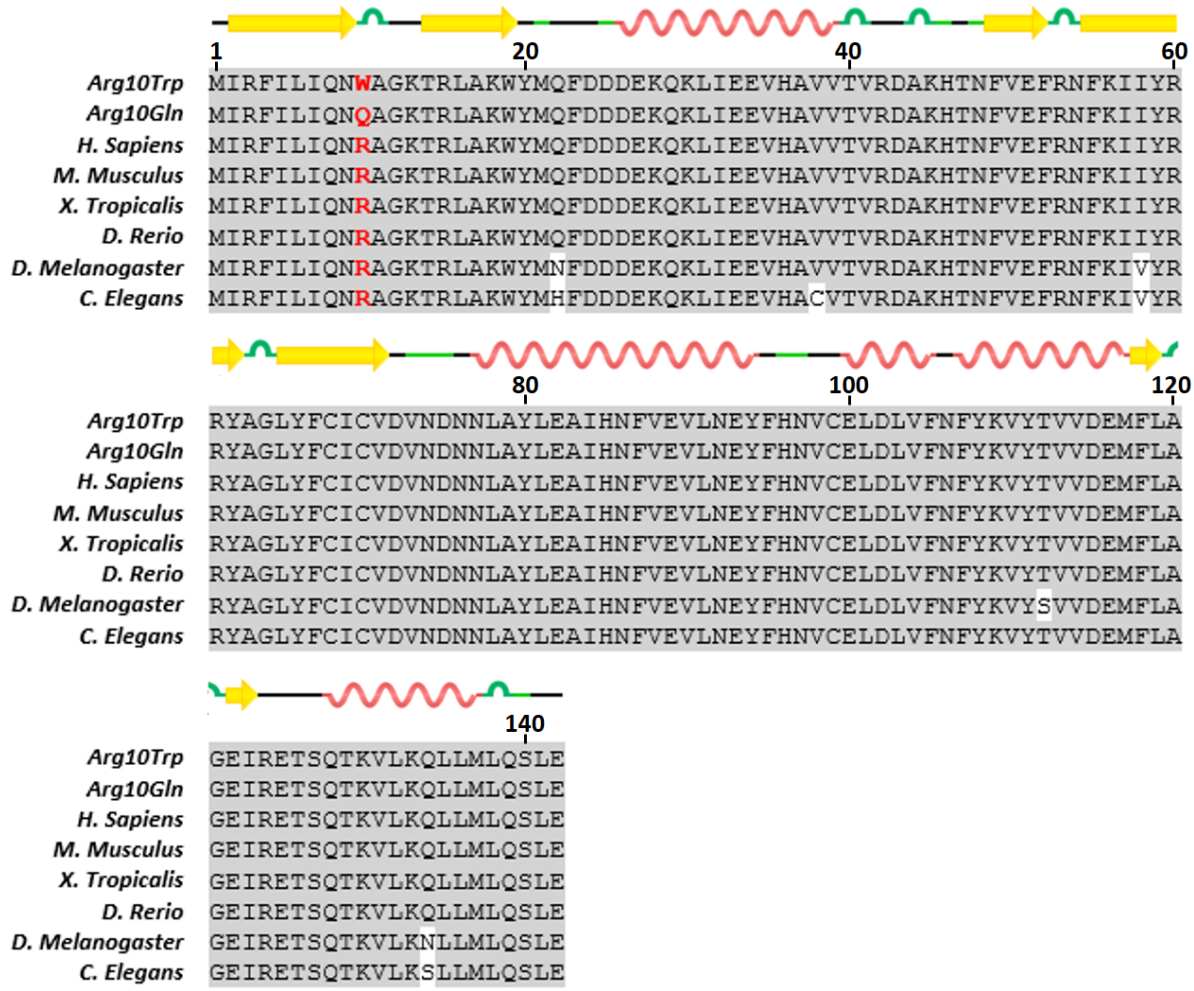


Figure 44. Multiple protein sequence alignment of AP2σ-subunit orthologs (adapted from Figure 10) showing the location of the variants identified in our cohort (Arg10Trp and Arg10Gln). The secondary structure of the protein is shown above (adapted from Jackson et al, Cell. 2010 (219)). Conserved residues are shaded grey. Codon 10, the site of the variants in our cohort mutations, is shown in red. Codon numbers are indicated every 20 residues in black. β-strands are indicated by yellow arrows; α-helices are indicated by red wavy lines; non-repetitive loops are in green.

Bioinformatic analysis of these variants was performed to determine the effect on AP2σ. This first entailed determining all possible variants of the Arg10 codon, and then seeking the occurrence frequency from the large genetic databases Genome Aggregation Database

(GnomAD v2.1.1)(250) and dbSNP (248) databases (Table 28). This provided insight into how rare variance of Arg10 is, and to therefore deduce how damaging it might be.

Four of the 9 possible nucleotide substitutions result in synonymous variants with the other 5 substitutions resulting in non-synonymous missense variants. Only one of the four possible synonymous variants is present in gnomAD or dbSNP (c.30G>A p.Arg10Arg). Of the 5 possible missense variants, only c.28C>T p.Arg10Trp and c.29G>A p.Arg10Gln, the variants observed in our patient cohort, have been previously submitted to ClinVar, a public archive of human genetic variants and interpretations of their relationships to diseases and other conditions (251). Of the nine possible Arg10 variants, phenotypic data was only available on ClinVar for Arg10Trp which has been designated a variant of uncertain significance (VUS) found in both a patient with neurodevelopmental disorders and a patient with FHH (Table 28).

Table 28. In silico assessment of all possible nucleotide changes in the AP2σ-Arg10 codon. [A]Present in our cohort. VUS = variant of uncertain significance.

Nucleotide change	Amino acid change	Type of variant	Allele frequency on gnomAD(250)	Allele frequency on dbSNP(248)	Designation on ClinVar(251)	SNP ID
c.28C>A	Arg10Arg	synonymous	0	0	-	-
c.28C>T	Arg10Trp[A]	missense	0	1	VUS	rs1297109231
c.28C>G	Arg10Gly	missense	0	0	-	-
c.29G>A	Arg10Gln[A]	missense	0.00000398	1	-	rs1064795235
c.29G>C	Arg10Pro	missense	0	0	-	-
c.29G>T	Arg10Leu	missense	0	0	-	-
c.30G>A	Arg10Arg	synonymous	0.00002785	1	-	-
c.30G>C	Arg10Arg	synonymous	0	0	-	-
c.30G>T	Arg10Arg	synonymous	0	0	-	-

8.2.2.1 Predicted effects on protein function

To investigate the effects of all the possible missense variants on the function of the protein the prediction software SIFT, Polyphen-2 and MutationTaster (252, 253, 263) were used

(Table 29). Arg10Trp was predicted to be deleterious, probably damaging, and disease causing by SIFT, PolyPhen-2 and MutationTaster, respectively. Arg10Gln was also predicted to be deleterious and disease causing by SIFT and MutationTaster respectively, but was only predicted to be possibly damaging by PolyPhen-2. The other missense variants were all predicted to be deleterious, probably damaging, and disease causing by SIFT, Polyphen-2 and MutationTaster. Other than Arg10Gln being predicted to be possible damaging, rather than probably damaging by PolyPhen-2, there was nothing to distinguish the observed variants, Arg10Trp and Arg10Gln, from those not observed in the sequencing datasets or our cohort (Table 29).

Table 29. Predicted effects on protein function of the possible non-synonymous AP2σ-Arg10 variants. [A]Present in our cohort.

Nucleotide change	Amino acid change	Type of variant	SIFT	PolyPhen-2	MutationTaster
c.29G>A	Arg10Gln[A]	Missense	Deleterious	Possibly damaging	Disease causing
c.29G>C	Arg10Pro	Missense	Deleterious	Probably damaging	Disease causing
c.29G>T	Arg10Leu	Missense	Deleterious	Probably damaging	Disease causing
c.28C>T	Arg10Trp[A]	Missense	Deleterious	Probably damaging	Disease causing
c.28C>G	Arg10Gly	Missense	Deleterious	Probably damaging	Disease causing

8.2.2.2 Predicted effects on protein structure

Although all the prediction software tools predicted that all the missense variants would affect protein function these tools often overestimate effects (281). We therefore performed additional bioinformatic analysis using PyMOL and the previously published crystal structure of the AP2 heterotetramer (48). Arg10 is predicted to form one polar contact with Asn10 on the β-subunit. The Arg10Trp variant, observed in our cohort, was not predicted to result in a change in polar contacts, however tryptophan is much bulkier than glutamine which may well affect protein structure and / or function Arg10Gln (also observed in our cohort), Arg10Gly, Arg10Leu

and Arg10Pro were all associated with a loss of polar contact with Asn10 on the β-subunit. Additionally, Arg10Pro was also associated with a loss of polar contact with Gly64 on the σ-subunit (Figure 45).

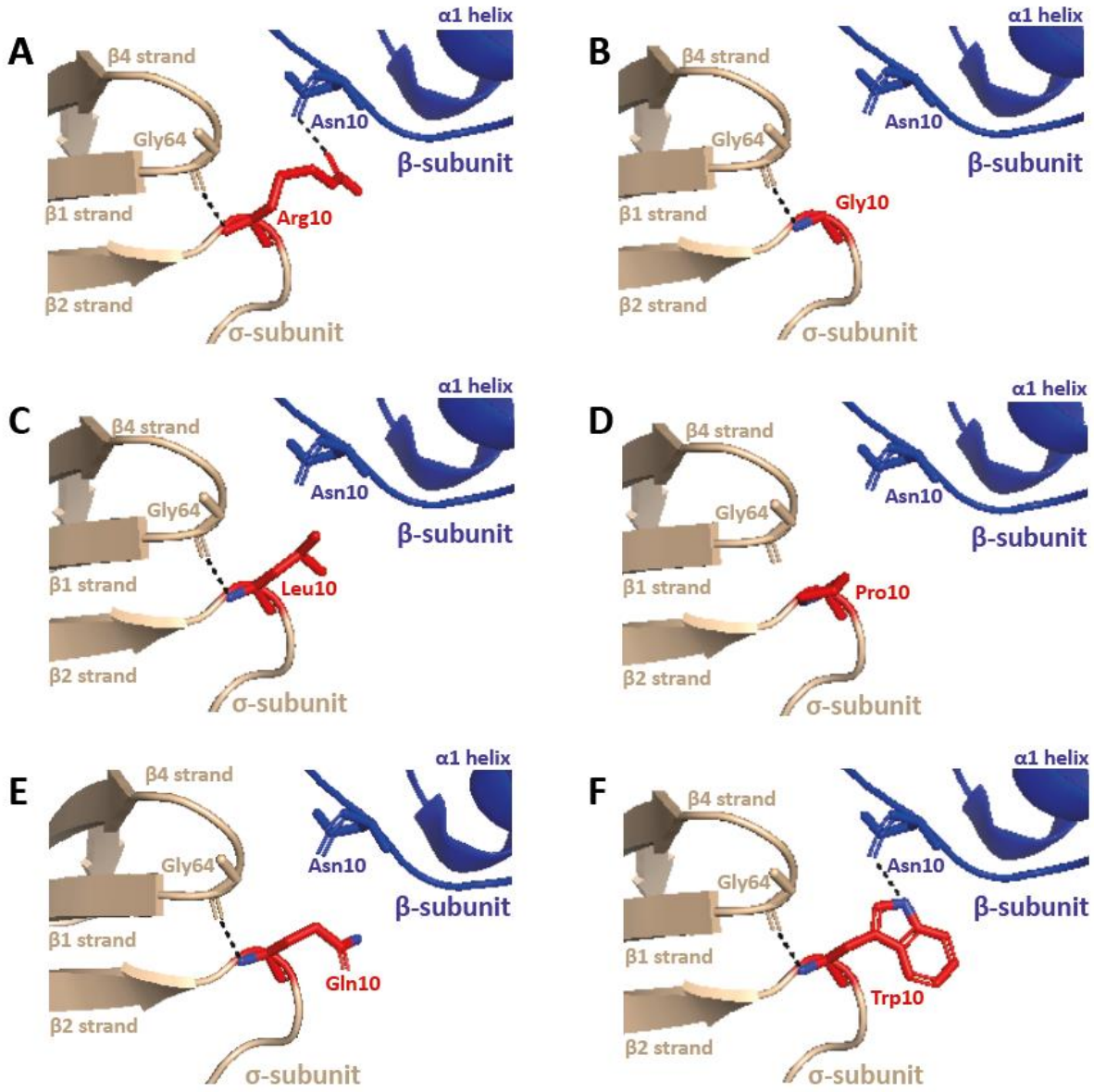


Figure 45. Predicated structural effects of the Arg10 variants. (A) Structural model of β strands 1, 2 and 4 of the AP2σ-subunit (brown), with the adjacent α1 helix of the AP2β-subunit (blue). Arg10 (shown in red) forms a polar contact with Gly64 of the AP2σ-subunit and Asn10 of the AP2β-subunit (shown in blue). (B) Mutation of Arg10 to Gly10 (shown in red) results in a loss of the polar contact

with Asn10 of the AP2β-subunit. (C) Mutation of Arg10 to Leu10 (shown in red) results in a loss of the polar contact with Asn10 of the AP2β-subunit. (D) Mutation of Arg10 to Pro10 (shown in red) results in the loss of both the polar contact with Gly64 of the AP2σ-subunit and also with Asn10 of the AP2β-subunit. (E) Mutation of Arg10 to Gln10 (shown in red) results in a loss of polar contact with Asn10 of the AP2β-subunit. (F) Mutation of Arg10 to Trp10 (shown in red) does not result in loss of any polar contacts, however tryptophan is much bulkier than glutamine which may well affect protein structure and / or function.

In this analysis, the least detrimental variant, Arg10Trp, which did not disrupt any polar contacts, but is much bulkier than glutamine so may exert effects through size, is one that is the most common within our patient cohort. The most detrimental variant, Arg10Pro which disrupts the polar contact with Asn10 of the AP2β-subunit and the polar contact with Gly64 on the σ-subunit, has not been observed. There is nothing to distinguish the other variant present in our cohort, Arg10Gln, from the other variants that have not been observed.

Looking at the *in silico* analysis as a whole, there is more agreement between the predictive softwares in this analysis than seen in chapter 6. The 2 variants seen in our cohort, Arg10Trp and Arg10Gln, are predicted to be less disrupting than the other variants. Arg10Trp is the only variant not predicted to cause a structural change, and Arg10Gln is the only variant predicted to be possibly damaging rather than probably damaging by MutationTaster (Table 30). As previously discussed in chapter 5 and in the literature (281), results from these predictive programs should be interpreted with caution, but this observation fits with the idea that more disruptive variants are not compatible with life and therefore not seen in sequencing datasets, and observed variants are less disruptive.

Table 30. Summary of the in silico assessment of the non-synonymous *AP2S1* variants. SIFT, PolyPhen-2 and MutationTaster prediction softwares were used to assess the predicted effects of the variants on the function of AP2σ. The predicted structural effect of each variant assessed using PyMOL molecular visualization system (256) and the previously published crystal structure of the AP2 heterotetramer (219) is also summarised. [A]Variant present in our cohort.

Variant	SIFT	PolyPhen-2	MutationTaster	Predicted structural effect
Arg10Gln[A]	Missense	Deleterious	Possibly damaging	Loss of the polar contact with Asn10 of the AP2β-subunit
Arg10Pro	Missense	Deleterious	Probably damaging	Loss of the polar contact with Asn10 of the AP2β-subunit and loss of polar contact with Gly64 on the σ-subunit
Arg10Leu	Missense	Deleterious	Probably damaging	Loss of the polar contact with Asn10 of the AP2β-subunit
Arg10Trp[A]	Missense	Deleterious	Probably damaging	No change
Arg10Gly	Missense	Deleterious	Probably damaging	Loss of the polar contact with Asn10 of the AP2β-subunit

8.2.3 *In vitro* assessment of AP2σ–Arg15Leu and the AP2σ-Arg10 variants

Patients with AP2σ-Arg15Leu mutations have FHH3, a condition characterised by hypercalcaemia, hypophosphataemia, and elevated or inappropriately normal parathyroid hormone level, and associated with neurocognitive defects. It remains to be established whether the neurocognitive defects occur as a result of the abnormal calcium physiology on the developing and developed nervous system, as a direct consequence of the mutation itself, or a combination of the two. The association of AP2σ-Arg10 variants with neurocognitive disorders, without a co-existing calcitropic phenotype, supports a role for the direct effect of the mutation in the pathogenesis. Further insight into the molecular effects of AP2σ-Arg15Leu and the AP2σ-Arg10 variants may help to unpick this.

As discussed, AP2σ-Arg15Leu mutations have already been demonstrated to impair CaSR endocytosis (179) and to disrupt intracellular calcium signalling (192). AP2-dependent CME

has been shown to affect processes involved in neurocognition (19, 274-276), and dysfunction of the early steps of endocytosis have been strongly implicated in developmental and epileptic encephalopathy caused by *AP2M1* mutations (19). It has been the experience of our group that cell lines expressing the AP2σ-Arg15 variants, in particular Arg15Leu, do not grow as well as those expressing AP2σ-WT (Figure 17) (192).

These observations led to the development of 2 hypotheses:

1. Arg15Leu and the AP2σ-Arg10 variants could be causing developmental delay by affecting the early stages of CME, perhaps by disruption of the interaction between AP2 and the dileucine motif of receptors involved in neuronal processes.
2. Arg15Leu and the AP2σ-Arg10 variants could be exerting an effect on the growth of cells through inhibiting cell proliferation.

To test these hypotheses new stable cell lines expressing wild-type AP2σ, AP2σ-Arg15Leu, or AP2σ-Arg10 variants were generated using HEK-293 cells that were also stably expressing the CaSR with a FLAG-tag. AP2σ-Arg10Trp was used as the model Arg10 variant as this is the most common variant in our cohort. CaSR was used as the model GPCR as it has non-calcitropic roles in the central nervous system (45) (Table 3), and this is the GPCR that we have most experience with as a group.

The HEK-293 cells stably expressing the CaSR with a FLAG-tag were generated and called "Flac2" cells. Variants of Flac2 cells were generated to co-express AP2σ-wild-type (WT), AP2σ-Arg15Leu and AP2σ-Arg10Trp with a hemagglutinin (HA) tag. The HA tag enabled easy detection of the transfected AP2σ protein and allowed discrimination from endogenous AP2σ protein. The expression of the AP2σ proteins in the stable cell lines was confirmed by Western

blot analysis using an anti-HA tag antibody (Figure 46). The results showed that Flac2 cells expressed FLAG-CaSR, and Flac2+AP2σ variant cells lines expressed the FLAG-CaSR and HA-AP2σ. The expression of alpha-tubulin was comparable between HEK-WT, Flac2, and Flac2-AP2σ-WT/variant cells, confirming that equal amounts of cell lysate were loaded onto each lane of the gel. The FLAG-tag and the HA tag were not detected in the native HEK-WT cells, as expected. The FLAG-tag was detected with comparable intensity between the Flac2 cells and the Flac2-AP2σ-WT/variant cells, confirming comparable expression of the stably transfected FLAG-CaSR. The HA tag was not detected in the Flac2 cells as expected. The HA tag was detected with comparable intensity between the Flac2-AP2σ-WT, Flac2-AP2σ-Arg15Leu, Flac2-AP2σ-Arg10Trp stably transfected cells, confirming comparable expression of AP2σ-HA between cell lines.

The AP2σ-Arg10Trp variant appears to have a lower molecular weight than AP2σ-WT and AP2σ-Arg15Leu. There are several possible reasons for this. It seems unlikely that it is due to misfolding of the protein as a consequence of the mutation itself as the gel is denaturing. It seems more likely that the lower molecular weight is due to an alteration of post-translational modifications (PTMs). PTMs increase the functional diversity of a protein through the covalent addition of functional groups or proteins, proteolytic cleavage of regulatory subunits or degradation of entire proteins, and influence almost all aspects of normal cell biology. These modifications include phosphorylation, methylation, glycosylation, ubiquitination or acetylation. PTMs occur at distinct amino acid sites and are usually mediated by enzymes which add or remove functional groups, or may cleave peptide bonds. Methylation is a common PTM that occurs at arginine amino acids and may regulate steps in the signalling

pathway. Mutation from arginine to tryptophan may prevent methylation or another PTM that would result in the addition of a functional group or protein, resulting in a lower molecular weight of the AP2σ protein and potentially explaining the loss of function associated with the variant. Alternatively, the mutated amino acid may result in cleavage of the protein by an enzyme, with the loss of amino acids through this cleavage causing the lower molecular weight.

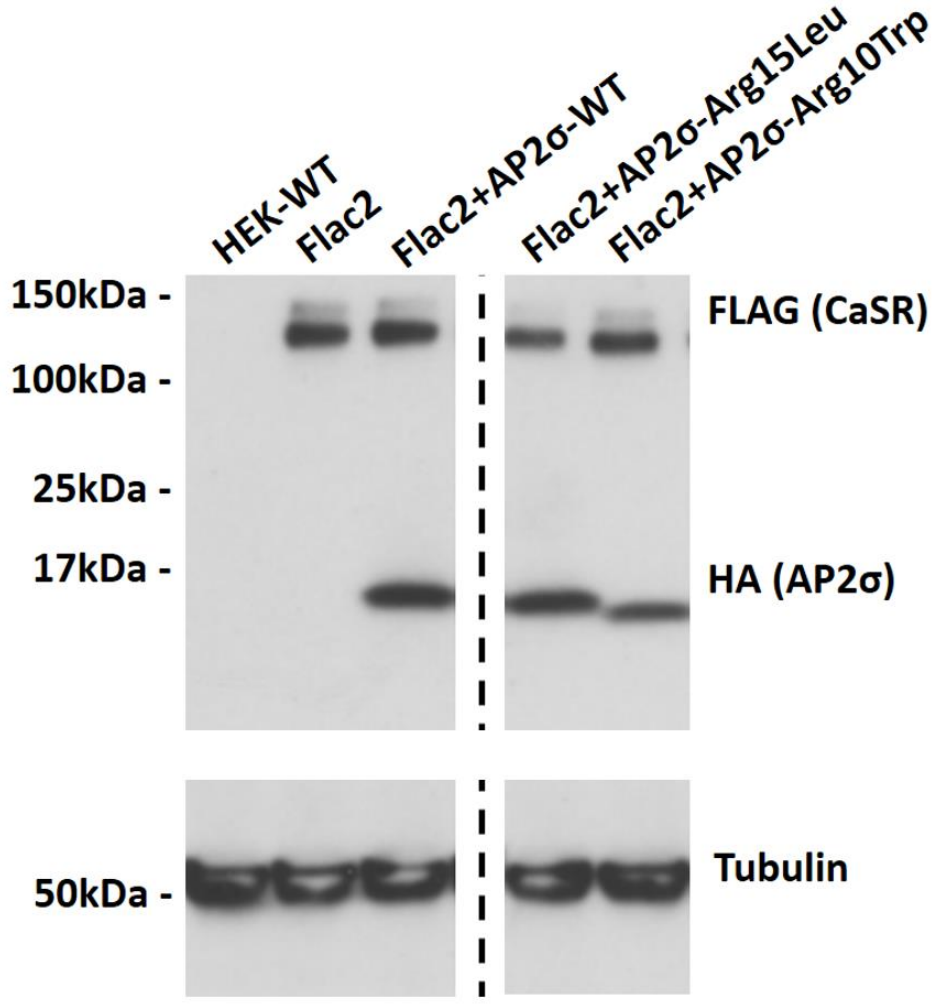


Figure 46. Western blot demonstrating the expression of the new cell lines. Cell lines were probed for the FLAG-tag attached to the CaSR, HA-tag attached to AP2σ, and tubulin control. Expected bands were a doublet at 130-150kDa for FLAG-CaSR, a band at 17kDa for HA-AP2σ and a band at 50kDa for

tubulin. HEK-WT cells expressed tubulin alone. Flac2 cells expressed the FLAG-tag attached to the CaSR and tubulin, and Flac2+AP2σ variant cells lines expressed the FLAG-tag attached to CaSR, HA tag attached to AP2σ and tubulin. The AP2σ-Arg10Trp variant appears to have a lower molecular weight than AP2σ-WT and AP2σ-Arg15Leu. This is likely to be due to the effect of the mutation on PTM of the AP2σ protein, either through preventing the addition of a functional group or protein, or the new mutant AP2σ sequence being the target of enzymatic cleavage.

8.2.3.1 Effects on cell proliferation

In preliminary observations I found that I had to use about 30-40% more Flac2-AP2σ-Arg15Leu cells, and 20-30% more FLac2-AP2σ-Arg10Trp cells, compared to Flac2-AP2σ-WT cells (when each type of cell was resuspended in the same volume of media), to get the same number of cells for use in the co-immunoprecipitation assay. This would suggest that the Arg15Leu and Arg10Trp variants affected cell proliferation, however formal investigations using cell proliferation assays were prevented due to the restrictions placed on laboratory experiments due to the SARS-CoV-2 (COVID-19) pandemic.

8.2.3.2 Effects on CaSR-AP2σ interaction

As previously described, the CaSR has important non-calcitropic roles in the central nervous system (45) (Table 3), and we hypothesised that AP2σ-Arg15Leu and the AP2σ-Arg10 variants may exert an effect on neurocognition through disrupting the interaction between the CaSR and AP2σ. This was investigated by co-immunoprecipitation using anti-FLAG antibodies to pull out the CaSR and co-bound proteins from FlaC2 cells.

Probing the IP with anti-HA antibodies revealed that the AP2σ-Arg15Leu mutation disrupts the CaSR-AP2σ interaction, as shown by a lower intensity ~17kDa band in the AP2σ-Arg15Leu lane compared with AP2σ-WT lane (Figure 47, Figure 48). In contrast, there is no reduction in

the amount of AP2σ-Arg10Trp in the IP suggesting that this variant does not affect the interaction between the CaSR and AP2σ (Figure 47). The lower molecular weight of the AP2σ-Arg10Trp variant compared to AP2σ-WT and AP2σ-Arg15Leu is consistently demonstrated.

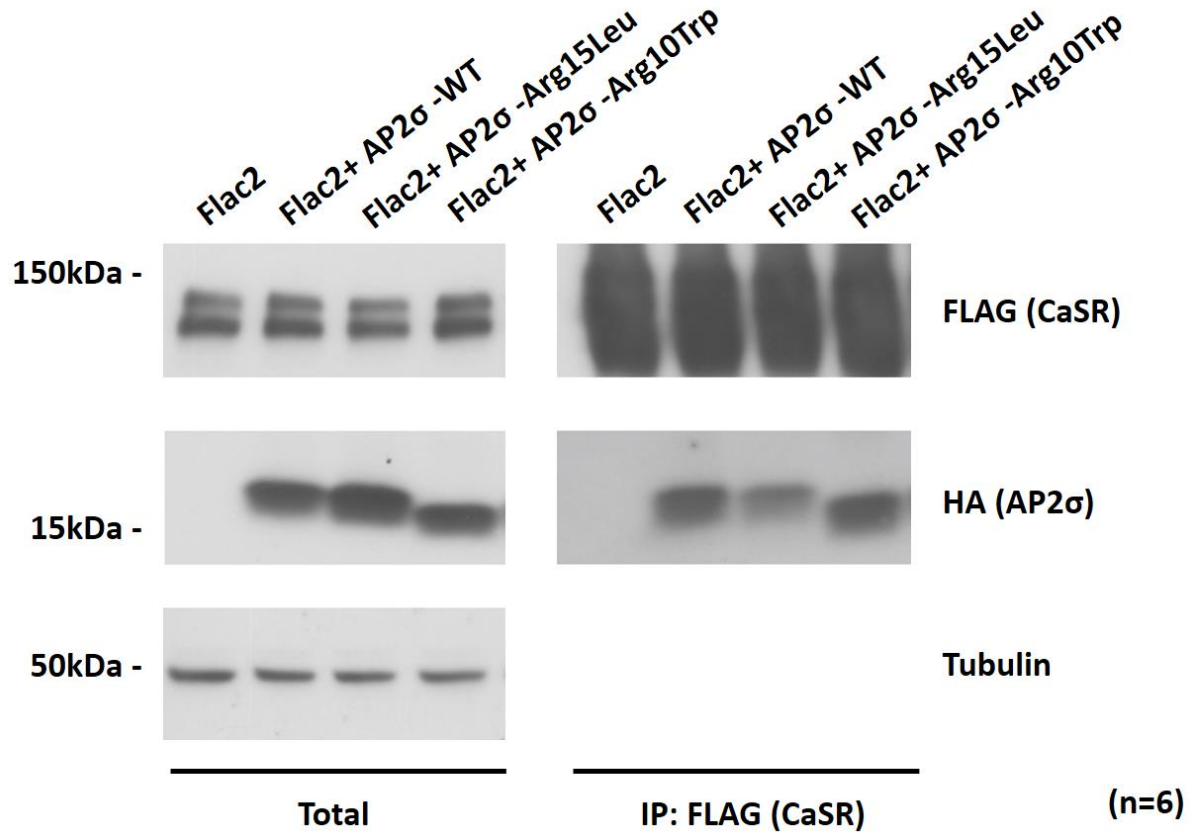


Figure 47. Western blot demonstrating the result of pulling down FLAG-CaSR for each cell line. Cell lines were probed for the FLAG-tag attached to the CaSR, HA-tag attached to AP2σ, and tubulin control. Expected bands were a doublet at 130-150kDa for FLAG-CaSR, 17kDa for HA-AP2σ and 50kDa for tubulin. After pull down, no HA-AP2σ is detected in the Flac2 cells. HA-AP2σ is detected in the Flac2+HA-AP2σ-WT, Flac2+HA-AP2σ-Arg15Leu and Flac2+HA-AP2σ-Arg10Trp cell lines, however, the band in the Flac2+HA-AP2σ-Arg15Leu cell line is less dense than in the Flac2+HA-AP2σ-WT cell line. The band in the Flac2+HA-AP2σ-Arg10Trp cell line is the same density as in the Flac2+HA-AP2σ-WT cell line, suggesting that the variant does not affect the interaction between the CaSR and AP2σ. The lower molecular weight of the AP2σ-Arg10Trp variant compared to AP2σ-WT and AP2σ-Arg15Leu is consistently demonstrated. This is likely to be due to the effect of the mutation on PTM of the

AP2σ protein, either through preventing the addition of a functional group or protein, or the new mutant AP2σ sequence being the target of enzymatic cleavage.

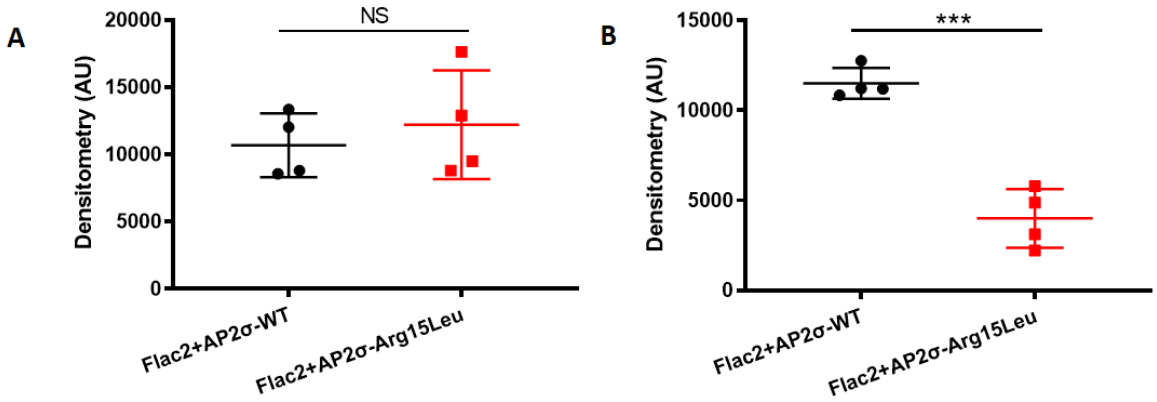


Figure 48. Densitometry analysis of 4 Western blots demonstrating the result of pulling down FLAG-CaSR for Flac2+HA-AP2σ-WT (black) and Flac2+HA-AP2σ-Arg15Leu (red) cell lines (n=4). (A) Densitometry of total cell lysate before pulling down FLAG-CaSR showed no significant difference. (B) Densitometry of cell lysates after pulling down FLAG-CaSR showed significantly less Flac2+HA-AP2σ-Arg15Leu than Flac2+HA-AP2σ-WT.

8.2.3.3 Cinacalcet drug studies

Cinacalcet has been shown to rectify impaired intracellular calcium signalling seen in cell lines expressing *AP2S1* mutations *in vitro* (210, 260), to lower plasma adjusted calcium in both WT and *Ap2s1*$^{+/R15L}$ mice *in vivo* (243), and to treat hypercalcaemia in FHH3 patients (210). Additionally, the CaSR has been identified as a possible drug target in the treatment of diseases of the CNS, with calcimimetics proposed as a potential therapy for neuroblastoma, and calcilytics found to be effective in counteracting the pathomechanism underlying Alzheimer's disease and ischaemia (280). We therefore decided to test the hypothesis that

cinacalcet acts by rescuing the impaired interaction between the CaSR and mutant AP2σ-Arg15Leu.

A dose of 10nM of cinacalcet was used as this dose was shown to rectify the impaired intracellular calcium signalling seen in cells expressing FHH3-causing *AP2S1* mutations (Figure 49).

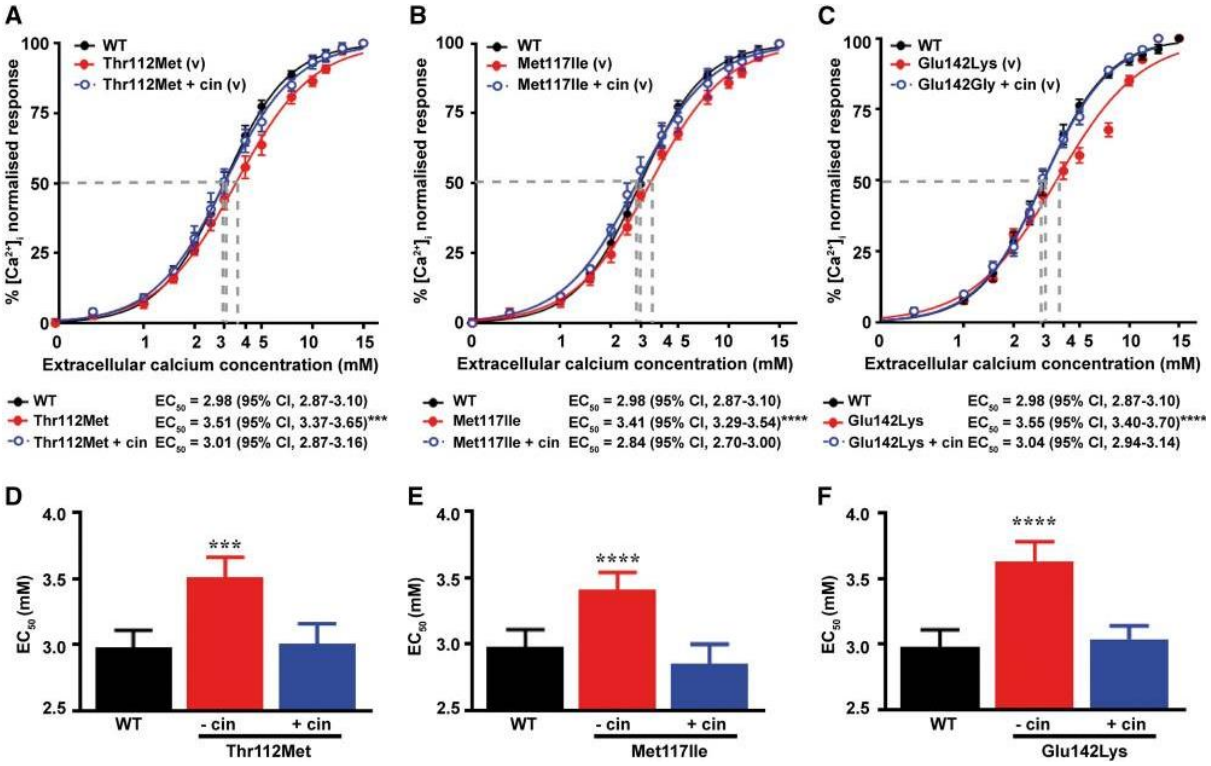


Figure 49. Figure and figure legend reproduced from Gorvin et al (2018) (260) "The effect of 10nM cinacalcet on intracellular calcium responses of cells expressing the AP2σ variants Thr112Met, Met117Ile and Glu142Lys. $Ca^{2+}{}_i$ responses, measured by flow cytometry, to changes in $[Ca^{2+}]_e$ of HEK-CaSR cells transfected with wild-type (WT) or (**A**) Thr112Met, (**B**) Met117Ile or (**C**) Glu122Gly variants (v) AP2σ proteins. The $Ca^{2+}{}_i$ responses to changes in $[Ca^{2+}]_e$ are expressed as a percentage of the maximum normalized responses and shown as the mean±SEM of 4–8 independent transfections. The Thr112Met, Met117Ile and Glu142Gly AP2σ variants led to a rightward shift in the concentration–response curve (red line), compared to WT, and the addition of 10 nM cinacalcet (cin) rectified these rightward shifts of the AP2σ variants (blue line). (**D–F**) Histograms showing the mean half-maximal

concentration (EC_{50}) with 95% confidence intervals (CI) and *P*-values of cells expressing WT (black bar), (**D**) Thr112Met, (**E**) Met117Ile and (**F**) Glu142Gly variants treated with vehicle (red bars), or treated with 10 nM cinacalcet (blue bars) AP2σ proteins. Statistical analysis was performed using the *F*-test. ****$P < 0.0001$, ***$P < 0.001$ compared to WT."

Flac2+AP2σ-WT cells and Flac2+AP2σ-Arg15Leu cells were incubated with 10nM cinacalcet for 15 minutes then investigated by co-immunoprecipitation, using anti-FLAG antibodies to pull out the CaSR and co-bound proteins, to assess whether there was an effect on the AP2σ–CaSR interaction. Probing the IPs with anti-HA antibodies revealed that cinacalcet had no effect on the amount of either the AP2σ-WT or AP2σ-Arg15Leu present (Figure 46). Cinacalcet therefore does not rectify the impaired CaSR-AP2σ interaction in the Arg15Leu cell line.

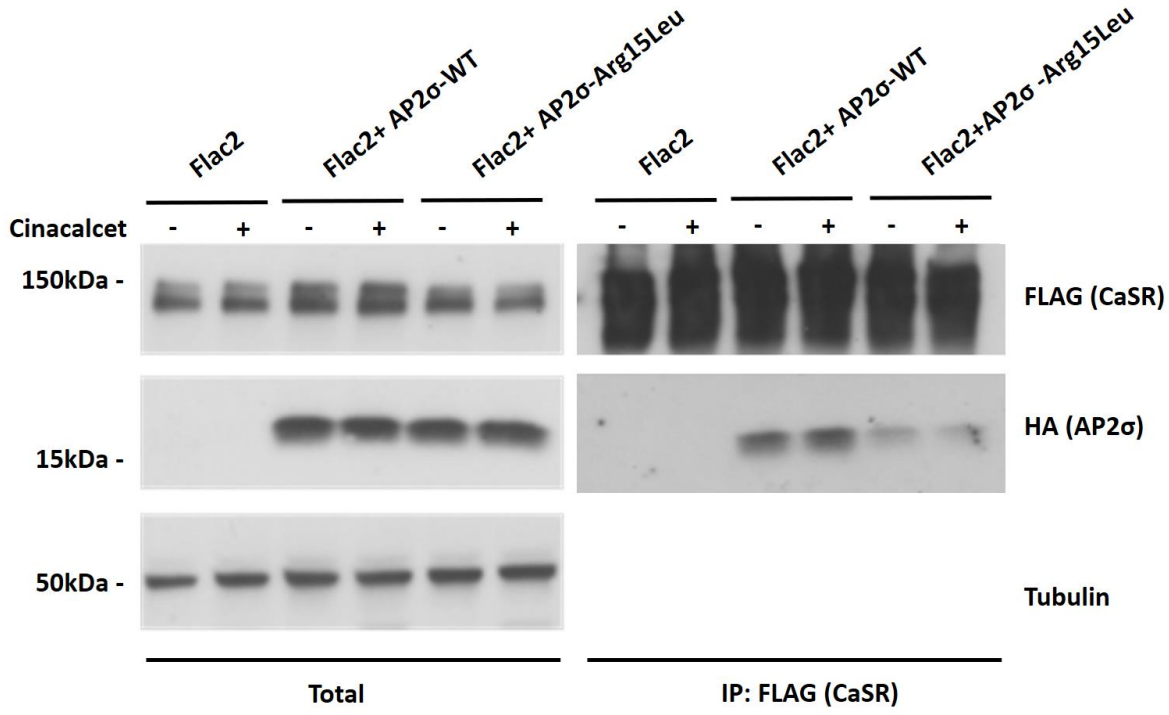


Figure 50. Western blot analysis following co-immunoprecipitation using an anti-FLAG antibody of cells treated with or without 10 nM cinacalcet. Total cell lysates were probed using anti-FLAG (CaSR), anti-HA (AP2σ) or anti-alpha-tubulin antibodies, while the IPs were probed using anti-FLAG (CaSR), or

anti-HA (AP2σ) antibodies. Reduced amounts of AP2σ-HA were detected in the Flac2+HA-AP2σ-Arg15Leu cell line IPs compared to Flac2+HA-AP2σ-WT IPs, however, treatment with cinacalcet had no effect on the amount of AP2σ detected.

It was my intention to investigate whether cinacalcet could rectify the observed impairment of cell proliferation in Flac2 cell lines expressing AP2σ-Arg10Trp, however, these studies were limited by the restrictions placed on laboratory experiments due to the SARS-CoV-2 (COVID-19) pandemic.

9 DISCUSSION

9.1 Investigation of AP2σ variants in large population datasets

These studies have identified 3 *AP2S1* variants in human subjects, Thr112Met, Met117Ile and Glu142Lys, that have been demonstrated to affect Ca^{2+}_i signalling *in vitro*, and, in Met117Ile where phenotypic data was available, the variant was associated with hypercalcaemia in a patient. To date, all known *AP2S1* mutations have been found on one codon, codon15, on exon 2 and all cause FHH3. The identification of these novel variants therefore potentially increases the spectrum of known mutations in *AP2S1.* Current UK recommendations suggest that exon 2 alone is screened when investigating patients for FHH3 and it is often the only exon investigated in research studies (224, 228, 282), however, the Thr112Met, Met117Ile and Glu142Lys variants are all located in exon 5 of *AP2S1*. The identification of these variants suggests a change in practice to sequence other exons within *AP2S1*, particularly exon 5 is warranted, to ensure that none are present in FHH patients.

These studies demonstrate the utility of large-scale sequencing databases in identifying genetic variants and the difficulty that can arise when trying to determine if they are pathogenic. In trying to evaluate whether or not a variant causes FHH3, an association with hypercalcaemia in a patient is clearly most useful, however this phenotypic data was only available for the 3 variants identified through the Regeneron DiscovEHR dataset, Arg15His, Phe52Tyr and Met117Ile, one of which, Arg15His, is already known to be a pathogenic mutation resulting in FHH3. Second in value to phenotypic data is experimental evidence showing the effect of a variant on intracellular calcium signalling, with variants that produce

the same effect as mutations known to cause FHH3 more likely to be pathogenic. We also used the *in silico* prediction tools SIFT, PolyPhen-2 and PyMOL to assess the *AP2S1* variants.

Arg15His has been shown to be a loss-of-function mutation that results in reduced sensitivity of the CaSR to $[Ca^{2+}]_e$. It was predicted to be deleterious and possibly damaging by SIFT and PolyPhen-2. It was shown to affect intracellular calcium signalling *in vitro*, and associated with hypercalcaemia in a patient in the Regeneron database. Met117Ile showed the same pattern in that it was associated with mild hypercalcaemia in a patient, was predicted to be deleterious and possibly damaging, was not predicted to have a structural effect and was shown to affect intracellular calcium signalling *in vitro*. Of the novel variants found in this study, Met117Ile therefore has the most evidence suggesting that it is pathogenic. The only other variant with paired phenotypic data available, Phe52Tyr, was associated with normocalcaemia in a patient and did not affect intracellular calcium signalling *in vitro*. This may suggest that Phe52Tyr does not cause FHH3 and that the predictions that it is deleterious and possibly damaging by SIFT and PolyPhen-2 may suggest that these tools are not always reliable. However, serial calcium measurements were not available for the patient with Phe52Tyr and we did not have comprehensive biochemistry results for them and it could be that their serum calcium concentration was lowered by other factors at the time of sampling, such as malabsorption, hypomagnesaemia, or even parathyroid gland impairment post thyroidectomy given that the patient is noted to be hypothyroid. Alternatively, this mutation may result in biased signalling, with no detectable effect on signalling through $G\alpha_{q/11}$ mediated intracellular calcium release, but effects on signalling through other pathways such as $G\alpha_{i/o}$, which were not examined in these studies.

Of the variants where phenotypic data was not available, Thr112Met and Glu142Lys have the most evidence to suggest that they are pathogenic as they were also demonstrated to affect Ca^{2+}_i signalling *in vitro.* They were also predicted to be deleterious and possibly damaging by SIFT and PolyPhen-2 and to result in changes in polar contacts by PyMOL. The remaining variants, Arg3His, Ala44Thr, Arg61His and Glu122Gly, did not affect intracellular calcium signalling *in vitro* and SIFT, PolyPhen-2 and PyMOL did not reliably agree with each other in their assessments. Structural analysis demonstrated that Arg 61 is proximal to the acidic LL moiety at position L(L0) and L(L+1) (32) and the interaction of the dileucine motif with AP2σ has been shown to be affected by mutating Arg63 to Trp63, a much bulkier amino acid side chain (32). It is possibly surprising therefore that the change in space filling properties when Arg61 mutates to His61 did not affect the interaction with the dileucine motif in a similar way.

Further analysis of the results of our *in silico* prediction tools shows that they did not reliably agree with each other, and did not predict which mutations would have functional consequences *in vitro* (Table 10). Crystal structural modelling of the 6 variants where SIFT and PolyPhen-2 concur (Arg15His, Phe52Tyr, Thr112Met, Met117Ile, Glu122Gly and Glu142Lys) did not demonstrate that all mutations predicted to be deleterious / pathogenic had effects on protein structure. Phe52Tyr and Met117Ile were not predicted to have an effect on the protein structure, whereas Thr112Met, Glu122Gly and Glu142Lys were all predicted to result in loss of a polar contact between AP2σ and AP2α. Additionally, mutation from the acidic amino acid Glu, to the basic amino acid Lys, is also likely to affect the protein structure and function through the change in the chemical property of this residue. The 3 variants where SIFT and PolyPhen-2 did not agree (Arg3His, Ala44Thr and Arg61His) had varying predicted

effects on AP2σ structure, including loss of 1 polar contact within AP2σ for Arg3His, no change for Ala44Thr and loss of 5 potential polar contacts predicted to affect dileucine motif binding for Arg61His. Met117Ile is associated with hypercalcaemia in a patient and SIFT and PolyPhen-2 agreed that it is likely to be deleterious and possibly damaging. However structural modelling predicts no resultant structural alteration. This may suggest that the agreement of SIFT and PolyPhen-2 is a more accurate predictor of pathogenicity than structural effects predicted by PyMOL. However, the structural analysis used looked only at polar contacts and modelling that takes into account "space filling", for example by the insertion of a large aromatic ring, may reveal 3D abnormalities.

These studies therefore highlight problems with *in silico* assessment of variants using pathogenicity prediction programs, which cannot be used to determine the effect of genetic variants in isolation. The 4 variants demonstrated to impair Ca^{2+}_i signalling, Arg15His, Met117Ile, Thr112Met and Glu142Lys could not have been predicted using these tools alone. *In silico* prediction tools have been demonstrated to have low clinical specificity in a study of population-level sequence data (281). However, another possibility is that variants predicted to be deleterious and possibly damaging have effects outside of calcium homeostasis, for example through impairment of CaSR signalling through non-$G\alpha_{q/11}$ pathways, and this is explored in our future studies.

Table 31. Summary of the *in silico* and *in vitro* investigations of the variants identified from the DiscovEHR and dbSNP and ExAC datasets. Variants associated with a significant change in the EC_{50} are shown in red. EC_{50}= half-maximal concentration of cells expressing either WT, loss-of-function control Arg15His or variant AP2σ. [A]Variant known to be an FHH3-causing mutation; [B]characterised in Hannan et al (2015)(192) [C]Variant found in large population dataset and associated with hypercalcaemia in a patient; . Statistical analysis performed using the F-test. ns=not significant; ***p<0.001; ****p<0.0001.

Variant	SIFT	PolyPhen-2	Predicted structural effect	EC_{50}	p-value
WT	-	-	-	2.87	-
Known FHH3-causing mutations:					
Arg15Cys[A]	Deleterious	Possibly damaging	Loss of 1 polar contact between AP2σ and AP2α[B]	3.02[B]	****
Arg15His[A,C]	Deleterious	Possibly damaging	Loss of 1 polar contact between AP2σ and AP2α[B]	3.66, 3.03[B]	****, ****
Arg15Leu[A]	Deleterious	Possibly damaging	Loss of 1 polar contact between AP2σ and AP2α[B]	3.07[B]	****
DiscovEHR dataset:					
Phe52Tyr	Deleterious	Possibly damaging	No change	2.82	ns
Met117Ile[C]	Deleterious	Possibly damaging	No change	3.41	****
dbSNP and ExAC datasets:					
Arg3His	Tolerated	Possibly damaging	Loss of 1 polar contact within AP2σ	3.02	ns
Ala44Thr	Deleterious	Benign	No change	3.07	ns
Arg61His	Tolerated	Damaging	Loss of 5 polar contacts, predicted to affect dileucine motif binding	3.22	ns
Thr112Met	Deleterious	Possibly damaging	Loss of 1 polar contact between AP2σ and AP2α	3.39	***
Glu122Gly	Deleterious	Damaging	Loss of 1 polar contact between AP2σ and AP2α	3.05	ns
Glu142Lys	Deleterious	Possibly damaging	Loss of 1 polar contact within AP2σ, and 1 polar contact between AP2σ and AP2α	3.63	****

The identification of 3 *AP2S1* mutations, Thr112Met, Met117Ile and Glu142Lys, demonstrated to affect Ca^{2+}_i signalling, provides insight into the structure-function relationship of AP2. AP2 is a heterotetrameric protein, made up of α-, β-, σ- and μ-subunits, with different conformational states when it is "active" and "inactive". Thr112Met and Met117Ile both occur on the α4-helix of AP2σ which closely associates with the α-subunit of

AP2, and interaction of these subunits is necessary in both states of the complex. Deleting AP2α in *C.elegans* has been shown to lead to instability of the AP2σ homolog, whilst the contacts between AP2β and AP2μ were unaffected (283). AP2σ and AP2α subunits have also both been shown to be involved in recognition of dileucine motif internalisation signals on transmembrane cargo, with mutations on either subunit leading to impaired internalisation (32). The Arg15His, Thr112Met and Glu142Lys variants are both predicted to disrupt polar contacts between AP2σ and AP2α, and are both associated with impaired Ca^{2+}_{I} signalling, thus they may exert their effect through destabilising the interaction between the α- and σ-subunits and impairing the function of AP2. Additionally, mutation from the acidic amino acid Glu to the basic amino acid Lys is also likely to affect the protein structure and function through the change in the chemical property of this residue.Met117Ile is not predicted to disrupt polar contacts, but the software used to predict the effects of mutations on protein structure may not capture all effects of a mutation on the protein structure *in vivo*, for example, the effects of the insertion of a large aromatic ring may interfere with interactions with other structures through the nature of its size. As Met117Ile also occurs on the α4-helix of the σ-subunit, it could also exert an effect on the interaction with AP2α, as Thr112Met and Glu142Lys are predicted to.

9.2 Establishing mouse models of FHH3

I have generated 3 *knock-in* mouse models using CRISPR-Cas technology (266), the *Ap2s1-Arg15Leu* mouse, the *Ap2s1-Arg15Cys* mouse and the *Ap2s1-Met117Ile* mouse. The *Ap2s1-Arg15Cys* and *Ap2s1-Arg15Leu* mouse harbour mutations seen in patients with FHH3, and

have established 2 mouse models of FHH3 where previously no mouse model existed. The *Ap2s1-Met117Ile* mouse has been generated to allow further investigation into the novel AP2σ variant described in chapter 5, that has been shown to be associated with reduced intracellular calcium signalling *in vitro*, and is associated with hypercalcaemia in a patient (260). It does not have a calcitropic phenotype.

9.2.1 The Ap2s1-Arg15Leu and Ap2s1-Arg15Cys mouse models

9.2.1.1 The *Ap2s1*$^{+/L15}$ mouse phenotype

The calcitropic phenotype of our *Ap2s1*$^{+/L15}$ mouse compares favourably to FHH3 patients harbouring heterozygous Arg15Leu mutations. The *Ap2s1*$^{+/L15}$ mouse is substantially hypercalcaemic (Figure 29, Table 14) as seen in FHH3 patients (192). However this hypercalcaemia is a more substantial elevation compared to WT mice than that seen in FHH3 patients with Arg15Leu mutations when compared to the normal range (Table 25). The *Ap2s1*$^{+/L15}$ mouse has significant hypermagnesaemia compared to WT litter mates (Figure 29, Table 14), a finding which is again demonstrated in FHH3 patients with Arg15Leu mutations. The increased PTH concentrations and hypophosphataemia seen in our *Ap2s1*$^{+/L15}$ mice (Figure 29, Table 14) has been demonstrated in two large FHH3 kindreds, where hypercalcaemic family members have significantly increased serum PTH concentrations with mild hypophosphatemia compared to normocalcaemic relatives (193, 194).

The *Ap2s1*$^{+/L15}$ mice were found to have elevated FGF23 concentrations (Figure 29, Table 14). FGF-23 is secreted by osteocytes in response to an elevated $1,25(OH)_2D_3$ or PTH concentration and acts on the kidney proximal tubules to inhibit reabsorption and increase excretion of

phosphate. It also inhibits 1α-hydroxylase, thereby exerting a negative feedback on $1,25(OH)_2D_3$ and promotes the action of $1,25(OH)_2D_3$ 24-hydroxylase, leading to lower levels of $1,25(OH)_2D_3$ and reduced calcium absorption from the gut. The elevated FGF23 concentrations seen in our mouse model may partly explain their hypophosphataemia, however, their 1,25-dihydroxyvitamin D concentrations were normal (Figure 29, Table 14) and might be expected to be lowered in the presence of an elevated FGF23. As 1,25-dihydroxyvitamin D synthesis is promoted by the action of PTH on 1α-hydroxylase, it may be that the elevated PTH concentration seen in our mice is enough to counteract this effect. Neither FGF23 or 1,25-dihydroxyvitamin D concentrations have been reported in FHH3 patients, but it would be interesting to see if the changes observed in our mouse model were also seen in humans. In support of this, FGF23 has been found to be elevated in both mouse models and patients with PHPT (284, 285).

However there were some differences between the calcitropic phenotype of the *Ap2s1*$^{+/L15}$ mouse and patients with FHH3. ALP activity was found to be significantly elevated in our mouse model (Figure 29, Table 14). The origin of this elevated ALP activity is unclear. Experimental studies have shown that mouse kidney, intestine and bone contain significant ALP activity, however, mouse colon and, in contrast to humans, mouse liver do not (286). The elevated ALP activity seen in the *Ap2s1*$^{+/L15}$ mouse is unlikely to be skeletal as the mice had normal concentrations of the bone turnover marker P1NP (Figure 32, Table 14), suggesting kidney or intestine as possible sources. Another difference between the *Ap2s1*$^{+/L15}$ mouse and patients with FHH3 is in urinary excretion of calcium. Both male and female FHH3 patients are hypocalciuric (UCCCR <0.01) (192, 194), whereas low urinary calcium excretion was only

observed in *Ap2s1*$^{+/L15}$ females and not males (Figure 29,Table 14). Male mice have been observed to have higher urinary calcium excretion than female mice due to an inhibitory effect of androgens on luminal transient receptor potential vanilloid-subtype 5 (TRPV5) active renal calcium transport (287), and 5α-DH-testosterone has been shown to upregulate TRPV5 in primary tubular cells *in vitro* (287). Studies of human stone-formers have shown that both urinary androgens and oestrogens are significantly associated with urinary calcium excretion, and that these associations are in part modified by diet (288). The effect of oestrogens, themselves influenced by a myriad of internal and external factors in free-living subjects, including the menstrual cycle, pregnancy, weight and environmental exposures to toxins, may explain why this observation is not seen in FHH3 patients. Reduced bone mineral density is a frequent finding in FHH3 patients, but was not seen in the *Ap2s1*$^{+/L15}$ mouse for reasons that are unclear.

Patients with FHH3 have been observed to have co-existing non-calcitropic conditions, including learning disabilities, autism and short stature, in addition to their calcitropic phenotype (192) (Table 6), and have been found to be shorter than patients with FHH1 (289). Adult *Ap2s1*$^{+/L15}$ mouse appeared grossly morphologically normal and were observed to behave similarly to WT mice with eating, drinking, grooming, activity levels and interacting with cage-mates. However, male, but not female, *Ap2s1*$^{+/L15}$ mice had a significantly reduced body weight compared to age-matched WT male mice (Table 14), which may be analogous to the short stature observed in patients. The reason for the sex difference in weight is unclear. Adult female, but not male, *Ap2s1*$^{+/L15}$ mice were found to have additional non-calcitropic features that have not been reported in patients. These included lower plasma urea

concentrations (Figure 31,Table 15), lower total cholesterol and HDL cholesterol (Figure 31,Table 15), and increased bilirubin concentrations (Figure 31, Table 15). The ubiquitous expression of AP2 may explain these findings. Urea-Transport A (UT-A) urea transporters are an important mechanism for delivering urea to the inner medullary interstitium and allowing the formation of concentrated urine. Regulating the retention of UT-A1 in the apical plasma membrane may be an important mechanism for controlling urea transport activity, and the endocytosis of these receptors has been shown to be mediated by both caveolae- and clathrin-coated pit pathways, which are likely to involve AP2 (290). AP2 has also been shown to play a role in the biliary excretion of bile salts, and the dysfunction of this mechanism has been shown to cause intrahepatic cholestasis (291). The ATP binding cassette transporter A-1 (ABCA1) regulates HDL cholesterol concentrations by promoting efflux of cellular cholesterol and the formation of HDL particles (292). ABCA1-mediated cholesterol efflux is influenced by clathrin-dependent and independent endocytic pathways (293), again likely to involve AP2. Arg15Leu mutation-mediated AP2 dysfunction in our mice may explain the elevations in urea, bilirubin and cholesterol concentrations, however why this effect is only seen in female mice remains unclear. Further studies are required to elucidate the mechanisms behind these observations and to assess whether the same changes can be seen in FHH3 patients.

In addition to the measurement of non-calcitropic biochemistry, the *Ap2s1-Arg15Leu* mouse was also analysed for evidence of non-calcitropic structural abnormalities to further investigate the non-calcitropic phenotype seen in some FHH3 patients. As the vast majority of *Ap2s1*$^{L15/L15}$ mice were not viable, the 2 male homozygotes who survived to adulthood may

not be representative of the majority of mice harbouring the homozygous mutation. For this reason we decided to use micro-CT of *Ap2s1-Arg15Leu* mouse embryos to allow analysis and comparison of greater numbers of each genotype at the same developmental stage.

Embryonic development of inbred C57BL/6 mice has been well characterised and it is expected for there to be a degree of intra- and inter-litter variation in actual stages of embryos where days of gestation are used for staging (272). However, the *Ap2s1*$^{L15/L15}$ mouse embryos had greater variability in embryo size than the WT and heterozygous embryos, such that 44% of homozygous mutant embryos were measured to be outside of the expected size range for their gestation (Figure 37). There was no clear difference in the mean embryo lengths or volumes, or the range of measurements, between the WT and *Ap2s1*$^{+/L15}$ embryos. The variability in size and possible increased volume of the *Ap2s1*$^{L15/L15}$ embryo group supports the idea that homozygosity affects the development of the embryo at an early stage, as evidenced by the high rate of embryonic lethality. It may be that other factors are affecting the development of *Ap2s1*$^{L15/L15}$ embryos. Most homozygotes appeared to have a larger volume when compared to WT and *Ap2s1*$^{+/L15}$ embryos, however there was one embryo which is clearly much smaller. Similarly, most *Ap2s1*$^{L15/L15}$ embryos died before or shortly after birth, however, 2 were able to survive until adulthood.

Abnormal kidney development was observed in 75% of heterozygous and 77% of homozygous mutant embryos. The *Ap2s1*$^{+/L15}$ and *Ap2s1*$^{L15/L15}$ mice kidneys do not have any clear difference in the overall size or shape of the kidneys when compared to the WT mouse kidney. However, the *Ap2s1*$^{+/L15}$ and *Ap2s1*$^{L15/L15}$ mice did have visibly dilated renal pelvises and calices when compared to the WT mouse, with this dilation more pronounced in the

Ap2s1$^{L15/L15}$ mouse than the *Ap2s1*$^{+/L15}$ mouse (Figure 38). The dilatation may reflect the direct effect of higher serum calcium concentrations on the embryo kidney, or may be due to the AP2σ mutation itself having direct effects on an alternative signalling pathway.

Similarly, abnormal brain ventricle development in the form of hydrocephalus was observed in 37% of *Ap2s1*$^{+/L15}$ mice and 44% of *Ap2s1*$^{L15/L15}$ mice, which may be due to a direct effect of higher serum calcium concentrations on the developing nervous system, or the AP2σ mutation itself having direct effects on an alternative signalling pathway. This evidence of CNS effects in mouse embryos harbouring *Ap2s1-Arg15Leu* mutations ties in with the finding of an association of learning disabilities in patients with FHH3 and congenital disorders of neurodevelopmental abnormalities in association with AP2μ mutations and mutations of other APs which predominately affect the skin and CNS (Table 1). Interestingly, 6 out of our cohort of 9 patients with Arg10 variants and neurodevelopmental disorders had MRI brains performed. Of these, 3 were normal and 3 were abnormal (one showed features of an intracerebral haemorrhage that had occurred at one month old, one showed medial temporal sclerosis and one showed white matter hypoplasia) (Table 22).

Cinacalcet has been shown to lower calcium and PTH concentrations in FHH3 patients (268-270), and was demonstrated to do the same in the *Ap2s1*$^{+/L15}$ mouse (Figure 35). A single 60mg/kg bolus of cinacalcet resulted in a rapid, but unsustained, lowering of plasma PTH by over 50%. The same dosing regimen caused a substantial lowering of plasma calcium, although concentrations remained above those seen in WT mice.

9.2.1.2 The *Ap2s1*$^{+/C15}$ mouse phenotype

The *Ap2s1*$^{+/C15}$ mouse was investigated for the calcitropic phenotype seen in FHH3 patients harbouring the Arg15Cys mutation. The *Ap2s1*$^{+/C15}$ mouse demonstrated the significant hypercalcaemia and hypophosphataemia (Figure 40, Table 19) described in FHH3. Some of the expected biochemical changes were demonstrated in a sex specific manner. Magnesium concentrations were significantly elevated in males, but not females (Figure 40, Table 19) for reasons that are unclear. As seen in the *Ap2s1*$^{+/L15}$ mouse, the UCCCR was significantly lower in females, but not males (Figure 40, Table 19). Deviations from the human FHH3 phenotype were also seen. Plasma ALP activity was again elevated, as seen in the *Ap2s1*$^{+/L15}$ mouse, but not in FHH3 patients, this time in male mice only (Figure 40, Table 19). Plasma PTH concentrations appeared higher than in WT mice, as would be expected, but this increase was not significant (Figure 40, Table 19). There were no significant changes in bone mineral density or bone turnover in the *Ap2s1*$^{+/C15}$ mice, as seen in the *Ap2s1*$^{+/L15}$ mice, and reduced BMD is a frequent observation in FHH3 patients (192). The *Ap2s1*$^{+/C15}$ mouse was also investigated for the non-calcitropic findings seen in the *Ap2s1*$^{+/L15}$ mouse (Table 19). In contrast to the *Ap2s1*$^{+/L15}$ mouse, cholesterol and bilirubin concentrations were not significantly different in the *Ap2s1*$^{+/C15}$ mouse than that seen in WT mice. However, the increased urea was again demonstrated in female, but not male mutant mice (Table 19).

9.2.1.3 Comparison of the *Ap2s1*$^{+/C15}$ and *Ap2s1*$^{+/L15}$ mouse

The calcitropic phenotypes of the *Ap2s1*$^{+/C15}$ and *Ap2s1*$^{+/L15}$ mouse were compared to each other and to the human FHH3 phenotypes (192) (Table 24, Table 25). As described in the results section, this data should be interpreted with caution as the experiments were not set up to facilitate this comparison. However, the three strains of mutant mice were generated

on the same background (C57BL/6J) and results were obtained using standard protocols across the groups. To allow comparison of the heterozygous and homozygous mutant mice against each other, all mutant groups were compared against a single group of WT mice, which is not ideal as in usual circumstances the best comparator is WT littermates. This comparison assumes that there is no difference between the WT littermates of any of the three mutant strains. To test this, the results of calcitropic testing from the WT littermates of each of the Ap2s1 mutant strains *Ap2s1-Met117Ile*, *Ap2s1-Arg15Cys* and *Ap2s1-Arg15Leu*, were compared with each other to look for significant differences between the groups. The results showed that there was no difference in mouse ages, plasma adjusted-calcium, PTH, phosphate, or ALP concentrations between the 3 strains. However, the *Ap2s1-Arg15Leu* WT mice were slightly smaller than the *Ap2s1-Arg15Cys* WT mice. Additionally, serum magnesium concentrations were higher in the *Ap2s1-Met117Ile* WT mice than the *Ap2s1-Arg15Leu* WT mice, and the *Ap2s1-Arg15Cys* WT mice had significantly higher urinary CCCR results than the *Ap2s1-Met117Ile* and *Ap2s1-Arg15Leu* WT mice (Table 23). These differences are likely to reflect variation in experimental conditions.

The mouse models have more significant elevations in their serum calcium concentrations than is seen in the human phenotype (~19.7% and ~27.5% higher than in WT mice, compared to ~10.4% above the upper limit of normal in FHH3 patients) (Table 25). Analysing FHH3 patients by genotype reveals that those with the Arg15Cys mutation have serum albumin-adjusted calcium concentrations ~8.8% higher, and those with the Arg15Leu mutation have serum albumin-adjusted calcium concentrations ~17.7% higher than the upper limit of normal (2.83 and 3.06 vs 2.60 mmol/l respectively). These data also show that the 2 mouse models

demonstrate the genotype-phenotype correlation in serum calcium concentrations seen in FHH3 patients (192), with serum calcium concentrations higher in the *Ap2s1*$^{+/L15}$ mouse than the *Ap2s1*$^{+/C15}$ mouse and (~27.5% higher vs ~19.7% higher compared to WT). However, this difference in hypercalcaemia is less pronounced than that seen between patients harbouring the Arg15Leu mutation compared to the Arg15Cys mutation (~17.7% compared to ~8.8%) (Table 25).

The number of *Ap2s1*$^{C15/C15}$ mice born did not differ from expected, however they had reduced survival, with 10/19 dying by 3 weeks of age, and 11 dying by 10 weeks of age (Table 18). *Ap2s1*$^{C15/C15}$ mice were found to weigh significantly less (Table 19) and to have lower bone mineral density than their WT litter mates (Table 20). Their serum calcium concentration was significantly higher than both WT and heterozygous mice (Figure 40, Table 19). Again, in contrast to the *Ap2s1*$^{+/C15}$ mouse, they did demonstrate significant hypermagnesaemia and lower urinary calcium excretion (Figure 40, Table 19).

The *Ap2s1*$^{L15/L15}$ homozygotes were sub-viable, with most dying within 48 hours (Table 13), much earlier than is seen in the *Casr*$^{-/-}$ (230) and *Ap2s1*$^{C15/C15}$ mice. The two male *Ap2s1*$^{L15/L15}$ mice that survived to adulthood both had more severe hypercalcaemia, higher PTH concentrations and lower phosphate concentrations than their male *Ap2s1*$^{+/L15}$ litter mates (Figure 35). The increased lethality associated with the homozygous *Ap2s1*$^{L15/L15}$ mutation when compared to the *Ap2s1*$^{C15/C15}$ mice could be explained by the mutations having a dose-dependent effect, where the Arg15Leu mutation has been shown to be more severe than the Arg15Cys mutation in heterozygotes (Table 25, Figure 42). Non-calcitropic phenotypes appear to be more common in FHH3 patients with the Arg15Leu mutation than the Arg15Cys

mutation (Table 6, Table 26). It could also be that the Arg15Leu mutation has a greater effect on AP2 function and CME outside of the CaSR and its role in calcium homeostasis.

Searching the literature has not revealed any reported cases of patients with homozygous or compound heterozygous mutations of *AP2S1*. NSHPT is a potentially fatal condition, caused by homozygous or compound heterozygous mutations of the CaSR, manifesting in the first few days of life. Patients have severe hypercalcaemia with associated complications including respiratory distress from hypotonia and rib cage deformities, bone under-mineralisation and multiple fractures. There is an existing mouse model of NSHPT, the $Casr^{-/-}$ mice (230), where deaths typically occur within 3-30 days after birth (230). The $Ap2s1^{C15/C15}$ and $Ap2s1^{L15/L15}$ mice both harbour homozygous mutations that effect a loss-of-function on the CaSR, therefore might be expected to recapitulate the NSHPT phenotype. However, this was not the case. The $Ap2s1^{C15/C15}$ mice were subviable, but significant numbers survived to adulthood without succumbing to the conditions that affect NSHPT patients. In contrast, the $Ap2s1^{L15/L15}$ mice were not viable and only 2 mice survived to adulthood for analysis. Additionally, examination of $Ap2s1^{L15/L15}$ mouse embryos revealed non-calcitropic abnormalities including hydrocephalus, which is not seen in NSHPT patients.

Age-related increases in plasma PTH concentrations have been described in one large FHH3 kindred found to be harbouring the Arg15Cys mutation (155, 193, 194). This was demonstrated in both the $Ap2s1^{+/C15}$ and $Ap2s1^{+/L15}$ mouse models, although in the $Ap2s1^{+/L15}$ mouse it was seen in females only. The aetiology of this age-related increase in PTH and basis of the gender differences remain to be elucidated.

9.2.2 The Ap2s1-Met117Ile mouse

Ap2s1-Met117Ile mutant mice were generated to further investigate the Met117Ile *AP2S1* variant described in chapter 6. This variant was found in a patient demonstrated to have mild hypercalcaemia, although information about co-existing medical problems was missing (Table 7). *In silico* modelling predicted that Met117Ile would be deleterious and possibly damaging in terms of protein function (Table 10) and that it would have no effect on protein structure. *In vitro* studies demonstrated that the variant impaired intracellular calcium signalling in a comparable way to the FHH3-causing mutation Arg15His (Figure 27, Figure 28). The *Ap2s1*$^{+/M117I}$ and *Ap2s1*$^{I117/I117}$ mice were healthy and fertile, the proportion of weaned offspring did not deviate significantly from the Mendelian inheritance expected ratio of 1:2:1 (Table 21) and all mice appeared phenotypically normal (Table 22). Plasma biochemical analysis revealed that *Ap2s1*$^{+/M117I}$ and *Ap2s1*$^{M117I/M117I}$ mice were not significantly hypercalcaemic and their plasma PTH, plasma phosphate concentrations and fractional excretion of calcium did not differ from WT (Table 22). In addition, no significant differences were seen in plasma ALP, magnesium, sodium, potassium, urea and creatinine between the groups, and there was no significant difference in bone mineral density (Table 22). Limited non-calcitropic phenotyping was performed (urea, creatinine and electrolytes), and again no differences were found between mutant mice and their WT litter mates. The *Ap2s1-Met117Ile* mutant mice therefore do not recapitulate the human FHH3 calcitropic phenotype. There are many possible explanations for this finding. For example the same mutations in mice of one genetic background may cause a completely different phenotype in mice of another genetic background, an effect attributable to so called modifier genes (294). It could be that the Met117Ile variant was subject to modifier genes in this experiment, and would

cause an FHH3-like phenotype in mice of another genetic background. It may also be that the variant is not associated with a calcitropic phenotype *in vivo*, and that the hypercalcaemia observed in the patient was caused by something else. However, this does not mean that the *in vitro* results were incorrect. The *in vitro* experiment examined the effect of the variant on intracellular calcium signalling in a single cell type system (HEK293 cells). It could not account for the myriad of other regulatory mechanisms designed to maintain homeostasis that are present in a complete organism, as well as possible effects of the variant on other tissue types that may negate the effects seen *in vitro*.

9.3 Investigation of *AP2S1* variants in patients with neurocognitive disorders

In chapter 8 we have described nine individuals with developmental delay of unknown aetiology who have been found to harbour heterozygous variants of the codon 10 on *AP2S1*. Of the nine individuals, 8 had a novel C-to-T transversion at nucleotide c.28, resulting in a missense substitution of the wild-type arginine (Arg) to a mutant tryptophan (Trp), and one patient had a novel heterozygous G-to-A transversion at nucleotide c.29, resulting in a missense substitution of the wild-type arginine to a mutant glutamine (Gln). Studies to investigate the effect of these AP2σ-Arg10 variants were limited due to restrictions placed on laboratory experiments by the SARS-CoV-2 (COVID-19) pandemic, however, preliminary investigations have been made.

Evidence supports a causative role for these AP2 variants in neurocognitive disorders. AP2-mediated CME has been shown to be involved in numerous neurocognitive processes (274-276) and patients with Arg15Leu mutations appear to have a high incidence of concurrent

neurocognitive disorders (Table 26). Additionally, a recent publication has demonstrated that a mutation in the μ-subunit of AP2, appears to cause learning difficulties by disrupting CME at an early stage (19). It seems feasible that mutations in AP2σ could affect CME and cause learning disabilities through a similar mechanism, possibly by disrupting the interaction between AP2σ and the other AP2 subunits, α, β and μ, and thus affecting AP2 complex formation and/or the conformational changes necessary for AP2 complex activation. Additionally, micro-CT analysis of *Ap2s1-Arg15Leu* mice embryos has demonstrated hydrocephalus in heterozygous and homozygous mutant mice, with the degree of hydrocephalus appearing to be more pronounced in the homozygous mice.

In these preliminary studies, only the AP2σ-Arg10Trp variant was investigated *in vitro* and it was not demonstrated to affect the stability of the interaction between the CaSR and AP2σ in co-IP studies. This supports the prediction from crystal structure modelling that Arg10Trp does not affect the Ap2s1 protein crystal structure or any of its interactions with other molecules. However, Arg10Trp does appear to reduce cell proliferation suggesting that it is having an adverse effect on cell function via a different mechanism. The AP2σ-Arg10Trp variant appears to have a lower molecular weight than AP2σ-WT and AP2σ-Arg15Leu on Western blotting which provides an interesting avenue for further investigation. There are several possible reasons for the lower molecular weight including misfolding of the protein due to the mutation itself, but this seems unlikely as the Western blot gel is denaturing. Other causes include changes to methylation of arginine residues or to other post-translational modifications. Phosphorylation of AP2μ has been shown to stabilise the open conformation of AP2 and enhance its ability to bind membranes (28). It may be that Arg10Trp mutations

affect post-translational modifications to AP2σ that in turn has effects on AP2 function. The other Arg10 variant in our cohort, AP2σ-Arg10Gln, was predicted to result in loss of a polar contact between the AP2σ and AP2β subunits, suggesting that it would affect the stability of the AP2 tetramer. This finding will benefit from further investigation *in vitro*.

Our immunoprecipitation studies have also demonstrated that the FHH3-causing AP2σ-Arg10Leu mutation disrupts the stability of the interaction between the CaSR and AP2σ. Crystal structure modeling of the Arg15Leu mutation predicts loss of a polar contact between AP2σ and the dileucine motif found on cargo proteins including the CaSR (192), and our studies support this mechanism *in vitro*. These findings suggest that the neurocognitive disorders found in some patients with Arg15Leu mutations could be caused by a disruption to CME at an early stage in a similar mechanism to that seen in some patients with AP2μ mutations.

10 FUTURE STUDIES

In chapter 6 we described how we identified novel variants in AP2S1 from large population datasets. This work has shown that variants on codons outside of Arg15, Thr112Met, Met117Ile and Glu142Lys, can affect intracellular calcium signalling and may cause FHH3 (260). These variants are all located in the α4-α5 helix region of AP2σ, which is known to form interactions with the AP2α subunit, important for AP2 function. The effect of these variants on AP2 complex stability can be determined through co-immunoprecipitation studies. This will help to determine if they affect the interaction between AP2σ and AP2α, and between the 2 subunits and the CaSR. To further investigate this, the 18 residues of the α4 helix will be individually mutated in the pBI-CMV4-RFP-*AP2S1* construct, and these constructs will be transiently transfected into HEK-CaSR cells to determine their effects on CaSR signalling. These further studies of α4 helix mutants will benefit from a high throughput intracellular calcium assay as an alternative to the flow cytometry based assay that has been used previously. The Fluo-4 assay, which can be run in a 96-well plate format on a PHERAStar instrument, allows automated injection of increasing Ca^{2+}_e to cells, and offers a high-throughput alternative to the flow cytometry assay (232). In order to use this assay effectively, the system requires optimisation with known AP2σ mutations to ensure that mutations can be detected. Optimisation of the fluo-4 assay is ongoing. Calcimimetic drugs have been shown to ameliorate the effects of FHH3-causing mutations both *in vitro* and *in vivo* (210). The high throughput assay will also be used to determine the effects of calcimimetic drugs on the 3 *AP2S1* variants found to be associated with impaired Ca^{2+}_i

signalling, Thr112Met, Met117Ile and Glu142Lys, and any variants of interest identified from the α4 helix investigation.

When evaluating the variants found in chapter 6, I found that variants predicted to be deleterious and damaging/possibly damaging using the *in silico* tools SIFT and PolyPhen-2 did not reliably produce an effect on intracellular calcium signalling in my experimental studies. In the dbSNP and ExAC datasets we identified a significantly lower number of missense and nonsense variants in *AP2S1* than the frequency expected for a protein of 142 amino acids, and the *AP2S1* gene is highly evolutionarily conserved, implying that each codon is likely to have important structure-function roles in the AP2σ protein. As AP2 is ubiquitously expressed, mutations affecting the complex may potentially exert effects on any number of intracellular processes. Therefore, these variants predicted to be deleterious and damaging/possibly damaging could have an effect *in vivo*, just not on calcium signalling.

Phe52Tyr was predicted to be deleterious and damaging/possibly damaging, but was not associated with hypercalcaemia in a patient and did not affect intracellular calcium signalling. This variant is therefore likely to be benign, but the possibility remains that it could be causing or contributing to one of the patients other medical problems. The remaining variants not associated with a change in intracellular calcium signalling, Arg3His, Ala44Thr, Arg61His and Glu122Gly, were identified from the dbSNP and ExAC datasets, which are often considered to be representative of the "normal" population, with variants assumed to be benign polymorphisms. However, the sequencing data is taken from patients with a range of diagnoses, such as type 2 diabetes, neuropsychiatric disorders and inflammatory bowel disease, which may have a genetic basis of their own and which these variants may be causing

or contributing to. The challenge lies in selecting the most likely of these variants to be pathogenic, and in the absence of robust phenotypic data, where to start with experimental studies. In chapter 8 we have described *AP2S1* variants that are associated with neurocognitive disorders and are planning to investigate the non-calcitropic effects of these variants. As a simple preliminary investigation, Arg3His, Ala44Thr, Arg61His and Glu122Gly could be included in this further analysis.

In chapter 7 I described how we have generated 2 mouse models of FHH3, the *Ap2s1-Arg15Leu* and *Ap2s1-Arg15Cys* mice, which recapitulate the human phenotype. These mice will enable further characterisation of the non-calcitropic phenotype associated with FHH3 and evaluation of the roles of AP2σ in calcium homeostasis and endosomal trafficking of the CaSR through pathophysiological studies that are difficult to undertake in patients. In the first instance, tissue from these mice may be used to confirm that the results of our investigations in vitro are also seen *in vivo*. Subsequent to my experimental studies, mouse kidneys have been used for co-IP studies and have confirmed that Leu15 impairs the interactions between AP2σ and the other subunits (AP2α, AP2β2 and AP2μ2) of the AP2 heterotetramer (243). Investigations are underway to determine if the *Ap2s1-Arg15Leu* mice exhibit any behavioural abnormalities suggestive of neurocognitive disorders, or have any other non-calcitropic abnormalities attributable to the mutation.

Age-related increases in plasma PTH concentrations have been described in one large FHH3 kindred found to be harbouring the Arg15Cys mutation (155, 193, 194). This was demonstrated in both the *Ap2s1*$^{+/C15}$ and *Ap2s1*$^{+/L15}$ mouse models, although in the *Ap2s1*$^{+/L15}$ mouse it was seen in females only. The aetiology of this age-related increase in PTH and basis

of the gender differences remains to be elucidated. Histological examination of the parathyroid glands in both mouse models will be undertaken in the first instance. This may reveal hyperplasia, the presence of a nodule or nodules or histologically normal looking glands in the affected mice.

We have also found abnormalities in the *Ap2s1-Arg15Leu* and *Ap2s1-Arg15Cys* mice which have not been documented in FHH3 patients harbouring these mutations. Urea, bilirubin, HDL and total cholesterol concentrations were found to be elevated in female, but not male, $Ap2s1^{+/L15}$ mice. Urea was also elevated in female, but not male $Ap2s1^{+/C15}$ and $Ap2s1^{C15/C15}$ mice, and an elevated total cholesterol was found in female, but not male $Ap2s1^{C15/C15}$ mice. Further studies are required to elucidate the mechanisms behind these observations and to assess whether the same changes can be seen in FHH3 patients, and if they also have a difference between the sexes in humans. FGF23 concentrations were also found to be elevated in $Ap2s1^{+/L15}$ mice. Neither FGF23 or 1,25-dihydroxyvitamin D concentrations have been reported in FHH3 patients, but it would be interesting to see if the changes observed in our mouse model were also seen in humans.

I also described the *Ap2s1-Met117Ile* mouse that does not appear to have a phenotype and have discussed the possible reasons for this. It would be interesting to further investigate the Met117Ile *in vitro* to determine its mechanism of action. It may be that it affects the interaction between the AP2 subunits, or between AP2 and the CaSR, as in the Arg15Leu mutation. It may have effects similar to those resulting in a change in molecular weight caused by Arg10 variant Arg10Trp that are not yet fully elucidated. If a mechanism were found, it would be interesting to determine how the effects are ameliorated *in vivo* and why they do

not do ameliorate the effects of Arg15Cys and Arg15Leu mutations. This could provide novel insights into intracellular calcium signalling and potentially suggest therapeutic drug targets. When interpreting these studies, it would be particularly interesting to have additional evidence to confirm that Met117Ile causes hypercalcaemia in patients, rather than is associated with it. In our patient with Met117Ile we did not have any clinical details, so it may be that the hypercalcaemia was secondary to another cause and Met117Ile does not cause a calcium phenotype in humans. As with the Thr112Met and Glu142Lys mutations which were shown to affect intracellular calcium signalling but for which paired phenotypic data was not available, in an ideal world we would have access to patients with the variants so that any hypercalcaemia can be determined and clinically assessed. A more likely scenario is that these variants are detected during the course of investigations for known-mutation negative FHH cases, or are found as more patients are added to the DiscovEHR-Regeneron database. It would be interesting to see if differences really did exist between the effects of Met117Ile in humans and mice, and to understand the reasons for this.

Studies to investigate the effect of AP2σ-Arg10 variants were limited due to restrictions placed on laboratory experiments by the SARS-CoV-2 (COVID-19) pandemic and I had made a plan for further work based on the initial findings presented in this thesis. However, I was limited in my capacity to undertake further lab work as restrictions lifted as I had already been redeployed to clinical work early. This project is now being taken forward by my supervisor, Dr Mark Stevenson, and I will describe both my plans, and the findings that have now been demonstrated.

I had planned to quantify the effect of AP2σ-Arg10Trp and AP2σ-Arg15Leu on cell growth using a proliferation assay. If reduced cell growth was confirmed then I planned to repeat the assay to include cells treated with cinacalcet to see if this can rectify the effect.

Arg10Trp was not demonstrated to affect the interaction between AP2σ and the CaSR. My plan was to repeat the co-immunoprecipitation experiment to include blotting for AP2α, AP2β and AP2μ-subunits to see if the Arg10Trp variants affect their interaction with each other and with the CaSR. This work has now been undertaken and Dr Mark Stevenson has demonstrated that the Arg10Trp variant affects the interaction between AP2σ and AP2μ.

Arg10Trp was demonstrated to have a lower molecular weight on Western blotting so I planned to to further investigate the cause of this using mass spectrometry, with a hope that Arg10Gln, and the other possible AP2σ-Arg10 variants, Arg10Pro, Arg10Leu and Arg10Gly, should also be investigated in the same way. Work on this has already begun, however the Arg10Gly variant has not been possible to generate and is not seen in humans suggesting it might have a catastrophic effect on protein function. The variants were not demonstrated to have any effect on post-translational modification, but the Arg10Trp variant has been found to be truncated. The current hypothesis is that the variant results in a novel enzyme binding site producing cleavage of AP2σ, and work on this continues.

AP2μ mutations have been demonstrated to affect the CME of transferrin and to cause neurocognitive dysfunction so I had considered investigating the effect of Arg10Trp, the other Arg10 variants, and the FHH3-associated Arg15 variants on this process. The *AP2S1* variants that did not affect intracellular calcium signalling, but were predicted to be deleterious and

damaging/possibly damaging in chapter 5, Arg3His, Ala44Thr, Arg61His and Glu122Gly, could also be included in these studies if resources allowed.

As described, work by Dr Mark Stevenson had demonstrated that the Arg10Trp variant affected the interaction between AP2σ and AP2μ. He has gone on to show that the Arg10Trp variant also affects the CME of transferrin, likely through disruption of AP2μ function, providing a link between the variant and neurocognitive disorders.

11 APPENDIX

Table 32. Whole body dual-energy X-ray absorptiometry (DXA) analysis of WT and *Ap2s1*$^{+/L15}$ mice, aged 16-17 weeks. BMC=bone mineral content; BMD=bone mineral density. [A]Corrected for body weight. All values are expressed as mean±SEM. One-way ANOVA followed by Sidak's test for pairwise multiple comparisons were used for all analyses. Data published in Hannan et al (2021) (243).

	Male		**Female**	
	WT	***Ap2s1*$^{+/L15}$**	**WT**	***Ap2s1*$^{+/L15}$**
BMC[A] (mg/g)	23.6±0.9 (n=12)	21.6±0.2 (n=10)	25.4±0.4 (n=11)	23.9±1.1 (n=11)
BMD (mg/cm^2)	75.2±1.2 (n=12)	71.4±0.9 (n=12)	70.5±0.9 (n=11)	67.6±1.6 (n=11)
Fat mass (%)	15.4±1.6 (n=12)	13.3±0.3 (n=11)	16.4±0.9 (n=11)	14.9±1.4 (n=11)

Table 33. Comparison of calcitropic biochemistry between male homozygous (*Ap2s1*$^{L15/L15}$) mice (aged 18-22 weeks) and age-matched male WT and male heterozygous (*Ap2s1*$^{+/L15}$) mice. [A]Individual values are shown for the two male homozygous mice. Adj-calcium=plasma albumin-adjusted calcium; PTH=parathyroid hormone. Data published in Hannan et al (2021) (243).

	WT	***Ap2s1*$^{+/L15}$**	**[A] *Ap2s1*$^{L15/L15}$**
Adj-calcium (mmol/l)	2.36±0.01 (n=4)	2.91±0.01 (n=5)	3.12, 3.22
PTH (ng/l)	42.0±11 (n=3)	94.3±24 (n=5)	134, 180
Phosphate (mmol/l)	1.92±0.10 (n=4)	1.32±0.05 (n=5)	1.17, 1.18

Table 34. Effect of a single 60 mg/kg bolus of cinacalcet on plasma adjusted calcium and parathyroid hormone (PTH) concentrations at 0, 1, 2 and 4 hours post dose in adult WT (*Ap2s1*$^{+/+}$) and *Ap2s1*$^{+/L15}$ mice, aged 15-22 weeks. Adj-calcium=plasma albumin-adjusted calcium. Mean±SEM values for respective groups are indicated. *p<0.05, **p<0.01; ***p<0.001, for time point mice versus 0 hours. One-way ANOVA followed by Sidak's test for pairwise multiple comparisons were used for all analyses. Data published in Hannan et al (2021) (243).

Time point	**WT**		***Ap2s1*$^{+/L15}$**	
(hours)	Adj-calcium (mmol/l)	PTH (ng/l)	Adj-calcium (mmol/l)	PTH (ng/l)
0	2.36± 0.01(n=8)	21.7± 5.6(n=7)	2.93± 0.03(n=7)	113.6± 11.3(n=7)*
1	2.17± 0.02(n=8)***	12.0± 2.0(n=8)	2.75± 0.02(n=6)**	66.1± 7.4(n=6)
2	2.00± 0.02(n=7)***	17.8± 6.8(n=6)	2.51± 0.03(n=7)***	123.0± 10.6(n=6)
4	1.95± 0.09(n=7)***	18.0± 3.6(n=7)	2.50± 0.03(n=6)**	239.0± 63.3(n=6)

Table 35. Age-related changes in plasma albumin-adjusted calcium (adj-calcium), and parathyroid hormone (PTH) of WT and *Ap2s1*$^{+/L15}$ mice from 8 weeks to 16 weeks. Adj-calcium=plasma albumin-adjusted calcium; wks=weeks. Mean±SEM values for respective groups are indicated. **p<0.01; for 8 week old mice versus 16

week old mice. One-way ANOVA followed by Sidak's test for pairwise multiple comparisons were used for analysis. Data published in Hannan et al (2021) (243).

	Male				**Female**			
	WT		***Ap2s1*$^{+/L15}$**		**WT**		***Ap2s1*$^{+/L15}$**	
	8 wks	16 wks	8 wks	16 wks	8 wks	16 wks	8 wks	16 wks
Adj-calcium (mmol/l)[A]	2.49±0.05 (n=4)	2.41±0.03 (n=8)	3.11±0.01 (n=5)	2.98±0.03 (n=4)	2.48±0.04 (n=6)	2.38±0.02 (n=9)	2.94±0.03 (n=5)	2.92±0.05 (n=5)
PTH (ng/l)	34.2±3.0 (n=5)	65.1±16.6 (n=9)	107.8±24.1 (n=5)	128.6±14.7 (n=5)	31.2±11.6 (n=5)	33.7±6.6 (n=9)	73.3±9.8 (n=5)	145.0±16.5 (n=5)**

12 REFERENCES

1. Mattera R, Boehm M, Chaudhuri R, Prabhu Y, Bonifacino JS. Conservation and diversification of dileucine signal recognition by adaptor protein (AP) complex variants. The Journal of biological chemistry. 2011;286(3):2022-30.

2. Dell'Angelica EC, Shotelersuk V, Aguilar RC, Gahl WA, Bonifacino JS. Altered trafficking of lysosomal proteins in Hermansky-Pudlak syndrome due to mutations in the beta 3A subunit of the AP-3 adaptor. Molecular cell. 1999;3(1):11-21.

3. Assoum M, Philippe C, Isidor B, Perrin L, Makrythanasis P, Sondheimer N, et al. Autosomal-Recessive Mutations in AP3B2, Adaptor-Related Protein Complex 3 Beta 2 Subunit, Cause an Early-Onset Epileptic Encephalopathy with Optic Atrophy. American journal of human genetics. 2016;99(6):1368-76.

4. Park SY, Guo X. Adaptor protein complexes and intracellular transport. Biosci Rep. 2014;34(4):e00123.

5. Wang YJ, Wang J, Sun HQ, Martinez M, Sun YX, Macia E, et al. Phosphatidylinositol 4 phosphate regulates targeting of clathrin adaptor AP-1 complexes to the Golgi. Cell. 2003;114(3):299-310.

6. Stamnes MA, Rothman JE. The binding of AP-1 clathrin adaptor particles to Golgi membranes requires ADP-ribosylation factor, a small GTP-binding protein. Cell. 1993;73(5):999-1005.

7. Bonifacino JS. Adaptor proteins involved in polarized sorting. The Journal of cell biology. 2014;204(1):7-17.

8. Gravotta D, Carvajal-Gonzalez JM, Mattera R, Deborde S, Banfelder JR, Bonifacino JS, et al. The clathrin adaptor AP-1A mediates basolateral polarity. Developmental cell. 2012;22(4):811-23.

9. Farías GG, Cuitino L, Guo X, Ren X, Jarnik M, Mattera R, et al. Signal-mediated, AP-1/clathrin-dependent sorting of transmembrane receptors to the somatodendritic domain of hippocampal neurons. Neuron. 2012;75(5):810-23.

10. Dell'Angelica EC, Mullins C, Bonifacino JS. AP-4, a novel protein complex related to clathrin adaptors. The Journal of biological chemistry. 1999;274(11):7278-85.

11. Matsuda S, Miura E, Matsuda K, Kakegawa W, Kohda K, Watanabe M, et al. Accumulation of AMPA receptors in autophagosomes in neuronal axons lacking adaptor protein AP-4. Neuron. 2008;57(5):730-45.

12. Simmen T, Höning S, Icking A, Tikkanen R, Hunziker W. AP-4 binds basolateral signals and participates in basolateral sorting in epithelial MDCK cells. Nature cell biology. 2002;4(2):154-9.

13. Hirst J, Borner GH, Edgar J, Hein MY, Mann M, Buchholz F, et al. Interaction between AP-5 and the hereditary spastic paraplegia proteins SPG11 and SPG15. Molecular biology of the cell. 2013;24(16):2558-69.

14. Dell'Angelica EC, Bonifacino JS. Coatopathies: Genetic Disorders of Protein Coats. Annu Rev Cell Dev Biol. 2019;35:131-68.

15. Montpetit A, Côté S, Brustein E, Drouin CA, Lapointe L, Boudreau M, et al. Disruption of AP1S1, causing a novel neurocutaneous syndrome, perturbs development of the skin and spinal cord. PLoS genetics. 2008;4(12):e1000296.

16. Tarpey PS, Stevens C, Teague J, Edkins S, O'Meara S, Avis T, et al. Mutations in the gene encoding the Sigma 2 subunit of the adaptor protein 1 complex, AP1S2, cause X-linked mental retardation. American journal of human genetics. 2006;79(6):1119-24.

17. Saillour Y, Zanni G, Des Portes V, Heron D, Guibaud L, Iba-Zizen MT, et al. Mutations in the AP1S2 gene encoding the sigma 2 subunit of the adaptor protein 1 complex are associated with syndromic X-linked mental retardation with hydrocephalus and calcifications in basal ganglia. Journal of medical genetics. 2007;44(11):739-44.

18. Setta-Kaffetzi N, Simpson MA, Navarini AA, Patel VM, Lu HC, Allen MH, et al. AP1S3 mutations are associated with pustular psoriasis and impaired Toll-like receptor 3 trafficking. American journal of human genetics. 2014;94(5):790-7.

19. Helbig I, Lopez-Hernandez T, Shor O, Galer P, Ganesan S, Pendziwiat M, et al. A Recurrent Missense Variant in AP2M1 Impairs Clathrin-Mediated Endocytosis and Causes Developmental and Epileptic Encephalopathy. American journal of human genetics. 2019;104(6):1060-72.

20. Nesbit MA, Hannan FM, Howles SA, Reed AA, Cranston T, Thakker CE, et al. Mutations in AP2S1 cause familial hypocalciuric hypercalcemia type 3. Nature genetics. 2013;45(1):93-7.

21. Ammann S, Schulz A, Krägeloh-Mann I, Dieckmann NM, Niethammer K, Fuchs S, et al. Mutations in AP3D1 associated with immunodeficiency and seizures define a new type of Hermansky-Pudlak syndrome. Blood. 2016;127(8):997-1006.

22. Moreno-De-Luca A, Helmers SL, Mao H, Burns TG, Melton AM, Schmidt KR, et al. Adaptor protein complex-4 (AP-4) deficiency causes a novel autosomal recessive cerebral palsy syndrome with microcephaly and intellectual disability. Journal of medical genetics. 2011;48(2):141-4.

23. Abou Jamra R, Philippe O, Raas-Rothschild A, Eck SH, Graf E, Buchert R, et al. Adaptor protein complex 4 deficiency causes severe autosomal-recessive intellectual disability, progressive spastic paraplegia, shy character, and short stature. American journal of human genetics. 2011;88(6):788-95.

24. Raza MH, Mattera R, Morell R, Sainz E, Rahn R, Gutierrez J, et al. Association between Rare Variants in AP4E1, a Component of Intracellular Trafficking, and Persistent Stuttering. American journal of human genetics. 2015;97(5):715-25.

25. Bauer P, Leshinsky-Silver E, Blumkin L, Schlipf N, Schröder C, Schicks J, et al. Mutation in the AP4B1 gene cause hereditary spastic paraplegia type 47 (SPG47). Neurogenetics. 2012;13(1):73-6.

26. Verkerk AJ, Schot R, Dumee B, Schellekens K, Swagemakers S, Bertoli-Avella AM, et al. Mutation in the AP4M1 gene provides a model for neuroaxonal injury in cerebral palsy. American journal of human genetics. 2009;85(1):40-52.

27. Słabicki M, Theis M, Krastev DB, Samsonov S, Mundwiller E, Junqueira M, et al. A genome-scale DNA repair RNAi screen identifies SPG48 as a novel gene associated with hereditary spastic paraplegia. PLoS biology. 2010;8(6):e1000408.

28. Mettlen M, Chen P-H, Srinivasan S, Danuser G, Schmid SL. Regulation of Clathrin-Mediated Endocytosis. Annual Review of Biochemistry. 2018;87(1):871-96.

29. Collins BM, McCoy AJ, Kent HM, Evans PR, Owen DJ. Molecular architecture and functional model of the endocytic AP2 complex. Cell. 2002;109(4):523-35.

30. Jackson LP, Kelly BT, McCoy AJ, Gaffry T, James LC, Collins BM, et al. A large-scale conformational change couples membrane recruitment to cargo binding in the AP2 clathrin adaptor complex. Cell. 2010;141(7):1220-9.

31. Kadlecova Z, Spielman SJ, Loerke D, Mohanakrishnan A, Reed DK, Schmid SL. Regulation of clathrin-mediated endocytosis by hierarchical allosteric activation of AP2. J Cell Biol. 2017;216(1):167-79.

32. Kelly BT, McCoy AJ, Späte K, Miller SE, Evans PR, Höning S, et al. A structural explanation for the binding of endocytic dileucine motifs by the AP2 complex. Nature. 2008;456(7224):976-9.

33. Kirchhausen T, Owen D, Harrison SC. Molecular structure, function, and dynamics of clathrin-mediated membrane traffic. Cold Spring Harbor perspectives in biology. 2014;6(5):a016725.

34. Sorkin A, von Zastrow M. Endocytosis and signalling: intertwining molecular networks. Nature reviews Molecular cell biology. 2009;10(9):609-22.

35. Kelly BT, Graham SC, Liska N, Dannhauser PN, Honing S, Ungewickell EJ, et al. Clathrin adaptors. AP2 controls clathrin polymerization with a membrane-activated switch. Science. 2014;345(6195):459-63.

36. Owen DJ, Vallis Y, Noble ME, Hunter JB, Dafforn TR, Evans PR, et al. A structural explanation for the binding of multiple ligands by the alpha-adaptin appendage domain. Cell. 1999;97(6):805-15.

37. Kaksonen M, Roux A. Mechanisms of clathrin-mediated endocytosis. Nature Reviews Molecular Cell Biology. 2018;19(5):313-26.

38. Wolfe BL, Trejo J. Clathrin-dependent mechanisms of G protein-coupled receptor endocytosis. Traffic. 2007;8(5):462-70.

39. Jean-Alphonse F, Bowersox S, Chen S, Beard G, Puthenveedu MA, Hanyaloglu AC. Spatially restricted G protein-coupled receptor activity via divergent endocytic compartments. The Journal of biological chemistry. 2014;289(7):3960-77.

40. Weinberg ZY, Puthenveedu MA. Regulation of G protein-coupled receptor signaling by plasma membrane organization and endocytosis. Traffic. 2019;20(2):121-9.

41. Herberger AL, Loretz CA. Vertebrate extracellular calcium-sensing receptor evolution: selection in relation to life history and habitat. Comparative biochemistry and physiology Part D, Genomics & proteomics. 2013;8(1):86-94.

42. Hannan FM, Nesbit MA, Zhang C, Cranston T, Curley AJ, Harding B, et al. Identification of 70 calcium-sensing receptor mutations in hyper- and hypo-calcaemic patients: evidence for clustering of extracellular domain mutations at calcium-binding sites. Human molecular genetics. 2012;21(12):2768-78.

43. Pollak MR, Brown EM, Chou YH, Hebert SC, Marx SJ, Steinmann B, et al. Mutations in the human Ca(2+)-sensing receptor gene cause familial hypocalciuric hypercalcemia and neonatal severe hyperparathyroidism. Cell. 1993;75(7):1297-303.

44. Pearce SH, Williamson C, Kifor O, Bai M, Coulthard MG, Davies M, et al. A familial syndrome of hypocalcemia with hypercalciuria due to mutations in the calcium-sensing receptor. The New England journal of medicine. 1996;335(15):1115-22.

45. Ruat M, Traiffort E. Roles of the calcium sensing receptor in the central nervous system. Best practice & research Clinical endocrinology & metabolism. 2013;27(3):429-42.

46. Uhlén M, Fagerberg L, Hallström BM, Lindskog C, Oksvold P, Mardinoglu A, et al. Proteomics. Tissue-based map of the human proteome. Science (New York, NY). 2015;347(6220):1260419.

47. Centeno PP, Herberger A, Mun H-C, Tu C, Nemeth EF, Chang W, et al. Phosphate acts directly on the calcium-sensing receptor to stimulate parathyroid hormone secretion. Nature Communications. 2019;10(1):4693.

48. Geng Y, Mosyak L, Kurinov I, Zuo H, Sturchler E, Cheng TC, et al. Structural mechanism of ligand activation in human calcium-sensing receptor. eLife. 2016;5.

49. Chang W, Tu C-L, Jean-Alphonse FG, Herberger A, Cheng Z, Hwong J, et al. PTH hypersecretion triggered by a GABA(B1) and Ca(2+)-sensing receptor heterocomplex in hyperparathyroidism. Nat Metab. 2020;2(3):243-55.

50. Thakker RV. The parathyroid glands, hypercalcemia and hypocalcemia. In: Goldman L, Schafer AL, editors. Cecil Goldman Medicine. 25th ed: Elsevier Ltd 2015. p. 1649-61.

51. Brown EM. Extracellular Ca2+ sensing, regulation of parathyroid cell function, and role of Ca2+ and other ions as extracellular (first) messengers. Physiological reviews. 1991;71(2):371-411.

52. Stokes VJ, Nielsen MF, Hannan FM, Thakker RV. Hypercalcemic Disorders in Children. Journal of bone and mineral research : the official journal of the American Society for Bone and Mineral Research. 2017;32(11):2157-70.

53. Lietman SA, Germain-Lee EL, Levine MA. Hypercalcemia in children and adolescents. Current opinion in pediatrics. 2010;22(4):508-15.

54. El Saleeby CM, Grottkau BE, Friedmann AM, Westra SJ, Sohani AR. Case records of the Massachusetts General Hospital. Case 4-2011. A 4-year-old boy with back pain and hypercalcemia. The New England journal of medicine. 2011;364(6):552-62.

55. Babar G, Alemzadeh R. A case of acute psychosis in an adolescent male. Case reports in endocrinology. 2014;2014:937631.

56. Hannan FM, Kallay E, Chang W, Brandi ML, Thakker RV. The calcium-sensing receptor in physiology and in calcitropic and noncalcitropic diseases. Nat Rev Endocrinol. 2018;15(1):33-51.

57. Hannan FM, Babinsky VN, Thakker RV. Disorders of the calcium-sensing receptor and partner proteins: insights into the molecular basis of calcium homeostasis. Journal of molecular endocrinology. 2016;57(3):R127-R42.

58. Regard JB, Sato IT, Coughlin SR. Anatomical profiling of G protein-coupled receptor expression. Cell. 2008;135(3):561-71.

59. VanHouten J, Dann P, McGeoch G, Brown EM, Krapcho K, Neville M, et al. The calcium-sensing receptor regulates mammary gland parathyroid hormone-related protein production and calcium transport. The Journal of clinical investigation. 2004;113(4):598-608.

60. Kim W, Wysolmerski JJ. Calcium-Sensing Receptor in Breast Physiology and Cancer. Frontiers in physiology. 2016;7:440-.

61. Fan Y, Liu W, Bi R, Densmore MJ, Sato T, Mannstadt M, et al. Interrelated role of Klotho and calcium-sensing receptor in parathyroid hormone synthesis and parathyroid hyperplasia. Proceedings of the National Academy of Sciences of the United States of America. 2018;115(16):E3749-E58.

62. Conigrave AD. The Calcium-Sensing Receptor and the Parathyroid: Past, Present, Future. Frontiers in physiology. 2016;7:563-.

63. Hendy GN, Canaff L. Calcium-Sensing Receptor Gene: Regulation of Expression. Frontiers in physiology. 2016;7:394-.

64. Graca JA, Schepelmann M, Brennan SC, Reens J, Chang W, Yan P, et al. Comparative expression of the extracellular calcium-sensing receptor in the mouse, rat, and human kidney. American journal of physiology Renal physiology. 2016;310(6):F518-33.

65. Atchison DK, Ortiz-Capisano MC, Beierwaltes WH. Acute activation of the calcium-sensing receptor inhibits plasma renin activity in vivo. Am J Physiol Regul Integr Comp Physiol. 2010;299(4):R1020-R6.

66. Loupy A, Ramakrishnan SK, Wootla B, Chambrey R, de la Faille R, Bourgeois S, et al. PTH-independent regulation of blood calcium concentration by the calcium-sensing receptor. The Journal of clinical investigation. 2012;122(9):3355-67.

67. Toka HR, Al-Romaih K, Koshy JM, DiBartolo S, 3rd, Kos CH, Quinn SJ, et al. Deficiency of the calcium-sensing receptor in the kidney causes parathyroid hormone-independent hypocalciuria. Journal of the American Society of Nephrology : JASN. 2012;23(11):1879-90.

68. Ba J, Brown D, Friedman PA. Calcium-sensing receptor regulation of PTH-inhibitable proximal tubule phosphate transport. American journal of physiology Renal physiology. 2003;285(6):F1233-43.

69. Topala CN, Schoeber JP, Searchfield LE, Riccardi D, Hoenderop JG, Bindels RJ. Activation of the Ca2+-sensing receptor stimulates the activity of the epithelial Ca2+ channel TRPV5. Cell calcium. 2009;45(4):331-9.

70. Renkema KY, Velic A, Dijkman HB, Verkaart S, van der Kemp AW, Nowik M, et al. The calcium-sensing receptor promotes urinary acidification to prevent nephrolithiasis. Journal of the American Society of Nephrology : JASN. 2009;20(8):1705-13.

71. Kantham L, Quinn SJ, Egbuna OI, Baxi K, Butters R, Pang JL, et al. The calcium-sensing receptor (CaSR) defends against hypercalcemia independently of its regulation of parathyroid hormone secretion. American journal of physiology Endocrinology and metabolism. 2009;297(4):E915-23.

72. Rodriguez L, Cheng Z, Chen TH, Tu C, Chang W. Extracellular calcium and parathyroid hormone-related peptide signaling modulate the pace of growth plate chondrocyte differentiation. Endocrinology. 2005;146(11):4597-608.

73. Dvorak-Ewell MM, Chen TH, Liang N, Garvey C, Liu B, Tu C, et al. Osteoblast extracellular Ca2+-sensing receptor regulates bone development, mineralization, and turnover. Journal of bone and mineral research : the official journal of the American Society for Bone and Mineral Research. 2011;26(12):2935-47.

74. Chang W, Tu C, Chen TH, Bikle D, Shoback D. The extracellular calcium-sensing receptor (CaSR) is a critical modulator of skeletal development. Science signaling. 2008;1(35):ra1.

75. Tan RSG, Lee CHL, Dimke H, Todd Alexander R. The role of calcium-sensing receptor signaling in regulating transepithelial calcium transport. Experimental Biology and Medicine. 2021;246(22):2407-19.

76. Gama L, Baxendale-Cox LM, Breitwieser GE. Ca2+-sensing receptors in intestinal epithelium. American Journal of Physiology-Cell Physiology. 1997;273(4):C1168-C75.

77. Chattopadhyay N, Cheng I, Rogers K, Riccardi D, Hall A, Diaz R, et al. Identification and localization of extracellular Ca2+-sensing receptor in rat intestine. American Journal of Physiology-Gastrointestinal and Liver Physiology. 1998;274(1):G122-G30.

78. Wongdee K, Rodrat M, Keadsai C, Jantarajit W, Teerapornpuntakit J, Thongbunchoo J, et al. Activation of calcium-sensing receptor by allosteric agonists cinacalcet and AC-265347 abolishes the

1, 25 (OH) 2D3-induced Ca2+ transport: Evidence that explains how the intestine prevents excessive Ca2+ absorption. Archives of biochemistry and biophysics. 2018;657:15-22.

79. Lee JJ, Liu X, O'Neill D, Beggs MR, Weissgerber P, Flockerzi V, et al. Activation of the calcium-sensing receptor attenuates TRPV6-dependent intestinal calcium absorption. JCI insight. 2019;4(11).

80. Cheng I, Klingensmith ME, Chattopadhyay N, Kifor O, Butters RR, Soybel DI, et al. Identification and localization of the extracellular calcium-sensing receptor in human breast. The Journal of clinical endocrinology and metabolism. 1998;83(2):703-7.

81. VanHouten JN, Neville MC, Wysolmerski JJ. The calcium-sensing receptor regulates plasma membrane calcium adenosine triphosphatase isoform 2 activity in mammary epithelial cells: a mechanism for calcium-regulated calcium transport into milk. Endocrinology. 2007;148(12):5943-54.

82. Brown EM, MacLeod RJ. Extracellular calcium sensing and extracellular calcium signaling. Physiological reviews. 2001;81(1):239-97.

83. Mizobuchi M, Hatamura I, Ogata H, Saji F, Uda S, Shiizaki K, et al. Calcimimetic compound upregulates decreased calcium-sensing receptor expression level in parathyroid glands of rats with chronic renal insufficiency. Journal of the American Society of Nephrology : JASN. 2004;15(10):2579-87.

84. Toka HR. New functional aspects of the extracellular calcium-sensing receptor. Current Opinion in Nephrology and Hypertension. 2014;23(4).

85. Riccardi D, Valenti G. Localization and function of the renal calcium-sensing receptor. Nature reviews Nephrology. 2016;12(7):414-25.

86. Lee JJ, Liu X, O'Neill D, Beggs MR, Weissgerber P, Flockerzi V, et al. Activation of the calcium sensing receptor attenuates TRPV6-dependent intestinal calcium absorption. JCI insight. 2019;5(11).

87. Bandyopadhyay S, Tfelt-Hansen J, Chattopadhyay N. Diverse roles of extracellular calcium-sensing receptor in the central nervous system. Journal of Neuroscience Research. 2010;88(10):2073-82.

88. Schepelmann M, Yarova PL, Lopez-Fernandez I, Davies TS, Brennan SC, Edwards PJ, et al. The vascular Ca2+-sensing receptor regulates blood vessel tone and blood pressure. American journal of physiology Cell physiology. 2016;310(3):C193-204.

89. Brennan SC, Wilkinson WJ, Tseng H-E, Finney B, Monk B, Dibble H, et al. The extracellular calcium-sensing receptor regulates human fetal lung development via CFTR. Scientific reports. 2016;6:21975-.

90. Liou AP, Sei Y, Zhao X, Feng J, Lu X, Thomas C, et al. The extracellular calcium-sensing receptor is required for cholecystokinin secretion in response to L-phenylalanine in acutely isolated intestinal I cells. American journal of physiology Gastrointestinal and liver physiology. 2011;300(4):G538-G46.

91. Alamshah A, Spreckley E, Norton M, Kinsey-Jones JS, Amin A, Ramgulam A, et al. l-phenylalanine modulates gut hormone release and glucose tolerance, and suppresses food intake through the calcium-sensing receptor in rodents. International journal of obesity (2005). 2017;41(11):1693-701.

92. Chattopadhyay N, Espinosa-Jeffrey A, Tfelt-Hansen J, Yano S, Bandyopadhyay S, Brown EM, et al. Calcium receptor expression and function in oligodendrocyte commitment and lineage progression: potential impact on reduced myelin basic protein in CaR-null mice. J Neurosci Res. 2008;86(10):2159-67.

93. Sundararaman SS, van der Vorst EPC. Calcium-Sensing Receptor (CaSR), Its Impact on Inflammation and the Consequences on Cardiovascular Health. International journal of molecular sciences. 2021;22(5):2478.

94. Alam MU, Kirton JP, Wilkinson FL, Towers E, Sinha S, Rouhi M, et al. Calcification is associated with loss of functional calcium-sensing receptor in vascular smooth muscle cells. Cardiovascular research. 2009;81(2):260-8.

95. Greenberg HZ, Shi J, Jahan KS, Martinucci MC, Gilbert SJ, Vanessa Ho WS, et al. Stimulation of calcium-sensing receptors induces endothelium-dependent vasorelaxations via nitric oxide production and activation of IKCa channels. Vascular pharmacology. 2016;80:75-84.

96. Molostvov G, Fletcher S, Bland R, Zehnder D. Extracellular calcium-sensing receptor mediated signalling is involved in human vascular smooth muscle cell proliferation and apoptosis. Cellular physiology and biochemistry : international journal of experimental cellular physiology, biochemistry, and pharmacology. 2008;22(5-6):413-22.

97. Sun YH, Liu MN, Li H, Shi S, Zhao YJ, Wang R, et al. Calcium-sensing receptor induces rat neonatal ventricular cardiomyocyte apoptosis. Biochemical and biophysical research communications. 2006;350(4):942-8.

98. Raggi P, Chertow GM, Torres PU, Csiky B, Naso A, Nossuli K, et al. The ADVANCE study: a randomized study to evaluate the effects of cinacalcet plus low-dose vitamin D on vascular calcification in patients on hemodialysis. Nephrology, dialysis, transplantation : official publication of the European Dialysis and Transplant Association - European Renal Association. 2011;26(4):1327-39.

99. Finney BA, del Moral PM, Wilkinson WJ, Cayzac S, Cole M, Warburton D, et al. Regulation of mouse lung development by the extracellular calcium-sensing receptor, CaR. J Physiol. 2008;586(24):6007-19.

100. Yarova PL, Stewart AL, Sathish V, Britt RD, Jr., Thompson MA, P Lowe AP, et al. Calcium-sensing receptor antagonists abrogate airway hyperresponsiveness and inflammation in allergic asthma. Sci Transl Med. 2015;7(284):284ra60-ra60.

101. Xu J, Wen X, Fu Z, Jiang Y, Hong W, Liu R, et al. Chronic hypoxia promoted pulmonary arterial smooth muscle cells proliferation through upregulated calcium-sensing receptorcanonical transient receptor potential 1/6 pathway. Microcirculation (New York, NY : 1994). 2021;28(6):e12715.

102. Engelstoft MS, Park WM, Sakata I, Kristensen LV, Husted AS, Osborne-Lawrence S, et al. Seven transmembrane G protein-coupled receptor repertoire of gastric ghrelin cells. Mol Metab. 2013;2(4):376-92.

103. Cheng SX, Lightfoot YL, Yang T, Zadeh M, Tang L, Sahay B, et al. Epithelial CaSR deficiency alters intestinal integrity and promotes proinflammatory immune responses. FEBS letters. 2014;588(22):4158-66.

104. Geibel J, Sritharan K, Geibel R, Geibel P, Persing JS, Seeger A, et al. Calcium-sensing receptor abrogates secretagogue- induced increases in intestinal net fluid secretion by enhancing cyclic nucleotide destruction. Proceedings of the National Academy of Sciences of the United States of America. 2006;103(25):9390-7.

105. Tang L, Jiang L, McIntyre ME, Petrova E, Cheng SX. Calcimimetic acts on enteric neuronal CaSR to reverse cholera toxin-induced intestinal electrolyte secretion. Scientific reports. 2018;8(1):7851.

106. Leach K, Hannan FM, Josephs TM, Keller AN, Møller TC, Ward DT, et al. International Union of Basic and Clinical Pharmacology. CVIII. Calcium-Sensing Receptor Nomenclature, Pharmacology, and Function. Pharmacological reviews. 2020;72(3):558-604.

107. Tharmalingam S, Wu C, Hampson DR. The calcium-sensing receptor and integrins modulate cerebellar granule cell precursor differentiation and migration. Developmental neurobiology. 2016;76(4):375-89.

108. Kim JY, Ho H, Kim N, Liu J, Tu C-L, Yenari MA, et al. Calcium-sensing receptor (CaSR) as a novel target for ischemic neuroprotection. Ann Clin Transl Neurol. 2014;1(11):851-66.

109. Ceglia L, Harris SS, Rasmussen HM, Dawson-Hughes B. Activation of the calcium sensing receptor stimulates gastrin and gastric acid secretion in healthy participants. Osteoporosis international : a journal established as result of cooperation between the European Foundation for Osteoporosis and the National Osteoporosis Foundation of the USA. 2009;20(1):71-8.

110. Dufner MM, Kirchhoff P, Remy C, Hafner P, Müller MK, Cheng SX, et al. The calcium-sensing receptor acts as a modulator of gastric acid secretion in freshly isolated human gastric glands. American journal of physiology Gastrointestinal and liver physiology. 2005;289(6):G1084-90.

111. Engelstoft MS, Park W-M, Sakata I, Kristensen LV, Husted AS, Osborne-Lawrence S, et al. Seven transmembrane G protein-coupled receptor repertoire of gastric ghrelin cells. Mol Metab. 2013;2(4):376-92.

112. Feng J, Petersen CD, Coy DH, Jiang J-K, Thomas CJ, Pollak MR, et al. Calcium-sensing receptor is a physiologic multimodal chemosensor regulating gastric G-cell growth and gastrin secretion. Proceedings of the National Academy of Sciences of the United States of America. 2010;107(41):17791-6.

113. Wu W, Zhou HR, Pestka JJ. Potential roles for calcium-sensing receptor (CaSR) and transient receptor potential ankyrin-1 (TRPA1) in murine anorectic response to deoxynivalenol (vomitoxin). Archives of toxicology. 2017;91(1):495-507.

114. Igarashi A, Ogasawara S, Takagi R, Okada K, Ito YM, Hara H, et al. Acute Oral Calcium Suppresses Food Intake Through Enhanced Peptide-YY Secretion Mediated by the Calcium-Sensing Receptor in Rats. The Journal of nutrition. 2021;151(5):1320-8.

115. Guo Y, Gao S, Jiang Z, Huang J, He X, Jin R, et al. Calcium-sensing receptor (CaSR) agonist R568 inhibits small intestinal motility of mice through neural and non-neural mechanisms. Food & function. 2021;12(23):11926-37.

116. Cheng SX. Calcium-sensing receptor inhibits secretagogue-induced electrolyte secretion by intestine via the enteric nervous system. American journal of physiology Gastrointestinal and liver physiology. 2012;303(1):G60-70.

117. Macleod RJ. CaSR function in the intestine: Hormone secretion, electrolyte absorption and secretion, paracrine non-canonical Wnt signaling and colonic crypt cell proliferation. Best practice & research Clinical endocrinology & metabolism. 2013;27(3):385-402.

118. Babinsky VN, Hannan FM, Ramracheya RD, Zhang Q, Nesbit MA, Hugill A, et al. Mutant Mice With Calcium-Sensing Receptor Activation Have Hyperglycemia That Is Rectified by Calcilytic Therapy. Endocrinology. 2017;158(8):2486-502.

119. Gray E, Muller D, Squires PE, Asare-Anane H, Huang GC, Amiel S, et al. Activation of the extracellular calcium-sensing receptor initiates insulin secretion from human islets of Langerhans: involvement of protein kinases. The Journal of endocrinology. 2006;190(3):703-10.

120. Bravo-Sagua R, Mattar P, Díaz X, Lavandero S, Cifuentes M. Calcium Sensing Receptor as a Novel Mediator of Adipose Tissue Dysfunction: Mechanisms and Potential Clinical Implications. Frontiers in physiology. 2016;7:395.

121. Tu CL, Bikle DD. Role of the calcium-sensing receptor in calcium regulation of epidermal differentiation and function. Best practice & research Clinical endocrinology & metabolism. 2013;27(3):415-27.

122. Boisen IM, Rehfeld A, Mos I, Poulsen NN, Nielsen JE, Schwarz P, et al. The calcium-sensing receptor is essential for calcium and bicarbonate sensitivity in human spermatozoa. The Journal of clinical endocrinology and metabolism. 2020.

123. Zhang C, Zhang T, Zou J, Miller CL, Gorkhali R, Yang J-Y, et al. Structural basis for regulation of human calcium-sensing receptor by magnesium ions and an unexpected tryptophan derivative co-agonist. Science Advances. 2016;2(5):e1600241.

124. Koehl A, Hu H, Feng D, Sun B, Zhang Y, Robertson MJ, et al. Structural insights into the activation of metabotropic glutamate receptors. Nature. 2019;566(7742):79-84.

125. Kim Y, Jeong E, Jeong JH, Kim Y, Cho Y. Structural Basis for Activation of the Heterodimeric GABA(B) Receptor. Journal of molecular biology. 2020;432(22):5966-84.

126. Mao C, Shen C, Li C, Shen DD, Xu C, Zhang S, et al. Cryo-EM structures of inactive and active GABA(B) receptor. Cell research. 2020;30(7):564-73.

127. Papasergi-Scott MM, Robertson MJ, Seven AB, Panova O, Mathiesen JM, Skiniotis G. Structures of metabotropic GABA(B) receptor. Nature. 2020;584(7820):310-4.

128. Park J, Fu Z, Frangaj A, Liu J, Mosyak L, Shen T, et al. Structure of human GABA(B) receptor in an inactive state. Nature. 2020;584(7820):304-9.

129. Shaye H, Ishchenko A, Lam JH, Han GW, Xue L, Rondard P, et al. Structural basis of the activation of a metabotropic GABA receptor. Nature. 2020;584(7820):298-303.

130. Ling S, Shi P, Liu S, Meng X, Zhou Y, Sun W, et al. Structural mechanism of cooperative activation of the human calcium-sensing receptor by Ca(2+) ions and L-tryptophan. Cell research. 2021;31(4):383-94.

131. Chen X, Wang L, Cui Q, Ding Z, Han L, Kou Y, et al. Structural insights into the activation of human calcium-sensing receptor. eLife. 2021;10:e68578.

132. Gorvin CM. Molecular and clinical insights from studies of calcium-sensing receptor mutations. Journal of molecular endocrinology. 2019;63(2):R1-r16.

133. Binet V, Duthey B, Lecaillon J, Vol C, Quoyer J, Labesse G, et al. Common structural requirements for heptahelical domain function in class A and class C G protein-coupled receptors. The Journal of biological chemistry. 2007;282(16):12154-63.

134. Chang W, Tu C, Cheng Z, Rodriguez L, Chen TH, Gassmann M, et al. Complex formation with the Type B gamma-aminobutyric acid receptor affects the expression and signal transduction of the extracellular calcium-sensing receptor. Studies with HEK-293 cells and neurons. The Journal of biological chemistry. 2007;282(34):25030-40.

135. Cheng Z, Tu C, Rodriguez L, Chen TH, Dvorak MM, Margeta M, et al. Type B gamma-aminobutyric acid receptors modulate the function of the extracellular Ca2+-sensing receptor and cell differentiation in murine growth plate chondrocytes. Endocrinology. 2007;148(10):4984-92.

136. Gama L, Wilt SG, Breitwieser GE. Heterodimerization of calcium sensing receptors with metabotropic glutamate receptors in neurons. The Journal of biological chemistry. 2001;276(42):39053-9.

137. Felder CB, Graul RC, Lee AY, Merkle HP, Sadee W. The Venus flytrap of periplasmic binding proteins: an ancient protein module present in multiple drug receptors. AAPS pharmSci. 1999;1(2):E2.

138. Thomsen AR, Hvidtfeldt M, Bräuner-Osborne H. Biased agonism of the calcium-sensing receptor. Cell calcium. 2012;51(2):107-16.

139. Gao Y, Robertson MJ, Rahman SN, Seven AB, Zhang C, Meyerowitz JG, et al. Asymmetric activation of the calcium-sensing receptor homodimer. Nature. 2021;595(7867):455-9.

140. Leach K, Gregory KJ, Kufareva I, Khajehali E, Cook AE, Abagyan R, et al. Towards a structural understanding of allosteric drugs at the human calcium-sensing receptor. Cell research. 2016;26(5):574-92.

141. Breitwieser GE. The calcium sensing receptor life cycle: trafficking, cell surface expression, and degradation. Best practice & research Clinical endocrinology & metabolism. 2013;27(3):303-13.

142. Zhuang X, Northup JK, Ray K. Large putative PEST-like sequence motif at the carboxyl tail of human calcium receptor directs lysosomal degradation and regulates cell surface receptor level. The Journal of biological chemistry. 2012;287(6):4165-76.

143. Leach K, Hannan FM, Josephs TM, Keller AN, Møller TC, Ward DT, et al. International Union of Basic and Clinical Pharmacology. CVIII. Calcium-Sensing Receptor Nomenclature, Pharmacology, and Function. Pharmacological reviews. 2020;72(3):558-604.

144. Munk C, Isberg V, Mordalski S, Harpsøe K, Rataj K, Hauser AS, et al. GPCRdb: the G protein-coupled receptor database - an introduction. Br J Pharmacol. 2016;173(14):2195-207.

145. Stenson PD, Ball EV, Mort M, Phillips AD, Shaw K, Cooper DN. The Human Gene Mutation Database (HGMD) and its exploitation in the fields of personalized genomics and molecular evolution. Current protocols in bioinformatics. 2012;Chapter 1:Unit1.13.

146. Binmahfouz LS, Centeno PP, Conigrave AD, Ward DT. Identification of Serine-875 as an Inhibitory Phosphorylation Site in the Calcium-Sensing Receptor. Molecular pharmacology. 2019;96(2):204-11.

147. Liu H, Yi P, Zhao W, Wu Y, Acher F, Pin J-P, et al. Illuminating the allosteric modulation of the calcium-sensing receptor. Proceedings of the National Academy of Sciences of the United States of America. 2020;117(35):21711-22.

148. Zhang C, Zhang T, Zou J, Miller CL, Gorkhali R, Yang J-Y, et al. Structural basis for regulation of human calcium-sensing receptor by magnesium ions and an unexpected tryptophan derivative co-agonist. Science advances. 2016;2(5):e1600241-e.

149. Stoy H, Gurevich VV. How genetic errors in GPCRs affect their function: Possible therapeutic strategies. Genes & diseases. 2015;2(2):108-32.

150. Park J, Selvam B, Sanematsu K, Shigemura N, Shukla D, Procko E. Structural architecture of a dimeric class C GPCR based on co-trafficking of sweet taste receptor subunits. The Journal of biological chemistry. 2019;294(13):4759-74.

151. Doré AS, Okrasa K, Patel JC, Serrano-Vega M, Bennett K, Cooke RM, et al. Structure of class C GPCR metabotropic glutamate receptor 5 transmembrane domain. Nature. 2014;511(7511):557-62.

152. Gama L, Breitwieser GE. A carboxyl-terminal domain controls the cooperativity for extracellular Ca2+ activation of the human calcium sensing receptor. A study with receptor-green fluorescent protein fusions. The Journal of biological chemistry. 1998;273(45):29712-8.

153. Grant MP, Stepanchick A, Cavanaugh A, Breitwieser GE. Agonist-driven maturation and plasma membrane insertion of calcium-sensing receptors dynamically control signal amplitude. Science signaling. 2011;4(200):ra78.

154. Breitwieser GE. Minireview: the intimate link between calcium sensing receptor trafficking and signaling: implications for disorders of calcium homeostasis. Molecular endocrinology (Baltimore, Md). 2012;26(9):1482-95.

155. Nesbit MA, Hannan FM, Howles SA, Babinsky VN, Head RA, Cranston T, et al. Mutations affecting G-protein subunit alpha11 in hypercalcemia and hypocalcemia. The New England journal of medicine. 2013;368(26):2476-86.

156. Thomsen AR, Smajilovic S, Bräuner-Osborne H. Novel strategies in drug discovery of the calcium-sensing receptor based on biased signaling. Current drug targets. 2012;13(10):1324-35.

157. Kamato D, Thach L, Bernard R, Chan V, Zheng W, Kaur H, et al. Structure, Function, Pharmacology, and Therapeutic Potential of the G Protein, Gα/q,11. Frontiers in Cardiovascular Medicine. 2015;2.

158. Hubbard KB, Hepler JR. Cell signalling diversity of the Gqα family of heterotrimeric G proteins. Cellular Signalling. 2006;18(2):135-50.

159. Wilkie TM, Scherle PA, Strathmann MP, Slepak VZ, Simon MI. Characterization of G-protein alpha subunits in the Gq class: expression in murine tissues and in stromal and hematopoietic cell lines. Proceedings of the National Academy of Sciences. 1991;88(22):10049-53.

160. Hannan FM, Olesen MK, Thakker RV. Calcimimetic and calcilytic therapies for inherited disorders of the calcium-sensing receptor signalling pathway. Br J Pharmacol. 2018;175(21):4083-94.

161. Hofer AM, Brown EM. Extracellular calcium sensing and signalling. Nature reviews Molecular cell biology. 2003;4(7):530-8.

162. Tfelt-Hansen J, MacLeod RJ, Chattopadhyay N, Yano S, Quinn S, Ren X, et al. Calcium-sensing receptor stimulates PTHrP release by pathways dependent on PKC, p38 MAPK, JNK, and ERK1/2 in H-500 cells. American journal of physiology Endocrinology and metabolism. 2003;285(2):E329-37.

163. Conigrave AD, Ward DT. Calcium-sensing receptor (CaSR): pharmacological properties and signaling pathways. Best practice & research Clinical endocrinology & metabolism. 2013;27(3):315-31.

164. Kifor O, MacLeod RJ, Diaz R, Bai M, Yamaguchi T, Yao T, et al. Regulation of MAP kinase by calcium-sensing receptor in bovine parathyroid and CaR-transfected HEK293 cells. American journal of physiology Renal physiology. 2001;280(2):F291-302.

165. Pi M, Spurney RF, Tu Q, Hinson T, Quarles LD. Calcium-sensing receptor activation of rho involves filamin and rho-guanine nucleotide exchange factor. Endocrinology. 2002;143(10):3830-8.

166. Oda Y, Hu L, Nguyen T, Fong C, Tu C-L, Bikle DD. Combined Deletion of the Vitamin D Receptor and Calcium-Sensing Receptor Delays Wound Re-epithelialization. Endocrinology. 2017;158(6):1929-38.

167. Mamillapalli R, VanHouten J, Zawalich W, Wysolmerski J. Switching of G-protein usage by the calcium-sensing receptor reverses its effect on parathyroid hormone-related protein secretion in normal versus malignant breast cells. The Journal of biological chemistry. 2008;283(36):24435-47.

168. Mamillapalli R, Wysolmerski J. The calcium-sensing receptor couples to Galpha(s) and regulates PTHrP and ACTH secretion in pituitary cells. The Journal of endocrinology. 2010;204(3):287-97.

169. Fox J, Lowe SH, Conklin RL, Petty BA, Nemeth EF. Calcimimetic compound NPS R-568 stimulates calcitonin secretion but selectively targets parathyroid gland Ca(2+) receptor in rats. The Journal of pharmacology and experimental therapeutics. 1999;290(2):480-6.

170. Smith JS, Lefkowitz RJ, Rajagopal S. Biased signalling: from simple switches to allosteric microprocessors. Nature Reviews Drug Discovery. 2018;17(4):243-60.

171. Davey AE, Leach K, Valant C, Conigrave AD, Sexton PM, Christopoulos A. Positive and negative allosteric modulators promote biased signaling at the calcium-sensing receptor. Endocrinology. 2012;153(3):1232-41.

172. Thomsen AR, Worm J, Jacobsen SE, Stahlhut M, Latta M, Bräuner-Osborne H. Strontium is a biased agonist of the calcium-sensing receptor in rat medullary thyroid carcinoma 6-23 cells. The Journal of pharmacology and experimental therapeutics. 2012;343(3):638-49.

173. Makita N, Ando T, Sato J, Manaka K, Mitani K, Kikuchi Y, et al. Cinacalcet corrects biased allosteric modulation of CaSR by AHH autoantibody. JCI insight. 2019;4(8):e126449.

174. Gorvin CM, Frost M, Malinauskas T, Cranston T, Boon H, Siebold C, et al. Calcium-sensing receptor residues with loss- and gain-of-function mutations are located in regions of conformational change and cause signalling bias. Human molecular genetics. 2018;27(21):3720-33.

175. Gorvin CM, Babinsky VN, Malinauskas T, Nissen PH, Schou AJ, Hanyaloglu AC, et al. A calcium-sensing receptor mutation causing hypocalcemia disrupts a transmembrane salt bridge to activate β-arrestin-biased signaling. Science signaling. 2018;11(518):eaan3714.

176. Rybchyn MS, Slater M, Conigrave AD, Mason RS. An Akt-dependent increase in canonical Wnt signaling and a decrease in sclerostin protein levels are involved in strontium ranelate-induced osteogenic effects in human osteoblasts. The Journal of biological chemistry. 2011;286(27):23771-9.

177. Rybchyn MS, Islam KS, Brennan-Speranza TC, Cheng Z, Brennan SC, Chang W, et al. Homer1 mediates CaSR-dependent activation of mTOR complex 2 and initiates a novel pathway for AKT-dependent β-catenin stabilization in osteoblasts. The Journal of biological chemistry. 2019;294(44):16337-50.

178. Gorvin CM, Rogers A, Hastoy B, Tarasov AI, Frost M, Sposini S, et al. AP2σ Mutations Impair Calcium-Sensing Receptor Trafficking and Signaling, and Show an Endosomal Pathway to Spatially Direct G-Protein Selectivity. Cell reports. 2018;22(4):1054-66.

179. Gorvin CM, Rogers A, Hastoy B, Tarasov AI, Frost M, Sposini S, et al. AP2? Mutations Impair Calcium-Sensing Receptor Trafficking and Signaling, and Show an Endosomal Pathway to Spatially Direct G-Protein Selectivity. Cell reports. 2018;22(4):1054-66.

180. Mos I, Jacobsen SE, Foster SR, Bräuner-Osborne H. Calcium-Sensing Receptor Internalization Is β-Arrestin-Dependent and Modulated by Allosteric Ligands. Molecular pharmacology. 2019;96(4):463-74.

181. Feinstein TN, Yui N, Webber MJ, Wehbi VL, Stevenson HP, King JD, Jr., et al. Noncanonical control of vasopressin receptor type 2 signaling by retromer and arrestin. The Journal of biological chemistry. 2013;288(39):27849-60.

182. Ferrandon S, Feinstein TN, Castro M, Wang B, Bouley R, Potts JT, et al. Sustained cyclic AMP production by parathyroid hormone receptor endocytosis. Nature chemical biology. 2009;5(10):734-42.

183. Calebiro D. Thyroid-stimulating hormone receptor activity after internalization. Annales d'endocrinologie. 2011;72(2):64-7.

184. Promega. Amino acid structures, codes and reference information 2022 [Available from: promega.co.uk/resources/tools/amino-acid-chart-amino-acid-structure/.

185. Attie MF, Gill JR, Stock JL, Spiegel AM, Downs RW, Levine MA, et al. Urinary calcium excretion in familial hypocalciuric hypercalcemia. Persistence of relative hypocalciuria after induction of hypoparathyroidism. The Journal of clinical investigation. 1983;72(2):667-76.

186. Hannan FM, Thakker RV. Calcium-sensing receptor (CaSR) mutations and disorders of calcium, electrolyte and water metabolism. Best practice & research Clinical endocrinology & metabolism. 2013;27(3):359-71.

187. Hannan FM, Nesbit MA, Christie PT, Lissens W, Van der Schueren B, Bex M, et al. A homozygous inactivating calcium-sensing receptor mutation, Pro339Thr, is associated with isolated primary hyperparathyroidism: correlation between location of mutations and severity of hypercalcaemia. Clinical endocrinology. 2010;73(6):715-22.

188. Bai M, Pearce SH, Kifor O, Trivedi S, Stauffer UG, Thakker RV, et al. In vivo and in vitro characterization of neonatal hyperparathyroidism resulting from a de novo, heterozygous mutation in the Ca2+-sensing receptor gene: normal maternal calcium homeostasis as a cause of secondary hyperparathyroidism in familial benign hypocalciuric hypercalcemia. The Journal of clinical investigation. 1997;99(1):88-96.

189. Dershem R, Gorvin CM, Metpally RPR, Krishnamurthy S, Smelser DT, Hannan FM, et al. Familial Hypocalciuric Hypercalcemia Type 1 and Autosomal-Dominant Hypocalcemia Type 1: Prevalence in a Large Healthcare Population. American journal of human genetics. 2020;106(6):734-47.

190. Gorvin CM, Cranston T, Hannan FM, Rust N, Qureshi A, Nesbit MA, et al. A G-protein Subunit-alpha11 Loss-of-Function Mutation, Thr54Met, Causes Familial Hypocalciuric Hypercalcemia Type 2 (FHH2). Journal of bone and mineral research : the official journal of the American Society for Bone and Mineral Research. 2016;31(6):1200-6.

191. Gorvin CM, Hannan FM, Cranston T, Valta H, Makitie O, Schalin-Jantti C, et al. Cinacalcet Rectifies Hypercalcemia in a Patient With Familial Hypocalciuric Hypercalcemia Type 2 (FHH2) Caused by a Germline Loss-of-Function Gα(11) Mutation. Journal of bone and mineral research : the official journal of the American Society for Bone and Mineral Research. 2018;33(1):32-41.

192. Hannan FM, Howles SA, Rogers A, Cranston T, Gorvin CM, Babinsky VN, et al. Adaptor protein-2 sigma subunit mutations causing familial hypocalciuric hypercalcaemia type 3 (FHH3) demonstrate genotype-phenotype correlations, codon bias and dominant-negative effects. Human molecular genetics. 2015;24(18):5079-92.

193. Nesbit MA, Hannan FM, Graham U, Whyte MP, Morrison PJ, Hunter SJ, et al. Identification of a second kindred with familial hypocalciuric hypercalcemia type 3 (FHH3) narrows localization to a <3.5 megabase pair region on chromosome 19q13.3. J Clin Endocrinol Metab. 2010;95(4):1947-54.

194. McMurtry CT, Schranck FW, Walkenhorst DA, Murphy WA, Kocher DB, Teitelbaum SL, et al. Significant developmental elevation in serum parathyroid hormone levels in a large kindred with familial benign (hypocalciuric) hypercalcemia. Am J Med. 1992;93(3):247-58.

195. Rogers A, Nesbit MA, Hannan FM, Howles SA, Gorvin CM, Cranston T, et al. Mutational analysis of the adaptor protein 2 sigma subunit (AP2S1) gene: search for autosomal dominant hypocalcemia type 3 (ADH3). The Journal of clinical endocrinology and metabolism. 2014;99(7):E1300-5.

196. Cavaco BM, Canaff L, Nolin-Lapalme A, Vieira M, Silva TN, Saramago A, et al. Homozygous Calcium-Sensing Receptor Polymorphism R544Q Presents as Hypocalcemic Hypoparathyroidism. The Journal of clinical endocrinology and metabolism. 2018;103(8):2879-88.

197. Lietman SA, Tenenbaum-Rakover Y, Jap TS, Yi-Chi W, De-Ming Y, Ding C, et al. A novel loss-of-function mutation, Gln459Arg, of the calcium-sensing receptor gene associated with apparent autosomal recessive inheritance of familial hypocalciuric hypercalcemia. The Journal of clinical endocrinology and metabolism. 2009;94(11):4372-9.

198. Vargas-Poussou R, Huang C, Hulin P, Houillier P, Jeunemaître X, Paillard M, et al. Functional characterization of a calcium-sensing receptor mutation in severe autosomal dominant hypocalcemia with a Bartter-like syndrome. Journal of the American Society of Nephrology : JASN. 2002;13(9):2259-66.

199. Watanabe S, Fukumoto S, Chang H, Takeuchi Y, Hasegawa Y, Okazaki R, et al. Association between activating mutations of calcium-sensing receptor and Bartter's syndrome. Lancet (London, England). 2002;360(9334):692-4.

200. Gorvin CM, Stokes VJ, Boon H, Cranston T, Glück AK, Bahl S, et al. Activating mutations of the G-protein subunit α 11 interdomain interface cause autosomal dominant hypocalcemia type 2. The Journal of Clinical Endocrinology & Metabolism. 2020;105(3):952-63.

201. Piret SE, Gorvin CM, Pagnamenta AT, Howles SA, Cranston T, Rust N, et al. Identification of a G-Protein Subunit-alpha11 Gain-of-Function Mutation, Val340Met, in a Family With Autosomal Dominant Hypocalcemia Type 2 (ADH2). Journal of bone and mineral research : the official journal of the American Society for Bone and Mineral Research. 2016;31(6):1207-14.

202. Li D, Opas EE, Tuluc F, Metzger DL, Hou C, Hakonarson H, et al. Autosomal dominant hypoparathyroidism caused by germline mutation in GNA11: phenotypic and molecular characterization. The Journal of clinical endocrinology and metabolism. 2014;99(9):E1774-83.

203. Tenhola S, Voutilainen R, Reyes M, Toiviainen-Salo S, Jüppner H, Mäkitie O. Impaired growth and intracranial calcifications in autosomal dominant hypocalcemia caused by a GNA11 mutation. European journal of endocrinology. 2016;175(3):211-8.

204. Al-Shanafey S, Al-Hosaini R, Al-Ashwal A, Al-Rabeeah A. Surgical management of severe neonatal hyperparathyroidism: one center's experience. Journal of pediatric surgery. 2010;45(4):714-7.

205. Hadedeya D, Kay J, Attia A, Omar M, Shalaby M, Youssef MR, et al. Effect of postsurgical chronic hypoparathyroidism on morbidity and mortality: a systematic review and meta-analysis. Gland surgery. 2021;10(10):3007-19.

206. Hannan FM, Babinsky VN, Thakker RV. Disorders of the calcium-sensing receptor and partner proteins: insights into the molecular basis of calcium homeostasis. Journal of molecular endocrinology. 2016;57(3):R127-42.

207. Theman TA, Collins MT, Dempster DW, Zhou H, Reynolds JC, Brahim JS, et al. PTH(1-34) replacement therapy in a child with hypoparathyroidism caused by a sporadic calcium receptor mutation. Journal of bone and mineral research : the official journal of the American Society for Bone and Mineral Research. 2009;24(5):964-73.

208. Festen-Spanjer B, Haring CM, Koster JB, Mudde AH. Correction of hypercalcaemia by cinacalcet in familial hypocalciuric hypercalcaemia. Clinical endocrinology. 2008;68(2):324-5.

209. Gorvin CM, Hannan FM, Cranston T, Valta H, Makitie O, Schalin-Jantti C, et al. Cinacalcet Rectifies Hypercalcemia in a Patient With Familial Hypocalciuric Hypercalcemia Type 2 (FHH2) Caused by a Germline Loss-of-Function Galpha11 Mutation. Journal of bone and mineral research : the official journal of the American Society for Bone and Mineral Research. 2017.

210. Howles SA, Hannan FM, Babinsky VN, Rogers A, Gorvin CM, Rust N, et al. Cinacalcet for Symptomatic Hypercalcemia Caused by AP2S1 Mutations. The New England journal of medicine. 2016;374(14):1396-8.

211. Gannon AW, Monk HM, Levine MA. Cinacalcet monotherapy in neonatal severe hyperparathyroidism: a case study and review. The Journal of clinical endocrinology and metabolism. 2014;99(1):7-11.

212. Garcia Soblechero E, Ferrer Castillo MT, Jimenez Crespo B, Dominguez Quintero ML, Gonzalez Fuentes C. Neonatal hypercalcemia due to a homozygous mutation in the calcium-sensing receptor: failure of cinacalcet. Neonatology. 2013;104(2):104-8.

213. Chavez-Abiega S, Mos I, Centeno PP, Elajnaf T, Schlattl W, Ward DT, et al. Sensing Extracellular Calcium - An Insight into the Structure and Function of the Calcium-Sensing Receptor (CaSR). Advances in experimental medicine and biology. 2020;1131:1031-63.

214. Oak AA, Chhetri PD, Rivera A, Verkman AS, Cil O. Repurposing calcium sensing receptor agonist cinacalcet for treatment of CFTR-mediated secretory diarrheas. JCI insight. 2021.

215. Li J, Liao P, Wang K, Miao Z, Xiao R, Zhu L, et al. Calcium Sensing Receptor Inhibits Growth of Human Lung Adenocarcinoma Possibly via the GSK3β/Cyclin D1 Pathway. Frontiers in cell and developmental biology. 2020;8:446.

216. Elajnaf T, Iamartino L, Mesteri I, Müller C, Bassetto M, Manhardt T, et al. Nutritional and Pharmacological Targeting of the Calcium-Sensing Receptor Influences Chemically Induced Colitis in Mice. Nutrients. 2019;11(12).

217. Alexander ST, Hunter T, Walter S, Dong J, Maclean D, Baruch A, et al. Critical Cysteine Residues in Both the Calcium-Sensing Receptor and the Allosteric Activator AMG 416 Underlie the Mechanism of Action. Molecular pharmacology. 2015;88(5):853-65.

218. Fitzpatrick LA, Dabrowski CE, Cicconetti G, Gordon DN, Papapoulos S, Bone HG, 3rd, et al. The effects of ronacaleret, a calcium-sensing receptor antagonist, on bone mineral density and biochemical markers of bone turnover in postmenopausal women with low bone mineral density. The Journal of clinical endocrinology and metabolism. 2011;96(8):2441-9.

219. Jackson LP, Kelly BT, McCoy AJ, Gaffry T, James LC, Collins BM, et al. A large-scale conformational change couples membrane recruitment to cargo binding in the AP2 clathrin adaptor complex. Cell. 2010;141(7):1220-9.

220. Karczewski KJ, Francioli LC, Tiao G, Cummings BB, Alföldi J, Wang Q, et al. The mutational constraint spectrum quantified from variation in 141,456 humans. Nature. 2020;581(7809):434-43.

221. Kerut S, Kovvuru KR, Yanes-Cardozo L, Garla VV. Familial hypocalciuric hypercalcaemia type 3: AP2S1 missense mutation. BMJ Case Rep. 2020;13(11).

222. Aashiq M, Malallah AJ, Khan F, Alsada M. Clinical and Biochemical Features in a Case of Familial Hypocalciuric Hypercalcemia Type 3 with AP2S1 Gene Mutation in Codon Arg15His. Case Rep Pediatr. 2020;2020:7312894.

223. Wong FCK, Wong WS, Kwok JSS, Tsui TKC, Lau KP, Chan MHM, et al. A Hong Kong Chinese kindred with familial hypocalciuric hypercalcaemia caused by AP2S1 mutation. F1000Res. 2019;8:1612.

224. Szalat A, Shpitzen S, Tsur A, Zalmon Koren I, Shilo S, Tripto-Shkolnik L, et al. Stepwise CaSR, AP2S1, and GNA11 sequencing in patients with suspected familial hypocalciuric hypercalcemia. Endocrine. 2017;55(3):741-7.

225. Hovden S, Jespersen ML, Nissen PH, Poulsen PL, Rolighed L, Ladefoged SA, et al. Multiple endocrine neoplasia phenocopy revealed as a co-occurring neuroendocrine tumor and familial hypocalciuric hypercalcemia type 3. Clin Case Rep. 2016;4(10):922-7.

226. Hovden S, Rejnmark L, Ladefoged SA, Nissen PH. AP2S1 and GNA11 mutations - not a common cause of familial hypocalciuric hypercalcemia. European journal of endocrinology. 2017;176(2):177-85.

227. Tenhola S, Hendy GN, Valta H, Canaff L, Lee BS, Wong BY, et al. Cinacalcet Treatment in an Adolescent With Concurrent 22q11.2 Deletion Syndrome and Familial Hypocalciuric Hypercalcemia Type 3 Caused by AP2S1 Mutation. J Clin Endocrinol Metab. 2015;100(7):2515-8.

228. Hendy GN, Canaff L, Newfield RS, Tripto-Shkolnik L, Wong BY, Lee BS, et al. Codon Arg15 mutations of the AP2S1 gene: common occurrence in familial hypocalciuric hypercalcemia cases negative for calcium-sensing receptor (CASR) mutations. The Journal of clinical endocrinology and metabolism. 2014;99(7):E1311-5.

229. Fujisawa Y, Yamaguchi R, Satake E, Ohtaka K, Nakanishi T, Ozono K, et al. Identification of AP2S1 mutation and effects of low calcium formula in an infant with hypercalcemia and hypercalciuria. J Clin Endocrinol Metab. 2013;98(12):E2022-7.

230. Ho C, Conner DA, Pollak MR, Ladd DJ, Kifor O, Warren HB, et al. A mouse model of human familial hypocalciuric hypercalcemia and neonatal severe hyperparathyroidism. Nature genetics. 1995;11(4):389-94.

231. Kos CH, Karaplis AC, Peng JB, Hediger MA, Goltzman D, Mohammad KS, et al. The calcium-sensing receptor is required for normal calcium homeostasis independent of parathyroid hormone. The Journal of clinical investigation. 2003;111(7):1021-8.

232. Howles SA, Hannan FM, Gorvin CM, Piret SE, Paudyal A, Stewart M, et al. Cinacalcet corrects hypercalcemia in mice with an inactivating Galpha11 mutation. JCI insight. 2017;2(20).

233. Wettschureck N, Lee E, Libutti SK, Offermanns S, Robey PG, Spiegel AM. Parathyroid-specific double knockout of Gq and G11 alpha-subunits leads to a phenotype resembling germline knockout

of the extracellular Ca2+ -sensing receptor. Molecular endocrinology (Baltimore, Md). 2007;21(1):274-80.

234. Caroline M Gorvin AR, Michelle Stewart, Anju Paudyal, Tertius A Hough, Lydia Teboul, Sara Wells, Steve DM Brown, Roger D Cox, Rajesh v Thakker. N-ethyl-N-nitrosourea–Induced Adaptor Protein 2 Sigma Subunit 1 (*Ap2s1*) Mutations Establish *Ap2s1* Loss-of-Function Mice. JBMR Plus. 2017;1(1):3-15.

235. Hough TA, Bogani D, Cheeseman MT, Favor J, Nesbit MA, Thakker RV, et al. Activating calcium-sensing receptor mutation in the mouse is associated with cataracts and ectopic calcification. Proceedings of the National Academy of Sciences of the United States of America. 2004;101(37):13566-71.

236. Dong B, Endo I, Ohnishi Y, Kondo T, Hasegawa T, Amizuka N, et al. Calcilytic Ameliorates Abnormalities of Mutant Calcium-Sensing Receptor (CaSR) Knock-In Mice Mimicking Autosomal Dominant Hypocalcemia (ADH). Journal of bone and mineral research : the official journal of the American Society for Bone and Mineral Research. 2015;30(11):1980-93.

237. Hannan FM, Gorvin CM, Babinsky VN, Olesen MK, Stewart M, Wells S, et al. Calcilytic NPSP795 Increases Plasma Calcium and PTH in an Autosomal Dominant Hypocalcemia Type 1 Mouse Model. JBMR plus. 2020;4(10):e10402.

238. Gorvin CM, Hannan FM, Howles SA, Babinsky VN, Piret SE, Rogers A, et al. Gα(11) mutation in mice causes hypocalcemia rectifiable by calcilytic therapy. JCI insight. 2017;2(3):e91103.

239. Roszko KL, Bi R, Gorvin CM, Brauner-Osborne H, Xiong XF, Inoue A, et al. Knockin mouse with mutant Galpha11 mimics human inherited hypocalcemia and is rescued by pharmacologic inhibitors. JCI insight. 2017;2(3):e91079.

240. Dewey FE, Murray MF, Overton JD, Habegger L, Leader JB, Fetterolf SN, et al. Distribution and clinical impact of functional variants in 50,726 whole-exome sequences from the DiscovEHR study. Science (New York, NY). 2016;354(6319).

241. Carey DJ, Fetterolf SN, Davis FD, Faucett WA, Kirchner HL, Mirshahi U, et al. The Geisinger MyCode community health initiative: an electronic health record-linked biobank for precision medicine research. Genetics in medicine : official journal of the American College of Medical Genetics. 2016;18(9):906-13.

242. Newey PJ, Gorvin CM, Thakker RV. Mutant prolactin receptor and familial hyperprolactinemia. The New England journal of medicine. 2014;370(10):977-8.

243. Hannan FM, Stevenson M, Bayliss AL, Stokes VJ, Stewart M, Kooblall KG, et al. Ap2s1 mutation causes hypercalcaemia in mice and impairs interaction between calcium-sensing receptor and adaptor protein-2. Human molecular genetics. 2021.

244. Heid CA, Stevens J, Livak KJ, Williams PM. Real time quantitative PCR. Genome research. 1996;6(10):986-94.

245. Woodward J. Bi-allelic SNP genotyping using the TaqMan® assay. Methods in molecular biology (Clifton, NJ). 2014;1145:67-74.

246. Mallya SM, Buchberger GK, Arnold A. Effects of anesthetic agents on serum parathyroid hormone and calcium concentrations in mice. Veterinary anaesthesia and analgesia. 2007;34(6):403-7.

247. Hotchkiss CE, Brommage R, Du M, Jerome CP. The anesthetic isoflurane decreases ionized calcium and increases parathyroid hormone and osteocalcin in cynomolgus monkeys. Bone. 1998;23(5):479-84.

248. Sherry ST, Ward MH, Kholodov M, Baker J, Phan L, Smigielski EM, et al. dbSNP: the NCBI database of genetic variation. Nucleic acids research. 2001;29(1):308-11.

249. Lek M, Karczewski KJ, Minikel EV, Samocha KE, Banks E, Fennell T, et al. Analysis of protein-coding genetic variation in 60,706 humans. Nature. 2016;536(7616):285-91.

250. Karczewski KJ, Francioli LC, Tiao G, Cummings BB, Alföldi J, Wang Q, et al. The mutational constraint spectrum quantified from variation in 141,456 humans. Nature. 2020;581(7809):434-43.

251. Landrum MJ, Chitipiralla S, Brown GR, Chen C, Gu B, Hart J, et al. ClinVar: improvements to accessing data. Nucleic acids research. 2020;48(D1):D835-d44.

252. Schwarz JM, Cooper DN, Schuelke M, Seelow D. MutationTaster2: mutation prediction for the deep-sequencing age. Nature methods. 2014;11(4):361-2.

253. Ng PC, Henikoff S. SIFT: Predicting amino acid changes that affect protein function. Nucleic acids research. 2003;31(13):3812-4.

254. Adzhubei I, Jordan DM, Sunyaev SR. Predicting functional effect of human missense mutations using PolyPhen-2. Current protocols in human genetics. 2013;Chapter 7:Unit7.20.

255. Adzhubei IA, Schmidt S, Peshkin L, Ramensky VE, Gerasimova A, Bork P, et al. A method and server for predicting damaging missense mutations. Nature methods. 2010;7(4):248-9.

256. Schrodinger. The PyMOL Molecular Graphics System. 1.3 ed. LLC.

257. Motulsky H. Interpreting results: One way ANOVA [14.01.22]. Available from: https://www.graphpad.com/guides/prism/latest/statistics/f_ratio_and_anova_table_(one-way_anova).htm.

258. Abdi H. The Bonferonni and Šidák Corrections for Multiple Comparisons. In: Salkind N, editor. Encyclopedia of Measurement and Statistics. Thousand Oaks (CA): Sage; 2007. p. 103-7.

259. Motulsky H. Bonferroni and Sidak methods [Last accessed 14.1.22]. Available from: https://www.graphpad.com/guides/prism/latest/statistics/stat_the_method_of_bonferroni.htm.

260. Gorvin CM, Metpally R, Stokes VJ, Hannan FM, Krishnamurthy SB, Overton JD, et al. Large-scale exome datasets reveal a new class of adaptor-related protein complex 2 sigma subunit (AP2sigma) mutations, located at the interface with the AP2 alpha subunit, that impair calcium-sensing receptor signalling. Human molecular genetics. 2018.

261. Gorvin C, Metpally R, D Overton J, D Reid J, Breitwieser G, V Thakker R. An Adaptor Protein 2 Sigma Subunit (AP2σ) Met117Ile Mutation within a Helix-Loop-Helix Structure Causes Familial Hypocalciuric Hypercalcaemia Type-32017.

262. Gorvin CM MR, Stokes VJ, Hannan FM, Krishnamurthy SB, Overton JD, Reid JG, Breitweiser GE, Thakker RV. Large-scale exome datasets reveal a new class of adaptor-related protein complex 2 sigma subunit (AP2σ) mutations, located at the interface with the AP2 alpha subunit that impair calcium-sensing receptor signaling. Human molecular genetics. 2018;24(18):5079-92.

263. Adzhubei I, Jordan DM, Sunyaev SR. Predicting functional effect of human missense mutations using PolyPhen-2. Current protocols in human genetics. 2013;Chapter 7:Unit7 20.

264. Firek AF, Kao PC, Heath H, 3rd. Plasma intact parathyroid hormone (PTH) and PTH-related peptide in familial benign hypercalcemia: greater responsiveness to endogenous PTH than in primary hyperparathyroidism. The Journal of clinical endocrinology and metabolism. 1991;72(3):541-6.

265. Marx SJ. Letter to the editor: Distinguishing typical primary hyperparathyroidism from familial hypocalciuric hypercalcemia by using an index of urinary calcium. The Journal of clinical endocrinology and metabolism. 2015;100(2):L29-30.

266. Ran FA, Hsu PD, Lin CY, Gootenberg JS, Konermann S, Trevino AE, et al. Double nicking by RNA-guided CRISPR Cas9 for enhanced genome editing specificity. Cell. 2013;154(6):1380-9.

267. Mianne J, Codner GF, Caulder A, Fell R, Hutchison M, King R, et al. Analysing the outcome of CRISPR-aided genome editing in embryos: Screening, genotyping and quality control. Methods. 2017;121-122:68-76.

268. Howles SA, Hannan FM, Babinsky VN, Rogers A, Gorvin CM, Rust N, et al. Cinacalcet for Symptomatic Hypercalcemia Caused by AP2S1 Mutations. N Engl J Med. 2016;374(14):1396-8.

269. Scheers I, Sokal E, Limaye N, Denoncin C, Stephenne X, Pirson Y, et al. Cinacalcet sustainedly prevents pancreatitis in a child with a compound heterozygous SPINK1/AP2S1 mutation. Pancreatology. 2019;19(6):801-4.

270. Tenhola S, Hendy GN, Valta H, Canaff L, Lee BS, Wong BY, et al. Cinacalcet Treatment in an Adolescent with Concurrent 22q11.2 Deletion Syndrome and FHH3 caused by AP2S1 Mutation. J Clin Endocrinol Metab. 2015;100:2515-8.

271. Hsu CW, Wong L, Rasmussen TL, Kalaga S, McElwee ML, Keith LC, et al. Three-dimensional microCT imaging of mouse development from early post-implantation to early postnatal stages. Developmental biology. 2016;419(2):229-36.

272. Miyake T, Cameron AM, Hall BK. Detailed staging of inbred C57BL/6 mice between Theiler's [1972] stages 18 and 21 (11-13 days of gestation) based on craniofacial development. Journal of craniofacial genetics and developmental biology. 1996;16(1):1-31.

273. Gibson UE, Heid CA, Williams PM. A novel method for real time quantitative RT-PCR. Genome research. 1996;6(10):995-1001.

274. Kononenko NL, Puchkov D, Classen GA, Walter AM, Pechstein A, Sawade L, et al. Clathrin/AP-2 mediate synaptic vesicle reformation from endosome-like vacuoles but are not essential for membrane retrieval at central synapses. Neuron. 2014;82(5):981-8.

275. Kittler JT, Chen G, Honing S, Bogdanov Y, McAinsh K, Arancibia-Carcamo IL, et al. Phospho-dependent binding of the clathrin AP2 adaptor complex to GABAA receptors regulates the efficacy of inhibitory synaptic transmission. Proceedings of the National Academy of Sciences of the United States of America. 2005;102(41):14871-6.

276. Lee SH, Liu L, Wang YT, Sheng M. Clathrin adaptor AP2 and NSF interact with overlapping sites of GluR2 and play distinct roles in AMPA receptor trafficking and hippocampal LTD. Neuron. 2002;36(4):661-74.

277. Liu XL, Lu YS, Gao JY, Marshall C, Xiao M, Miao DS, et al. Calcium sensing receptor absence delays postnatal brain development via direct and indirect mechanisms. Molecular neurobiology. 2013;48(3):590-600.

278. Stepanchick A, McKenna J, McGovern O, Huang Y, Breitwieser GE. Calcium sensing receptor mutations implicated in pancreatitis and idiopathic epilepsy syndrome disrupt an arginine-rich

retention motif. Cellular physiology and biochemistry : international journal of experimental cellular physiology, biochemistry, and pharmacology. 2010;26(3):363-74.

279. Kapoor A, Satishchandra P, Ratnapriya R, Reddy R, Kadandale J, Shankar SK, et al. An idiopathic epilepsy syndrome linked to 3q13.3-q21 and missense mutations in the extracellular calcium sensing receptor gene. Annals of neurology. 2008;64(2):158-67.

280. Giudice ML, Mihalik B, Dinnyés A, Kobolák J. The Nervous System Relevance of the Calcium Sensing Receptor in Health and Disease. Molecules. 2019;24(14):2546.

281. Newey PJ, Berg JN, Zhou K, Palmer CNA, Thakker RV. Utility of Population-Level DNA Sequence Data in the Diagnosis of Hereditary Endocrine Disease. Journal of the Endocrine Society. 2017;1(12):1507-26.

282. Tenhola S, Hendy GN, Valta H, Canaff L, Lee BS, Wong BY, et al. Cinacalcet Treatment in an Adolescent With Concurrent 22q11.2 Deletion Syndrome and Familial Hypocalciuric Hypercalcemia Type 3 Caused by AP2S1 Mutation. The Journal of clinical endocrinology and metabolism. 2015;100(7):2515-8.

283. Gu M, Liu Q, Watanabe S, Sun L, Hollopeter G, Grant BD, et al. AP2 hemicomplexes contribute independently to synaptic vesicle endocytosis. Elife. 2013;2:e00190.

284. Kawata T, Imanishi Y, Kobayashi K, Miki T, Arnold A, Inaba M, et al. Parathyroid hormone regulates fibroblast growth factor-23 in a mouse model of primary hyperparathyroidism. J Am Soc Nephrol. 2007;18(10):2683-8.

285. Yamashita H, Yamashita T, Miyamoto M, Shigematsu T, Kazama JJ, Shimada T, et al. Fibroblast growth factor (FGF)-23 in patients with primary hyperparathyroidism. Eur J Endocrinol. 2004;151(1):55-60.

286. Halling Linder C, Englund UH, Narisawa S, Millan JL, Magnusson P. Isozyme profile and tissue-origin of alkaline phosphatases in mouse serum. Bone. 2013;53(2):399-408.

287. Hsu YJ, Dimke H, Schoeber JP, Hsu SC, Lin SH, Chu P, et al. Testosterone increases urinary calcium excretion and inhibits expression of renal calcium transport proteins. Kidney international. 2010;77(7):601-8.

288. Fuster DG, Morard GA, Schneider L, Mattmann C, Lüthi D, Vogt B, et al. Association of urinary sex steroid hormones with urinary calcium, oxalate and citrate excretion in kidney stone formers. Nephrology, dialysis, transplantation : official publication of the European Dialysis and Transplant Association - European Renal Association. 2020.

289. Vargas-Poussou R, Mansour-Hendili L, Baron S, Bertocchio J-P, Travers C, Simian C, et al. Familial Hypocalciuric Hypercalcemia Types 1 and 3 and Primary Hyperparathyroidism: Similarities and Differences. The Journal of Clinical Endocrinology & Metabolism. 2016;101(5):2185-95.

290. Huang H, Feng X, Zhuang J, Fröhlich O, Klein JD, Cai H, et al. Internalization of UT-A1 urea transporter is dynamin dependent and mediated by both caveolae- and clathrin-coated pit pathways. American Journal of Physiology-Renal Physiology. 2010;299(6):F1389-F95.

291. Hayashi H, Inamura K, Aida K, Naoi S, Horikawa R, Nagasaka H, et al. AP2 adaptor complex mediates bile salt export pump internalization and modulates its hepatocanalicular expression and transport function. Hepatology (Baltimore, Md). 2012;55(6):1889-900.

292. Wang N, Silver DL, Thiele C, Tall AR. ATP-binding cassette transporter A1 (ABCA1) functions as a cholesterol efflux regulatory protein. J Biol Chem. 2001;276(26):23742-7.

293. Mukhamedova N, Hoang A, Cui HL, Carmichael I, Fu Y, Bukrinsky M, et al. Small GTPase ARF6 Regulates Endocytic Pathway Leading to Degradation of ATP-Binding Cassette Transporter A1. Arterioscler Thromb Vasc Biol. 2016;36(12):2292-303.

294. Montagutelli X. Effect of the genetic background on the phenotype of mouse mutations. Journal of the American Society of Nephrology : JASN. 2000;11 Suppl 16:S101-5.